RADC-TR-84-185 Interim Report September 1984



ACOSS ELEVEN (ACTIVE CONTROL OF SPACE STRUCTURES)

The Charles Stark Draper Laboratory, Inc.

Sponsored by Defense Advanced Research Projects Agency (DOD) ARPA Order No. 3655

APPROVED FOR PUBLIC RELEASE; DISTRIBUTION UNLIMITED



The views and conclusions contained in this document are those of the authors and should not be interpreted as necessarily representing the official policies, either expressed or implied, of the Defense Advanced Research Projects Agency or the U.S. Government.

THE COUPY

ROME AIR DEVELOPMENT CENTER Air Force Systems Command Griffiss Air Force Base, NY 13441 This report has been reviewed by the RADC Public Affairs Office (PA) and is releasable to the National Technical Information Service (NTIS). At NTIS it will be releasable to the general public, including foreign nations.

RADC-TR-84-185 has been reviewed and is approved for publication.

APPROVED:

RICHARD W. CARMAN Project Engineer

Richard W. Carman

APPROVED:

LAWRENCE J. HILLEBRAND, Colonel, USAF

aurena Hillebran

Chief, Surveillance Division

FOR THE COMMANDER: July a. Rits

JOHN A. RITZ Acting Chief, Plans Office

If your address has changed or if you wish to be removed from the RADC mailing list, or if the addressee is no longer employed by your organization, please notify RADC (OCSP), Griffiss AFB NY 13441-5700. This will assist us in maintaining a current mailing list.

Do not return copies of this report unless contractual obligations or notices on a specific document requires that it be returned.

RADC-TR-84-185 Interim Report September 1984

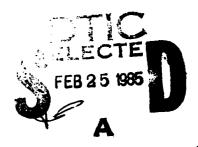


ACOSS ELEVEN (ACTIVE CONTROL OF SPACE STRUCTURES)

The Charles Stark Draper Laboratory, Inc.

Sponsored by
Defense Advanced Research Projects Agency (DOD)
ARPA Order No. 3655

APPROVED FOR PUBLIC RELEASE: DISTRIBUTION UNLIMITED



The views and conclusions contained in this document are those of the authors and should not be interpreted as necessarily representing the official policies, either expressed or implied, of the Defense Advanced Research Projects Agency or the U.S. Government.

IF FILE COP

ROME AIR DEVELOPMENT CENTER Air Force Systems Command Griffiss Air Force Base, NY 13441

ACOSS ELEVEN (ACTIVE CONTROL OF SPACE STRUCTURES)

T.H. Brooks
D.R. Hegg
D.B. Kasle
G.J. Kissel
T.C. Henderson
J.P. Govignon
F.N.R. Ayer
D.R. Hegg
G.J. Kissel
N.H. McClamroch
M.J. Villalba
I.G. Rosen

Contractor: The Charles Stark Draper Laboratory, Inc.

Contract Number: F30602-81-C-0180

Effective Date of Contract: 27 April 1981 Contract Expiration Date: 27 April 1984

Short Title of Work: ACOSS Eleven (Active Control of Space

Structures)

Program Code Number: 4E20

Period of Work Covered: May 1983 - Oct 1983

Principal Investigator: Dr. Keto Soosaar

Phone: 617-484-3125

Project Engineer: Richard W. Carman

Phone: 315-330-4481

Approved for public release; distribution unlimited

This research was supported by the Defense Advanced Research Projects Agency of the Department of Defense and was monitored by Richard W. Carman (OCSP) Griffiss AFB NY 13441-5700, under Contract F30602-81-C-0180

UNCLASSIFIED	
SECURITY CLASSIFICATION OF	THIS PAGE

			REPORT DOCUME	NTATION PAGE	E		ľ
18 REPORT SECURITY CLASSIFICATION			16. RESTRICTIVE M	ARKINGS			
UNCLASSIFIED			N/A			<u>·</u>	
26 SECURITY CLASSIFICATION AUTHORITY			3. DISTRIBUTION/A	VAILABILITY O	FREPORT		
N/A				Approved for	public rel	ease; distri	Lbution
DECLASSIFICATION/D	NRDINO	LDING SCHED	HULE	unlimited		,	
N/A				L			
PERFORMING ORGANIZ	ATION P	REPORT NUM	BER(\$)	5. MONITORING OR	GANIZATION RI	PORT NUMBER	3)
CSDL-R-1687				RADC-TR-84-19	35		•
A NAME OF PERFORMING			SE OFFICE SYMBOL	74 NAME OF MON!	TORING ORGAN	ZATION	
The Charles Star		per	(If applicable)	<u>.</u>	_	4	•
Laboratory, Inc.			<u> </u>	Rome Air Deve			
L. ADDRESS (City, State or				76. ADDRESS (City,			
555 Technology S	•			Griffiss AFB	NY 13441-5	/00	1
Cambridge MA 021	139			1			1
. NAME OF FUNDING/SF	ONSORII	NG	B. OFFICE SYMBOL	9. PROCUREMENT	NSTRUMENT ID	ENTIFICATION N	UMBER
ORGANIZATION Defe	ense A	dvanced	(If applicable)				ł
Research Project			STO	F30602-81-C-0			
L ADDRESS (City, State or		de)		16. SOURCE OF FUR	NOING NOS.		
1400 Wilson Blvd				PROGRAM	PROJECT	TASK	WORK UNIT
Arlington VA 222	209			ELEMENT NO.	NO.	NO.	NO.
				62301E	C655	01	04
1. TITLE (Include Security					•		
ACOSS ELEVEN (AC		CONTROL C	F SPACE STRUCTU	RES)			
2. PERSONAL AUTHORIS	-			_			7
			Transference T T	Corrigion D V			
T.H. Brooks, D.I	s. Kas	le. T.C.		44 0			
34 TYPE OF REPORT	s. Kas	135 TIME C		14. DATE OF REPOR	RT (Yr., Mo., Day)	16. PAGE C	OUNT
3a Type of Report Interim		136. TIME CO	OVERED	44 0	RT (Yr., Mo., Day)		OUNT
3d type of Report <u>Interim</u> 6. Supplementary not		135 TIME C		14. DATE OF REPOR	RT (Yr., Mo., Day)	16. PAGE C	OUNT
3a Type of Report Interim		135 TIME C		14. DATE OF REPOR	RT (Yr., Mo., Day)	16. PAGE C	OUNT
34 TYPE OF REPORT Interim 8. Supplementary NOT N/A	FATION	135 TIME C	83 TO CCL 83	14. DATE OF REPOR	RT (Yr., Mo., Doy) - 1984	18. PAGE 6	O
34 TYPE OF REPORT INTERIM 6. SUPPLEMENTARY NOT N/A 7. COSAN O	TATION ODES	13b. TIME CO	83 TO CCL 83	14. DATE OF REPOR	RT (Yr., Mo., Doy) - 1984	18. PAGE 6	O
34 TYPE OF REPORT INTERIM 6. SUPPLEMENTARY NOT N/A 7. COSAN C FIELD GROUP	TATION ODES	135 TIME C	18 SUBJECT TERMS (C Space-based IR	September September	RT (Yr., Mo., Day) 1984 1984 eccessry and identify Systems	18. PAGE 6 28	O .
34 TYPE OF REPORT INTERIM 6. SUPPLEMENTARY NOT N/A 7. COSAN O	TATION ODES	13b. TIME CO	18 SUBJECT TERMS (C Space-based IR Infrared Terre	September September on tim on truerse if me Surveillance strial Scene S	T (Yr., Mo., Dey) 1984 1984 Systems Simulation	18. PAGE 6 28 Ty by block number	O .
34 TYPE OF REPORT Interim 8. SUPPLEMENTARY NOT N/A 7. COSAN C FIELD GROUP 17	DOES SU	FROM MAY	18 SUBJECT TERMS CONTROL OF SPACE-DASED TERMS	September September Surveillance strial Scene S ted Simulation	1984 1984 regreery and identify stems Simulation to the Cont'd (/y by block number Signal Proce	COUNT O
34 TYPE OF REPORT Interim 8. SUPPLEMENTARY NOT N/A 7. COSAN C FIELD GROUP 17	DOES SU	FROM MAY	18 SUBJECT TERMS CONTROL OF SPACE-DASED TERMS	September September Surveillance strial Scene S ted Simulation	1984 1984 regreery and identify stems Simulation to the Cont'd (/y by block number Signal Proce	COUNT O
3. TYPE OF REPORT Intexim 8. SUPPLEMENTARY NOT N/A 7. COSA'N O FIELD GROUP 17 9. ABSTRACT (Continue o SIMULATION - BSTEEL	DOES SU	FROM MAY	18. SUBJECT TERMS (C Space-based IR Infrared Terre: Draper Integral Idinally by Nach number erall objective	September September Surveillance strial Scene S ted Simulation of the Simula	1984 1984 Systems Simulation as (Cont'd cation Extens	79 by block number Signal Processon reverse)	essors
3A TYPE OF REPORT Interim 6. SUPPLEMENTARY NOT N/A 7. COSATI O FIELD GROUP 17 17 9. ARETRACT (Continue o SIMULATION ESTEL identify and que	ODES SUITE STONE STONE STONE STONE	e. gr.	18. SUBJECT TERMS (C Space-based IR Infrared Terre: Draper Integral Identity by Nach number erall objective meric missing se	September September Surveillance strial Scene S ted Simulation of the Simula cenario and se	1984 1984 Systems Simulation sis (Cont'd cation Extenses parame	79 by block number Signal Processon reverse) sion Projecteters (as we	essors t is to
Interim Supplementary NOT N/A COSANC FIELD GROUP 17 SASSTRACT (Continue of SIMULATION ESTEL identify and que interactions) wh	ODES SUITED STONE	e. GR. The over those gerive the	18. SUBJECT TERMS (C Space-based IR Infrared Terrei Draper Integral Idinally by block number erall objective meric missing superformance of	September September Surveillance strial Scene S ted Simulation of the Simula cenario and sethe space-base	1984 1984 Systems Simulation Sas (Cont'd cation Extenses parameted storing Sto	7 by Nock number Signal Procession Project eters (as we like surveille	essors is to ell as their
Interim Supplementary NOT N/A COSAN C FIELD GROUP 17 S. ABSTRACT (Continue of SIMULATION POTE identify and que interactions) will The approach tal	n rooms in Stoke antify hich diken to	B. GR. The over those gerive the achieve	Is subject teams of Space-based IR Infrared Terres Draper Integral identity by block number reall objective meric missing superformance of this overall objection	September September September Surveillance strial Scene S ted Simulation of the Simula cenario and se the space-base jective has pr	1984 1984 1984 Systems Simulation Since (Cont'd Cont'd Con	y by block number Signal Procession Project eters (as well a surveillating two tains	essors t is to ell as their ance systems a avenues:
Interim Supplementary NOT N/A COSAN C FIELD GROUP 17 SASTRACT (Continue of STMULATION POTE identify and que interactions) wh The approach tal Simulation Enhan	n recent of the state of the st	a. GR. The over those gerive the achieve ts; and S	Is subject terms of Space-based IR Infrared Terres Draper Integral identity by block number retail objective meric missing superformance of this overall objection imulation Application in the superformance of the superf	September September September Surveillance strial Scene S ted Simulation of the Simula cenario and se the space-base jective has pr cations. Duri	1984 1984 1984 Systems Simulation Sincord Cont'd Co	y by block number Signal Procession Project eters (as well as surveillable two trains one trains on the trains of the trains o	essors t is to ell as their ance systems a avenues:
Interim Supplementary NOT N/A T. COSAN OF SINCE GROUP 17 SASTRACT (Continue of SIMULATION POTE identify and que interactions) where the simulation Enhance the Simulation Interaction I	NODES SUNTANIAN NOTIONAL NOTIONAL	B. GR. B. GR. Chickenson and Secretary and	Is subject terms of Space-based IR Infrared Terres Draper Integral district meric missing superformance of this overall objective involves of this overall objective involves of this overall objective involves o	September September September Surveillance strial Scene S ted Simulation of the Simula cenario and se the space-base jective has pr cations. Duri trated in three	1984 1984 1984 Systems Simulation Simulation Extendents Cont'd Co	Ay block number Signal Procession Project eters (as well surveillable two training train	essors t is to ell as their ance systems n avenues: ing period, n of the
Interim Supplementary Not N/A COSAN C FIELD GROUP 17 ABSTRACT (Continue of SIMULATION POTE identify and qua interactions) wh The approach tal Simulation Enhant the Simulation I Generic Scene St	NOOES NO	B. GR. The over those gerive the achieve ts; and Sements effort developments.	Is subject teams of Space-based IR Infrared Terrer Draper Integral identity by block number reall objective meric missing superformance of this overall objection in the subject of the su	September September September Surveillance strial Scene S ted Simulation of the Simulation the space-base jective has protations. Duri trated in three ments to the S	1984 1984 1984 Systems Simulation Simulation Extension parameted storing Stockeded aletting the currice areas: Signal Procession	Ay Nock number Signal Procession Project eters (as well as surveillating two main rent reports continuation essor Simulation essor e	essors t is to ell as their ance systems a avenues: ing period, a of the ation; and
Interim Supplementary NOT N/A COSAN C FIELD GROUP 17 SAMULATION BOTE identify and que interactions) wi The approach tal Simulation Enhan the Simulation I Generic Scene Si expansion of the	n reverse in reverse i	B. GR. B. GR. B. GR. Chieve the achieve ts; and Sements effon devel bilities	18 SUBJECT TERMS (C) Space-based IR Infrared Terre Draper Integral identity by block number erail objective meric missing se performance of this overall ob- imulation Appli- fort has concen- copment; enhance of the Integrat-	September September Surveillance strial Scene S ted Simulation of the Simulation the space-base jective has pr cations. Duri trated in three ments to the S ed Large Space	1984 1984 1984 1984 Systems Simulation Simulation Extenses parameted storing Stoceeded alcong the current areas: Signal Process Structures	Ay block number Signal Procession Project eters (as well as years to make the property of the	essors t is to ell as their ance systems a avenues: ing period, n of the ation; and n. The
Interim Supplementary Not N/A COSANC FIELD GROUP 17 SAMETRACT (Continue of SIMULATION ESTEN identify and que interactions) wh The approach tal Simulation Enhant the Simulation If Generic Scene Si expansion of the Simulation Appli	SUNSTANDA TO THE PROPERTY OF T	a. GR. The over those gerive the achieve ts; and Sements efficients are sements effort the sements effort t	Is subject teams of Space-based IR Infrared Terres Draper Integral evall objective meric missing superformance of this overall objimulation Application to the Integration of the Integration as been focus	September September Surveillance strial Scene S ted Simulation of the Simula cenario and se the space-base jective has pr cations. Duri trated in thre ments to the S ed Large Space ed most recent	Tyr. Me. Devi 1984 1984 Systems Simulation Simulation Statement of the current of the curren	ry by block number 28 28 28 28 28 28 29 20 20 20 20 20 20 20 20 20 20 20 20 20	essors t is to ell as their ance systems a avenues: ing period, a of the ation; and the evaluation
Interim Supplementary NOT N/A T. COSAN OF FIELD GROUP 17 S. ABSTRACT (Continue of SIMULATION ESTEL identify and qual interactions) where the simulation Enhance the Simulation of the Simulation Applic of algorithms for	NATION NATION NATIONS ANTIFY HICH di Ken to Ancemen Enhance imulat e capa ication or line	B. GR. The over those gerive the achieve ts; and Sements efion developments of the sements of t	Ta Subject TERMS (Cot 83) To Cot 83 To Cot 84 To Cot	September September September Surveillance strial Scene S ted Simulation of the Simulation of the Simulation the space-base jective has protations. Duri trated in three ments to the S ed Large Space ed most recent ion.	1984 1984	Ay Nock number 28 Signal Processon reverse) Sion Project eters (as well as surveillation two main report continuation essor Simulation and continuation and c	essors t is to ell as their ance systems a avenues: ing period, a of the ation; and a. The evaluation tien Technology
Interim Supplementary NOT N/A T. COSAN OF FIELD GROUP 17 S. ABSTRACT (Continue of SIMULATION ESTEL identify and qual interactions) where the simulation Enhance the Simulation of the Simulation Applic of algorithms for	NATION NATION NATIONS ANTIFY HICH di Ken to Ancemen Enhance imulat e capa ication or line	B. GR. The over those gerive the achieve ts; and Sements efion developments of the sements of t	Ta Subject TERMS (Cot 83) To Cot 83 To Cot 84 To Cot	September September September Surveillance strial Scene S ted Simulation of the Simulation of the Simulation the space-base jective has protations. Duri trated in three ments to the S ed Large Space ed most recent ion.	1984 1984	Ay Nock number 28 Signal Processon reverse) Sion Project eters (as well as surveillation two main report continuation essor Simulation and continuation and c	essors t is to ell as their ance systems a avenues: ing period, a of the ation; and a. The evaluation tien Technology
Interim Supplementary NOT N/A T. COSAN C FIELD GROUP 17 S. ABSTRACT (Continue of SIMULATION ESTEL identify and quainteractions) when the Simulation Enhant the Simulation Enhant the Simulation of the Simulation Application Appli	NSTONS antify hich diken to neemen Enhancimulate capa ication or line	The over the achieve ts; and Sements efion developments efforte-of-sighthin the	Is subject teams of Space-based IR Infrared Terred	September September September Surveillance strial Scene S ted Simulation of the Simulation of the Simulation the space-base jective has protations. Duri trated in three ments to the S ed Large Space ed most recent ion. Ro	1984 1984 1984 1984 1984 1984 1984 1984	Ty by Nock number 28 Signal Processor Project eters (as well as surveillating two main reportion tinuation essor Simulation and ets Fabrica acterization	essors is to ell as their ance systems a avenues: ing period, a of the ation; and a. The evaluation their Technology
Interim Supplementary Not N/A T. COSAN C FIELD GROUP 17 S. ABSTRACT (Continue of SIMULATION ESTEL identify and quainteractions) where the Simulation Enhance the Simulation Enhance the Simulation of the Simulation Application Application Application Application Control Price (Continue of Simulation Enhanced Price (Continue of Simulation Enhanced Price (Continue of Simulation Application Applic	NOTES NO	The over the achieve ts; and Sements effort e-of-sight thin the pace mirr	Is susject teams of Space-based IR Infrared Terred	September September September Surveillance strial Scene S ted Simulation of the Simulation of the Simulation the space-base jective has protations. Duri trated in three ments to the S ed Large Space ed most recent ion. Root e ROFT program by examining	1984 1984 1984 1984 1984 1984 1984 1984	Signal Processor (as well as surveillation and case of material of material	essors is to ell as their ance systems a avenues: ing period, a of the ation; and a. The evaluation tien Technology
Interim Supplementary Not N/A COSANC FIELD GROUP 17 SAMETRACT (Continue of SIMULATION ESTER identify and que interactions) what the simulation Enhant the Simulation Enhant the Simulation of the Simulation Application Application of the Simulation Application Application of the Simulation Application Appli	NSTONE antify hich diken to ncemen Enhanceimulate capaication or linuxiarge she per	The over the achieve ts; and Sements efion develobilities the cof-sight thin the pace mirr formance	Is susject teams (c Space-based IR Infrared Terrer Draper Integral evall objective meric missing seperformance of this overall objimulation Application for the Integrate has been focus it jitter reduct framework of theory is obtained of mirrors. The	September September Surveillance strial Scene S ted Simulation of the Simulation the space-base jective has pr cations. Duri trated in three ments to the S ed Large Space ed most recent ion. Ro ROFT program by examining e study recogn	Systems Systems Simulation as (Cont'd of the current of the curren	ry by block number 28 Signal Processor Project eters (as well as well as well as well as simulation and continuation as Simulation and continuation and contin	essors is to ell as their ance systems a avenues: ing period, a of the ation; and a. The evaluation tien Technology
Interim Supplementary Not N/A T. COSAN C FIELD GROUP 17 S. ABSTRACT (Continue of SIMULATION ESTEL identify and quainteractions) where the Simulation Enhance the Simulation Enhance the Simulation of the Simulation Application Application Application Application Control Price (Continue of Simulation Enhanced Price (Continue of Simulation Enhanced Price (Continue of Simulation Application Applic	NSTONE antify hich diken to ncemen Enhanceimulate capaication or linuxiarge she per	The over the achieve ts; and Sements efion develobilities the cof-sight thin the pace mirr formance	Is susject teams (c Space-based IR Infrared Terrer Draper Integral evall objective meric missing seperformance of this overall objimulation Application for the Integrate has been focus it jitter reduct framework of theory is obtained of mirrors. The	September September September Surveillance strial Scene S ted Simulation of the Simulation of the Simulation the space-base jective has protations. Duri trated in three ments to the S ed Large Space ed most recent ion. Root e ROFT program by examining	Systems Systems Simulation as (Cont'd of the current of the curren	ry by block number 28 Signal Processor Project eters (as well as well as well as well as simulation and continuation as Simulation and continuation and contin	essors is to ell as their ance systems a avenues: ing period, a of the ation; and a. The evaluation tien Technology
Interim Supplementary Not N/A T. COSAN OF SINCE GROUP 17 S. ABSTRACT (Continue of SIMULATION POTEIN during and quainteractions) when the Simulation Enhanthe Simulation Enhanthe Simulation Application of the Simulation Application algorithms for the Simulation Application of algorithms for the Simulation Application Applicat	NSTONS antify hich di ken to ncemen Enhance imulate e capa ication or line arge s he per	B. GR. The over the achieve ts; and Sements effort e-of-sight thin the pace mirr formance	Is subject teams of Space-based IR Infrared Terrer Draper Integral erail objective meric missing superformance of this overall objective subject to the second of the Integration of the Integration in the Integration of the	September September September Surveillance strial Scene S ted Simulation of the Simulation of the Simulation the space-base jective has protations. Durit trated in three ments to the S ed Large Space ed most recent ion. Role ROFT program by examining e study recogn 21. AASTRACT SECU	Systems Systems Simulation as (Cont'd of the current of the curren	ry by block number 28 Signal Processor Project eters (as well as well as well as well as simulation and continuation as Simulation and continuation and contin	essors is to ell as their ance systems a avenues: ing period, a of the ation; and a. The evaluation tien Technology
Interim Supplementary NOT N/A 7. COSATIC FIELD GROUP 17 S. ARETRACT (Continue of SIMULATION ESTEL identify and quainteractions) where the Simulation Enhant the Simulation Enhant the Simulation of the Simulation Application of the Simulation Application Applicatio	n greens in STONE antify hich diken to ncemen Enhancimulate capa ication or line arge she per	The over the achieve ts; and Sements effort e-of-sight thin the pace mirr formance	Is subject teams of Space-based IR Infrared Terrer Draper Integral erail objective meric missing superformance of this overall objective subject to the second of the Integration of the Integration in the Integration of the	September September Surveillance strial Scene S ted Simulation of the Simulation the space-base jective has pr cations. Duri trated in three ments to the S ed Large Space ed most recent ion. Ro ROFT program by examining e study recogn	Systems Systems Simulation as (Cont'd of the current of the curren	ry by block number 28 Signal Processor Project eters (as well as well as well as well as simulation and continuation as Simulation and continuation and contin	essors is to ell as their ance systems a avenues: ing period, a of the ation; and a. The evaluation tien Technology
Interim Supplementary Not N/A T. COSAN OF SINCE GROUP 17 S. ABSTRACT (Continue of SIMULATION POTEIN during and quainteractions) when the Simulation Enhanthe Simulation Enhanthe Simulation Application of the Simulation Application algorithms for the Simulation Application of algorithms for the Simulation Application Applicat	n greens in STONE antify hich diken to ncemen Enhancimulate capa ication or line arge she per	The over the achieve ts; and Sements effort e-of-sight thin the pace mirr formance	Is subject teams of Space-based IR Infrared Terrer Draper Integral erail objective meric missing superformance of this overall objective subject to the second of the Integration of the Integration in the Integration of the	September September September Surveillance strial Scene S ted Simulation of the Simulation of the Simulation the space-base jective has protations. Durit trated in three ments to the S ed Large Space ed most recent ion. Robert Program by examining e study recogn 21. ASSTRACT SECU- UNCLASSIFIED	1984 1984 1984 1984 1984 1984 1984 1984 1984 1984 1986	ry by block number 28 Signal Processor Project eters (as well as well as well as well as simulation and continuation as Simulation and continuation and contin	essors t is to ell as their ance systems a avenues: ling period, a of the ation; and a. The evaluation turn Technolog a of b for (over)
Interim Supplementary NOT N/A 7. COSATIC FIELD GROUP 17 S. ARETRACT (Continue of SIMULATION ESTEL identify and quainteractions) where the Simulation Enhant the Simulation Enhant the Simulation of the Simulation Application of the Simulation Application Applicatio	NSTONE antify hich diken to ncemen Enhanceimulate capalication or linury arge she per ASILITY	The over the achieve ts; and Sements effort e-of-sight thin the pace mirr formance	Is subject teams of Space-based IR Infrared Terrer Draper Integral erail objective meric missing superformance of this overall objective subject to the second of the Integration of the Integration in the Integration of the	September September September Surveillance strial Scene S ted Simulation of the Simula cenario and se the space-base jective has pr cations. Duri trated in three ments to the S ed Large Space ed most recent ion. Ro e ROFT program by examining e study recogn 21. ASSTRACT SECU UNCLASSIFIED 22b. TELEPHONE No. (Include Area Co	1984 1984	Ty by Nock number 28 Signal Processor Project eters (as well as a well as a well as simulation essor Simulation and (as Fabrica eterization of material differences CATION	essors t is to ell as their ance systems a avenues: ing period, a of the ation; and a. The evaluation twin Technolog a for (over).
Interim Supplementary Not N/A COSAR C FIELD GROUP 17 S. ARETRACT (Continue of SIMULATION ESTER Identify and quadrateristic and interactions) will approach tall simulation Enhant the Simulation Enhant the Simulation of Expansion of the Simulation Application of algorithms for HALO OPTICS/ROP materials for is properties on the Distribution/AVAIL COSAR	NOTES NO	The over the achieve ts; and Sements effort e-of-sight thin the pace mirr formance	Is subject teams of Space-based IR Infrared Terrer Draper Integral erail objective meric missing superformance of this overall objective subject to the second of the Integration of the Integration in the Integration of the	September September September Surveillance strial Scene S ted Simulation of the Simulation of the Simulation the space-base jective has protations. Durit trated in three ments to the S ed Large Space ed most recent ion. Robert Program by examining e study recogn 21. ASSTRACT SECU- UNCLASSIFIED	1984 1984	ry by block number 28 Signal Processor Project eters (as well as well as well as well as simulation and continuation at the simulation and continuation of material differences cation	essors t is to ell as their ance systems a avenues: ing period, a of the ation; and a. The evaluation twin Technolog a for (over).

UNCLASSIFIED

SECURITY CLASSIFICATION OF THIS PAGE

material requirements between IR systems and laser applications.

ACTIVE—CONTROL OF SPACE STRUCTURES: Research in active structural control encompasses design of reduced-order controllers for vibration suppression; development of approaches to system parameter identification; and generation of large-angle slew maneuvers. In this report, theoretical advances and demonstrations in the first two categories are presented. A scientific experiment to examine the process of synthesizing feedback controllers for precision pointing of a passive optical system in a wideband disturbance environment is continued. Design demonstrations with ACOSS Model No. 2 suggest the attractiveness of rotational actuators. Explicit conditions for geometric stability with sampled-date feedback incorporating output estimation are given. Use of second-order dynamic models avoids masking the special features of the open-loop dynamics. A parametric power spectrum estimation technique is developed to enable high-resolution identification of finite-dimensional system models. Processing operates on data available from vehicles in flight. A spline-based approximation technique to estimate parameters of infinite-dimensional models is developed. Application is made to a cantilevered beam with tip mass represented by a hybrid system of ordinary and partial differential equations.

Block 12. Personel Author(s) (Cont'd)

G.J. Kissel, N.H. McClamroch, M.J. Villalba, I.G. Rosen

Block 18. Subject Terms (Cont'd)

Materials Characterization for Space Optics Large Flexible Space Structures Line-of-Sight Stabilization Precision Pointing Clustered Natural Frequencies Vibration Control Wideband Disburbance Accommodation Active Control Synthesis Recuced-Order Modeling Active Transducer Selection Colocation Least-Squares Approximation Disturbance-Rejection Control Linear-Quadratic-Gaussian Control Scientific Experiment ACOSS Model No. 2 Sampled-Data Control Second-Order Difference Equations State Extimation Output Estimation Velocity Feedback Displacement Feedback Geometric Stability

High Resolution System Identification

Parametric Power Spectrum Estimation Autocorrelation Desampling Yule-Walker Pole Estimation Sensitivity Moore-Walker Pole Estimation Condition Number Singular Values . Infinite-Dimensional System Identification Cantilever Beam with Tip Mass Hybrid Systems of Differential Equations Banach Space Hilbert Space Sobolev Space Linear Semigroup Theory Cubic Spline-Based Approximation Lebesque Convergence Theorems Steepest Descent

UNCLASSIFIED

SECURITY CLASSIFICATION OF THIS PAGE

E

Accession For	$\overline{}$
NTIS GRAEI	
In managed	
*	
Distribution/ Assilability Co	
dval. and/o	
Dist Special	
M	

ACKNOWLEDGEMENT

■ 大きない からか マーディング からない 10mm

からいことには自己はないというとは、これのはなかなる。これのなから、これではないはないは、これにはないとないとなっているとはない。

This report was prepared by The Charles Stark Draper Laboratory, Inc., under Contract F30602-81-C-0180. This research was supported by the Advanced Research Projects Agency of the Department of Defense (STO/Lt. Col. Allen F. Herzberg) and monitored by the Rome Air Development Center (OCSP/Mr. Richard W. Carman).



The Program Manager for ACOSS-Eleven at CSDL is Dr. Keto Soosaar. The individual Project Leaders are: Mr. Thomas H. Brooks (Simulation Extensions), Mr. Francois N. R. Ayer (HALO Optics/ROFT) and Mr. Robert R. Strunce (Active Control of Space Structures). The authors of this report are: Mr. Thomas H. Brooks (Section 1.1); Photon Research Associates - Mr. David Anding, GENESSIS Program Manager (Section 2.1); Mr. David B. Kasle (Section 2.2); Mr. Timothy C. Henderson (Section 2.3); Mr. Jacques P. Govignon (Section 2.4); Mr. Francois N. R. Ayer (Sections 1.2, 3); Dr. Daniel R. Hegg (Sections 1.3, 4, 5); Mr. Glen J. Kissel (Section 5); Dr. N. Harris McClamroch of the University of Michigan (Section 6); Mr. Michael J. Villalba (Section 7); and Dr. I. Gary Rosen (Section 8). Assistance from Mr. Saul Serben (Software support -Sections 2.1, 2.3, 2.4); Dr. Eliezer Fogel (Sections 5, 7); Dr. N. Harris McClamroch and Mr. Patrick B. Battstone (Section 5); and Dr. H. Thomas Banks of Brown University, Major James Crowley of the United States Air Force Academy, Mr. Joel A. Storch, and Mr. Stephen S. Gates (Section 8) is gratefully acknowledged. Ms. Mary M. Markley and Ms. Lisa J. Gorman (Sections 1-3), and Ms. Lisa E. Kern (Sections 4-8) did the typing.

Publication of this report does not constitute approval by the Defense Advanced Research Projects Agency or the United States Government of the findings or conclusions contained herein. It is published for the exchange and stimulation of ideas.

TABLE OF CONTENTS

Section	<u>n</u>		Ţ	age
1	INTR	ODUCTIO	v	1
	1.1	Simulat	tion Extensions	1
	1.2	Generi	Requirements for the ROFT Program	1
	1.3	Active	Control of Space Structures	3
2	SIMU	LATION 1	EXTENSIONS	. 5
	2.1	Generic	Scene Simulation (GENESSIS)	5
		2.1.1	Background	5
		2.1.2	GENESSIS II Overview	. 5
		2.1.3	New Software	6
	2.2	Signal	Processor Enhancements	14
		2.2.1	Signal Processor Review	14
		2.2.2	Spatial Pixel Integration	18
		2.2.3	Track Acquisition	21
		2.2.4	Simple Thresholding	34
		2.2.5	CFAR Algorithm Development	40
		2.2.6	Track Discrimination	44
		2.2.7	Areas of Future Investigation	46
	2.3	Integra	ated Large Space Structure Simulation (ILS3)	48
		2.3.1	Introduction	48
		2.3.2	Output Optical Grid	50
		2.3.3	Search	51
		2.3.4	Interpolation Methods	59
		2.3.5	Wavefront Error Computation	69
		2.3.6	Summary	73

Section	1	<u>Pag</u>	<u>e</u>
	2.4	Investigation of Line-of-Sight Jitter Reduction	
			4
		2.4.1 Introduction 7	74
		2.4.2 Reduction of Jitter Effects 7	14
		2.4.3 Application to a Representative Surveillance	
		Problem 7	7
		2.4.4 Results	32
		2.4.5 Conclusions	35
		References8	37
		Appendix 1: Signal Processor Simulation	
		User's Guide 8	88
		Appendix 2: Effects of Target Phasing	
		on Signal Processor Performance 9	92
3	GENE	RIC REQUIREMENTS FOR THE ROFT PROGRAM)1
	3.1	Introduction and Approach)1
		3.1.1 Introduction 10)1
		3.1.2 Objective and Approach 10)2
	3.2	Materials for Space Optics)3
		3.2.1 Introduction and Approach)3
		3.2.2 Equations Relating Mirror Distortions to	
		Disturbances 10)7
		3.2.3 Material Properties and Figures of Merit 11	4
	3.3	Conclusions and Recommendations	9
4	ACTI	VE CONTROL OF FLEXIBLE SPACE STRUCTURES A PERSPECTIVE 12	27
	4.1	Scope 12	27
	4.2	Vibration Control 12	27
	4.3	System Identification 12	29
	4.4	Current Directions	30

Section	<u>1</u>	<u>P</u>	age
5	PROGE	RESS ON SYNTHESIS OF ACTIVE CONTROL FOR WIDEBAND	
	DIST	URBANCE ACCOMMODATION WITH ACOSS MODEL NO. 2	133
	5.1	Motivation	
	5.2	The Experimental ApproachA Review	134
	3. 3		
		5.3.1 Active Transducer Selection	
		5.3.2 Controller Design and Evaluation	147
	5.4	Work in Progress	
		References	
6	CTA DI	ILIZATION OF FLEXIBLE STRUCTURES USING SAMPLED DATA	
O		BACK	166
	6.1	Overview	133
	6.2	Recursions for Sampled Data Controlled Flexible	
		Structures	
	6.3	Importance of Controller Dynamics	
	6.4	Stabilization Based on Estimated State Feedback	159
	6.5	Stabilization Based on Estimated Output Velocity	
		Feedback	161
	6.6	Stabilization Based on Estimated Output Displacement	
		Feedback	167
	6.7	Conclusions	172
	6.8	Appendix	173
		Pafarances	174

Section	<u>1</u>			Page
7	ON T	E USE OF AUTOCORRELATIO	N DESAMPLING IN HIGH	
	RESO	UTION SPECTRUM ESTIMATI	ON	175
	7.1			
			•••••	-
			re	
	7.2		um Estimation	
	,		ion Sequence Model	
			tion	
	7.3		n Parameter Estimation	
	, ,,	•	of Sensitivity	
			e Condition Number	
			le Location	
	7.4		in Improving Spectral Resolution	
			sampling the Autocorrelation	
			•••••	224
		-	toregressive Coefficients	
			stimates from Desampled	
			timates	228
	7.5			
	, .,	•		
8		IC SPLINE BASED APPROXI		
			HYBRID SYSTEMS INVOLVING	
			• • • • • • • • • • • • • • • • • • • •	
	8.1		•••••••	
	8.2	The Identification Prob	lem and its Abstract Formulation	237

Section	Page
8.3	The Approximation Scheme and Convergence Results 24
8.4	A Numerical Example
8.5	Concluding Remarks
	References

SECTION 1

INTRODUCTION

1.1 Simulation Extensions

The objective of this project is to identify and quantify those generic mission, scenario and sensor parameters (as well as their interactions) which drive the performance of space-based staring IR surveillance systems. These efforts have been divided into two broad tasks: Simulation Enhancements, and Simulation Applications.

Work in the Simulation Enhancements area is directed toward generalizing those models in the Draper Integrated Simulations (DIS) which are too limited in scope or perhaps restricted to one particular system. During the current reporting period these efforts have been concentrated in three areas: continuation of the Generic Scene Simulation Development; Signal Processor Simulation enhancements; and Integrated Large Space Structures Simulation (ILS³) enhancements.

The Simulation Applications effort studies issues related to generic surveillance system performance drivers using tools from the Simulation Enhancement effort. During the current reporting period this effort has focussed on simulation and evaluation of algorithms for line-of-sight jitter reduction in staring mosaic sensors.

1.2 Generic Requirements for the ROFT Program

The development of space-based infrared surveillance systems and space-based lasers is subordinated primarily to the availability of very large, high precision optics. Current technology and existing facilities cannot produce in a timely fashion, high performance mirrors, both in quality and quantity, to respond to the needs of the systems envisioned. The Rapid Optics Fabrication Technology (ROFT) Program will attempt to discover and develop technologies which will significantly decrease the time it takes to produce optics.

The objective of this study reported in Section 3, is to provide broad requirements and constraints for the mechanical and thermal properties of materials envisioned for the design and rapid fabrication of large space mirrors. By inspecting the constitutive equations relating mirror deformations to input disturbances, the relative importance of material parameters is identified. It is also recognized that the requirements on mirror material properties can vary widely depending on the space applications. Surveillance systems, operating at cryogenic temperatures impose different demands on materials than do the laser systems for which the operational temperature is expected to vary between 300° K and 400° K. Dynamic environments exhibit significant differences as well, and this difference may impact the choice of other properties required of the mirror materials.

It must be emphasized that this study does not presuppose a specific mirror concept with defined structural and configurational characteristics. While this approach is intentional for the findings to remain general, it limits our ability to obtain specific requirements for the contemplated mirror materials. Furthermore the effectiveness of possible controls (whether thermal or mechanical), in terms of relieving demands on material properties can only be evaluated in the context of a defined mirror concept. As a result only estimates on mirror material requirements can be provided and they have been derived from simplified analytical expressions and engineering experience in the design, modelling and analyses of space mirrors.

For a large number of existing and potential materials, that include metals, composites and ceramics, all relevant properties have been tabulated for two extreme operational temperatures (150° K and 350° K). The plots relating important material parameters can be useful in delineating domains of acceptability for a potential new material. The proposed material requirements can be viewed as somewhat flexible so as to permit tradeoffs between properties for a particular design concept. Past experience has shown that the most likely candidate for such a mirror will probably be a thin face-sheet on actuators supported by a thermally stable substrate.

However, it is hoped that dramatic changes and/or improvements in some thermal properties, especially, might lead to completely novel concepts that ultimately could be produced at the desired rapid rate.

It should be remembered that the objective of the ROFT program is the rapid fabrication of high precision large space optics. The results of this study can only support this attempt by providing guidelines to the designer and fabrication engineer who selects possible materials. The generic specifications of mirror materials, therefore, can be viewed as constraints to the selection of a material amenable to rapid fabrication processes. Many other issues related to optical and perhaps electrical material properties need to be considered. Finally the fabrication process could be adversely affected by some mechanical and thermal properties of a material that is otherwise acceptable in the final product.

1.3 Active Control of Space Structures

Space-based passive optical surveillance systems require a capability for active control to achieve precision attitude regulation and rapid reorientation in spite of structural vibrations induced by actuators or by disturbances. Because of the inherent limitations on the achievable accuracy in modeling complex interconnected structures, a capability for system parameter identification is required in order to attain specified control system performance. In the present report, contributions toward the understanding of vibration control using both analog and digital models are made, and techniques for system identification in both finite-dimensional and infinite-dimensional systems are developed. A detailed overview of results to be presented is given in Section 4. Large-angle slew results are not included.

A continued presentation of results relating to systematic examination of the process for synthesis of active controllers in a wideband disturbance environment is given in Section 5. The emphasis is upon evaluating the comparative efficacy of active transducer configurations in achieving specified regulation with the ACOSS Model No. 2 structural model. Rotational actuators emerge as particularly attractive because the number of

actuators required to achieve acceptable performance is relatively small. Sampled-data analysis of flexible structures using second-order dynamic models and focused on developing closed-loop stability criteria is given in Section 6. Explicit stability guarantees are obtained using dynamic compensation approaches of practical interest which do not require full state estimation. A signal processing algorithm appropriate for in-flight parameter estimation with finite-dimensional structural models is developed in Section 7. The approach is especially tailored to be capable of the high resolution needed for structures with clustered frequencies and small damping. Finally, a spline-based approach to parameter estimation with infinite-dimensional structural models is developed and successfully applied to a beam example in Section 8. The latter result derives significance from the fact that there is growing practical interest in distributed parameter identification because of current hardware experiments on distributed sensing and actuation.

SECTION 2

SIMULATION EXTENSIONS

2.1 Generic Scene Simulation (GENESSIS)

2.1.1 Background

In support of the Draper Integrated Simulations Extensions effort, Photon Research Associates (PRA) has developed (under subcontract to CSDL) a computer code capable of generating and manipulating terrestrial scenes as a function of major surveillance system and mission parameters. This code (called GENESSIS) has the capability to interface with the Defense Mapping Agency (DMA) data base of terrestrial scenes as the source of scene input data. Consequently, the code is able to simulate any scene for which DMA data exists.

Because it was desirable to have a functioning code as soon as possible, the code was developed in two phases (each phase spanning approximately one calendar year). The first phase provided a functional synthetic scene simulation computer code [1] with some limitations. In particular, some of the higher-order phenomena controlling scene radiance (e.g., cloud shadowing) were neglected, some of the phenomenological treatments utilized simplifying approximations, and the input data base was limited to five terrestrial scenes and two cloud representations. A number of these restrictions were eliminated during the subsequent phase.

The following paragraphs present the status of the GENESSIS code at the end of the final phase. Additions and modifications of GENESSIS I are summarized, which upgrade it to GENESSIS II.

2.1.2 GENESSIS II Overview

The GENESSIS II effort consisted of performing the following tasks:

 Development of geometric representations of three cloud patterns (scenes), each for a different cloud type.

- 2) Development of software which assigns surface level temperature and wind speeds as continuously variable quantities interpolated from user-specified values at selected locations.
- 3) Modification of the bi-cubic spline interpolation routine to eliminate edge artifacts caused by abrupt altitude changes.

Task 3 was a redirected effort and also included the generation of additional software documentation and support to CSDL in the use of GENESSIS

I. The program deliverables included the following:

- 1) New software to generate and utilize spatially variable surface level temperatures and wind speeds.
- 2) Three additional cloud scenes (stratus, altocumulus and cirrus).
- 3) New and modified software to eliminate edge artifacts produced by the bi-cubic spline interpolation routine.
- 4) Additional Atmospheric, Geometric, and Radiance Module software documentation.

2.1.3 New Software

New software consists of two parts: an off-line fitting/smoothing routine which generates temperature and wind speed arrays from user supplied data; and interpolation software internal to GENESSIS which utilizes the off-line produced data to supply point-by-point wind speed and temperature values to the Radiance Module.

2.1.3.1 The Surface Level Parameter Generation Program

SPGNER creates an N×M matrix of temperature or wind speed values from a set of user specified data. This array maps onto the scene, thereby allowing the user to supply the Radiance Module with spatially varying wind speed and air temperatures.

In general, ground truth data or user selected values of wind speed and air temperature will be available at only a few specific points for a given scene. SPGNER produces a smoothly varying array of values from these known points using the iterative numerical technique of successive over-relaxation. [2] Input values are not altered by the routine.

An example of SPGNER usage is shown in Figure 2-1. The array elements 1-5 represent a minimum set of user specified inputs of air temperature or wind speed. The boundary (points 1-4) and at least one internal point must always be specified. As many additional points as desired may be included. Elements are referenced by their row, column position, e.g., point 5 is element (3,4). Surface parameter arrays may be any dimension (square or rectangular) up to 128 × 128 that maps conveniently onto the scene, but both the wind speed and air temperature arrays must have the same dimensions.

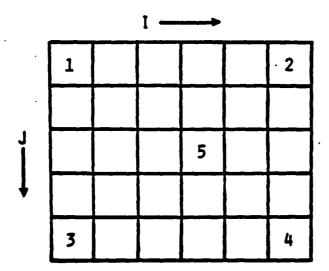


Figure 2-1. Example of inputs to subroutine SPGNER.

2.1.3.1.1 Inputs

ACCES REPORTED A CONTRACTOR OF THE CONTRACTOR OF

Card numbers refer to sample input list shown in Table 2-1.

Card 1) NCOL, NROW, DBSW (216, 2X, 1A4)

- NCOL The number of columns in the surface parameter output array.
- NROW The number of rows in the surface parameter output array.
- DBSW Debug switch. If equal to 1 an ASCII echo of a portion of the surface parameter array is produced.

 If equal to 0 no ASCII echo of the surface parameter array is made.

SPGNER reads and processes the boundaries, then reads and processes the interior points. The boundary edges are input and processed in the following order: top, bottom, left, right.

CONCERNO PROPERTY OF THE SECOND SECON

Table 2-1. Sample SPGNER input list. Values are air temperatures.

13	64	64	1
2)	ţ,		
3)	1	284. 0	
4)	16	288. 0	
5)	32	283. 0	
6)	48	283. 0	
7)	64	283. 0	
8)	5		•
9)	3	284. 0	
10)	16	288. 0	
11)	32	283.0	
12)	4(1	283 0	
13)	64	283. 0	
14)	i.		
15)	1	284. 0	
16)	64	284.0	
17)	٤٠		
18)	1	283. 0	
19)	64	283.0	
20)	6		
21)	16	48	300.0
55).	32	48	300. O
23)	63	48	300.0
24)	16	32	300.0
25)	コン	32	300.0
26)	63	35	300.0

Card 2) NPTS (16)

NPTS - The number of top edge boundary values to be read.

Cards 3-7) TEMP, ARRAY2(I) (I = 1, NPTS)

TEMP - Column location of input value along top edge counted left to right.

ARRAY2(I) - Value (temperature or wind speed) to be assigned to surface parameter array.

Card 8) NPTS (16)

NPTS - The number of bottom edge boundary values to be read.

Cards 9-13) TEMP, ARRAY2(I) (I = 1, NPTS) (I6, F10.2)

TEMP - Column location of input value along bottom edge counted left to right.

ARRAY2(I) - Value (temperature or wind speed) to be assigned to surface parameter array.

Card 14) NPTS (16)

スプラフィン 海風 アオタクシス 自動をなるななな 無力できない 空間です

NPTS - The number of left edge boundary values to be read.

Cards 15-16) TEMP, ARRAY2(I) (I = 1, NPTS) (I6, F10.2)

TEMP - The row location of the input value along the left edge counted top to bottom.

ARRAY2(I) - Value (temperature or wind speed) to be assigned to surface parameter array.

Card 17) NPTS (16)

NPTS - The number of right edge boundary values to be read.

Cards 18-19) TEMP, ARRAY2(I) (I = 1, NPTS) (I6, F10.2)

TEMP - The row location of the input value along the right edge counted top to bottom.

ARRAY2(I) - Value (temperature or wind speed) to be assigned to surface parameter array.

Card 20) NPTS (16)

NPTS - The number of interior values to be read.

Cards 21-26 RINDX, CINDX, VAL (216, F10.2)

RINDX - Row location of interior point counted top to bottom.

CINDX - Column location of interior point counted left to right.

VAL - Value (temperature or wind speed) to be assigned to surface parameter array.

2.1.3.1.2 File Units

FORTRAN UNIT	READ, WRITE OR READ/WRITE	FILE
5	R	User generated input list
7	W	ASCII echo of input, and sur- face parameter array if requested
8	W	Binary output used by Radiance

2.1.3.2 Internal Surface Parameter Interpolation Routine

SURFIN interpolates (bi-linear) on the surface parameter arrays generated by SPGNER. Added to the radiance module, it provides wind speed and air temperature values for each radiance grid point. Surface parameter files must be at a resolution less than or equal to that of the scene file. Both temperature and wind speed matrices are held in core.

SURFIN requires modification of the DEVNUM common block and the addition of three new common blocks: SRFCOM, TMPCOM and WNDCOM.

2.1.3.2.1 Additional Radiance Module Inputs

SURFIN requires the inclusion of two additional parameters to the Radiance Module inputs list. Table 2-2 contains an example of the new input list. Cards marked with an (*) are new or changed. Changes and additions are described below.

Table 2-2. Revised Radiance Module input list.

11	3	7	1 1981 2	210.		
2)		10. 4	12. 0	16.76	-149. 5	67. 7G
3)		Q.	-149. 5	67. 7 8		
4)	100	100				
* 5)		280.				
6)		0025	. 0025	. 025	. 025	
. 7)	4	4				
* 8)	64	64				
~ 9)	0	1				
10)						

Card 5) (changed) SSTSL (F10.2)

SSTSL - Temperature of the subsoil layer (deg K). The variable TASL, the sea level air temperature, has been deleted from Card 5. Air temperatures are now spatially variable and read from file.

Card 8) (new) NCSGND, NRSGND (215)

NCSGND - The number of columns in the wind speed/air temperature arrays. This dimension must be the same for both arrays.

NRSGND - The number of rows in the wind speed/air temperature arrays. This dimension must be the same for both arrays.

Card 9) (new) STORLT, ICLDSC (15)

STORLT - A selector switch with values 0 or 1.

STORIT = 0: Air temperatures are assumed to be local values and are not degraded by the atmospheric lapse rate.

STORLT = 1: Air temperatures are assumed to be sea level values and will be degraded by the atmospheric lapse rate.

ICLDSC - A selector switch with values 0 or 1.

- ICLDSC = 1. Scene is a cloud file. Checks must be made for
 zero altitude in the 16 point bi-cubic local
 neighborhood. (See 2.1.3.3.1)

2.1.3.2.2 Additional File Units

を 100mm では、 1

SURFIN requires two additional FORTRAN file units.

FORT RAN UNIT	READ, WRITE OR READ/WRITE	FILE
40	R	Air Temperature binary file.
41	R	Wind speed binary file.

2.1.3.3 Internal Bi-cubic Spline Additions

Previously, the solution of the bi-cubic spline would "ring" at all cloud edges where radical variations in altitude could be encountered by adjacent grid points. Unrealistic altitudes were consequently assigned to all interpolated grid points near cloud edges. This shortcoming of the software is corrected by the subroutine described below.

2.1.3.3.1 Subroutine EDGER

The BICUBIC and BICNRM routines have been modified to detect zero (non-cloud) altitudes present in the 16 point neighborhood used by the bi-cubic spline interpolation algorithm. This indicates the presence of a cloud edge.

When a cloud edge is detected, subroutine EDGER is called. EDGER performs directional linear extrapolation as needed to produce non-zero

cloud altitudes at all locations in the 16 point local neighborhood where zero values of altitude have been detected. The new non-zero values are consistent with local scene altitude and slope. These extrapolated values temporarily replace the previously zero altitudes during execution of the bi-cubic spline algorithms.

Since the local neighborhood no longer contains adjacent points having large variations in altitude, the solution of the bi-cubic spline does not ring. Neither the shape or size of the cloud edge or the scene file is altered by EDGER.

The installation of EDGER requires the addition of a new common block EDGCOM. Note that EDGER must be installed in both the Geometric and Radiance Modules.

2.1.3.3.2 Additional Geometric Module Inputs

EDGER requires the inclusion of one additional parameter to the Geometric Module inputs list. Table 2-3 contains an example of the new input list. The card marked with an (*) is changed. Changes are described below.

Table 2-3. Revised Geometric Module inputs list.

Card 7) (changed) CTRLSW, ICLDSC (215)

- CTRLWS A selector switch with values 1-7. CTRLSW is a GENESSIS I input and has not been altered.
- ICLDSC A selector switch with values 0 or 1. ICLDSC is
 a new input. See Section 2.1.3.2.1, Card 9.

2.2 Signal Processor Enhancements

The continuing investigation of signal processing algorithms at the Charles Stark Draper Laboratory is documented in this section. Whereas the previously reported work^[3] was an in-depth description of signal processing principles for staring mosaic sensors as well as CSDL's efforts to simulate the High Resolution Acquisition Processor of Mini-HALO, this effort is concerned more with reporting work performed since the time of the last report and less with presenting the first principles. Some of these investigations, such as studies of clutter leakage as a function of jitter amplitude and threshold level, have been documented in detail elsewhere.^[4] Other investigations, such as studies of line-of-sight (LOS) jitter suppression algorithms are documented in Section 2.4 of this report.

2.2.1 Signal Processor Review

The signal processor simulation is part of the Draper Integrated Simulations (DIS). The DIS is a sophisticated analysis tool developed under DARPA support for overall evaluation and performance assessment of space-based surveillance systems. The DIS models in detail the mechanical, optical, control, signal collection and signal processing subsystems in a highly interactive fashion. It is composed of a number of large data bases (including a library of simulated earth scenes) and two principal simulation packages: the Integrated Large Space Structures Simulation (IIS3) and the Space-Based Surveillance Systems Simulation (SBS3). ILS3 simulates the space platform; it assesses the geometrical and pointing performance of satellites and their sensors as influenced by thermal, structural, dynamic, and control forces. SBS³ uses the ILS³ outputs and models the performance of space-based surveillance systems with respect to their intended missions using nominal and perturbed values for the target, background, optics, line-of-sight, optical filters, focal plane, and signal processor. Figure 2-2 presents a simplified block diagram of the DIS.

The signal processor block of the SBS³ shown in Figure 2-2 is the Draper Signal Processor Simulation (DSPS), for which CSDL has been develop-

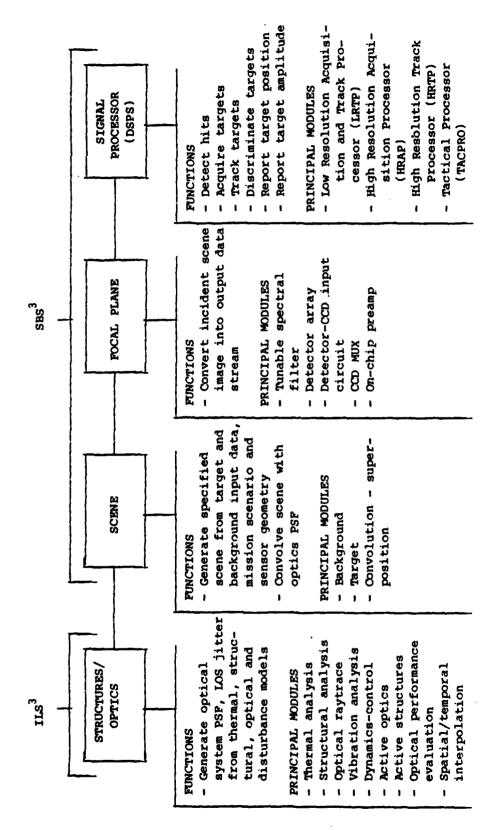


Figure 2-2. Draper integrated simulations block diagram.

ing models and simulations for some time*. The DSPS is composed of four separate processors, as illustrated in Figure 2-3.

Reference [6] dealt primarily with the simulation of the High Resolution Acquisition Processor (HRAP), which was the processor on which the majority of investigation had been concentrated. Since that time, CSDL has devoted more effort to development of the Low Resolution Acquisition and Track Processor (LRTP), and these two simulations have been combined into one software package. The simulation user has the option of selecting the HRAP or the LRTP for processing a given set of input data frames (the HRAP and LRTP run independently, not interactively). In addition, there are numerous other options available to the user, comprising a menu which specifies the signal processor configuration for a given run. In fact, by tailoring the input parameters, the user can implement a number of different signal processor configurations which do not necessarily correspond to either the HRAP or the LRTP. The signal processor configuration control parameters are tabulated in Appendix 1.

The CSDL HRAP/LRTP simulation is divided into a number of modules, which generally perform operations on the input data in a sequential fashion, frame by frame. The first of these modules is the differencing module, which computes the zeroth, first, second, or third order differences (as specified by the simulation user) for a set of input data frames. A difference is essentially a derivative of the signal amplitude with time; zeroth order corresponds to raw data, first order differencing corresponds to a first derivative, and so on.

Next is the thresholding module, which detects potential targets by comparing one or more difference frames with templates (normalized to a predetermined threshold level) which reflect the minimum expected pattern in the differencing that a changing target would generate. Variations on this technique include simple thresholding (which employs only one frame

^{*}References 5 through 7 chronicle the development of this activity culminating in the work reported in Reference 3. The DSPS originated as a functional simulation of the HALO Processor (HSP), but since has evolved in directions independent of the HSP.

SIGNAL PROCESSOR	Funct ion
High Resolution Acquisition Processor (HRAP)	Acquire Point-Source Targets
High Resolution Track Processor (HRTP)	Track Point-Source Targets Acquired by HRAP
Low Resolution Acquisition and Track Processor (LRTP)	Acquire and Track Resolved Targets (e.g. Plumes)
Tactical Processor (TACPRO)	Detect Explosions and Other Tactical Events

Figure 2-3. Components of Draper Signal Processor Simulation (DSPS).

at a time), Multi-Threshold Detection (or MTD, which employs a multi-frame template), and Rationalized Exceedance Thresholding (RET, which is similar to MTD but has more rigorous requirements). A variety of thresholding templates can be used, depending on the difference order employed.

The threshold level setting module is called by the thresholding module in order to determine the signal level to which the thresholding templates will be normalized. The threshold level can be read in, computed on the basis of a noise estimate, or set to be proportional to the standard deviation of the current frame of data or differencing. The threshold level can be periodically reset by a Constant False Alarm Rate (CFAR) loop.

Clustering and centroiding follow threshold level setting and thresholding. The clustering module selects groups of thresholded hits for centroiding. The centroiding module computes the moment of each group of hits. There are several options for the amplitude basis for clustering and centroiding, or, if the user chooses, these modules can be bypassed altogether.

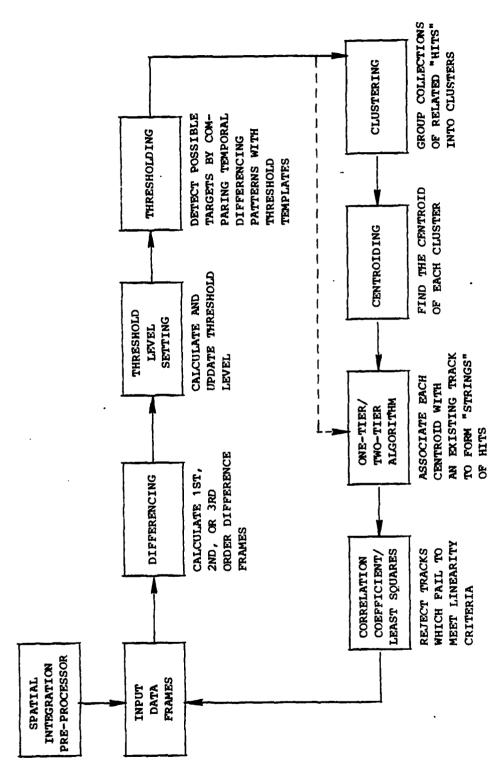
The output of the centroiding module is fed to the acquisition module. The acquisition module can employ the two tier algorithm or the one tier algorithm for high resolution or low resolution targets, respectively. The acquisition algorithms form tracks by associating any set of sequential and contiguous hits into a track. There are flexible criteria for determining when a track has a sufficient number of data points to be considered acquired.

Tracks which are generated by the two tier acquisition algorithm are handed over to the least squares line fitting module or the correlation coefficient module. These modules eliminate false tracks by rejecting any tracks which have 1) points at a greater than acceptable distance from the track's least squares generated line, or 2) a correlation coefficient less than some minimum allowable limit.

Figure 2-4 illustrates the collection of modules which comprise the CSDL HRAP/LRTP simulation. A number of these modules have recently been created, enhanced, and/or exercised, as discussed in the following sections.

2.2.2 Spatial Pixel Integration

Certain types of targets appear on the focal plane as resolved images (e.g., plumes) rather than point sources. A plume may spread over multiple pixels, whereas the objective of the processor is to localize target positions to a single point. One method of accomplishing this localization is centroiding, i.e., computing the center of gravity (cg), of a contiguous clump of hits, assuming in the process that the clump is a single target, rather than multiple contiguous targets. This approach works well in the case of point source targets, which may cover only a few contiguous pixels due to jitter and optics induced spreading. However, objects such as plumes may cover many more pixels. The IRTP, which deals with this class of targets, responds to this situation by providing the option of spatially integrating the pixels so that each n × n block of pixels is treated as a single pixel. The dimension n is a user input and the outputs of the pixels in the block are summed so that the whole block can be thought of as a single low resolution pixel.



という。 では、 では、 では、 できるのののです。

Figure 2-4. HRAP/LRTP modules and data flow.

Figure 2-5 illustrates the effect of spatial integration, beginning with a 48 × 48 input data frame and deriving the corresponding 24 × 24 and 12 × 12 low resolution data frames. The absolute values of the pixel outputs in all three frames are scaled from one to nine for purposes of graphical output. In performing spatial integration, the user can specify any size of low resolution pixel and any subset of the high resolution input data frames as the low resolution field of view.

Figure 2-6 compares the target acquisition process for the three cases presented in Figure 2-5. The acquisition algorithm used in all three cases was the one tier low resolution acquisition algorithm described in the next section. The system track threshold level reduction factor was 0.5 for all three cases and the threshold levels of 3, 9, and 27 were chosen as approximately the lowest thresholds for which there was no significant clutter leakage. Both of these figures illustrate a number of important points. In Figure 2-5, the majority of the target's energy falls in row 41, column 44 of the 48 × 48 high resolution input frame, row 21, column 22 of the 24 \times 24 low resolution frame, and row 11, column 11 of the 12 ×.12 low resolution frame. It can be seen that as spatial integration increases, so does the dilution of the target signal, and hence the signalto-noise (S/N) ratio decreases. Figure 2-6 shows how the loss in resolution makes target motion less apparent. Also, note that in the high resolution case in Figure 2-6, the 48 × 48 processor configuration detects two targets, an artifact of the target's spreading over a number of pixels as the plume grows larger.

In summary, the performance of a given processor is critically linked to the degree of spatial integration invoked. If the spatial integration is too coarse, the processor must deal with a lower S/N ratio, loss of
resolution, and the resulting problem of the target's motion being less
apparent. In addition, the threshold level must be increased as pixel size
increases. While less coarse spatial integration ameliorates these problems, it can introduce its own difficulties: it may require more processing than the hardware can handle, and it renders the processor more sensitive to jitter and the associated clutter leakage. In addition, too small

a pixel size causes the processor to suffer confusion from the multiple targets it detects due to a single target covering multiple pixels, as illustrated by the example in Figure 2-6.

A future area of investigation will be the dynamics of spatial integration: how it effects various aspects of processor performance as a function of processor configuration and scene/target characteristics, and how to choose an optimal low resolution pixel size. Another subject meriting investigation is the interaction of spatial integration with threshold level and system track threshold level reduction factor.

2.2.3 Track Acquisition

In the HRAP/LRTP simulation, input frames of raw data are subjected in sequence to a series of operations: differencing (which reduces N_F frames of data to $N_F - O_D$ frames of difference, where O_D is the difference order); thresholding (which in turn produces $N_F - 2 \times O_D$ frames of threshold hits); and clustering and centroiding (which again produce $N_F - 2 \times O_D$ frames of centroids). The final product of these processes is a set of frames which contain the target(s) as well as numerous extraneous hits caused by system and scene noise, clutter leakage, etc.

The next phase of processing is track acquisition. The HRAP and LRTP use somewhat different acquisition algorithms because of the differing behavior of high resolution and low resolution targets.

2.2.3.1 High Resolution Acquisition Review: Two Tier Algorithm

In the case of high resolution targets, the centroided target hits are unique with respect to the other hits, because the target moves from one pixel to an adjacent pixel in each frame (assuming reasonably good velocity match). Neglecting structured clutter leakage (such as an entire cloud edge that "lights up" as a line of hits), and assuming a reasonable number of noise hits, it is unlikely that many of the noise hits would exhibit the same sort of apparent regular motion. Therefore, the high resolution acquisition strategy is to search for hits that form tracks by moving from one pixel to the next in each frame.

CURRENT DATA/DIFFERENCE FRAME

2 1 3 1 2 1 1 1 2 3 2 1 1 1 4 2 3 3 3 1 1 4 3 1 3 1 1 1 1 2 2 1 4 1 1 1 . 1 2 1 3 1 2 3 1 413 11. 2 1 1 1 3 3 3 3 3 1 1 1 3 · 1 2 1 1 3 5 i 2 3 1 1 . 1 2 1 2 1 2 4 2 2 1 1 1 1 2 1 1 2 2 11 431 4. ? 412 2132 12 2 3 . 3 1 2 5 1 . 2 4 2 1 2 1 2 3 1 5 2 2 3 . 3 2 1 1 2 1 12 13 1 1 2 3 1 3 2 3 2 . 2 2 3 1 2 1 4 3 1 3 1 1 1 5 1 3 1 2 2 1 1 1 2 3 2 3 4 4 3 3 3 3 2 3 1 2 5 2 4 1 4 3 2 2 2 3 3 3 3 3 3 2 2 1 4 2 1 2 1 3 1 21 2 12111 2111 11.3 31 3 2 3 2 3 4 2 2 3 6 1 1 1 2 2 1 2 1 18 3 118 3 1 2 2 2 1 3 6 4 3 1 1 1 3 . 1 2 2 1 . 5 . 2 1 3 5 2 4 4 3 5 1 1 C 2 1 2 1 1 3 1 5 3 4 4 1 4 2 2 1 3 3 3 5 2 3 2 2 1 23 24 25 3 3 3 6 2 1 2 3 2 3 5 3 1 1 3 1 3 1 2 2 2 2 2 2 1 1 1 3 1 5 2 2 1 23231 2232 2123 1321 2.1 2 1 3412 2.1 3 1 3 4 1 2 2 2 1 1 3 3 5 1 2 3 3 5 4 2 1 2 2 2 2 2 2 3 4 2 1 2 1 1 2 2 1 5 2 2 1 1 . 3 1 1 2 3 2 2 3 1 2 2 3 3 2 2 1 6 3 . 2 2 2 2 2 28 1 1 2 2 5 3 2 2 1 1 2 2 2 1 127 3 1 1 2 1 4 1 4 2 1 5 2 2 3 2 2 2 1 2 1 2 . 3 2 1 4 1 3 1 3 4 4 2 1 2 4 3 . 2 1 5 2 1 2 2 1 5 2 1 2 2 1 5 5 4 2 .31.15.51 . 3 2 1 . 5 2 3 3 3 2 1 2 1 1 33 34 35 1 4 3 2 1 3 1 2 2 2 2 . 1 2 1 2 2 1 1 2 2 1 . 1 2 4 2 1 1 3 2 3 4 1 . 2 3 2 2 2 1 2 2 3 Z 3 1 1 1 2 2 1 2 ž 1 i 1 3 2 2 3 2 3 2 1 1 2 2 1 ī 5 1 3 1 1 1 3 3 3 4 . 1 3 1 1 2 2 2 4 3 1 1 1 3 2 1 2 2 2 2 3 2 2 1

Figure 2-5a. Scaled high resolution input data frame (48×48) .

CURRENT DATA/DIFFERENCE FRAME

1 2 3 4 5 6 7 8 9101112131415161718192021222324 133 1313143 1 18 331136 111111316311331111 1 36 11141441 346313 1 3.413313 1113441 6 1 3311 4411 3331 141.13114 13114. 3 3 1 3613113168 3 1 1 3 4 1 1 1 3 1 3 3 4 4 5 1 3 3 1 6 3 1 3 1 1 1 3 4 1 3 6 1 13311 353 1 34 141113 3 13 31.3.331 4 3 3 6 3 3 1 1 . 3 3 3 3 3 3 3 411411 3 131. 3113 1 3 33311111314131111 3111

Figure 2-5b. Scaled low resolution data frame (24 × 24).

CURRENT DATA/DIFFERENCE FRAME

1 2 3 4 5 6 7 8 9101112 1 3 5 4 3 3 4 5 6 6 6 6 7 9 1 2 6 5 3 6 6 6 6 4 3 5 4 3 5 2 3 4 4 2 6 6 5 6 6 4 3 5 4 3 5 2 4 5 7 3 6 4 6 5 6 6 4 3 2 4 5 6 5 7 7 6 5 4 4 5 6 5 2 5 6 5 5 6 6 6 5 6 6 5 4 3 4 6 7 5 6 5 4 6 6 3 5 6 6 7 5 7 8 6 5 4 5 4 4 3 7 7 3 6 4 8 9 1 5 5 4 7 5 6 6 5 5 6 3 9 10 6 5 5 6 6 6 6 5 4 5 3 6 310 11 3 4 4 6 7 5 5 3 5 3 5 711 12 7 3 5 5 3 6 4 4 4 5 5 311 1 2 3 4 5 6 7 8 9101112

Figure 2-5c. Scaled low resolution data frame (12×12) .

CURRENT FRAME OF TRACK FILES

		• ,				•			•			٠			•			٠			•			•				•	
		•				•			•			٠			•			•			•			•				•	
	•	•	٠	•	•	•	•	•	•	•	•	٠	•	•	•	•	•	•	•	•	•	•	•	•	•	•		•	•
		_				_			_			_			_														
		•				•			•			•			•			•			•			•				•	
									•																				
	•	•	•		•				•	•	•		•	•	•		•		•	•	•		•		•	•		•	•
		•				•			•			٠			•			•			•			•				•	
		•				•			•			•			•			•			•			•				•	
	_				_	_	_		_	_	_		_	_		_	_	_	_	_	_	_	_	_		_			
	-	•	•		•	·	•	•	•	•	٠	٠	•	٠	•	•	•	٠	•	•	•	•	•	•	•	•		•	•
		•							•																				
		•				•			•			•			•			•			•			•				•	
	•	•	•	•	•		•	•	• •	•	•		•	•	•	•	•		•	•	•	•	•		•	•		•	•
		•				•			•			•			•			•			•			•				•	
		_	•												_			_						_				_	
		•				٠			•			•			•			٠			•			٠				•	
	•			,		•	•		•	•			•	•			•												
		•				٠			•			٠			•			•			•			٠				•	
	_	•				•			•			•			•			•			•			•				•	
	•	•	•	•	•		•	•	:	•	•		•	•	:	•	•		•	•	:	•	•		•	•		:	•
									-			-			-			•			•			•				•	
		•				•						•			•			•			•			•				•	
	•	•	٠	•	•	•	•	•	•	•	•	•	•	•	•	•	•	٠	•	•	٠	•	•	•	•	•		•	•
		•				•			•			٠			•			•			•			•				•	
																										i	+		
				,			•		•	•		-			•		•				•			-		•	+	•	
		•				•			•			•						•						•			٠	•	
		•				•			•			٠			•			•			•			•				•	
	•	•	•	•	•	•	•	•	•	•	•	•	•	•	•	•	•	٠	•	•	•	•	•	•	•	٠		•	•
																		_											
		-				-			•			-			•			•			•			-				-	

Frames = 19-45 Average Hits per Frame = 3
Threshold = 3.0 Total System Tracks = 2
Haflev = 0.5 Total Acquired Tracks = 6

Figure 2-6a. High resolution acquired tracks (48 \times 48).

CURRENT FRAME OF TRACK FILES

	1	2	3	4	5	6	7	8	91	LOI	111	121	31	41516	1718	3192	:02	212	222	232	4
1														•							1
1 2																					2
3																					3
4 5																					4
5														•							5
6	-		-		-		•		•	-	-			_	-	-	-	-			6
7					_					_							_				7
7 8					•					•				-			-				8
9					_												_				9
10		•			•					•				•			•				1Ó
11	•		•		•		•		•		•		•	•	•	•		•		•	11
12					•					•				•			•				īż
13																					13
					•					•				•			•				
14																					14
15	•		٠		•		•		•	•	•		•	•	•	•	•	•		٠	15
16																					16
17					٠					•				•			٠				17
18																			_		18
19					•					•				•			•		1		19
20	•		•		•		٠		•		•		•	•	•	•		•	1	٠	20
21					•					•				•			•				21
22																					22
23					•									•							23
24																					24
	1	2	3	4	5	6	7	8	93	LO	113	121	31	41516	171	B192	202	21	222	232	4

Frames = 29-45 Average Hits per Frame = 1 Threshold = 9.0 Total System Tracks = 1 Haflev = 0.5 Total Acquired Tracks = 1

Figure 2-6b. Low resolution acquired tracks (24 × 24).

CURRENT FRAME OF TRACK FILES

	1	2	3	4	5	6	7	8	91	101	112	
1												1
2												2
2												3
4												4
5												5
										•	•	6
6 7										_		7
8					•					•		8
9												9
10									_	•	1	10
ii	-		•				•		•	_	_	īī
12					•					•		12
	1	2	3	4	5	6	7	8	91	LO	1112	

Frames = 32-45

Threshold = 27.0

Haflev = 0.5

Average Hits per Frame = 0.5

Total System Tracks = 1

Total Acquired Tracks = 1

Figure 2-6c. Low resolution acquired tracks (12 \times 12).

An algorithm that searches for just such track-forming hits was discussed earlier. [3] It is called the two tier algorithm because it uses two tiers of search gates. A search gate is a group of contiguous pixels which the processor chooses as the area in which it will search for the current hit of a hit string that is already in progress; this area corresponds to the pixels in which the next hit could be expected to appear if it were moving as a high resolution target moves. The first tier of search gates is designed to locate the next hit of a hit string which just recorded a hit. A miss is recorded whenever the first tier search gate fails to locate a hit in the designated area in the current frame. In this case there are two possible recourses, depending on whether or not the hit string is a system track. A hit string achieves system track status when it meets a minimum length criterion of recording M1 hits after being in existence for N₁ frames. If the hit string is a pre-system track, then it is dropped and no further hit searches are made for that particular string. However, if it is a system track then the second tier is invoked in the next frame. The second tier employs a larger search gate than the first tier, since there is greater uncertainty in a target's expected position immediately following a miss. If the second tier detects a hit in the designated area, the search for new hits is resumed, again using the first tier until such time as there is another miss. However, if there is a second consecutive miss, then the track is dropped.

The two tier acquisition algorithm proceeds as follows: the pixel position (row and column) of each hit in the first frame of centroiding is recorded. In the second frame of centroiding a search is made in the eight pixels which surround each pixel that recorded a hit in the first frame:

1	2	3
4	0	5
6	7	8

This is the initial nondirectional search gate for a single unassociated hit. In the figure, zero marks the position of the initial hit from the previous frame. If no hits occur in any of the eight pixels, the search is discontinued. If a hit does occur in any of the eight pixels, the search is continued, and the direction of the resultant track is given by the number of the pixel (1 through 8) in which the hit appears. The two tier algorithm always chooses a search gate based on the apparent direction of motion which is derived from the positions of the last two observed hits in the string. Thus, if a hit does occur in the initial search gate, then the direction of motion is deduced and a smaller directional search gate is chosen to be used in the next frame as shown in Figure 2-7. The directional search gates each cover three pixels and are shown (along with their method of choice) in Figure 2-8. Notice that this choice of directional search applies not only for tracks which are just starting but also for any hit string whose two most recently recorded hits are denoted by 1 and 2. The next search gate is determined by the locations of hit 2 and any new hit which occurs at the proper time in the directional search gate. In this case hit 2 is relabeled hit 1 and the brand new hit becomes hit 2. This process uniquely determines which search gate is to be used in the next frame.

If two hits appear in either the initial non-directional search gate or any of the eight directional search gates, they are processed individually as independent tracks. If either of these split tracks records a miss in the frame immediately following the split, then that track is dropped. This would effectively handle high resolution targets that split into parts. On the other hand, if one hit appears simultaneously in two search gates, the gates "share" the hit independently. Crossing target tracks are handled in this manner.

A miss in a hit string which is not yet a system track (i.e. which has not yet met a M_1 hits out of N_1 frames criterion) causes that string to be dropped. However if the miss occurs in a system track, the second tier search gates are invoked. Just as there are two basic first tier directional search gate types which have four possible orientations, there are

1	2	Corner Hit
1	2	Edge Hit
1	2	Corner Hit

Figure 2-7. Gate selection.

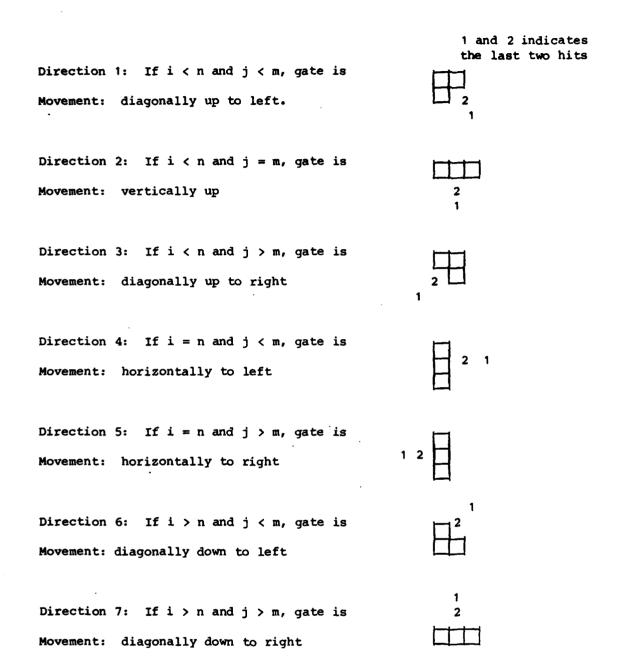


Figure 2-8. Directional search gates. Hit #1 is in row n, column m. Hit # is in row i, column j.

also two basic second tier search gates which can have the same four orientations. The two second tier search gates, which are simply the first tier gates augmented by five more pixels in locations where a target can be expected to appear, are shown in Figure 2-9.

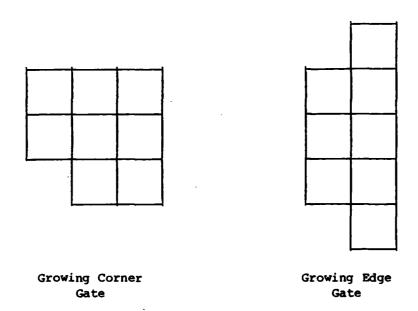


Figure 2-9. Growing gate size after miss (second tier).

If a second tier search fails to find a hit, then the track is dropped. However if there is a hit within the second tier search gate, then the hit search is resumed using the first tier gates. As with the first tier, the new direction is derived from the two most recently observed track hits. If there is no change in row or column between the next-to-last hit and the last hit found in the second tier, then the motion is determined to be horizontal or vertical, respectively. If there is a change in both row and column, however, then the track direction is determined to be diagonal. Also, as with the first tier, multiple hits are processed independently and are subject to track drop if a miss immediately follows the split.

An example of the two tier algorithm being used for acquisition is shown in Figure 2-10. Notice that the maximum change in direction from one frame to the next allowed by the two tier algorithm is 45°.

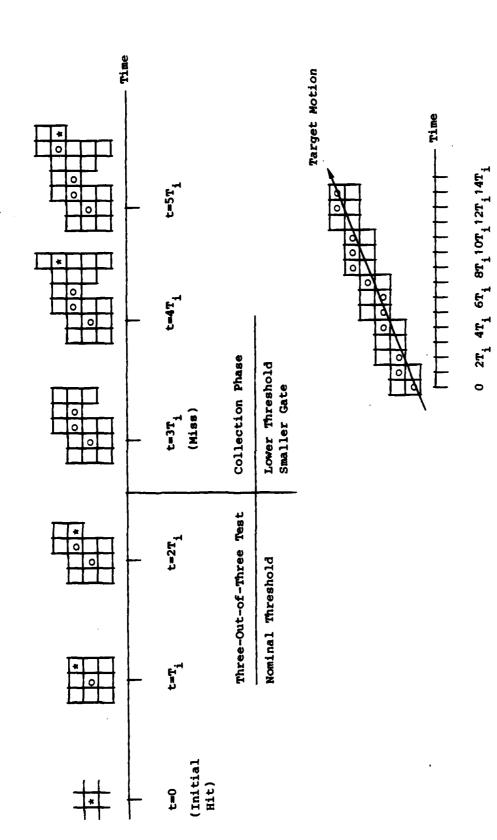


Figure 2-10. Example of two-tier gates.

2.2.3.2 M out of N Criterion

Once a hit string has recorded M_1 hits in N_1 frames of existence, it is promoted to a system track. At this point in time the information regarding the system track's direction of motion can be used to increase the probability of successfully acquiring it. This is done by reducing the threshold level in only those pixels which are part of the next search gate for that system track. For example, the processor could cut the threshold level in half in the pixels which are part of the next search gate for any system track before thresholding, clustering, and centroiding can produce the next frame to be input to the two tier algorithm.

As Figure 2-10 illustrates, the two tier algorithm can follow a target indefinitely assuming that two consecutive misses never occur. Eventually however the target is classified as an acquired track, and is passed to the High Resolution Track Processor (HRTP). This occurs when the HRAP has recorded M_2 hits for a target track which has been in existence for the previous N_2 frames. After handover to the HRTP, the HRAP receives target position updates from the HRTP so that the target will not be acquired again.

2.2.3.3 Low Resolution Acquisition: One Tier Algorithm

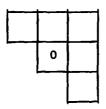
The operation of the low resolution acquisition algorithm is similar to that of its high resolution counterpart. However, unlike high resolution targets which move from one pixel to the next in succeeding frames, a low resolution target may remain in the same pixel over a number of frames. This implies that a different type of search gate must be used for acquiring and tracking low resolution targets. In fact, the LRTP uses only one search gate, a 3 × 3 pixel block as illustrated below:

1	2	3
4	0	5
6	7	8

All nine pixels are included in the target search, and the gate is centered on the position in which a given target last appeared. This gate does not change, regardless of the target's direction of motion. Nor does it change if a miss occurs in a track: there is no second tier. The search gate allows a target to remain motionless by its very nature.

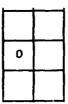
Just as in the high resolution case, the low resolution acquisition processor drops any track after two consecutive misses or after a single miss if that miss was immediately preceded by a track split. Also, like the HRAP, the LRTP threshold level can be manipulated when a track is promoted to system track status. An example of the low resolution acquisition algorithm has already been presented: the tracks in Figure 2-6a,b,c were acquired by the LRTP. Unlike the HRAP, the LRTP does not hand an acquired track over to another special purpose tracking processor (like the HRTP), but rather continues to track the target itself using the same algorithm employed in the acquisition phase. This last feature of the LRTP may not provide optimal performance, and CSDL is investigating alternatives.

Another alternative CSDL is considering is the introduction of modified search gates which could be tailored to target motion, similar to those used by the HRAP. For example, if a track had last moved diagonally to the upper right, then, rather than employing a full 3 × 3 search gate, the following gate could be used:



where "0" marks the position where the target was last detected. This method is based on the assumption that a strategic track cannot change direction by more than 90° over a short period of time. Similarly for vertical or horizontal tracks, another six pixel gate could be employed.

In the case of a horizontal track moving to the right it would look like this:



where "0" again marks the position of the most recent detection of the target. This algorithm would serve a dual purpose. Not only would it limit target motion to certain trajectories which are within prescribed behavioral bounds, but it would also curb the number of tracks generated by a single target covering several pixels. Experience has shown that this last problem of multiple acquisitions from a single large target is a serious one, particularly when the threshold level is dropped for system tracks which are being tracked by oversized 3 × 3 pixel search gates. CSDL has already implemented a system which performs much the same function by examining the history of the directions in which a track has moved and requiring that the most recent direction of motion be no more than 90° different from any of the previous directions. This technique is even more restrictive of target motion than the six pixel directional search gate scheme, and it is certainly more complex and less elegant. Functionally, however, it effectively curbs an overabundance of false tracks, and prevents the phenomenon of a legitimate track being dropped for suffering a single miss immediately after a target split due to excessive clutter.

2.2.4 Simple Thresholding

It became clear with review that the simple thresholding algorithm discussed elsewhere $^{[3]}$ had some flaws; as a solution, CSDL proposed the following slightly modified algorithm. Let $\mathbf{L}_{\mathbf{T}}$ equal the threshold level $\mathbf{P}_{nmi}^{\mathbf{K}}$ equal the contents of pixel n,m in frame #i of the Kth order difference. The conditions for having a hit in pixel n,m of frame #i are listed below for the various difference orders:

Oth order: $P_{nmi}^{0} > L_{T}$ positive contrast $P_{nmi}^{0} < -L_{T}$ negative contrast $P_{nmi}^{1} > L_{T}$ positive contrast $P_{nmi}^{1} < -L_{T}$ negative contrast $P_{nmi}^{1} < -L_{T}$ negative contrast $P_{nmi}^{2} > L_{T}$ negative contrast $P_{nmi}^{2} > L_{T}$ negative contrast $P_{nmi}^{2} > L_{T}$ negative contrast $P_{nmi}^{3} > L_{T}$ negative contrast $P_{nmi}^{3} < -L_{T}$ negative contrast $P_{nmi}^{3} < -L_{T}$ negative contrast

In each case the exceedance is given by $E_{nmi} = |P_{nmi}^K| - L_T$. Notice the reversal of sign (+ for -) in second order simple thresholding. The rationale behind this change is that the idealized second order difference pattern is 1, -2, 1 and it is optimal to employ that element of the difference pattern with the maximum magnitude, in this case the -2 element.

Of course idealized temporal difference patterns rarely occur in reality; factors such as line-of-sight jitter and phasing corrupt the difference patterns. Appendix 2 examines the effects of phasing on difference patterns in a number of examples. Each example shows raw data and the resultant first, second, and third order differences for a given phase. A target is said to be out of phase when its appearance in a given pixel is split between two frames (even though the actual period of time that it dwells in the pixel is equal to the length of the frame time). A target is in phase when it appears in a given pixel for one frame only.

In each example the appearance of a target is split between the fourth and fifth frames. The examples are labeled by the ratio of the time spent by the target in the fourth frame to time spent in the fifth frame; for instance, 60:40 phasing means that the target was in the pixel for 60% of frame four and 40% of frame five. The background is assumed to be zero for simplicity.

Notice the differences in amplitude and phasing for the various difference orders. Assuming simple thresholding, the frame in which a target would be detected is indicated (for each example) by circling that frame for each of the difference orders.

The Appendix 2 phasing examples were used to evaluate the performance of the various orders of simple thresholding. The results of this evaluation are illustrated in Table 2-4. Several properties of simple thresholding are evident. First order simple thresholding detects a hit one frame late for phasing in the 67:33 to 51:49 range. Second order simple thresholding records two consecutive hits for 50:50 phasing. Third order simple thresholding detects a hit one frame early in the range of 49:51 to 41:59 and records two consecutive hits for 40:60 phasing. In addition, the ambiguous 50:50 case produces a bias in the earlier frame for third order simple thresholding and the later frame for first order simple thresholding.

For purposes of performing clustering and centroiding, a knowledge of which frame of data or difference corresponds to the current frame of thresholding is required. If the current frame of simple thresholding is frame #i, the corresponding frames are:

frame #i of the exceedance

着さらのはのに見いている

frame #i of the difference

frame #i + K - 1 of the data, except in the case of K = 0 which corresponds to frame #i of the data (where K is the difference order employed)

Table 2-4. Simple thresholding performance for various degrees of phasing.

FOURTH FRAME TO FIFTH FRAME RATIO (PHASING)	DIFFERENCE ORDER	MAXIMUM POSSIBLE THRESHOLD LEVEL	COMMENTS
100:0	0	100 100	Correct Performance
	. 2 3	200 300	
95:5	0	95	Correct
	1 2 3	90 185 280	Performance
90:10	0 1 2 3	90 80 170 260	Correct Performance
85:15	0 1 2 3	85 70 155 240	Correct Performance
80:20	0 1 2 3	80 60 140 220	Correct Performance
75: 25	0 1 2 3	75 50 125 200	Correct Performance
70:30	0 1 2 3	70 40 110 180	Correct Performance

Table 2-4. Simple thresholding performance for various degrees of phasing. (Cont.)

FOURTH FRAME TO FIFTH FRAME RATIO (PHASING)	DIFFERENCE ORDER	MAXIMUM POSSIBLE THRESHOLD LEVEL	COMMENTS
65:35	0 1	65 35	One frame late
·	2 3	95 160	
60:40	0	60	
]	1	40	One frame late
	2	80	
	3	140	
55:45	0	55	
ł i	1	45	One frame late
	2	65	
}	3	120	
50:50	0	50	Generates 2 consecutive hits
	1	50	Biased towards later frame
	2	50	Generates 2 consecutive hits
	3	100	Biased towards earlier frame
45:55	0	55	
	1	55	J
	2	65	
	3	80	One frame early
40:60	0	60	
[1	60	
	2	80	[
	3	60	Generates 2 consecutive hits
35:65	0	65	Correct
Í	1	65	Performance
	2	95	.
	3	90	
			

Table 2-4. Simple thresholding performance for various degrees of phasing. (Cont.)

FOURTH FRAME TO FIFTH FRAME RATIO (PHASING)	DIFFERENCE ORDER	MAXIMUM POSSIBLE THRESHOLD LEVEL	COMMENTS
30:70	0	70	Correct
	1	70	Performance
	2	110	
	3	120	
25:75	0	75	Correct
	1	75	Performance
	2	125	
	3	150	
20:80	0	80	Correct
	1	80	Performance
	2	140	
	3	180	
15:85	0	85	Correct .
	1	85	Performance
	2	155	
	3	210	
10:90	0	90	Correct
	1	90	Performance
	2	170	i
	3	240	
5:95	0	95	Correct
	1	95	Performance
	2	185	
ļ	3	270	
0:100	0	100	Correct
	1	100	Performance
	2	200	
j	3	300	l

Similarly for the case of Multi-Threshold Detection (MTD), frame #i of the thresholding corresponds to:

frame #i of the exceedance

frame numbers i through i + K of the difference (were K is again the difference order)

frame #i + K of the data

For clustering or centroiding based on differencing, perhaps the amplitude used should be calculated as the sum of the absolute values of the difference of the pixel in question for frames i through i + K:

Amplitude =
$$\sum_{j=0}^{K} |P_{nmi+j}^{K}|$$
 (2-2)

2.2.5 CFAR Algorithm Development

Initial investigations into candidate Constant False Alarm Rate (CFAR) algorithms were based upon the conservative assumption that such an algorithm would be applied only once to each frame of thresholded data, due to the anticipated real time operational requirements and time lines of a signal processor. However, an iterative type of CFAR algorithm which could potentially be applied a number of times to each thresholded frame offers a number of advantages and would be feasible in signal processors with less restrictive timing requirements.

After investigating the iterative approach, the following CFAR algorithm was developed (which is similar to Newton's method for finding roots of a polynomial). The inputs to the this algorithm are as follows:

- Op difference order used
- $\mathbf{L}_{\mathbf{r}}$ current threshold level

NHITS - current number of threshold hits

NOPT - optimal number of hits

MARGIN - allowed variance between NHITS and NOPT

NOPT, MARGIN, and ITER are all user inputs. Recall that Newton's method treats a polynomial as if it were piece-wise linear, by calculating the local tangent and then interpolating via that tangent to another point on the polynomial. The new local tangent is computed at the current point and is used in turn to interpolate to the next point. Each iteration of this procedure yields a point which is closer to the desired position on the curve, so the procedure is repeated until the desired level of accuracy is achieved.

The proposed CFAR algorithm differs from Newton's method in that its uses a secant for the interpolation, rather than the local tangent. Empirical investigations have shown that, typically, the relation between the number of exceedances (NHITS) and the threshold level ($L_{\rm T}$) for a given frame has the form of the curve shown in Figure 2-11. Suppose that after thresholding the current frame the number of exceedances corresponds to point A on the curve, for which the threshold level was too low, thereby generating too many hits. The objective is to determine the optimal threshold level which generates NOPT hits. An initial rather crude interpolation can be performed by assuming that the amount by which NHITS differs from NOPT is proportional to the amount by which $L_{\rm T}$ differs from the optimal threshold level, i.e., if NHITS is 20% too high (or low), then $L_{\rm T}$ must also be 20% too low (or high). The threshold level $L_{\rm T}$ is adjusted accordingly, and the entire frame can then be re-thresholded, which in this case produces a number of hits corresponding to point B in Figure 2-11.

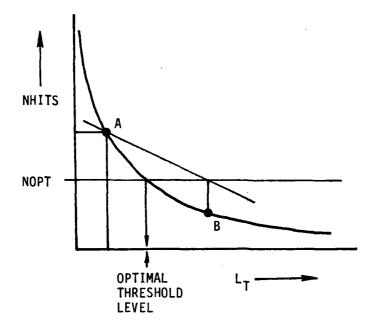


Figure 2-11. Initial CFAR threshold level correction.

A more accurate interpolation of the ideal threshold level can then be performed by assuming a straight-line between points A and B as an approximation to the curve. This new interpolated threshold level can be used to re-threshold the frame, producing a number of hits corresponding to point C in Figure 2-12. This interpolation/re-thresholding CFAR procedure (using the latest point generated and the one which preceded it) is repeated ITER times, or until NHITS - NOPT is less than MARGIN or the allowed variance, whichever comes first. Note that it is desirable to have NHITS less than NOPT but as close as possible, since ultimately the hardware of any real signal processor will be limited in the amount of exceedances it can process in real time.

If the input data frames are composed of integers or whole numbers, then the minimum change in threshold level which will produce a change in the number of exceedances is:

for all orders of simple thresholding, 0th order MTD and 1st order MTD

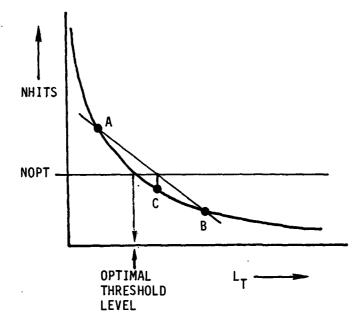


Figure 2-12. CFAR iteration.

- 1/2 for 2nd order MTD
- 1/3 for 3rd order MTD

Iterations of the CFAR loop should cease when the change in the threshold level proposed by the interpolation is less than the appropriate number shown above. The final threshold level generated is then the initial threshold level for the next frame.

The CSDL HRAP/LRTP simulation currently has implemented three methods of threshold level setting: read in threshold level; noise estimate times threshold to noise ratio (NE × TNR); and standard deviation over an entire frame times threshold to noise ratio (SD × TNR). All three of these options have been exercised, and it is clear that optimally setting the threshold level is critical to the success of the processor's performance. Any one of these options could be combined with a CFAR loop for threshold level maintenance. An important area for future work is the interaction

of threshold level initialization with threshold level maintenance as well as methods of optimizing threshold level setting algorithms. Another area of investigation will be the performance of threshold level setting algorithms as a function of scene and sensor characteristics. For example, one threshold level setting algorithm might work well for AC coupled focal planes, while another might be superior for DC coupled focal planes.

2.2.6 Track Discrimination

Although the one tier and two tier acquisition algorithms are successful in eliminating many non-target generated hits, it is possible for a set of unrelated false hits to be mistaken for a track. Most strategic target tracks (both high resolution and low resolution) tend to form straight lines over short distances, whereas most false tracks are not. The strategy of a track discrimination algorithm is to filter out those acquired tracks which are not sufficiently "straight" from those that are. Two algorithms have been implemented to accomplish this objective in the CSDL HRAP/LRTP simulation, and they are described in the following two sections.

2.2.6.1 Least-Squares Line-Fitting Algorithm

The algorithm described here is a modification and improvement of the old least-squares algorithm described elsewhere. [3] The logic of the algorithm is as follows: the HRAP/LRTP is constantly acquiring hits which are placed in track files, forming possible tracks. Suppose now that a given track file has just accumulated N hits, so that it passes some criterion (like the 12 out of 14 test) which requires a minimum number of hits in a given number of frames. Each of the hits in this track file has X and Y coordinates; let the coordinates of the ith hit be X_i and Y_i . The equation of the line

$$Y = mX + b \tag{2-3}$$

which describes the track is found by employing a least-squares straightline fit to find the slope, m, and the intercept, b:

$$m = \frac{N \sum_{i} Y_{i} - (\sum_{i}) (\sum_{i})}{N \sum_{i} Z_{i}^{2} - (\sum_{i})^{2}}$$
 (2-4)

$$b = \frac{(\Sigma Y_{i}) (\Sigma X_{i})^{2} - (\Sigma X_{i}) (\Sigma X_{i} Y_{i})}{N\Sigma X_{i}^{2} - (\Sigma X_{i})^{2}}$$
(2-5)

Reasoning that a strategic track would be a reasonably straight line over short distances, the algorithm requires that all hits in a track file be within a distance DMAX of the least-squares computed line. The perpendicular distance of the ith hit to the line is given by

distance =
$$\frac{mX_{i} - Y_{i} + b}{\pm \sqrt{m^{2} + 1}}$$
 (2-6)

The distance of each hit in the track file is computed; if any of the hits has a distance which is greater than the allowed limit, DMAX, then that track file is dropped. The modification to this algorithm comes from the observation that the algorithm fails when the slope of a track approaches infinity (vertical). The solution is straightforward: simply exchange the roles of X and Y in the least-squares fit whenever the slope dy/dx exceeds

1. The line to be determined is now

$$X = mY + b (2-7)$$

and the slope and intercept are given by

$$m = \frac{N\Sigma x_i y_i - (\Sigma x_i) (\Sigma y_i)}{N\Sigma y_i^2 - (\Sigma y_i)^2}$$
 (2-8)

$$b = \frac{(\Sigma X_{i}) (\Sigma Y_{i})^{2} - (\Sigma Y_{i}) (\Sigma X_{i} Y_{i})}{N\Sigma Y_{i}^{2} - (\Sigma Y_{i})^{2}}$$
(2-9)

The perpendicular distance of the ith point to this line is given by

distance =
$$\frac{mY_{1} - X_{1} + b}{\pm \sqrt{m^{2} + 1}}$$
 (2-10)

Once again if any hit in a track file has a perpendicular distance greater than the allowed limit, DMAX, that track is dropped.

2.2.6.2 Correlation Coefficient Algorithm

The coefficient of correlation is a measure of association between two variables. When the absolute value of the correlation coefficient R_{XY} between X and Y approaches 1, this is indicative of a strong relation between X and Y with little scatter about the line which defines the X-Y relation. The correlation coefficient is given by

$$R_{xy} = \frac{N\Sigma X_{i}Y_{i} - \Sigma X_{i}\Sigma Y_{i}}{N\sqrt{\Sigma X_{i}^{2} - (\Sigma X_{i})^{2}}\sqrt{\Sigma Y_{i}^{2} - (\Sigma Y_{i})^{2}}}$$
(2-11)

The correlation coefficient algorithm measures this quantity for each eligible track. If the R_{XY} falls below some minimum acceptable limit, RMIN, for any track file, then that track is dropped. Notice that the correlation coefficient algorithm has one major weakness: it has a tendency to rule out near-vertical and near-horizontal tracks, as can be seen from the equation defining R_{XY} . This is because a vertical or horizontal track may be "straight", but it cannot show any correlation between X and Y.

2.2.7 Areas of Future Investigation

Several signal processing issues merit further study, particularly the issue of threshold level setting and maintenance. CSDL plans to examine the relationship between threshold level and clutter leakage in greater detail as a function of scene, sensor, difference order, and spatial integration. After implementation and test of the CFAR algorithm (described in

Section 2.2.5) is completed, CSDL intends to explore the performance of this algorithm against different scenes and signal processor configurations. Spatial integration is another subject requiring further study, as are the new low resolution acquisition search gates (described in Section 2.2.3.3). CSDL intends to investigate these and other related areas which impact processor performance.

In the course of investigating an algorithm, a number of questions arise:

- (1) How does the algorithm affect processor performance?
- (2) How does it couple with other algorithms for various processor configurations?
- (3) How can the algorithm be optimized?

Experience to date indicates that algorithms perform optimally when they can vary their own parameters dynamically, responding to a given situation in a manner which is tailored to the current circumstances. It is hoped that future efforts can include an investigation into the implementation of such "dynamic" algorithms.

2.3 Integrated Large Space Structures Simulation (ILS³)

2.3.1 Introduction

The ILS³ structures/optics simulation is a tool which can be used to simulate the performance of a flexible optical system subject to onboard and environmental disturbances and control system forces. The output of this program is the optical point-spread function (PSF) of the system which can then be used as an input to the SBS³ sensor simulation. This section describes the first step in a series of enhancements which broaden the types of systems which can be simulated by removing the modelling restrictions which were part of the original program.^[9] The fundamental structure of ILS³ is shown in Figure 2-13. It consists of three groups of basic functional modules. In the first group, the node point displacements of a finite element model subjected to static or dynamic loads are computed. In the second group, these node point displacements are transformed into optical wavefront errors. Finally, in the third group the wavefront errors are processed to compute IOS errors, PSF, etc.

The subject of the sections to follow is the enhancement of the . second group of modules, known as the interface programs. In these programs the previously computed displacements at the node points of the finite-element model of the surface are transformed into optical wavefront errors at a rectangular grid of points. This is accomplished by interpolating the known node point displacements to find the displacements at the points in the output grid for each reflective surface in the system. These displacements can then be combined using the information obtained from a raytrace of the system to determine the wavefront error at each point in the grid. If the system contains only one mirror (which is spherical or paraboloidal) and a point feed the wavefront errors for on-axis operation can be computed directly from the geometry of the system without the need for a raytrace.

The following sections will describe the methods used to perform the interpolation of the node point displacements to find the displacements on the optical grid. The interpolation actually involves two steps: 1) a search to determine where on the finite element model each optical grid

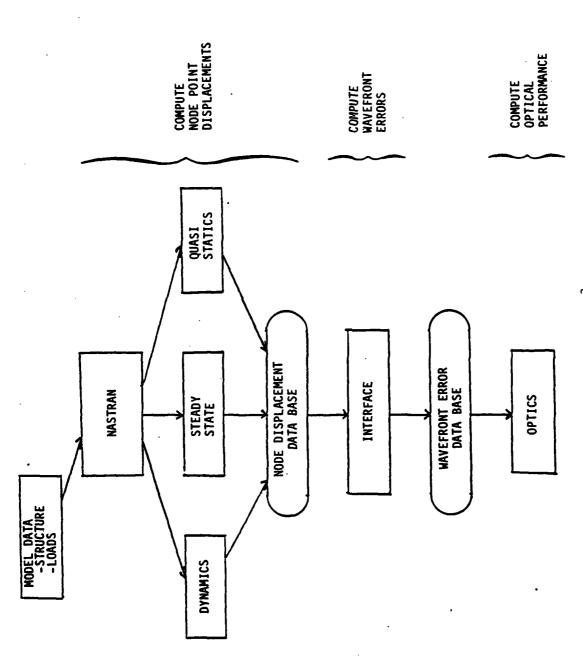


Figure 2-13. ILS³ structure.

point lies; and 2) the computation of the interpolation coefficients for each point. The algorithms used in both steps have been designed to allow any type of finite element model for the mirror surface.

2.3.2 Output Optical Grid

Before the search and interpolation methods can be implemented, a grid of optical points must be established. The wavefront errors will be evaluated at the optical points which lie on the mirror. These points are assumed to form a rectangular grid which lies in a plane parallel to the outgoing wavefront. The points will be defined in the X-Y plane of the optical coordinate system. The origin of this coordinate system will be located at the vertex of the optical surface. This is shown in Figure 2-14. The spacing of the optical points in the grid will be input by the user.

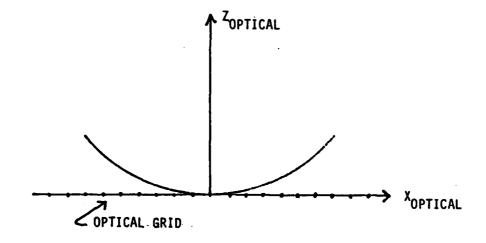


Figure 2-14. Optical coordinate system.

All node-point locations and displacements in the finite-element model will be transformed to the optical coordinate system before performing the search and interpolation. The rotation matrix from the input global coordinate system to the optical system is

$$R_{O} = \begin{bmatrix} v_{X}^{T} \\ v_{Y}^{T} \\ v_{Z}^{T} \end{bmatrix}$$

$$(2-12)$$

where V_X , V_Y , and V_Z are the direction cosine vectors of the optical system axes expressed in the global system. The node-point location transformation will be

$$\left\{ \begin{array}{c} X \\ Y \\ Z \end{array} \right\}_{\text{OPTICAL}} = R_{O} \left\{ \begin{array}{c} X \\ Y \\ Z \end{array} \right\}_{\text{GLOBAL}} - \left\{ \begin{array}{c} X_{O} \\ Y_{O} \\ Z_{O} \end{array} \right\}$$
 (2-13)

where x_0 , y_0 , and z_0 are the coordinates of the origin of the optical system expressed in the global system. The displacements and rotations at each point will be transformed by the equation

$$\left\{ \begin{array}{c} UX \\ UY \\ UZ \end{array} \right\}_{\text{OPTICAL}} = R_{O} \left\{ \begin{array}{c} UX \\ UY \\ UZ \end{array} \right\}_{\text{GLOBAL}} \left\{ \begin{array}{c} \theta X \\ \theta Y \\ \theta Z \end{array} \right\}_{\text{OPTICAL}} = R_{O} \left\{ \begin{array}{c} \theta X \\ \theta Y \\ \theta Z \end{array} \right\}_{\text{GLOBAL}}$$

2.3.3 Search

In order to evaluate the interpolation coefficients for the optical grid points, it must first be determined where in the finite element mesh each point lies. This will be done by searching each element in the model of the mirror surface for all optical points which lie within the boundaries of the element. Since the elements have an arbitrary shape with three or four sides, this search can be time consuming.

One method which will simplify the search is to use the geometric shape functions which are the basis of the finite element formulation. These functions express the location of any interior point in terms of the location of the corner nodes. For generality, and later application to the interpolation function, a "natural" coordinate system will be used to express these functions. This coordinate system is a function of the element boundaries, not global location of the element, but there is a unique relationship between the two coordinate systems for each element. The natural coordinate system for a typical element is shown in Figure 2-15. The coordinates ε , η are attached to the element and scaled so that the sides are defined by $\varepsilon = -1$, $\varepsilon = +1$, $\eta = -1$, $\eta = +1$. A triangular element is represented by collapsing edge 3-4.

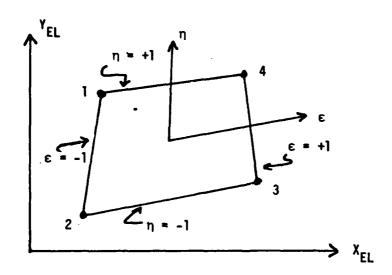


Figure 2-15. Element natural coordinate system.

In order for an optical point to lie inside the boundary of an element its ε , η coordinates must be in the range $-1 \le \varepsilon \le +1$ and $-1 \le \eta \le +1$. The implementation of this approach will now be described in detail.

Starting with a typical element which is part of the mirror surface of interest, the coordinates of the node points which define the element are transformed to the optical coordinate system, as described in Section

2.3.1. The minimum and maximum x and y values for the corner node coordinates of the element are found in order to define the search region. Only those optical points which lie within the region will be checked with respect to this element. This region is shown in Figure 2-16.

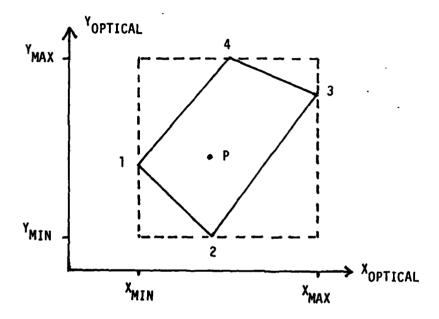


Figure 2-16. Element search region.

Those points within the search region must be checked to see if they lie within the element boundaries. In order to utilize the natural coordinate system, the coordinates of the corner nodes and the optical point must be rotated to a system in which the x, y plane is parallel with the plane of the element. This transformation is

$$\begin{bmatrix} x \\ y \\ z \end{bmatrix}_{EL} = R1 \begin{bmatrix} x \\ y \\ z \end{bmatrix}_{OPTICAL}$$
 (2-15)

where

R1 = coordinate transformation matrix from the optical system to an element system

$$R1 = \begin{bmatrix} v_X^T \\ v_Y^T \\ v_Z^T \end{bmatrix}$$

$$3x3$$
(2-16)

$$v_{x} = \frac{1}{L_{23}} \begin{bmatrix} x_{3} - x_{2} \\ y_{3} - y_{2} \\ z_{3} - z_{2} \end{bmatrix}$$
 (2-17)

$$v_{xy} = \frac{1}{L_{13}} \begin{bmatrix} x_1 - x_2 \\ y_1 - y_2 \\ z_1 - z_2 \end{bmatrix}$$
 (2-18)

$$V_{z} = V_{x} \times V_{yy} \tag{2-19}$$

$$v_{y} = v_{z} \times v_{x} \tag{2-20}$$

Before the optical point P can be rotated from the optical coordinate system to the element system, the Z coordinate, in the optical system, of the projection of the optical point onto the element plane must be found. This projection is along the optical Z axis as shown in Figure 2-17.

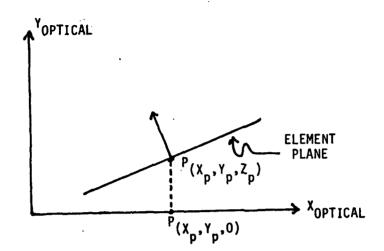


Figure 2-17. Optical point surface intersection.

The equation of the element plane is

$$Ax + By + Cz + D = 0$$
 (2-21)

where

$$\begin{bmatrix} A \\ B \\ C \end{bmatrix} = V_2$$
 (2-22)

x, y, z = A point on the plane expressed in the optical coordinate system

Substituting the known coordinates of corner node 1 into the equation and solving for D results in

$$D = -Ax_1 - By_1 - Cz_1$$
 (2-23)

when this value and the x, y coordinates of optical point P are substituted into this equation the z coordinate can be found:

$$Z_{p} = \frac{-D - Ax_{p} - By_{p}}{C}$$
 (2-24)

The x,y coordinates in the element system of the optical point P expressed in terms of the unknown ϵ , η coordinates and the x, y locations of the corner nodes are

$$x_{p} = \frac{1}{4} \left[(1 - \epsilon)(1 + \eta)x_{1} + (1 - \epsilon)(1 - \eta)x_{2} + (1 + \epsilon)(1 - \eta)x_{3} + (1 + \epsilon)(1 + \eta)x_{4} \right]$$
(2-25)

$$Y_{p} = \frac{1}{4} \left[(1 - \epsilon)(1 + \eta)Y_{1} + (1 - \epsilon)(1 - \eta)Y_{2} + (1 + \epsilon)(1 - \eta)Y_{3} + (1 + \epsilon)(1 + \eta)Y_{4} \right]$$
(2-26)

Collecting terms and rewriting results in

$$X_{p} = A_{1} + A_{2}\varepsilon + A_{3}\eta + A_{4}\varepsilon\eta \qquad (2-27)$$

$$Y_p = B_1 + B_2 \varepsilon + B_3 \eta + B_4 \varepsilon \eta$$
 (2-28)

where

$$A_{1} = \frac{1}{4} (x_{1} + x_{2} + x_{3} + x_{4})$$

$$A_{2} = \frac{1}{4} (-x_{1} - x_{2} + x_{3} + x_{4})$$

$$A_{3} = \frac{1}{4} (x_{1} - x_{2} - x_{3} + x_{4})$$

$$A_{4} = \frac{1}{4} (-x_{1} + x_{2} - x_{3} + x_{4})$$

$$B_{1} = \frac{1}{4} (y_{1} + y_{2} + y_{3} + y_{4})$$

$$B_{2} = \frac{1}{4} (-y_{2} - y_{2} + y_{3} + y_{4})$$

$$B_{3} = \frac{1}{4} (y_{1} - y_{2} - y_{3} + y_{4})$$

$$B_{4} = \frac{1}{4} (-y_{1} + y_{2} - y_{3} + y_{4})$$

Solving the first equation for ϵ results in

$$\varepsilon = \frac{-A_1 - A_3 \eta + X_p}{A_2 + A_4 \eta}$$
 (2-30)

(2-29)

Substituting this expression for ϵ into the equation for Y_p results in a quadratic equation in η :

$$c_3^2 n + c_2 n + c_1 = 0$$
 (2-31)

where

$$C_{1} = A_{2}B_{1} - A_{1}B_{2} - A_{2}Y_{p} + B_{2}X_{p}$$

$$C_{2} = A_{4}B_{1} - A_{1}B_{4} - A_{3}B_{2} + A_{2}B_{3} - A_{4}Y_{p} + B_{4}X_{p}$$

$$C_{3} = A_{4}B_{3} - A_{3}B_{4}$$

$$(2-32)$$

In solving this equation for η , if $C_3 = 0$, then

$$\eta = -C_1/C_2 \tag{2-33}$$

Otherwise

$$\eta = \frac{-c_2 \mp \sqrt{c_2^2 - 4c_1c_3}}{2c_3}$$
 (2-34)

If all of the roots lie outside the range, $-1 \le n \le +1$, then the optical point P is outside the boundaries of the element. If a root is in the correct range then it can be substituted into the previous equation to find ε . If it lies in the range $-1 \le \varepsilon \le +1$, then point P is in the element. Once an optical point in the element has been found, the coefficients for interpolation of the corner node displacements can be determined. This procedure will be described in Section 2.3.4.

This procedure will be repeated for all optical points which lie within the search region for this element. When this is complete, the search proceeds to the next element in the mirror model until the locations of all optical points have been found.

2.3.4 Interpolation Methods

Once an optical point is found to lie within a given element, the displacement at the optical point can be found by interpolating the known displacements at the element node points. The interpolation is simple if the mirror behaves as a rigid body with respect to the support structure. In this case the motion of any point on the surface is a function of the motion of the support points. The interpolation functions for a rigid mirror on two types of kinematic mounts are described in Section 2.3.4.1. If the flexibility of the mirror is included in the finite-element model, a more complicated interpolation is required.

A number of interpolation methods are available, but many of these are only applicable to a surface modelled by a square or rectangular grid of points. In general a finite-element mesh of the surface will be non-uniform with the density of node points varying across the optical surface. The generality of the grid can be accounted for by utilizing the basic principles of the finite-element method in which the displacement at any point on the interior of an element can be expressed as a function of the known displacements at the node points defining the element. These displacement shape functions can be expressed in either the global coordinate system or the natural coordinate system for the elements. A variety of shape functions can be developed depending on how the optical surface has been modelled. An interpolation methodology for a mirror modelled by plate bending elements is discussed in Section 2.3.4.2.

2.3.4.1 Rigid Mirror Interpolation

When a mirror is stiff enough that the elastic deformations are expected to be small compared to the allowable values, it will behave and can be modelled as a rigid body. It is assumed that a rigid mirror will be attached to the supporting structure by a kinematic mount. This mount will permit only rigid-body motion of the supporting structure to be transferred to the mirror. Thus the motion of any point on the mirror will be a function of the motion of the support points only. The number of support DOF's must equal the number of allowable rigid-body motions. For a three dimensional model six independent supports are required.

Several types of kinematic mounts have been designed. Two of the most common will be described in this section and included in the program. Other types of mounts can be added later if desired.

The first type of kinematic mount is shown in Figure 2-18 along with the local mount coordinate system. In this type of mount, point A is supported in the local x, y, and z translational directions, point B in the local y and z directions and point C in the z direction. The motion of any optical point P can be expressed in terms of the motion of the support points as

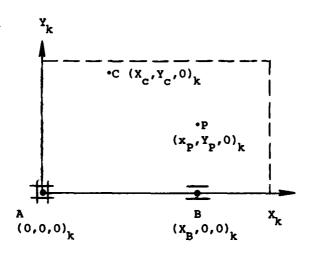


Figure 2-18. Kinematic mount type #1.

$$UX_{\mathbf{p}} = UX_{\mathbf{A}} + Z_{\mathbf{p}} \theta \mathbf{y} - Y_{\mathbf{p}} \theta \mathbf{z}$$

$$UY_{\mathbf{p}} = UY_{\mathbf{A}} - Z_{\mathbf{p}} \theta \mathbf{x} + X_{\mathbf{p}} \theta \mathbf{z}$$

$$UZ_{\mathbf{p}} = UZ_{\mathbf{A}} + Y_{\mathbf{p}} \theta \mathbf{x} - X_{\mathbf{p}} \theta \mathbf{z}$$

$$(2-35)$$

where

$$\theta x = \left[UZ_{C} - UZ_{A} + x_{C} (UZ_{A} - UZ_{B})/x_{B} \right]/Y_{C}$$

$$\theta y = \left(UZ_{A} - UZ_{B} \right)/x_{B}$$

$$\theta z = \left(UY_{B} - UY_{A} \right)/x_{B}$$
(2-36)

These equations assume that the location and displacement vectors of the support points and the optical points are expressed in the local coordinate system of the kinematic mount. The transformations from the optical system to the local mount system for any point i are

$$\begin{bmatrix} x \\ y \\ z \end{bmatrix}_{i}^{k} = R_{k} \begin{bmatrix} x \\ y \\ z \end{bmatrix}_{i}^{o} - \begin{cases} x \\ y \\ z \end{bmatrix}_{A}^{o}$$
 Location (2-37)

where

$$R_{k} = \begin{bmatrix} v_{xk}^{T} \\ v_{xk}^{T} \\ v_{zk}^{T} \end{bmatrix}$$
 (2-39)

$$v_{Xk} = \frac{1}{L_{AB}} \begin{bmatrix} x_B - x_A \\ y_B - y_A \\ z_B - z_A \end{bmatrix}^{\circ}$$

$$v_{XYk} = \frac{1}{L_{AC}} \begin{bmatrix} x_C - x_A \\ y_C - y_A \\ z_C - z_A \end{bmatrix}^{\circ}$$

$$v_{XYk} = \sqrt{2} x_K \times \sqrt{2} x_K$$

$$v_{Yk} = \sqrt{2} x_K \times \sqrt{2} x_K$$

The second type of kinematic mount is shown in Figure 2-19. In this mount the motion at each of the three support points is restrained in both the local Z direction and the tangential direction of the circle formed by three points. The local mount coordinate system is located at the center of this circle and is oriented so that point A lies on the negative Y-axis.

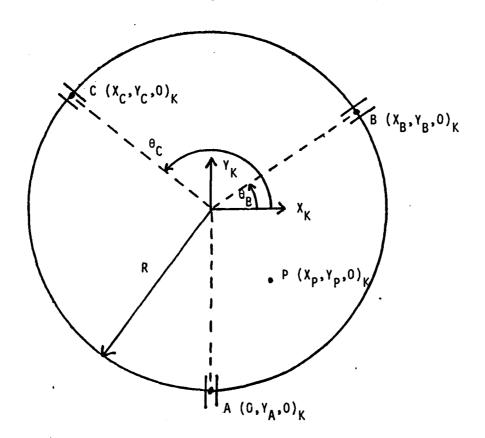


Figure 2-19. Kinematic mount type #2.

The displacement of any optical point P can be expressed in terms of the displacements of the support points by the relationships shown below.

The displacements of point P as a function of the motions of the center of the mount circle, point D, are

$$\begin{aligned}
\mathbf{U}\mathbf{x}_{\mathbf{p}} &= \mathbf{U}\mathbf{x}_{\mathbf{D}} + \mathbf{z}_{\mathbf{p}} \theta \mathbf{y}_{\mathbf{D}} - \mathbf{y}_{\mathbf{p}} \theta \mathbf{z}_{\mathbf{D}} \\
\mathbf{U}\mathbf{y}_{\mathbf{p}} &= \mathbf{U}\mathbf{y}_{\mathbf{D}} - \mathbf{z}_{\mathbf{p}} \theta \mathbf{x}_{\mathbf{D}} + \mathbf{x}_{\mathbf{p}} \theta \mathbf{z}_{\mathbf{D}} \\
\mathbf{U}\mathbf{z}_{\mathbf{p}} &= \mathbf{U}\mathbf{z}_{\mathbf{D}} - \mathbf{y}_{\mathbf{p}} \theta \mathbf{x}_{\mathbf{D}} + \mathbf{x}_{\mathbf{p}} \theta \mathbf{y}_{\mathbf{D}}
\end{aligned}$$

The motions of point D can be expressed in terms of the tangential, UT_1 , and out-of-plane, UZ_1 , displacements of the support points

$$ux_{D} = \frac{1}{A} [(x_{B} - x_{C})uT_{A} + x_{C}uT_{B} - x_{B}uT_{C}]$$

$$uy_{D} = \frac{1}{A} [(y_{B} - y_{C})uT_{A} + (R + y_{C})uT_{B} - (R + y_{B})uT_{C}]$$

$$uz_{D} = \frac{1}{R \cdot A} [(z_{B}y_{C} - x_{C}y_{B})uz_{A} - R \cdot x_{C}uz_{B} + R \cdot x_{B}uz_{C}]$$

$$\theta x_{D} = \frac{1}{R \cdot A} [(x_{D} - x_{B})uz_{A} - x_{C}uz_{B} + x_{B}uz_{C}]$$

$$\theta y_{D} = \frac{1}{R \cdot A} [(x_{C} - y_{B})uz_{A} - (R + y_{C})uz_{B} + (R + y_{B})uz_{C}]$$

$$\theta z_{D} = \frac{1}{R \cdot A} [(x_{B}y_{C} - y_{B}x_{C})/R \cdot uT_{A} - x_{C}uT_{B} + x_{B}uT_{C}]$$

where

$$A = X_{B} - X_{C} + (X_{B}Y_{C} - Y_{B}X_{C})/R$$

$$R = -Y_{A}$$
(2-43)

The tangential displacements are related to the local X- and Y-axis displacements by the equations

Finally, the node-point locations and displacements used in the previous equations are assumed to be in the local kinematic mount coordinate system. The transformation from the optical system to the mount system is a function of the location of the center of the mount circle, point B. This location can be found by transforming the coordinates of points A, B and C to an intermediate coordinate system in which the X-Y plane is the plane formed by the points and solving the equation of a circle. Once the location of point D is known, the transformation from the intermediate system to the mount system can be found. This transformation is then used to convert the location and displacements of the support points and the location of the optical point to the local system. After the displacements at the optical point is found it is converted back to the optical system using the inverse transformation.

2.3.4.2 Flexible Mirror Interpolation

When a mirror surface is modelled as a continuous elastic surface, the displacement of the optical points can be expressed as a function of the displacements and rotations at the node points of the element containing each optical point. The relationship between the node points and the optical points for each element will utilize shape functions expressed in the natural coordinate system which was used previously in the search methodology. The development of displacement shape functions for the plate and shell elements, which are typically used to model a mirror surface, has been the subject of extensive research. One relatively simple model, which has been selected for implementation into ILS³, is presented here. Other models could be included at a later date if necessary.

The shape function model chosen is based on an eight-node quadrilateral element. As shown in Figure 2-20 the three translational displacements at each node point are known. The displacements at any point Pinside the element can be expressed as a function of the nodal displacements and the location of P in the natural coordinate system, (ϵ_p, η_p) , as

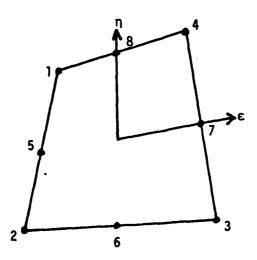


Figure 2-20. Eight node element numbering.

$$UX_{\mathbf{p}} = \sum_{i=1}^{8} H_{i}(\varepsilon_{\mathbf{p}}, \eta_{\mathbf{p}}) UX_{i}$$

$$UY_{\mathbf{p}} = \sum_{i=1}^{8} H_{i}(\varepsilon_{\mathbf{p}}, \eta_{\mathbf{p}}) UY_{i}$$

$$UZ_{\mathbf{p}} = \sum_{i=1}^{8} H_{i}(\varepsilon_{\mathbf{p}}, \eta_{\mathbf{p}}) UZ_{i}$$

$$(2-45)$$

where the shape function H_i at each node is

$$H_{i}(\varepsilon_{p}, \eta_{p}) = \frac{1}{4} (1 + \varepsilon_{p} \varepsilon_{i}) (1 + \eta_{p} \eta_{i}) (\varepsilon_{p} \varepsilon_{i} + \eta_{p} \eta_{i} - 1) \quad i = 1, 2, 3, 4$$

$$H_{i}(\varepsilon_{p}, \eta_{p}) = \frac{1}{2} (1 - \varepsilon_{p}^{2}) (1 + \eta_{p} \eta_{i}) \quad i = 6, 8$$

$$H_{i}(\varepsilon_{p} \eta_{p}) = \frac{1}{2} (1 - \eta_{p}^{2}) (1 + \varepsilon_{p} \varepsilon_{i}) \quad i = 5, 7$$

This set of shape functions allows a quadratic distribution of displacements along the edges with some higher order terms included in the interior. If the elements used in the finite-element model of the surface permit only linear or quadratic displacement fields, these functions can be used. When higher order elements are used in the model, a higher order interpolation model should be used.

When an element is modelled with eight nodes, the interpolation equations can be used directly. If an element is modelled as a four-node quadrilateral or as a triangle with three or six nodes, adjustments can be made to the interpolation functions. In the case of a four-node quadrilateral, as shown in Figure 2-21, the midside displacements can be found by interpolating the displacements, and rotations (if present) at the corners.

If the rotations are not defined at the corners, the midside displacement is simply the average of the displacements at the corners. When the rotations are present, the midside displacement can be found by averaging the end displacements and adding the displacement due to the end rotations. As an example, an edge of a typical element is shown in Figure 2-22.

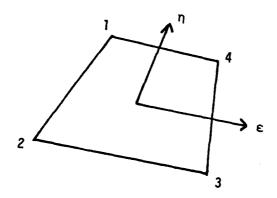


Figure 2-21. Four-node quadrilateral.

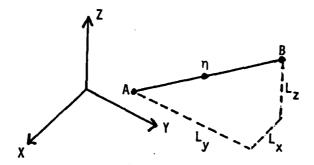


Figure 2-22. Element edge interpolation.

The displacement at midside point m can be expressed as

$$UX_{m} = \frac{UX_{A} + UX_{B}}{2} + \frac{(\theta Y_{A} - \theta Y_{B})L_{z}}{8} - \frac{(\theta Z_{A} - \theta Z_{B})L_{y}}{8}$$
(2-47)

$$UY_{m} = \frac{UY_{A} + UY_{B}}{2} - \frac{(\theta X_{A} - \theta X_{B})L_{z}}{8} + \frac{(\theta Z_{A} - \theta Z_{B})L_{x}}{8}$$

$$UZ_{m} = \frac{UZ_{A} + UZ_{B}}{2} + \frac{(\theta X_{A} - \theta X_{B})L_{y}}{8} - \frac{(\theta Y_{A} - \theta Y_{B})L_{x}}{8}$$

When the element is triangular, with three or six nodes as shown in Figure 2-23, the shape functions can be modified by assuming that the edge between nodes 3 and 4 collapses to a point as shown in Figure 2-24. The new shape functions are

$$H_{i}(\varepsilon_{p}, \eta_{p}) = \frac{1}{4} (1 + \varepsilon_{p} \varepsilon_{i}) (1 + \eta_{p} \eta_{i}) (\varepsilon_{p} \varepsilon_{i} + \eta_{p} \eta_{i} - 1) \quad i = 1, 2$$

$$H_{i}(\varepsilon_{p}, \eta_{p}) = \frac{1}{2} (1 + \varepsilon_{p} \varepsilon_{i}) \varepsilon_{p} \varepsilon_{i} \quad i = 3$$

$$H_{i}(\varepsilon_{p}, \eta_{p}) = \frac{1}{2} (1 - \eta_{p}^{2}) (1 + \varepsilon_{p} \varepsilon_{i}) \quad i = 4$$

$$H_{i}(\varepsilon_{p}, \eta_{p}) = \frac{1}{2} (1 - \varepsilon_{p}^{2}) (1 + \eta_{p} \eta_{i}) \quad i = 5, 6$$

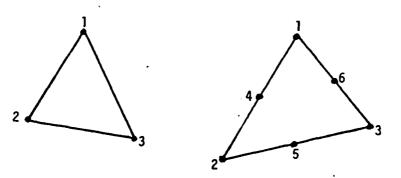


Figure 2-23. Triangular element geometry.

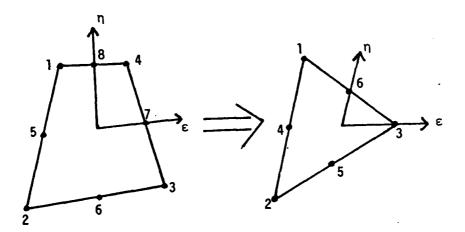


Figure 2-24. Triangular element generation.

These interpolation functions will be unique for each optical point. They can be saved for later use with additional displacement vectors to avoid the cost of recalculation. Once the displacements at each optical point have been determined, the wavefront error at each point can be found. This is discussed in the next section.

2.3.5 Wavefront Error Computation

Once the optical grid has been established and the displacements at the grid points have been found by interpolation, the next step is to determine the wavefront error at each optical point. For a single mirror system with an optional feed this is a simple task if the surface is spherical, paraboloidal, or flat, and only on-axis operation is to be studied. All other types of systems require a raytrace.

Given a system with a single surface and a feed as shown in Figure 2-25, and assuming small displacements, the wavefront error at any point due to surface displacements is equal to

$$WFE_{i} = 2 \cdot NZ_{i}(N_{i} \cdot U_{i}) \qquad (2-50)$$

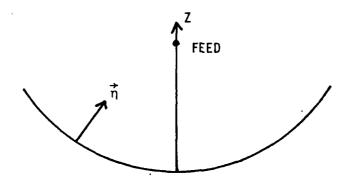


Figure 2-25.

where N_i = surface normal vector at point i

 $NZ_{i} = Z$ axis component of N_{i}

 $\dot{\vec{U}}_{i}$ = surface displacement vector at point i

This is shown in Figure 2-26. The wavefront error at point i due to motion of the point feed is equal to

$$WFE_{i} = -2N_{x}N_{z}Ux_{f} - 2N_{y}N_{z}Uy_{f} - (2N_{z}^{2} - 1)Uz_{f}$$
 (2-51)

as shown in Figure 2-26. Both components of the wavefront error are dependent on the surface normal vector at point i. The normal vector is a function of the location of the point on the surface and the type of surface. Given below are the equations for the normal vector at a point i (x, y, z) for two surface types. Both equations assume that the point locations are given in a coordinate system with the origin located at the vertex of the surface and the Z-axis parallel to the optical axis.

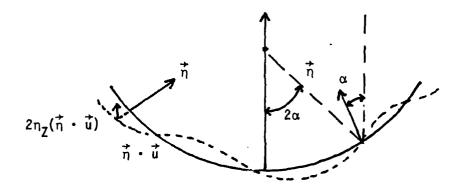
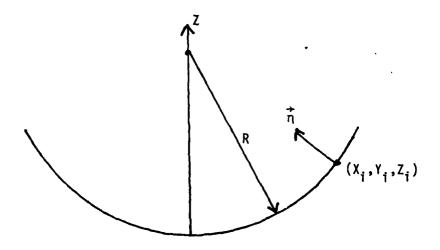


Figure 2-26.

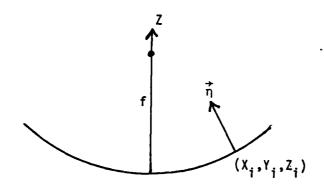
Spherical Surface:



$$N_{x} = X_{i}/R$$
 $N_{y} = -Y_{i}/R$
 $N_{z} = \sqrt{R^{2} - X_{i}^{2} - Y_{i}^{2}}/R$

(2-52)

Paraboloidal Surface:



$$r = \sqrt{x_i^2 + y_i^2}$$

$$N_{x} = \frac{-x_{i}}{\sqrt{4f^{2} + x_{i}^{2} + Y_{i}^{2}}}.$$

$$N_{y} = \frac{-y_{i}}{\sqrt{4f^{2} + x_{i}^{2} + Y_{i}^{2}}}$$

$$N_{z} = \frac{2_{f}}{\sqrt{4f^{2} + x_{i}^{2} + Y_{i}^{2}}}$$
(2-53)

Using these equations, the wavefront error at each optical point can be computed. These will be stored in a data base for input to the optics module.

2.3.6 Summary

A new interface program for single-mirror systems has been developed for the ILS³. This program will compute the wavefront errors at a user specified grid of points by interpolating the displacements at the node points of the finite-element model of the system. The program is capable of handling both rigid and flexible mirrors and is designed to be modular to permit the addition of higher order interpolation functions at a later date. The outputs of the program are the wavefront errors at the optical points. These can then be input to the ILS³ optics module to compute the PSF and LOS errors.

The methods described here will be used in the next work phase to update the multiple mirror interface program. The final result of these efforts will be a program which can be used with any system finite-element model without many of the earlier restrictions.

2.4 Investigation of Line-Of-Sight Jitter Reduction Algorithms

2.4.1 Introduction

As has been shown earlier, [9] the Draper Integrated Simulations (DIS) provides a natural test bed for examining the behavior of current and proposed space-based surveillance systems. In particular, since (LOS) stability has been found to be a major performance-limiting factor for a broad class of downward-staring surveillance systems, a technique proposed by D. Fried [10,11] for reduction of the LOS jitter effects has been examined and evaluated using the DIS. In the sections to follow, this technique is discussed and results from this investigation are reported, including limits of applicability as well as conditions under which the best performance is achieved for a realistic case.

2.4.2 Reduction of Jitter Effects

Moving targets are most commonly detected by mosaic sensors through differencing of successive frames. Unfortunately, the changes in the detectors' output are not due only to moving or changing targets, but also to jitter and drift of the sensor LOS and to detector noise. Under certain conditions, there is some retrievable information about the jitter in the sequence of frame outputs from the detector array. Assume that the focal plane data rate is higher than the cut-off frequency of the jitter, and the jitter amplitude is much smaller than the spatial resolution of the sensor optics/detector. Then, in the absence of detector noise, the movement of the sensor between two arbitrary frames can be estimated and this estimate used to correct the output before further processing to extract the target.

2.4.2.1 Jitter Estimation

The estimation method used is essentially that proposed by D. Fried, et. al., and will be briefly reviewed here. Figure 2-27 is a schematic of a portion of the mosaic array which has moved by ox and oy between two frames at times t and t' respectively.

If $S_{A,t}$ (respectively, $S_{A,t}$) and $S_{B,t}$ (respectively, $S_{B,t}$) are the voltage output of adjacent detectors A and B at time t (respec-

tively, t'), and Δ is the center-to-center detector spacing, then, with the restrictions mentioned previously,

$$S_{A,t} = S_{A,t} + \alpha \delta x + \beta \delta y \qquad (2-54)$$

$$S_{B,t} = S_{A,t} + \alpha_A \Delta$$
 (2-55)

$$S_{B,t}$$
, $\tilde{s}_{A,t} + \alpha_A(\Delta + \delta_X) + \beta_A \delta_Y$ (2-56)

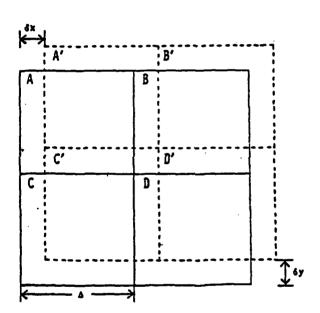


Figure 2-27. Two arbitrary frames displaced by δx and δy .

Using these approximations, it can be shown that

$$\hat{\delta}_{x} = \frac{\Delta}{4} \left\langle \frac{(s_{A,t} - s_{B,t})^{2} - (s_{A,t} - s_{B,t})^{2}}{(s_{A,t} - s_{B,t})^{2}} \right\rangle$$
 (2-57)

is a good estimate of the displacements δx . The symbols < > represents the averaging operator over a portion of, or, perhaps the entire, focal

plane. A similar expression can be obtained for by using pairs of detectors A and C. With the same restrictions as before, it follows that

$$S_{C,t} = S_{A,t} + \beta_A \Delta \qquad (2-58)$$

$$S_{C,t'} \stackrel{\sim}{=} S_{A,t} + \alpha_A \delta x + \beta_A (\Delta + \delta y) \qquad (2-59)$$

and thus

$$\hat{\delta}_{y} = \frac{\Delta}{4} \left\langle \frac{(s_{A,t} - s_{C,t})^{2} - (s_{A,t} - s_{C,t})^{2}}{(s_{A,t} - s_{C,t})^{2}} \right\rangle$$
 (2-60)

The first goal of this work is to simulate, with realistic scenes, jitter and detector noise data, the estimation of LOS jitter from the detector output. Proper mechanization considerations of the focal plane with respect to the dynamic range problem and A/D conversion are also included because these factors have a strong influence on the results.

2.4.2.2 Correction of Jitter Effects

Depending on the scenario selected, there are several ways of implementing the correction of the jitter effects. One method is to employ a stabilization mirror with a feedback using the estimated values of the jitter, but this approach may be difficult to implement in the case of sensors with a wide field-of-view. The method selected here accomplishes the correction through data processing. It has the advantage of allowing for localized correction of the jitter effects when the field-of-view is large and/or the aperture is large and requires segmentation of the optical elements.

A combination of Eqs. (2-54), (2-55), (2-56), (2-58) and (2-59) could be used to solve for α and β after replacing δx and δy by their estimates δx and δy . Equation (2-54) assumes linearity over a small range, but Eqs. (2-55), (2-56), (2-58) and (2-59) assume linearity of the detector output over a much larger range, implying either no high spatial frequency

content in the background or a large (PSF) compared to the pixel size. Realistic simulation studies of surveillance systems in which LOS jitter is a major performance-limiting factor have shown [9] that rarely, in fact, is either one of these conditions ever realized. One reason they can be used to obtain estimates on and by is because of the averaging process involved in their calculation. Consequently it is desirable to use only equations similar to Eq. (2-54). In Eqs. (2-54), (2-55), (2-56), (2-58) and (2-59), the values of α and β are time dependent, but, if the drift is slow enough so that over a certain time interval T the LOS position has not changed more than a fraction of the pixel size, then α and β can be assumed to be constant during that time interval. In this case α and β are determined for each detector using a sequence of operations like Eq. (2-54) at times t, t + Δ t, ..., t + $n\Delta$ t ($n\Delta$ t << T) with a least-squares procedure. When using this method, the scene itself and the responsivity of the detectors are assumed not to change during that time interval. The correction will be applied during the interval T using values of α and β which have been calculated only during the interval $n\Delta t$. This is critical since, in this manner, the target information will not be lost except for the pixel containing the target at the time of the least-squares calculation. Even for this pixel, if the least-squares procedure is done on a sequence short enough compared to the dwell time of the target over a detector pixel, the target information is only partially lost.

This correction scheme is inserted after the A/D conversion following the focal plane simulation and prior to any temporal frame integration that might be employed to match target dwell-time to overall frame-time. After frame integration, information about the jitter would be buried more deeply in the output data.

2.4.3 Application To A Representative Surveillance Problem

Consider a point-source target moving across a scene such as the Santa Cruz region (Figure 2-28). For a typical mission, scenario and sensor configuration, the dependence (as found from simulation) of threshold contrast intensity for target acquisition on the level of LOS jitter behaves as illustrated in Figure 2-29. A realistic level of focal plane

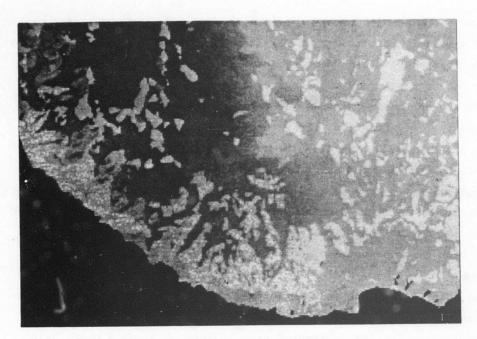


Figure 2-28. Santa Cruz background.

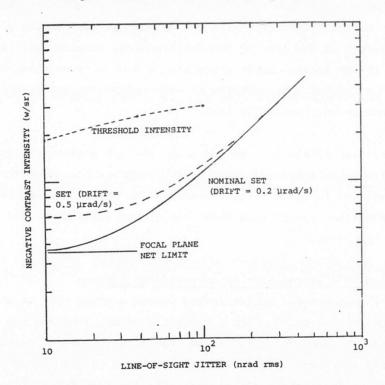


Figure 2-29. Typical dependence of threshold target ontrast intensity on LOS jitter, with LOS drift and focal plane NET as parameters.

noise has been included, and LOS drift effects have been shown for two representative values. The target image is assumed to be perfectly phased with respect to the focal plane, i.e., trajectory following the middle of a row of detectors and dwell time matched to frame time. The SET and NET represent the system-equivalent target and noise-equivalent target after third-order differencing. The threshold intensity curve is for the lowest contrast intensity allowing track formation with a criterion of 12 hits out of 14 consecutive frames. Figure 2-29 shows that the detection of the target is limited by detector noise and jitter effects. It is a realistic scenario, and because of the detector noise it is a stressing case for the jitter suppression technique. Figure 2-30 shows some details of the processor behavior as a function of the threshold used after third-order differencing. It can be seen that the target is acquired when the threshold is selected such that the number of pixels showing a false hit is about 7% of the total number of pixels.

The PSF used for this case was a two-dimensional Gaussian. Most of the results presented below are for a PSF with 91% of the energy included in one detector when the center of the PSF is at the center of the detector. In some cases a comparison has been made with a large PSF for which this value is 46%. Figure 2-31 shows the percentage of irradiance over the neighboring pixels for those two PSFs.

The jitter information was derived from power spectral density (PSD) data obtained from a representative third generation gyro (TGG) manufactured by the C.S. Draper Laboratory (CSDL). To this data was added a 5 Hz roll off to simulate platform damping corresponding to a representative attitude control loop. Figure 2-32 shows the PSD of the TGG, the PSD of the TGG with the 5 Hz roll off and the spectrum of the jitter sampled at 80 frames/sec. The high frequency increase of the sampled data is created by the aliasing due to the sampling and correctly reproduces what happens in the actual equipment. The low frequency discrepancy has no effect on the results because it is included separately as the drift. When the jitter time-history is averaged to obtain 10 samples per second, the PSF is broadened accordingly to compensate. Figure 2-33 shows a time sequence of

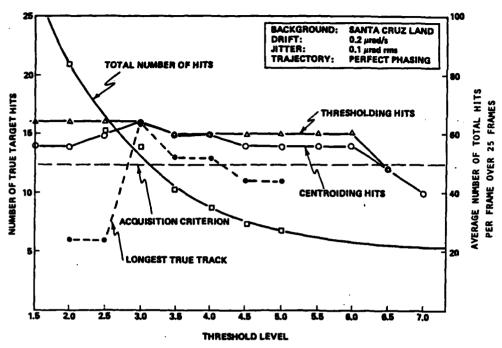


Figure 2-30. Signal processor performance as a function of threshold level after third-order differencing (one frame $= 25 \times 25$ pixels).

0.06	2.20	0.06		0	0.02	0.10	0.02	0
2.20	90.96	2.20		0.02	- 2.50	10.50	2.50	0.02
0.06	2.20	0.06		0.10	10.50	46.00	10.50	0.10
a. Small PSF grid.			0.02	2.50	10.50	2.50	0.02	
				0	0.02	0.1	0.02	0

Large PSF grid.

Figure 2-31. Irradiance distribution over the focal plane resulting from two point-spread functions used in the simulation study.

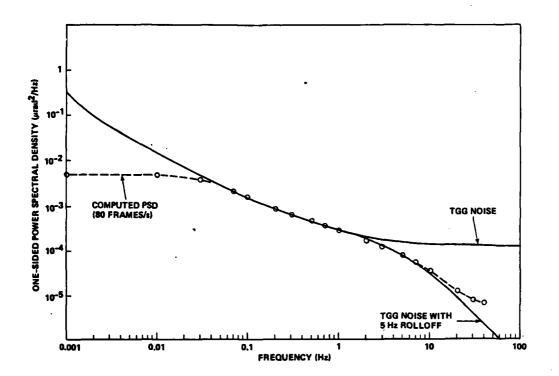


Figure 2-32. Line-of-sight jitter model.

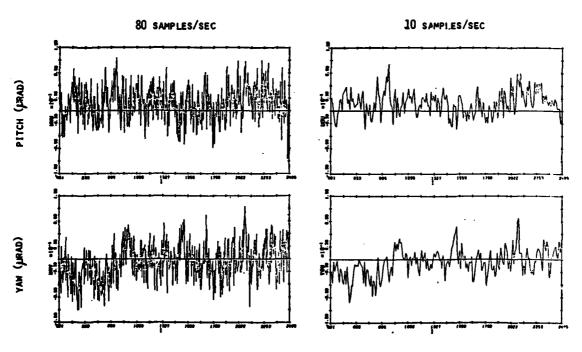


Figure 2-33. Graphical illustration of line-of-sight jitter time histories derived from the jitter model.

jitter displacements used in the simulation. In summary, the LOS perturbations are simulated by using a linear drift corresponding to the low frequency LOS perturbation, a jitter corresponding to the mid-range, and a broadening of the PSF corresponding to the high frequency.

The focal plane model is that of a generic planar hybrid [12] as illustrated in Figure 2-34. It is based on realistic noise characteristics and transimpedance data. The fixed pattern noise due to non-uniformity of the transimpedance is also included. In this mechanization, a dc bias with reset is included to increase the dynamic range of the focal plane. The reset information is kept in memory so that a signal restoration can be performed after A/D conversion. Note that the signal information can be restored for all but the first frame unless a calibrated reference voltage corresponding to a known input photon flux is used as bias.

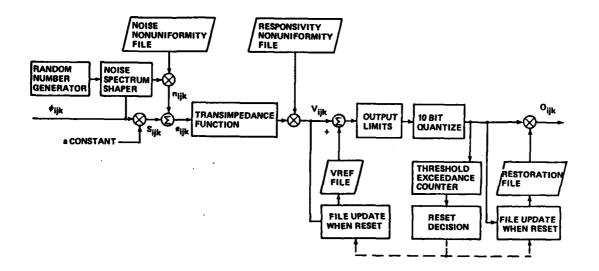


Figure 2-34. Generic planar hybrid focal plane model.

2.4.4 Results

TABLE TO STATE OF THE PROPERTY OF THE PARTY OF THE PARTY

In order to make the correction scheme possible, some of the hardware parameters of the focal plane must be appropriately selected. For the estimation of the jitter, the information regarding the spatial slope of the pixel output as a function of position must be preserved. Therefore the reset function must be suppressed. This is achieved by selecting an initial reference voltage approximately equal to the mid-value over the array of the voltage outputs of the multiplexer for the scene considered and by selecting an off-chip amplifier gain small enough so that no detectors reach saturation. This second point creates the need for a finer discretization level in the A/D conversion process. For the scenario considered, it was necessary to go from a quantization of 10 bits to 13 bits. An heterogeneous background like the Santa Cruz coastal area which includes highly structured land as well as relatively benign sea regions is a stressing background, because of the dynamic range involved, but the off-chip amplifier gain required was still within realistic limits.

The focal plane of a wide angle sensor is typically divided into submodules of 64 × 64 pixels. The estimation of the jitter for a submodule can be achieved with a smaller portion of the focal plane in order to reduce the computational load. It was found that a window of 20 × 20 pixels was sufficient, but for convenience a window of 25 × 25 pixels was used in order to deal with only one window size for estimation and correction. Such a size allows the tracking of a target in a meaningful way. To further reduce the computational load and improve the quality of the estimation, pairs of detectors which produce a small value of the denominator in Eqs. (2-57) and (2-60) were not included in the estimation. Also, if the value of the estimated jitter for a certain frame is small, no correction is applied for that frame.

Several methods can be devised to reduce the computational load of the correction calculation. The pixels for which $\left|\alpha \delta x\right|$ and $\left|\beta \delta y\right|$ are small do not need to be corrected, but knowing the range of δx and δy , it might be simpler to create a table of pixels for which $\alpha \delta x_m$ and $\beta \delta y_m$ are smaller than a predetermined value, δx_m and δy_m being for example estimated upper limits for 95% of the cases. More work is needed in order to find the optimum situation.

A study of the influence of the PSF size has shown that the large PSF (see Figure 2-31) allows a 25% improvement in clutter reduction compared to the small PSF. For the remainder of the study, the more realistic small PSF was used.

For the Santa Cruz background, it was found that the fixed pattern noise induces a reduction of the estimated value of the jitter, and therefore a poorer correction when compared to an homogeneous background. The reason is that the fixed pattern noise is confused with spatial variations of intensity over the sea portion and the intensity should vary when there is jitter. As the intensity does not vary with time but for the noise, the estimator concludes that there is no jitter and lowers the output of the averaging. The results presented here were generated with a detector responsivity randomly distributed over the focal plane area according to a Gaussian distribution with a sigma value of 15 percent.

The jitter correction scheme was used for a range of rms jitter values from 0.1 to 1 microradians. In this range it is found that the effect of the correction scheme is about equivalent to a reduction of the jitter by a factor of five.

Figures 2-35 and 2-36 show in a pictorial way an example of the results of the detection and tracking of three targets over the Santa Cruz area with an average contrast intensity equal to the limiting value shown on Figure 2-29 for an rms jitter level of 0.1 microradians. The numbers correspond to the track number in the track file, and the plus signs correspond to pixel locations which are used by several tracks. The three targets are selected such that there is no velocity mismatch column-wise (i.e., in the horizontal velocity component). The tracks are crossing, but the targets are not crossing. The improvement in the tracking of the two targets travelling above the land area can be seen. The target following the coastline is not detected, but observation of the intermediate results shows that this target could reach the status of 12 hits out of 14 possible hits given a longer observation period. For comparison the results for the same case are shown with ideal shot noise only. After correction the three

targets are perfectly tracked, which indicates that the process of tracking a target after jitter correction is noise limited.

2.4.5 Conclusions

The computational correction of jitter effects appears effective for the detection and tracking of moving targets such as aircraft from a space-based sensor. This work is still in progress, and better and more complete results are expected by optimizing some of the parameters used in the jitter estimation and correction. It has also been shown that the DIS simulation can be of value to the designer of space-based sensors.

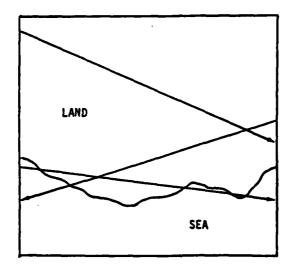


Figure 2-35. Coastline and target trajectories.

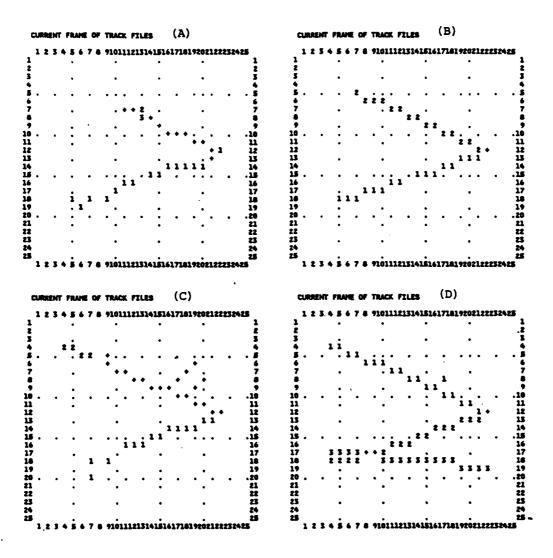


Figure 2-36. Content of track file after 25 frames of input (19 frames of third order differencing:

- A Real noise before jitter effect correction (JEC)
- B Real noise after JEC
- C Shot noise before JEC
- D Shot noise after JEC

REFERENCES

(1) "ACOSS Eleven Third Interim Technical Report," Vol. 1, CSDL Report CSDL-R-1598, December 1982.

2202222 essective throughter and enterly

- (2) Amies, W.F., "Numerical Methods for Partial Differential Equations," New York, Barnes and Noble, 1970.
- (3) This reference will be made available to qualified military and government agencies on request from RADC (OCSP) Griffiss AFB NY 13441-5700.
- (4) "ACOSS Eleven, Fourth Semi-Annual Technical Report," Vol. 1, CSDL Report CSDL-R-1648, June 1983.
- (5) This reference will be made available to qualified military and government agencies on request from RADC(OCSP) Griffiss AFB NY 13441-5700.
- (6) This reference will be made available to qualified military and government agencies on request from RADC (OCSP) Griffiss AFB NY 13441-5700.
- (7) "Functional Description of Signal Processing Methods," J. Valge, CSDL Report C-5231, December 1979.
- (8) This reference will be made available to qualified military and government agencies on request from RADC (OCSP) Griffiss AFB NY 13441-5700.
- (9) This reference will be made available to qualified military and government agencies on request from RADC (OCSP) Griffiss AFB NY 13441-5700.
- (10) Williams, R.I., and D.L. Fried, "Line-of-Sight Vibration Compensation Using The Background Clutter Pattern," The Optical Sciences Company, Report No. TR-442, October 1981.
- (11) Fried, D.L., and D.L. Hench, Computational Cancellation of Vibration Induced Clutter Leakage Using Polynomial Approximation, The Optical Sciences Company, Report No. DR-267, October 1982.
- This reference will be made available to qualified military and government agencies on request from RADC (OCSP) Griffiss AFB NY 13441-5700.

APPENDIX 1

SIGNAL PROCESSOR SIMULATION USER'S GUIDE

The simulation user has a menu of variables, listed below, which allow for a number of different processor configurations. In addition, minor changes to the simulation can also be made to allow for different processor configurations.

IOPT: Difference Order

0 = zeroth order

1 = first order

2 = second order

3 = third order

BOPT: Threshold Level Selection

1 = read in

 $2 = NE \times TNR$

3 = standard deviation of entire frame × TNR

LHRES: Acquisition Algorithm

0 = low resolution

1 = high resolution

DORDER: Difference Order used for Low Resolution Noise

Estimate

1 = first order

2 = second order

3 = third order

TOPT: Thresholding Polarity

-1 = negative contrast
+1 = positive contrast

0 = both

TPATRN: Thresholding Option

0 = simple 1 = HAC MTD

2 = CSDL MTD

3 = idealized MTD

IRET: Rationalized Exceedance Option

0 = no

1,2,3 = rational exceedance thresholding 1,2,3

IPOUT: Output to Image Processor Files

0 = no

1 = yes

ICFAR: CFAR Loop Control of Threshold Level

0 = no

1 = yes

CFARN: Optimum Number of Hits for CFAR loop

KNTLIM: Maximum Number of CFAR Loop Iterations per Frame

IOXTRA: Extra Data Option

0 = no print

1 = print

IPEAK: Centroid Option

0 = use whole centroid
1 = use only peak value

JCENT:

Cluster/Centroid Basis

1 = raw data

2 = differencing

3 = threshold exceedance

NPDROP:

Minimum Number of Points Needed to Perform

Least Squares Test or Correlation Coefficient Test

MINHT1, MAXFR1, MINHT2, MAXFR2:

MINHT1 out of MAXFR1 criterion for system track MINHT2 out of MAXFR2 criterion for acquired track

NSUBL:

Number of Subframes per Frame

NSUBF:

Number of Frames used for Noise Estimate

LSCC:

Track Discrimination

0 = least squares

1 = correlation coefficient

DMAX/RMIN: Maximum Allowed Variance from Least Squares

/Minimum Allowed Correlation Coefficient

HAFLEV:

Factor by Which Threshold is Reduced (or Increased)

for Pixels in System Track Search Gate

GAMMA:

Exponent for CFAR Loop Feedback

XKAPPA:

Multiplier for CFAR Loop Feedback

TNR:

Threshold to Noise Ratio used to Compute Noise

Estimate Threshold Level

User Input Threshold Level

INFIL: Number of File Containing Target and Background

Data to be Read in, Frame by Frame

MF, NF: Input Data Set Dimensions

MFC, NFC: Number of Rows and Columns Used

MLR, NLR: Number of Rows and Columns of Low/High Resolution Data Produced

KFN: Number of Frames Used

KX: Output Device

IR: Row Offset

なける場所の名のからのは個別できないのはのの個別

JC: Column Offset

KOFFS: Frame Number Offset

XMULT: Pixel Multiplication Factor

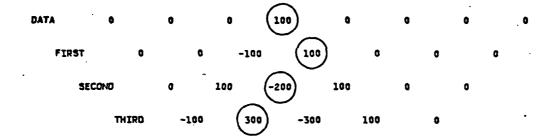
APPENDIX 2

EFFECTS OF TARGET PHASING ON SIGNAL PROCESSOR PERFORMANCE

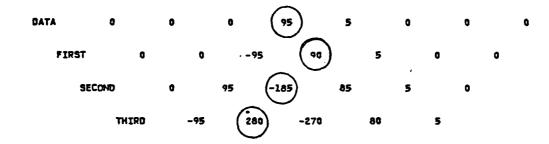
The following examples of raw data and the resultant first-, second-, and third-order differences show the effects of phasing. A target is said to be out of phase when its appearance in a given pixel is split between two frames (even though the actual period of time that it dwells in the pixel is equal to length of the frame time). A target is in phase when it appears in a given pixel for one frame only.

In the following examples the appearance of a target is split between the fourth and fifth frames. The examples are labeled by the ratio of the time spent by the target in the fourth frame to the time spent in the fifth frame; for instance, 60:40 phasing means that the target was in the pixel for 60% of frame four and 40% of frame five. The background is assumed to be zero for simplicity.

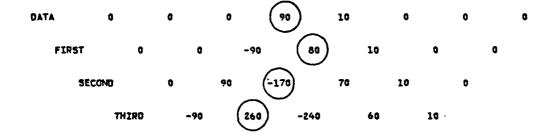
Example 1 - 100:0 Phasing



Example 2 - 95:5 Phasing



Example 3 - 90:10 Phasing



Example 4 - 85:15 Phasing

DATA 0 0 0 85 15 0 0 0

FIRST 0 0 -85 70 15 0 0

SECOND 0 85 -155 55 15 0

THIRD -85 (240) -210 40 15

Example 5 - 80:20 Phasing

Example 6 - 75:25 Phasing

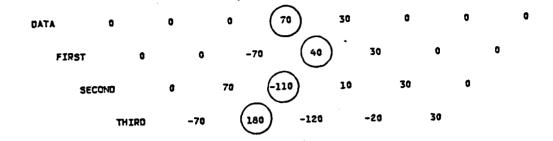
DATA 0 0 0 75 25 0 0

FIRST 0 0 -75 50 25 0 0

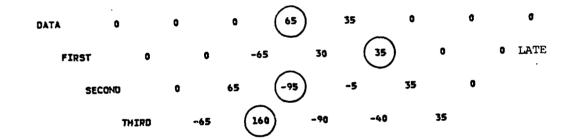
SECOND 0 75 -125 25 25 0

THIRD -75 200 -150 0 25

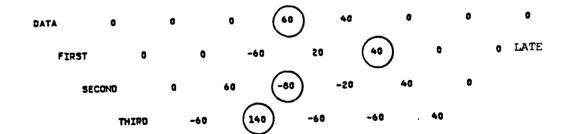
Example 7 - 70:30 Phasing



Example 8 - 65:35 Phasing



Example 9 - 60:40 Phasing



Example 10 - 55:45 Phasing

DATA 0 0 0 55 45 0 0 0

FIRST 0 0 -55 10 45 0 0 LATE

SECOND 0 55 -65 -35 45 0

THIRD -55 (120) -30 -80 45

Example 11 - 50:50 Phasing

DATA 0 0 0 50 50 0 0 0 TWICE

FIRST 0 0 -50 0 50 0 0 LATE

SECOND 0 50 -50 50 0 TWICE

THIRD -50 100 0 -100 50 EARLY

Example 12 - 45:55 Phasing

DATA 0 0 0 45 55 0 0 0

FIRST 0 0 -45 -10 55 0 0

SECOND 0 45 -35 -65 55 0

THIRD -45 (80) 30 -120 55 EARLY

Example 13 - 40:60 Phasing

DATA 0 0 0 40 60 0 0 0

FIRST 0 0 -40 -20 60 0 0

SECOND 0 40 -20 -80 60 0

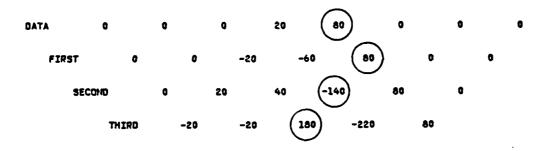
THIRD -40 60 60 -140 60 TWICE

Example 14 - 35:65 Phasing

THIRD -35 40 90 -160 65

Example 15 - 30:70 Phasing

Examp	le 16 -	25:75 P	hasing						
DATA	0	c .	0	25 -50	75	a . ₀ .	0	0	•
FIRST	BECCND .	0	-25 25		-125 -200	75 75	đ	J	
	THIRD	-25		(130)	-200		•		
Examç	ole 17 -	20:80	Phasing						



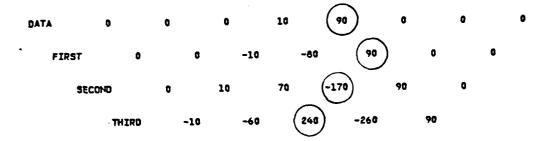
DATA 0 0 0 15 85 0 0

FIRST 0 0 -15 -70 85 0 0

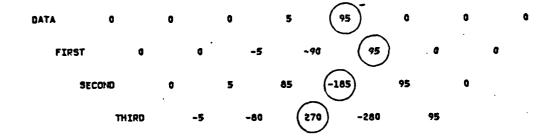
SECOND 0 15 55 -155 65 0

Example 18 - 15:85 Phasing

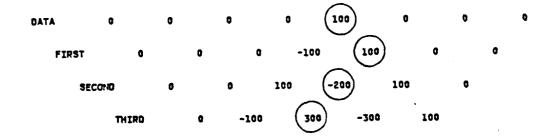
Example 19 - 10:90 Phasing



Example 20 - 5:95 Phasing



Example 21 - 0:100 Phasing



DIANK P. Adl

SECTION 3

GENERIC REQUIREMENTS FOR THE ROFT PROGRAM

3.1 Introduction and Approach

3.1.1 Introduction

The development of space-based infrared surveillance systems and space-based lasers is subordinated primarily to the availability of very large, high precision optics. Current technology and existing facilities cannot produce in a timely fashion high performance mirrors, both in quality and quantity, to respond to the needs of the systems envisioned. The Rapid Optics Fabrication Technology (ROFT) Program will attempt to discover and develop technologies which will significantly decrease the time it takes to make such optics. The goal of the ROFT program is to make possible a significant increase in mirror production rate, from the traditional one square meter per year to about 100 M² per year. Such an increase represents a giant step forward and it will be necessary to exhaust all possible avenues capable of enhancing rapid fabrication procedures of high quality optics.

The technology has been developed to make single mirrors having acceptable weight and appropriate performance characteristics for laser and multi-mission surveillance systems. Programs like HALO and LAMP recently have demonstrated the ability to make mirrors capable of controlling their figure to the required surface accuracy under the disturbances of both orbital and control environments. The design of these mirrors was preoccupied mainly with adequate performance in orbit, but did not address the question of making these high quality optics in large quantities. Significant departures in the design approach and in the fabrication procedures of these mirrors must be incorporated. In attempting to achieve the desired high rate of production, new technology must be concerned with each step of the mirror fabrication process: material production, blank fabrication, mirror generation, grinding, polishing, metrology and assembly. In order to remain completely general in its approach, the ROFT program will also

address unconventional system concepts which could have the potential to circumvent the need for large, high-quality traditional mirrors. Additionally, some effort will be channeled towards the rapid development of optical metering trusses since the fabrication here is also crucial, but not nearly as much as for the mirrors.

3.1.2 Objective and Approach

The overall objective of this CSDL effort is to provide broad requirements and constraints for the mechanical, thermal and optical properties of materials envisioned for the design and fabrication of new optics concepts. Specifications on the structural assemblies insuring proper relative position of various optical elements also need be determined. Due to significant differences in operating modes, the main telescope of the IR-type system calls for different requirements than those associated with the beam expander structure of a space-based laser. It is understood that this study, which is a subset of the ROFT program plan, provides only generic specifications so as not to restrict the freedom of the designer in his attempt to develop a new technology. These broad material and configurational requirements should allow ample latitude in trading-off material properties and structural concepts, and thus enhance the chances for the successful development of a rapid fabrication process while insuring adequate optics performance under the expected orbital and control environments.

In addressing the design of the space mirrors, two distinct applications have been considered: (a) optics appropriate for use as the main optics in an infrared (IR) surveillance system; (b) optics appropriate for use as the primary mirror of a beam expander for a space-based laser system. The incident flux in the aperture plane of the IR system differs greatly from that of a laser. The first case (IR) requires an operating temperature of about 150° K and the flux received from the earth was assumed to be 10 W/M² for visible wavelengths and 5 W/M² for the infrared portion of the spectrum. A laser system, however, operates at a temperature of 200° K to 400° K and an incident flux representative of such systems was assumed to be 40 KW/m² at 2.8 µm wavelength. Absorptance

values might vary from 10% for IR surveillance systems to less than 1% for laser applications. This important difference between these two conditions necessarily lead to two different requirements on the thermal properties of mirror materials.

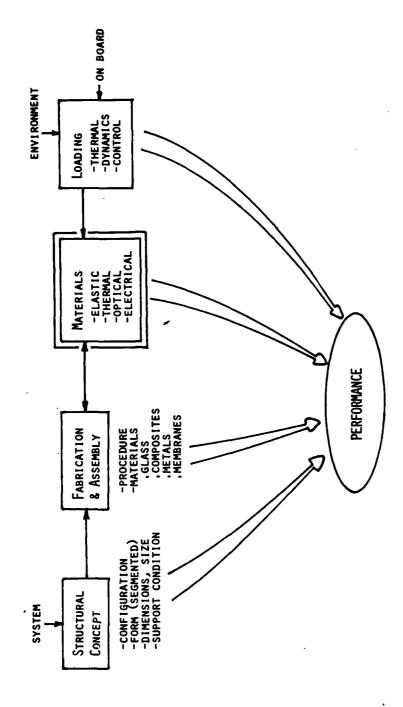
In a similar way the telescope of a surveillance system and the metering structure of a beam expander must perform under very different operating conditions. While the telescope is exposed to relatively small dynamic disturbances (e.g., cryo-cooler wheel imbalance), the beam expander must operate in the presence of large vibrational inputs from laser firing and also point accurately a few seconds after a rapid slew maneuver. Design ratio values for these two structures will reflect this major difference.

The general requirements for mirror materials for both applications are that the mirror surface be of good optical properties. These materials should have a very low coefficient of thermal expansion and a very small variation of this coefficient. They should exhibit a low density combined with a high modulus of elasticity and micro-yield strength. A very important requirement for the ROFT program is that a proposed mirror material must be amenable to rapid fabrication or replication at low cost and remain within reasonable weight constraints. Finally the mirror concepts must be deployable in space and exhibit very little outgassing.

3.2 Materials for Space Optics

3.2.1 Introduction and Approach

The performance of a large high precision space mirror is subordinated to a number of variables that are, in some cases, closely interrelated. Starting with the definition of a structural concept, fabrication and assembly procedures must be devised so as to permit the rapid production of the mirror. In addition the material selected must exhibit optical, elastic and thermal properties that will insure an acceptable performance for the mirror exposed to the rigors of environmental and control disturbances. Figure 3-1 attempts to illustrate more graphically the impact of various parameters on the ultimate mirror performance. While each of



THE PROPERTY OF THE PROPERTY O

Mirror performance is affected by variables in four main categories. Figure 3-1.

the four categories is important and deserves careful attention, the present study deals only with the impact of material properties by examining their contributions to mirror performance.

In order to evaluate mirror structural performance, loadings must be established: guidelines have been assumed for the environments expected for IR surveillance systems and laser applications. Table 3-1 provides key values for operational and soak temperatures, absorbed flux and some measure of dynamic disturbance for each system. Note the major differences between the absorbed flux of IR and laser system (ratio of 40,000) that will be reflected in the respective material constant requirements.

Table 3-1. Assumed operating conditions for IR and laser cases.

DESCRIPTION	IR	LASER
- OPERATING TEMPERATURE T_0	150° к	350° κ
- SOAK TEMPERATURE ΔT_{U}	150° к	50° κ
- ABSORBED FLUX Q	U.01 W/m ²	400 W/m ²
- DYNAMIC FORCE FO	1 N	10 N
- MIRROR RADIUS R	10 m	100 m
- OPERATIONAL WAVELENGTH	2.7-12 μm	0.6-2.7 μm

The optical systems studies typically place an overall surface accuracy requirement on the mirror surface. The total error allowed must be compared to the RSS'ed value of a number of contributors, from fabrication and assembly errors to static and dynamic distortions as well as errors of sensing and control nature. Figure 3-2 presents a list of possible error sources under four groups. The allocation of errors can only be made once a specific configuration is selected and materials are determined, a fabrication and assembly procedure is proposed and the various thermal and dynamic control schemes are decided. Many trade-offs are possible between

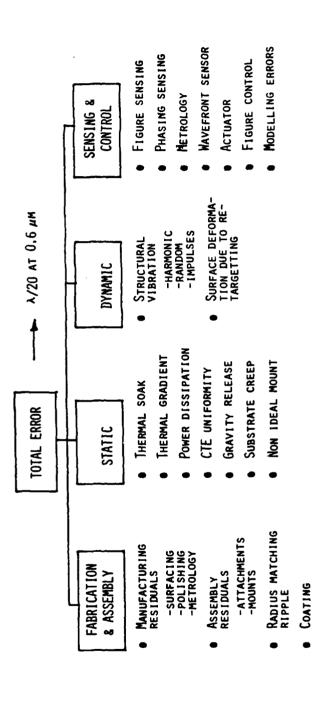


Figure 3-2. Mirror surface error budget--possible contributors.

the various error contributors and must be integrated into the mirror design and fabrication decisions.

The next section examines mirror materials properties and their ability to minimize static, thermal and dynamic load induced deflections.

3.2.2 Equations Relating Mirror Distortions to Disturbances

The performance of a mirror structure, regardless of its structural concept, can be estimated from the equations expressing the distortions as a function of the structural characteristics and the expected loadings. The mirror deformation δ is affected by the three following contributions:

- (1) geometry and boundary conditions of the structure (F_G) ,
- (2) the material mechanical and thermal properties (F_M) , and
- (3) the loading conditions (F_L) in an expression of the form

$$\delta = F_G \cdot F_M \cdot F_L$$

The approach suggested here will attempt to uncover those material properties (entering the equation through F_M) that affect most adversely a mirror exposed to the various loading conditions expected in space applications. It is an easy task to compare the effectiveness of various applicable mirror materials if F_G and F_L are given. But this is not the case in this investigation. While the disturbances or loading conditions (F_L) can be relatively well defined, the factor F_G that involves the structural concept and the support conditions might vary significantly if the mirror concept is to remain general. One should note also that the mirror design concept influences greatly temperature variations of its structural elements and thus indirectly affects the loading. The intent of this discussion is to underline the difficulties involved in attempting to remain very general for mirror concepts and yet produce specific requirements on material properties.

The behavior of a mirror is, for simplicity, associated with the central deflection or sag δ of a thin circular plate with an initial

curvature of radius R. The plate is assumed simply supported along its periphery. (See Figure 3-3) The equations can be expressed either in terms of constant mass per unit area (m) or constant mirror thickness (h). The "constant mass" expression is useful for comparison where the launching cost factor is important. The materials evaluation that follows does not impose the constraints of constant mass. As a result the designer can enjoy greater flexibility in his decisions.

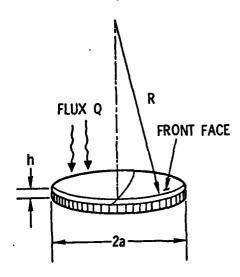


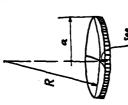
Figure 3-3. Mirror description.

The equations expressing the sag of a mirror due to a uniform pressure (examples are gravity and polishing loads) and the expression of the response of the plate to a harmonic forcing function identify the same material parameter. Figure 3-4 provides the equations and identifies all the material constants.

Figure 3-5 addresses the thermal distortions in a steady-state response while Figure 3-6 identifies those parameters critical to several transient thermal response measures.

A serious problem exists due to laser beam spikes impinging on the mirror surface. The inhomogeneities of the coefficient of thermal expan-

GRAVITY RELEASE, UNIFORM PRESSURE



FOR A GIVEN CONSTANT MASS m. h = m

$$= \frac{3}{4} a^4 \frac{(1 - v^2)\rho^3}{E} \left(\frac{I_S}{I}\right) \frac{q}{m^2}$$

OR FOR A GIVEN THICKNESS h,

MOMENT OF INERTIA OF NON SOLID SECTION OF SAME AREA

GRAVITY ACCELERATION MOMENT OF INERTIA OF SOLID SECTION

MIRROR RADIUS
YOUNG'S MODULUS
POISSON'S RATIO
MIRROR THICKNESS

MASS DENSITY

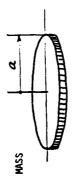
$$\delta = \frac{3}{4} a^4 \frac{q}{h^2} \left(\frac{1}{1} \right) \rho (1 - v^2)$$

DYNAMIC

-FLAT PLATE FUNDAMENTAL FREQUENCY

$$\omega_1 = 1.52 \frac{m}{a^2} \sqrt{\frac{E}{3(1 - v^2)} \left(\frac{1}{1s}\right)}$$

FOR CONSTANT MASS



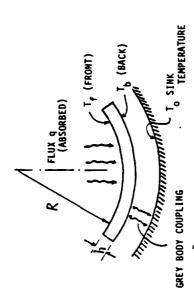
FLAT PLATE, SIMPLY SUPPORTED

-STEADY STATE RESPONSE TO HARMONIC DISTURBANCE $\delta = \frac{F_0}{13.6} \frac{a^2}{m^3} \left[\frac{\rho^3 (1-\sqrt{2})}{E} \right] \frac{i}{E} \qquad \xi = \text{DAMPING RATIO}$

WHERE F * Fosin w_it @ CENTER OF PLATE

Equations relating distortion (sag) to gravity and dynamic loadings. Figure 3-4.

STEADY-STATE THERMAL



ABSOLUTE TEMPERATURE

■ 10 mm | 1

$$T_{f} = q \left[\frac{h}{k} + \frac{1}{401^{3} E} \right] + T_{0}$$

$$T_{b} = q \left[\frac{1}{401^{3} E} \right] + T_{0}$$

K = THERMAL CONDUCTIVITY

σ = STEFAN-BOLTZMAN CONSTANT

E = GREY BODY COUPLING FACTOR = 1.0 FOR BLACK BODY RADIATION

 $\delta = \frac{a^2}{2R} \alpha \left[\frac{h}{2k} + \frac{1}{4 \alpha \Gamma_0^3 F} \right] q$

UNIFORM SIZE ATU

(NOTE: S = O FOR THAT PLATE SINCE R = ∞)

q (6 IS INDEPENDENT OF h)

SOAK (BULK TEMP, CHANGE) & = $\frac{2}{2R}$ \$\alpha\$ \text{AT_U}

LINEAR GRADIENT ∆T_G

å = AVERAGE BETWEEN T1 8 T2

Figure 3-5. Equations relating distortions (sag) to disturbances in thermal steady-state.

- RATE OF CHANGE
$$\frac{dT}{dt} \sim \frac{9}{\text{pch}}$$
 pch = THERMAL CAPACITANCE $\sim \frac{9}{\text{mc}}$ FOR CONSTANT MASS

TIME NEEDED FOR TEMPERATURE TO "REACH" BACK FACE

$$t \approx 0.008 \frac{pch^2}{k}$$
 hg $(T - T_0)$ $\leq 0.08 \frac{cm^2}{pk}$ FOR h = m/p

k pch² t - AVERAGE FOURIER NUMBER FO

CORRESPONDING SAG (ASSUMES LINEAR DISTRIBUTION)

$$\delta \cong -0.16 \text{ a}^2 \frac{\alpha}{K} q$$

• Average rate for SAG
$$\frac{\delta}{t} \approx 2 \frac{a^2}{h^2} \frac{\alpha}{\rho c}$$
9 or $2 \frac{a^2}{m^2} \frac{\rho \alpha}{c}$

Equations relating distortions (sag) to disturbances in a transient thermal state. Figure 3-6.

sion a leads to a similar problem of nearly unpredictable distortions.

Figure 3-7 suggests equations to quantify the severity of the corresponding distortions in terms of material properties.

The contributors to the total mirror sag need to be added in some fashion to be compared to an allowable δ . The following inequality can be proposed as a necessary condition for acceptable mirror performance. Note that the value of the allowable δ is modified so as to reflect the RSS'ing of the individual deformations as well as the relationship between the RMS value of the mirror surface deviations and its central sag δ .

$$\delta_{\text{TOTAL}} = C_{1} \left[\begin{array}{c|c} \rho(1-\nu^{2}) \\ \hline \end{array} \right] + C_{2} \left[\begin{array}{c|c} \alpha \\ \hline \end{array} \right] + C_{3} \left[\begin{array}{c|c} \alpha \end{array} \right]$$

$$\cdot \text{UNIFORM RISE OF T}$$

$$(\text{ONLY IF R} \neq 0)$$

$$+ C_{2}^{*} \left[\begin{array}{c|c} \alpha \\ \hline \end{array} \right] + C_{4} \left[\begin{array}{c|c} \overline{\alpha} \end{array} \right] + C_{5} \left[\begin{array}{c|c} \alpha \\ \hline \end{array} \right] + C_{6} \left[\begin{array}{c|c} \Delta \alpha \end{array} \right] \leq \delta_{\text{ALL}}$$

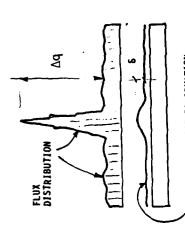
$$\cdot \text{T GRADIENT} \quad \cdot \text{BULK T} \quad \cdot \text{FLUX} \quad \cdot \alpha \text{ INHOMOG.}$$

$$\text{CHANGE} \quad \text{SPIKE}$$

In this equation, individual material constants and combinations of these properties are identified as the critical values in response to various disturbances inputs. While it would be very useful to derive from this inequality the optimum material properties, a "unique" solution is not possible as long as other configurational and control parameters are not defined. These difficulties derive from the insufficient mirror concept description and the following uncertainties:

- (a) Coefficients C_i are a strong function of specific structural configuration
- (b) Figure control effectiveness in reducing each contributor cannot be quantified

■ LASER BEAM SPIKES AND INHOMOGENEITIES



- "UNCONTROLLABLE" GROWTH NORMAL TO SURFACE WILL HAPPEN FROM:
- (1) LOCAL SHARP FLUX CHANGE A9 (BEAM SPIKES) UP TO 10X AVERAGE 9
- (2) CTE INHOMOGENEITY WITH CONSTANT FLUX 9

MIRROR SURFACE DEFORMATION

δ ≥ Δ9 · t · α

3

- Δg = BEAM SPIKE INTENSITY [W/m²]
 - t = LASING DURATION [SEC]

ASSUMPTION: *NO CONDUCTIVITY SIDEWISE

*SEMI-INFINITE SOLID

*NO SHEAR RESTRAINT FROM PLATE

- (2) $\delta = \frac{3}{4} \frac{a^2}{m} \rho(\alpha_2 \alpha_1) \Delta \Gamma_0$
- ΔΤ = UNIFORM TEMPERATURE RISE "BIMETALLIS" BEAM WITH EQUAL THICKNESSES.
- hi * h2 , Ei * E2 , BUT ay # a2

Figure 3-7. Estimates of mirror distortions for beam spikes or CTE inhomogeneities.

- (c) Gravity release term will be impacted by manufacturing and assembly procedures
- (d) The equations used relate to an idealized circular thin mirror face sheet model, simply supported along its periphery.

It is possible to appreciate the major differences between IR and laser systems by comparing the values of the constant $C_{\bf i}$ for both cases. In this comparison the mirror design and materials used are assumed to be the same for both applications. Table 3-2 illustrates the importance of each loading for both IR and laser systems, by comparing the coefficients $C_{\bf i}$.

Existing materials often proposed for space mirror concepts are now examined in terms of their relative properties and figures of merit.

3.2.3 Material Properties and Figures of Merit

The equations presented above furnish the engineer with a useful tool to assess the respective merits of various mirror materials. It is apparent that materials properties such as α , $\Delta\alpha$, k, C, E and ρ determine to a great extent the mirror distortions likely to be encountered in space applications. Tables 3-3 and 3-4 list 34 candidate materials and their relevant properties at both 150° K (IR applications) and 350° K (laser systems). These materials include: (a) metals, (b) composites, and (c) glassy materials. Some of these materials are well known while others are developmental. While in some cases properties were not available and left as such (NA), in others reasonable assumptions could be made. ($\Delta\alpha$ was assumed to be 5% of α , if not known.) Note that the same property value often varies significantly between the two operational temperatures considered.

Table 3-5 is an attempt to place some desirable bounds on the most important material properties and parameters involving several constants. Those are best estimates based on both analytical derivations and engineering experience with space mirror designs and analyses. It is understood that these constraints are not mandatory but can serve as

Table 3-2. Values of coefficients C₁ for IR and laser applications.

LOADING	COEFFICIENT EXPRESSION	MATER I AL PARAMETER	COEFFICIENT C ₁	ENT C ₁ LASER	CLASER CIR
· GRAVITY	$c_1 = \frac{3}{4} \frac{4}{h^2} g$	p(1 - ³)	28.3	28.3	1.0
· FLUX	$c_2 = \frac{a^2}{2}q \left(\frac{h}{2R} + 1 \right)$	티노	9.8 × 10 ⁻⁵	3.92	4 × 10 ⁴
• FLUX	$c_3 = \frac{a^2}{2R} \frac{q}{4\sigma I_0^3 E}$	ä	1,28 × 10 ⁻⁵	4 × 10 ⁻³	3.1 × 10 ²
- SUAK	C4 = 2R aTu	18	1.47 × 10 ⁻¹	4.9 × 10 ⁻³	0.03
• FLUX SPIKES	C ₅ = Aq • t	alg		2 × 10 ⁴	1
٠ ۵۵	C ₆ ≅ ½ ∆T _u • h	ΦΦ	0.75	0.25	0.33
· Δα (SPIKES)	C ₆ = Aq • t	ρc	l	2 × 10 ⁴	1

NOTE: A constant plate thickness h ≈ 0.01 m was used in the equations.

Table 3-3. Materials properties for IR applications (150 $^{\circ}$ K).

	::	į	S)	w	2	alpha	d-alpha	==	'		u	_
Haterial	:: ::	2	(kg/e++3) 18E3	(N/e++2) 10E10		(1/'K) 18E-6	(1/'K) 10E-6	(1/'K) 19E-6	(1/.K)	(X9/R)	(W/a-'K) (J/kg-'K)) (N/a++2) 10E6
	;; ;;	# H H H H H H H H H H H H H H H H H H H				17 15 15 16 17 17 17 18	** ** ** ** ** **	M M M M M M M M	## 10 10 10 10 10 11 11 11	H H H H H H H H H H H H H H H H H H H	14 64 94 94 91 91 91 91	## ## ## ## ## ## ## ##
Alueines	::	52	2.7	7.5	1.33	17.88	12.00	28.88	28.0		648.8	150.0
BeCu	==	150	8.28	12.70	1.21	16.78	1.78	16.79	16.7		428.8	130.1
Deryllius	::	51	1.83	29.38	£. 15	3.78	9.9	8.8	8.		627.8	38.
Copper	==	5	8.98	11.8	1.36	16.50	1.78	16.50	16.5	393.8	386.	≨
lavar	==	2	8.18	15.50	1.29	₹:	1.61		-		48.0	≨
LA-685	==	25	8.13	13.8	1.29	==		= :	=		=	≨
Nol ybdenua	::	<u>15</u>	18.28	31.4	1.32	5.4		5.4	5.4		258.1	200.0
Hickel	::	150	8.9	19.30	6.36	13.30	1.17	13.38	13.3		468.8	55.2
OFHC Copper	::	15	8.98	11.78	.35	17.68	1.19	17.6	17.6		385.	1.1
StSt (418)	==	15	7.9	29.86	1.31	18.28	1.51	18.28	18.2		460:0	241.4
Titanium	==	52	4.5	11.80	. 3	18.8	F. 3	18.80	18.9		548.8	¥
Carbon/Carbon	::	22	2.88	÷	1. 38	÷.5	. E.	-F. St	-4.5		937.8	15.2
Carbon/Graphite	==	12	1.85	=	=		3.8	8 .3	.3		9.8 9	78.6
Graphite/Aluminum	==	25	2.39	16.8	1.25	S. E	:		16.0		62B.B	S
Sraphi te/Epoxy	==	<u>2</u>	1.85	18.38	1. 38	1.17		1.17	=======================================		886.1	71.1
Graphite/Ng14Li	==	5	1.65	32. H		1.34	2.8	=:	19.		818.1	≨
Beryllium oxide	::	2	 	36.58	1.26	5.68	1. 28	5.6	5.6		1045.0	172.8
Boron carbide	::	20	2.50	£8.8	1.28	3.10	8. 16	3.18	3.1		9.88.8	≨
CERVIT	==	2	2.50	18.38	1.28	1.15	=	1.15	1.2		928.8	≨
Diaeond	==	2	3.51	75. E	9.28	. 3	1.15	. 35	=		520.0	400.0
Fused Quartz	==	53	2.28	7.E	1,28	.55	1.13	.53	9.		€	ş
Ge-Cordierite	==	25	2.7	5.52	1.12	-1.17	Ξ.	-1.17	7		358.0	¥
Glassy Carbon	==	15	 2		1.28	2.2	=:	3.8	3.		786.	≨
Graphite (para.)	==	<u>5</u> 2	2.3	24.10	1.28	1.12	=	1.12	-:		794.	≨
Graphite (perp.)	::	2	2.30	9.69	1.28	5.8	8.29	5.8	8		7:1.0	¥
Pyrex-7748	::	12	2.35	8 .9	1.21	3.20	6. 16	3.2	3.2		\$	\$
Pyroceras-9668	::	25	2.50	8.71	1.28	.	1.12	₹.	j.		*	≨
Sic	::	158	3.28	45. E	1.28		÷.		3.3		255.	≨
Si02 (7948)	::	135	2.28	9.9	9 . :	1.17	1.29	1.21	1.2		418.B	≨
Silicon	==	2	2.48	≅	. 18	3. E	.15	3 .	J		78.8	
Slip-Cast Silica	==	<u> </u>	1.9	7.B	1.20	. S.	1.13	1.54	.5		42B. B	\$
ULE Silica (7971)	::	<u>s</u> :	2.2	99.9	6. 17	÷.5	=	-1.26	7.7		428.0	≨
Vycar - 7986	::	15	2.18	6.73	1.20	3	==	.	æ.		≨	≨
lerodur	==	2	2.55	9.83	1.21	1. 15	=	1.15	1.2		921.8	≨

Table 3-4. Materials properties for laser applications (350 $^{\circ}$ K).

Naterial	=======================================	Teap.	Rha (kg/a++3) (18E3	E (N/a+£2) 10£16	2	alpha (1/'K) (0E-6	d-alpha (1/ 'K) 18E-6	a !! (1/'K) 1@E-6	10E-6	(K/n-'K)) (J/kg-'K)	y (N/a++2) 10E6
	==											
Alusinus	==	350	2.70	7.10	9.33	24.98	12.89	23.80	23.88	237.00	966.88	150.00
BeCu	::	328	8.78	12.78	0.21	16.78	9 .8	16.70	16.70	173.68	420.00	100.00
Beryllium	==	35	1.83	28.58	9.85	13.00	9.9	13.00	13.88	290.09	1889.00	38.68
Copper	==	358	8.8	11.88	1.36	16.59	0.83	16.50	16.58	393.88	380.00	¥
Invar	==	350	8. E	14.86	8.29	9 . 6	89.8	1.68	1.68	12.6	515.00	165.88
LA-685	==	358	8.13	13.80	€.29	8 .18	9.8	f. 18	8 s	18.98	582.08	¥
Mol ybdenua	::	358	18.28	31.48	8.32	5.4	8.27	5.48	5.40	134.80	259.99	289.80
Nickel	==	358	8.9	19.30	8.38	13.39	9.67	13, 30	13.38	83.80	469.88	55.28
OFHC Copper	==	358	8.38	11.78	8. 35	17.68	.88	17.68	17.68	398.88	385.88	10.98
StSt (418)	::	350	7.98	29.80	1.31	10.28	1.02	18.28	10.28	25.80	469.88	241.88
Titanium	::	358	4.58	11.80	0.38	18.80	8.38	18.00	18.60	17.89	549.88	¥
Carbon/Carbon	==	320	2.48	5	8.30	-1.54	8.03	¥.5	-0.54	138.86	837.00	15.20
Carbon/Graphite	==	328	1.85	19.38	9.14	6. 38	3.86	6. 30	.38	173.88	833.88	78.88
Graphite/Aluminum	።	356	2.39	16.00	6.25	5.8	5.88	5.58	18.6	125.80	758.88	¥
Graphite/Epoxy	==	358	1.85	10.38	0.30	8.87	8.79	1.87	39.6	1.48	849.86	79.88
Graphite/Mg14Li	==	328	1.65	31.58	9,38	.95	2.88	. 33	24.88	24.86	1838.88	耋
Beryllium oxide	==	359	3.00	36.58	1.26	2.6	6.28	5.68	5.68	218.88	1945.80	172.00
Boron carbide	::	358	2.58	48.89	1.21	3.19	8. 16	3.18	3.18	38.88	960.08	×
CERVIT	::	358	2.50	19.38	8.28	9.15		0.15	9.15	1.58	928.88	*
Diamond	==	356	3.51	95.88	1.21	9 .95	. :	8.95	9.95	900.00	524.88	486.86
Fused Quartz	::	350	2.28	7.00	1.28	6.55	E. 8 3	5.53	4.55	1.38	787.88	æ
Ge-Cordierite	==	356	2.78	5.52	6.62	-6.63	=	-6.63	÷.	2.43	586.88	¥.
Glassy Carbon	==	358	 2.	d. 50	1.20	3.28	2.89	2.18	2.19	13.89	753.88	Æ
Graphite (para.)	==	358	2.38	24.19	1.21	9. 12	6.	1.12	0.12	489.88	794.88	¥
Graphite (perp.)	==	35	2.30	9 . 69	0.20	5.8	0.29	5.8	5.88	3.88	711.88	¥
Pyrex-7748	::	358	2.35	98. 9	1.21	3.28	9.19	3.29	3,28	1.13	1847.88	¥
Pyroceram-9688	::	358	2.50	8.78	1.20	E. 49	1.12	₹.	9.40	1.97	796.88	≨
Sic	==	350	3.28	42.80	1.21	3.60	# ·	3.68	3.68	71.20	761.88	Æ
Si02 (7948)	==	358	2.20	9.9	9. 14	6.56	0.20	.1.56	9.56	1.48	758.88	æ
Silicon	==	356	2.48	14.30	6 . 18	3.86	9. 15	3.58	3.88	118.90	789.88	140.80
Slip-Cast Silica	==	358	9	7.88	9.20	9.54	0.83	9.54	0.54	9.33	921.88	Æ
ULE Silica (7971)	==	32	2.28	9.9	1.17	8.83	8.4	1.13	9.83	1.31	779.88	¥
Vycor-7988	==	358	2.18	6.78	0.28	9 .88		8.8	.	9.92	796.88	×
Zerodur	::	350	2.55	9.83	8.28	6.15	6.61	1.15	8. 15	6.83	821.00	¥

Table 3-5. Desirable elastic and thermal properties for potential mirror materials.

THESE VALUES ARE BEST ESTIMATES BASED ON BOTH ANALYTICAL DERIVATIONS AND ENGINEERING EXPERIENCE WITH MIRRUR DESIGN AND ANALYSES

	ш	a	8	γ	ρ/Ε α/k	a/k	α/ρς
	K/m ²	kg/m ³	K/m ² kg/m ³ 1° k	1° k	kg/N - m m/W	m/W	m ³ /J
I.R	2 10 × 10 10	≤ 2 × 10 ³	≤ 5 × 10 ⁻⁶	$\frac{1}{2} 10 \times 10^{10}$ $\frac{1}{2} 2 \times 10^3$ $\frac{1}{2} 5 \times 10^{-6}$ $\frac{1}{2} 1 \times 10^{-6}$ $\frac{1}{2} 2 \times 10^{-8}$ $\frac{1}{2} 10^{-7}$ $\frac{1}{2} 2 \times 10^{-12}$	≤ 2 × 10 ⁻⁸	<u><</u> 10 ^{−7}	< 2 × 10 ⁻¹²
LASER	2 10 × 10 ¹⁰	< 2 × 10 ³	< 0.1 × 10 ⁻⁶	LASER $\frac{10 \times 10^{10}}{2.0 \times 10^{3}} < 2 \times 10^{3} < 0.1 \times 10^{-6} < 0.02 \times 10^{-6} < 2 \times 10^{-8} < 10^{-8} < 10^{-8} < 0.5 \times 10^{-12}$	\(\lambda \) \q	√ 10 ⁻⁸	< 0.5 × 10 ⁻¹²

0.02 × 10 ⁻¹²	·LA-685 ·Ge-Cord. ·ULE
1.7 × 10 ⁻⁹	•c/6r
0.5 × 10 ⁻⁸	-Gr/MgL1 -BoC
BEST VALUE 48 × 10 ¹⁰ 1.50 × 10 ³ < 0.1 × 10 ⁻⁶ 0.01 × 10 ⁻⁶ 0.5 × 10 ⁻⁸ 1.7 × 10 ⁻⁹ 0.02 × 10 ⁻¹² (350° K)	•CERVIT
< 0.1 × 10 ⁻⁶	•Glassy−C •Gr/Ep*
1.50 × 10 ³	-Glassy-C
48 × 10 ¹⁰	-8oC
BEST VALUE (350° K)	MATERIAL

* α can vary widely with different ply orientatioin. α varies with I, can even be negative.

reasonable guidelines to initiate trade-offs between them. The table also identifies the existing materials that exhibit the best properties in each category.

In order to appreciate where the existing material properties fall with respect to desired values, several plots relating critical parameters have been generated. It is possible to see more directly which materials proposed for mirror applications fall within a region of acceptability. For example, Figure 3-8 identifies the materials on the left of the $\frac{\rho(1-\nu^2)}{E} \cdot \frac{\alpha}{K} = 10^{-15} \text{ line as the most promising for a IR surveillance system. Figures 3-9, 3-10, and 3-11 present similar plots for other important parameters so as to provide a more direct insight into the merits of candidate mirror materials and identify interesting groups.$

3.3. Conclusions and Recommendations

The objective of this study was to provide broad requirements and constraints for the mechanical and thermal properties of materials envisioned for the design and rapid fabrication of large space mirrors. By inspecting the constitutive equations relating mirror deformations to input disturbances, the relative importance of material parameters was identified. It was also recognized that the requirements on mirror material properties can vary widely depending on the space applications. Surveillance systems, operating at cryogenic temperatures impose different demands on materials than do the laser systems for which the operational temperature is expected to vary from 300° K to 400° K. Dynamic environments exhibit significant differences as well, and this difference may impact the choice of other properties on the mirror materials.

It must be emphasized that this study did not presuppose a specific mirror concept with defined structural and configurational characteristics. While this approach was intentional for the findings to remain general, it limits our ability to obtain specific requirements for the contemplated mirror materials. Furthermore the effectiveness of possible controls (whether thermal or mechanical), in terms of relieving demands on material properties can only be evaluated in the context of a defined mir-

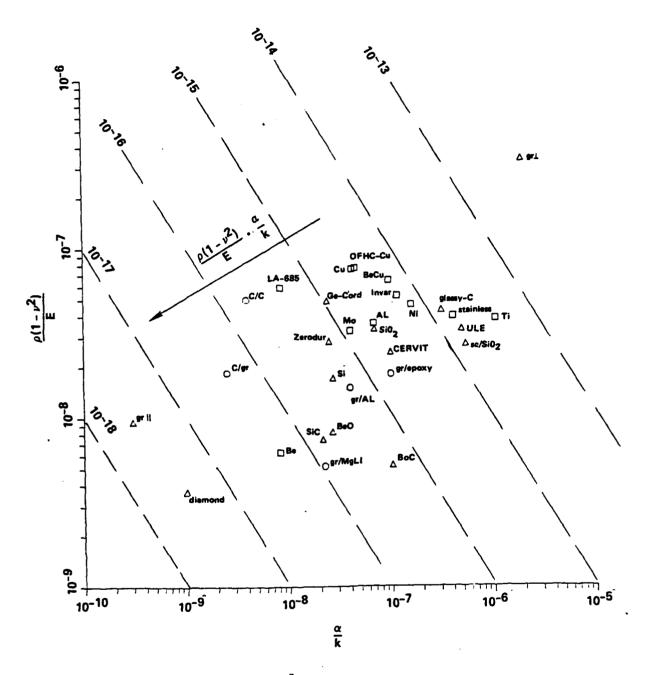


Figure 3-8. Plot of $\frac{\rho(1-v^2)}{E}$ versus $\frac{\alpha}{k}$ for mirror materials. (IR applications at 150° K)

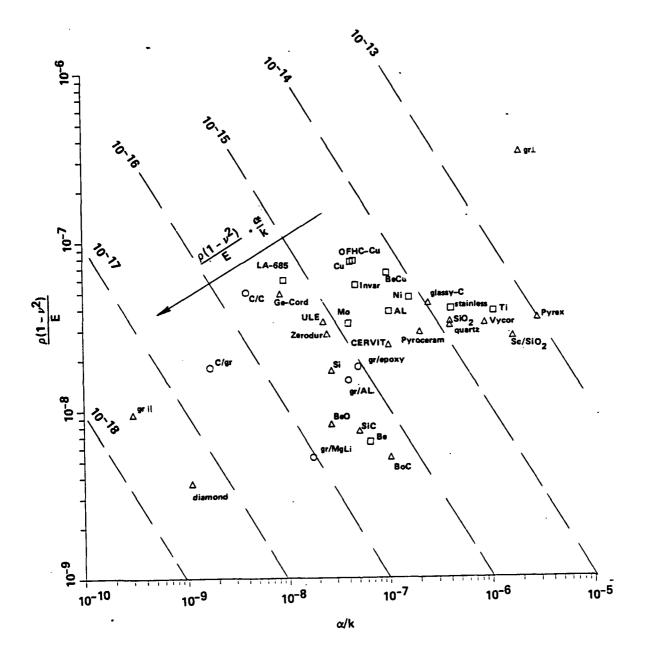
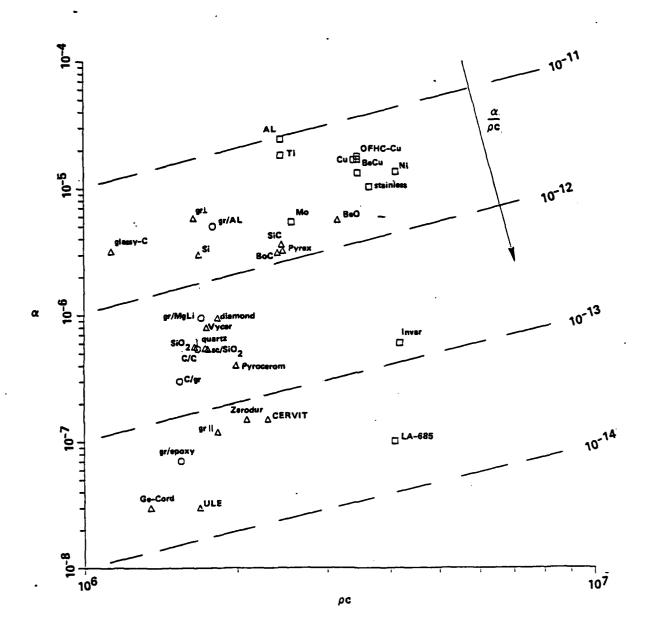


Figure 3-9. Plot of $\frac{\rho(1-\nu^2)}{E}$ versus $\frac{\alpha}{k}$ for mirror materials. (Laser applications at 350° K)



「これないである」
「これできない」
「これできない

Figure 3-10. Plot of α versus ρc for mirror materials. (Laser applications at 350 $^{\circ}$ K)

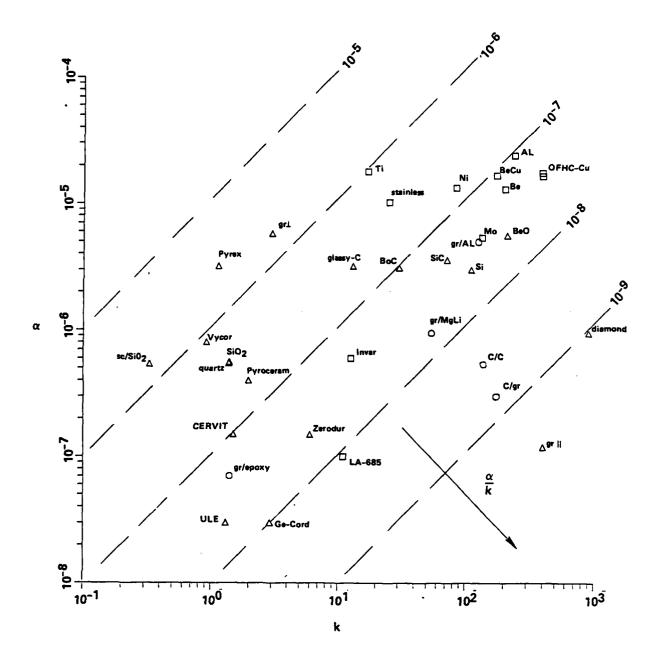


Figure 3-11. Plot of α versus k for mirror materials. (Laser applications at 350 $^{\circ}$ K)

ror concept. As a result only estimates on mirror material requirements could be provided and they have been derived from simplified analytical expressions and engineering experience in the design, modelling and analyses of space mirrors.

For a large number of existing and potential materials, that include metals, composites and ceramics, all relevant properties have been tabulated for two extreme operational temperatures (150° K and 350° K). The plots relating important material parameters can be useful in delineating domains of acceptability for a potential new material. One should emphasize that the proposed material requirements should be viewed as somewhat flexible so as to permit tradeoffs between properties for a particular design concept. Past experience has shown that the most likely candidate for such a mirror will probably be a thin face-sheet on actuators supported by a thermally stable substrate. However, it is hoped that dramatic changes and/or improvements in some thermal properties, especially, might lead to completely novel concepts that ultimately could be produced at the desired rapid rate.

It should be remembered that the objective of the ROFT program is the rapid fabrication of high precision large space optics. The results of this study can only support this attempt by providing guidelines to the designer and fabrication engineer who selects possible materials. The generic specifications on mirror materials, therefore, can be viewed as constraints to the selection of a material amenable to rapid fabrication processes. Many other issues related to optical and perhaps electrical material properties need to be considered. Finally the fabrication process could be adversely affected by some mechanical and thermal properties of a material that is otherwise acceptable in the final product.

SECTION 4

ACTIVE CONTROL OF FLEXIBLE SPACE STRUCTURES--A PERSPECTIVE

4.1 Scope

In the remainder of the present report, several key topics relating to the active control of flexible space structures are treated in depth. The topics discussed fall into two categories: vibration suppression via stable closed-loop control, and identification of parameters characterizing the system dynamics. The process of active control synthesis for attitude regulation of an optical system support structure subject to vibrations induced by wideband disturbances is examined systematically. In addition, the question of closed-loop stability for sampled-data vibration controllers in general that allow noncolocation of actuators and sensors is treated. The problem of identifying the spectral dynamic characteristics of a finite-dimensional structural model with closely-spaced modes based on in-flight observation data is discussed from a signal processing perspective. Finally, the problem of identifying the parameters of an infinite-dimensional structural model employing spline-based finite-dimensional approximations is examined. Applications to ACOSS Model No. 2 (for wideband disturbance accommodation) and to a cantilevered beam with tip mass (for infinitedimensional parameter identification) are given. A brief summary of the results to be reported is given in the remainder of Section 4.

4.2 Vibration Control

The perceived need for active control to suppress structural vibrations in space-based optical support structures arises principally

from the incompatibility between precision pointing requirements and the inherent dynamic characteristics of the structure -- in particular, characteristic structural frequencies low enough to be excited by an attitude controller, and very light damping. The presence of wideband disturbances greatly aggravates the structural control problem. As a consequence, the matters of determining reduced-order dynamic models and of selecting actuators and sensors are elevated to a level of importance comparable to that of developing a feedback structure for the controller. A systematic approach to examining the mutual interactions among these three key elements of the overall control synthesis process was developed for application to the problem of wideband (0-5 Hz) disturbance rejection with ACOSS Model No. 2. Initial results from this study were presented in the preceding reporting period. Observations from further examination of the synthesis process are reported in Section 5. The class of allowable actuators (together with colocated sensors of compatible type) is enlarged to include rotational actuation capability. Using standard linear-quadratic-Gaussian design techniques for establishing controller feedback structure, it is seen that the use of rotational actuators gives comparable closed-loop system performance with substantially fewer actuators than has been obtained using actuators of other types (i.e., translational, axial). The use of translational actuators at the kinematic mounts attaching the optical surfaces to the support structure is also investigated. Although these locations seem attractive a priori, because the variables to be regulated are expressible as linear combinations of kinematic mount displacements, their employment as actuator locations leads to closed-loop system performance that is highly sensitive to reduction in the number of actuators, and compares poorly overall with results obtained using rotational actuators.

会員では、「CECCE TO A CARA CARA TO A CARACTER T

Previous work initiated a study of sampled-data control for flexible structures which employed the natural Eulerian models of the structural dynamics (i.e., second-order difference equations) instead of

first-order state space models. In Section 6, this study is expanded to allow the use of dynamic feedback compensation. The emphasis is upon developing explicit conditions which guarantee asymptotic closed-loop stability. Explicit conditions are not found if the controller requires an estimate of the full state. However, it is shown that quite general control laws can be formulated requiring estimation only of rate (or of displacement) information for which explicit stability conditions are readily obtained. The results are based upon a fundamental stability theorem for second-order recursions. Insight due to the employment of Eulerian models, in preference to state-space models, for the system dynamics facilitates making such connections.

4.3 System Identification

At present, the only feasible engineering tool for developing mathematical models for complex structures is the finite element method. Unfortunately, for flexible structures, this method gives poor accuracy for almost half of the characteristic structural frequencies. Flexible structure controllers must therefore be relatively insensitive (i.e., robust) to (deterministic) uncertainties in the structural model. Robustness needs to be viewed from the perspective of both stability and performance. Although satisfactory stability robustness is likely to emerge from advances in controller synthesis approaches, it is unlikely that satisfactory performance robustness will be possible, when precision performance is required, without incorporating system identification processing as part of the control strategy.

In Section 7, an approach to system identification directly applicable to inflight parameter estimation is discussed in detail. The work builds upon foundational study presented in a previous report. Initial data required for the identification process consists of a discrete-time response history at each sensor, consequent to independent impulsive excitation at the location of each actuator and at the anticipated location of each disturbance. Identification processing

provides spectral information (i.e., characteristic frequencies, damping ratios, and corresponding complex amplitudes) about the system, and is tailored especially for structures with closely-spaced natural frequencies and very low damping. A unique aspect of the approach as formulated previously and which led to the capability for the necessary high resolution was the use of the data-sampling rate as a parameter instead of (as is usually done when high resolution is not essential) as a constant of the problem. The results given in Section 7 describe techniques for adequately dealing with the problem of high resolution identification when the freedom to adjust the sampling rate is not available.

In contrast to the preceding discussion, it is quite feasible to develop continuum structural dynamic models of relatively homogeneous structures. Moreover, techniques for distributed actuation and sensing for such flexible structures are currently the subject of serious experimental investigation in hardware. As a result, the need for control and identification strategies employing continuum models is rapidly being transformed from a theoretical abstraction into a practical reality. In Section 8, a practical approach to distributed-parameter identification is presented. The formulation of the identification problem is based upon an abstract representation of the partial differential equations and boundary conditions which describe the dynamics of the unknown system. Using cubic spline functions, a sequence of finite-dimensional identification problems is generated. Each of these problems is solvable using widely-available and reliable mathematical software. The sequence of solutions is shown to converge to a solution of the original continuum identification problem. The approach is successfully applied to a vibrating cantilever beam having a tip mass, whose structural model is a hybrid system of ordinary and partial differential equations.

4.4 Current Directions

Substantial ongoing work in vibration control, large-angle slew control, and system identification has not been treated in the present

report. A brief sketch of the nature of such work is as follows. Examination of the synthesis process for vibration control under the influence of wideband disturbances is proceeding along several distinct directions. First, the spectral identification process discussed in Section 7 is being employed to generate an iterative refinement of the reduced-order model used for design. Second, the constraint of colocation in active transducer selection is being eliminated. Actuators are selected (as previously) for maximal influence upon optical line of sight error, while sensors are selected for maximal sensitivity to the unknown disturbances. Finally, robustness-enhancing modifications to the linear-quadratic-Gaussian design technique are being incorporated. In regard to large-angle slew control, previously reported results for linear and terminal tracking are being extended so as to incorporate perturbation feedback and deterministic disturbance rejection.

Although the infinite-dimensional identification algorithm described in Section 8 is based upon cubic splines, it actually relies upon quintic splines to represent displacement because of the choice of state variables. At present, a method is being developed that uses a more direct approach than the abstract operator formulation and which really does use cubic splines. Preliminary results indicate that this approach will perform as well as the approach presented in the present report, but with greater computational efficiency.

Blank Pare

SECTION 5

PROGRESS ON SYNTHESIS OF ACTIVE CONTROL FOR WIDEBAND DISTURBANCE ACCOMMODATION WITH ACOSS MODEL NO. 2

5.1 Motivation

The control problem under investigation for optical support structures generically represented by ACOSS Model No. 2 is a severe one. The structural model exhibits characteristic frequencies some of which extend down into the anticipated attitude control band, others of which are very closely spaced, and it also exhibits very light inherent damping. Performance specifications for regulation of the optical line of sight are extremely tight, and they are to be achieved in spite of a wideband disturbance environment. In order to mount an effective attack upon this problem, several key elements of the control synthesis process must be carefully examined -- in particular with respect to their mutual interactions, which are not generally well understood. These elements include: selection of a structural model; selection of reduced-order models for controller design and evaluation; selection of active transducers; and determination of a feedback strategy for the controller. A scientific experiment to examine these interactions was defined in Reference 5-1 and initial results were reported in Reference 5-2.

In the present section, current results from the experiment are described and specific directions of ongoing work are outlined. In order to make the section reasonably self-contained, a concise summary of the experimental approach is given in Section 5.2. Current results are

described in Section 5.3. These pertain principally to the situations in which the class of actuator candidates is: (i) enlarged to include nodal rotation actuators; and (ii) restricted to the degrees of freedom associated with the mirror kinematic mounts. The principal directions of ongoing work are outlined in some detail in Section 5.4.

5.2 The Experimental Approach—A Review

Motion of the controlled structure is governed by the following equations:

$$\dot{\eta} + 2Z\Omega\dot{\eta} + \Omega^2 \eta = (\phi^T B_A) u_A + (\phi^T B_D) u_D$$
 (5-1)

$$y = \left(\Phi^{T} c_{p}^{T}\right)^{T} n + \left(\Phi^{T} c_{v}^{T}\right)^{T} \mathring{n}$$
 (5-2)

$$z = (\phi^T D^T)^T n \qquad (5-3)$$

Here $\eta = (\eta_1, \dots, \eta_n)^T$ is the vector of modal coordinates retained in the reduced-order model; $\Omega = \operatorname{diag}(\omega_1)$: $n \times n$ is the matrix of characteristic structural frequencies; Φ : $v \times n$ is the truncation of the principal-axis matrix of transformation defining the modal coordinates (mode shapes of the reduced-order model), v being the number of physical generalized coordinates; $Z = \operatorname{diag}(\zeta_1, \dots, \zeta_n)$: $n \times n$ is the matrix of assumed modal damping ratios representing inherent structural damping; $u_A = (u_1, \dots, u_m)^T$ is the vector of inputs to the actuators; $u_D = (w_1, \dots, w_q)^T$ is the vector of disturbance inputs; $v = (v_1, \dots, v_q)^T$ is the vector of outputs from the sensors; $v = (v_1, \dots, v_q)^T$ is the vector of optical system line-of-sight (LOS) errors to be regulated; and $v_A = v \times v_A$, $v_A = v \times$

For the current investigation, structural parameters for Revision 1 of ACOSS Model No. 2 have been chosen [Refs. 5-3, 5-4], assuming uniform modal damping of $\zeta_1 = 0.001$. A wideband disturbance having constant-amplitude power spectral density between 0 and 5 Hz is assumed to be applied at node 37 on the upper support truss and node 46 on the equipment section, each in a fixed direction [Ref. 5-5, Sec. 2]. The experimental approach consists of examining the influence, upon the stability and performance of the closed-loop-controlled structure, of a sequence of changes in various aspects of the key elements (cf. Sec. 5.1) of the synthesis process. This approach leads to a family of end-to-end active control syntheses which differ from one another in one or more variables of the synthesis process [Ref. 5-1].

Selection of reduced-order models for design is based upon ranking of the structural modes according to the root-mean-square amplitude of their response to excitation by the disturbances. A model obtained by selecting any consecutive number (e.g., the first r) of the highest-ranked modes is invariably interlaced; i.e., retains modes contiguous in frequency with modes that are deleted by the selection [Ref. 5-2, Sec. 2]. Since the use of interlaced design models has led to several undesirable consequences (cf. Sec. 5.3), only contiguous (i.e., not interlaced) reduced-order models are employed at present for both design and evaluation. In ongoing work, system identification techniques are also being used to generate reduced-order models for design, as indicated in Section 5.4.

Selection of actuators (both by function and location) is based upon the least-squares approximation technique described in Section 2 of Reference 5-2. Briefly, one defines a collection $\mathscr A$ of actuator candidates whose elements are some of the actuator modal influence vectors $\Phi^T b_A^j$: n×l in Eq. (5-1), and a collection $\mathscr B$ of objective vectors whose elements are the modal line-of-sight error vectors $\Phi^L b_A^{\text{LOSX}} \stackrel{\Delta}{=} \Phi^T d_{LOSX}$,

b^{LOSY} $\stackrel{\Delta}{=} \Phi^{T} d_{LOSY}$: n×l in Eq. (5-3). The selection process extracts a subcollection \mathcal{A}' of \mathcal{A} , and generates coefficient vectors x', y' of corresponding dimension, that minimize

$$J_W(x^*; A^*, b^{LOSX}) \stackrel{\Delta}{=} (b^{LOSX} - A^*x^*)^T W(b^{LOSX} - A^*x^*)$$
 and (5-4)

$$J_W(y'; A', b^{LOSY}) \stackrel{\Delta}{=} (b^{LOSY} - A'y')^T W(b^{LOSY} - A'y')$$
 (5-5)

respectively, and such that the subcollection \mathscr{A}' is minimal with respect to acceptable increases in the corresponding minimum values. Columns of the matrix A' are elements of the subcollection \mathscr{A}' in some rearrangement, and W: n×n is a symmetric positive-definite weighting matrix. The results reported to date were generated subject to the assumption of colocated force actuators and rate sensors; i.e., having selected force (or moment) actuators as described in the preceding, a linear (or angular) rate sensor is placed at each selected actuator location. The colocation assumption is being relaxed in ongoing work, as indicated in Section 5.4.

The controller feedback strategy used in obtaining the results reported to date is the disturbance-rejection control; i.e., a linear-quadratic-Gaussian (LOG) design in which the structural model is augmented with first-order dynamic models of each disturbance [Ref. 5-5]. Adjustments in the feedback strategy have been deliberately postponed in order to develop a deeper understanding of the influence of reduced-order model selection and of active transducer selection upon the overall synthesis process. Design iterations are terminated as soon as the performance specifications listed below are achieved across the reduced-order design model:

LOSX
$$\stackrel{\Delta}{=} |(\bar{z}_1(w_1), \bar{z}_1(w_2))| \le 0.05 \, \mu\text{-rad}$$
 (5-6)

LOSY
$$\triangleq |(\bar{z}_2(w_1), \bar{z}_2(w_2))| \leq 0.05 \mu - rad$$
 (5-7)

Here $z_1(w_j)$ denotes the root-mean-square value of the response in the i-th component of the optical system error vector (cf. Eq. (5-3)) to the j-th disturbance input (cf. Eq. (5-1)), and I·I denotes the usual two-dimensional Euclidean norm. By using an expanding family of contiguous reduced-order evaluation models, a maximal family with respect to which a particular controller is stable is identified. Restrictions imposed to date upon the determination of controller feedback strategy are being relaxed in ongoing work, as indicated in Section 5.4.

5.3 Current Results

The results reported in the present section build upon those reported in Reference 5-2. Principally, the consequences of enlarging the collection of actuator candidates to include rotational actuation capability at nodes (of the finite-element model), and of restricting the candidate collection to those actuators corresponding to the degrees of freedom available in the kinematic mounting for the mirrors, are examined. Rate sensors of the corresponding type (i.e., linear or angular) are assumed to be colocated with the various actuators selected. Transducer selections and corresponding controller designs incorporating rotational actuators exhibit comparable performance to previously reported results while requiring substantially fewer actuators. In comparison, the apparent attractiveness of kinematic mount locations for actuator placement is dimmed.

5.3.1 Active Transducer Selection

Previously reported results appear as rows A through D (not including the lower portion of row C) in Table 5-1. Recall that the <u>level of reduction</u> Δ associated with a minimal selection is defined by $\Delta = n - p$ [Ref. 5-2], where n is the number of modes retained in the reduced order model, and p is the number of actuators retained in the minimal selection. <u>Richness</u> refers to the richness of the lattice of alternatives for elimination leading to a minimal selection.

Active transducer selection: design example specifications and results. Table 5-1.

Rank 1-11	Axial only	Sparse	Selection (p)	Reduction (△)
-		Moderate (-)	(axial) 14 (axial)	4
		Moderate (+)	12 (translation)	9
Trans Rest	Transl. 6 Rotation (µ = 485) Axial and Restricted Nodal Translation	Very rich	9 (translation)	6
¥	(μ = 289) Axial and Nodal Rotation (μ = 311)	Very rich	5 (rotation)	13
Tra	Kinematic Mount Translation Dir. (µ = 23)	Sparse	7 (translation)	11

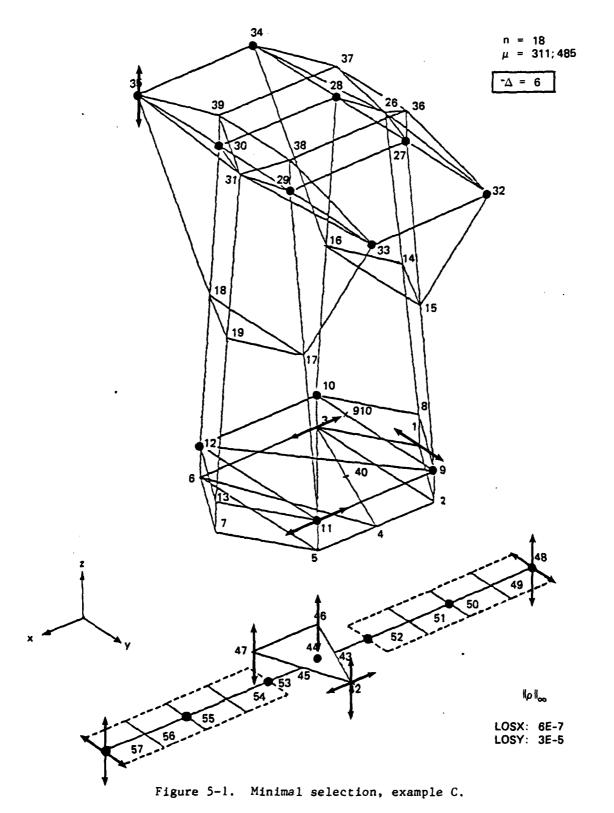
* Mode 19 excluded from simulation

Nodal rotation actuators. In example E, the actuator candidate class of is initially enlarged to include nodal rotation capability, in addition to the nodal translation and axial (i.e. node-connecting) actuators considered with example C. The first observation is the surprising fact that such enlargement of of does not lead to a minimal selection involving nodal rotation actuators. Instead the selections that emerge from the reduction process coincide with those of example C after the second step; in particular, the minimal selection consists only of nodal translation actuators as indicated in Table 5-1 and shown in Fig. 5-1. Evidently, the rearrangement of the elements of of generated by the OR-factorization occurring in the initial step of the reduction process [Ref. 5-2] induces a partial ordering among the elements that may be represented roughly as follows:

$$A = [\mathcal{A}] = [A_{\text{Translation}} : A_{\text{Rotation}} : A_{\text{Axial}}]$$
 (5-8)

where the matrix A displays the elements of \mathcal{A} in blocks according to rank within the partial ordering (the rank being nonincreasing in proceeding from left to right, both between and within adjacent blocks). Equation (5-8) is approximate in the sense that it represents only a predominant pattern, not a precise decomposition; i.e., observation supports the hypothesis that the first block contains predominantly nodal translation actuator influence vectors, although not exclusively so, with corresponding remarks for the other blocks. The relative placement of the second and third blocks in Eq. (5-8) is supported by a comparison of the selections in examples B and C.

Selections of nodal rotation actuators are obtained by removing nodal translation actuators (corresponding to the initial block in Eq. (5-8)) from the candidate class A. The preselection produced by the initial elimination from the reduced candidate class is shown in Fig. 5-2. The presence of one axial actuator in this selection shows that



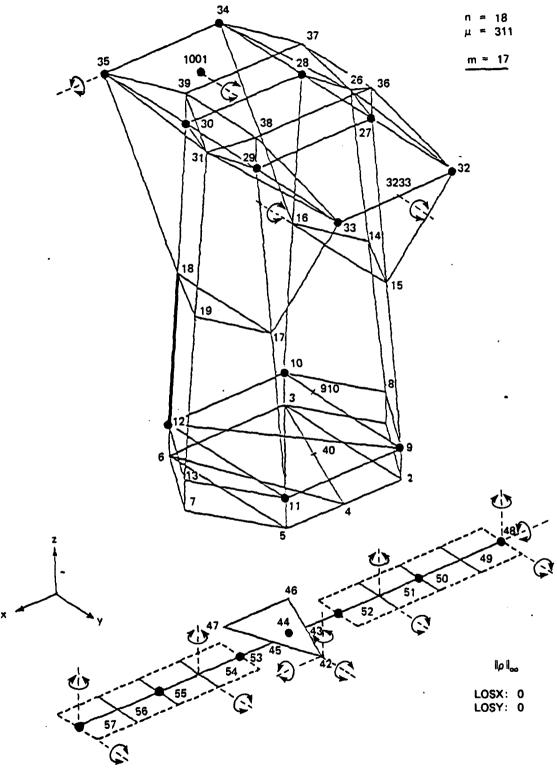


Figure 5-2. Preselection E-17, example E.

Eq. (5-8) is not a precise decomposition; on the other hand, Fig. 5-2 clearly supports the predominant pattern suggested in Eq. (5-8). The (single) minimal selection in example E is shown in Fig. 5-3. Although the associated level of reduction is quite large, this undoubtedly is due in part to the presence of one actuator at node 1001, the center of mass of the primary mirror. It is unlikely that a rotational actuator (e.g., a control moment gyro) could be tolerated at such a location. Setting this fact aside, however, a comparison of Figs. 5-1 and 5-3 suggests that if reducing the number of actuators is of great importance, rotational actuators may be quite attractive for this reason alone (among others). As discussed in Section 5.3.2, both selections lead to comparable closed-loop performance.

Kinematic mount actuators. In the finite element model, each of the four mirrors are represented as being joined to the support structure by mounting attachments at three points (A_1, B_1, C_1) , i = P, S, T, F, at which relative motion is allowed only in specific degrees of freedom as shown in Fig. 5-4. Subscripts refer to the primary (P), secondary (S), tertiary (T), and focal plane (F) mirrors, respectively. Such restraints serve to prevent the transmission of other than rigid-body motion between the mirrors and the support structure [Ref. 5-4]. The kinematic mount locations are of potential interest from the viewpoint of actuator placement since the optical system error vector z in Eq. (5-3) can also be expressed as a linear combination of displacements at the kinematic mount locations [Ref. 5-4]. Using nodal translation actuators in the degrees of freedom shown by Fig. 5-4 as the class ${\mathscr A}$ of actuator candidates for example KM, the initial reduction is shown in Fig. 5-5 and the single minimal selection is shown in Fig. 5-6. Note that no actuators are located on the lower body (equipment section or solar panels) and that the minimal selection contains no y-translation capability.

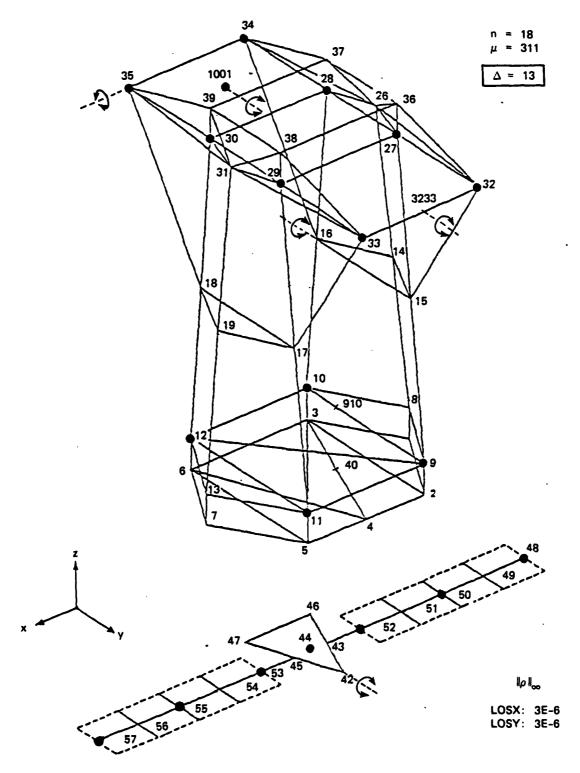


Figure 5-3. Minimal selection, example ${\tt E.}$

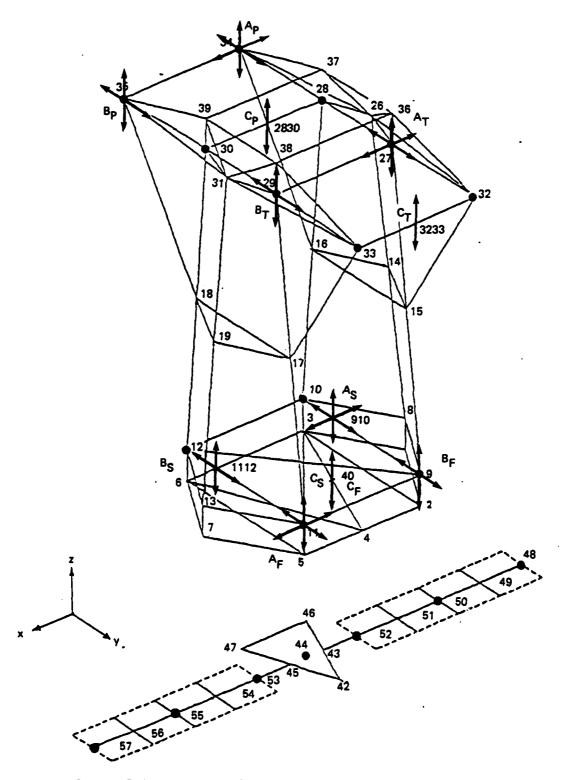


Figure 5-4. Degrees of freedom at mirror kinematic mounts.

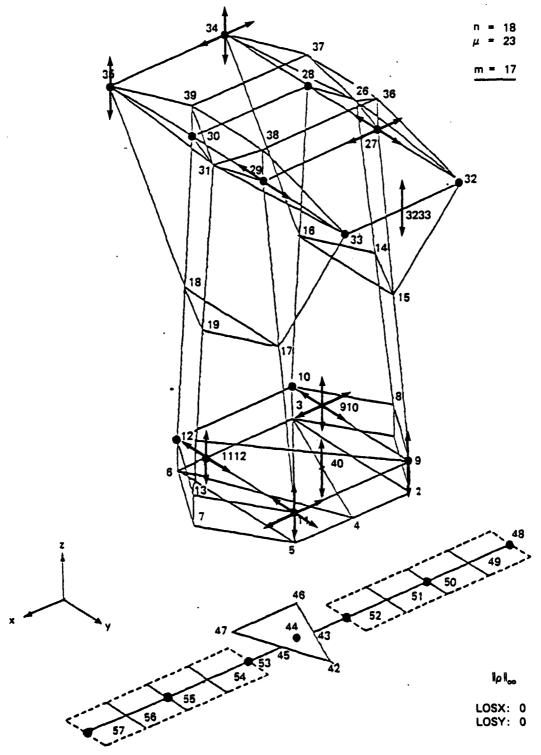


Figure 5-5. Preselection KM-17, example KM.

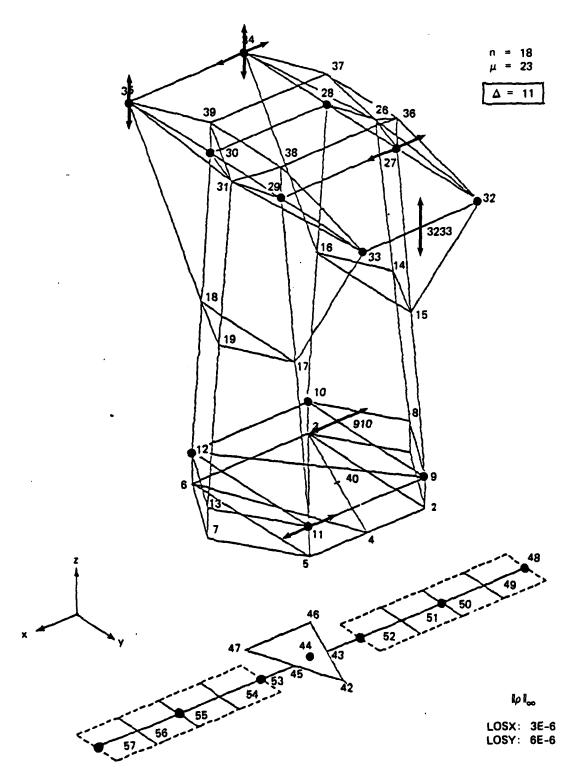


Figure 5-6. Minimal selection, example KM.

5.3.2 Controller Design and Evaluation

The theory underlying the disturbance rejection control design incorporating the LQG approach is well known [Ref. 5-6, Sec. 3.6] and has been discussed previously [Ref. 5-5, Sec. 4] in the context of the present application. In order to associate the design parameters that appear in the discussion to follow, recall that the (steady-state) regulator design is accomplished to minimize

$$J \stackrel{\Delta}{=} \int_{0}^{\infty} (z^{T}Qz + \rho_{R} u_{A}^{T}Ru_{A}) dt$$

where u_A is the input variable to the structure (Eq. (5-1)) and z is the variable to be regulated (here, optical system LOS error (Eq. (5-3))). The matrix $0 \triangleq \operatorname{diag}(q_1)$: 3×3 and the scalar $\rho_R > 0$ are design parameters; the matrix R: $m\times m$ is taken to be the identity matrix. The measurement equation Eq. (5-2), being deterministic, would lead to a singular problem in Kalman filter design if used as it stands. To avoid this complication, the design proceeds upon the assumption that Eq. (5-2) contains additive noise with covariance matrix $\rho_0 I_{\ell}$, where $\rho_0 > 0$ is small and I_{ℓ} is the $\ell \times \ell$ identity matrix.

Previously reported results appear as rows B through D-9A in Table 5-2, and should also have exhibited row A as shown. The latter represents a closed-loop design and evaluation using the interlaced design model and the axial actuators chosen for example A as indicated in Table 5-1. The evaluation demonstrates that a disturbance rejection controller that meets the specifications of Eqs. (5-6), (5-7) when connected across the interlaced design model consisting of the eleven modes 7-10, 12-14, 16, 22-24 is unstable when connected across the contiguous closure (i.e., modes 7-24 inclusive) of the design model. Such unacceptable behavior is one of the reasons for restricting attention to contiguous design models in subsequent synthesis trials.

Table 5-2. Controller design and evaluation.

Modes in Stable Eval- uation			7–156	Un- stable	7-29	7–39	7-36	7-29	7-33	7-61	7-33
-36)	DEFOCUS Stable	(10 ⁻³ m)	0.025			31.44 19.16 0.03848	0.01347				
LQG (modes 7-36)	LOSY		0.05			19.16	6.2				
u)	YSOT	(µr)	0.05			31.44	15.84			_	
(4)	DEFOCUS	(10 ⁻³ m) (µr) (µr)	0.025			0.00136	0.02025 0.03204 0.00188 0.02124 0.06888 0.001883 15.84				
LQG (modes 7-24)	LOSY	(nr)	0.05			0.00532 0.00851 0.00136 0.00644 0.05073 0.00136	88890*0				
a)	YSOT	(µr)	0.05			77900*0	0.02124				•
(4)	DEFOCUS	(10 ⁻³ m)	0.025	0.00180	0.00408	9£100*0	88100*0	0,00345	0.00496	0*00360	0.00378
LQ (modes 7-24)	LOSY	(pr)	\$0*0	0.02093 0.00180	0.01958 0.01146 0.00408	15800*0	0.03204	0.03317 0.00345	0.05587 0.04776 0.00496	0.02868 0.08904 0.00360	0.03469 0.01381 0.00378
	LOSX	(pr)	\$0*0	0.0364	0.01958	0.00532	0.02025	0.0257	0.05587	0.02868	0.03469
	o æ	and P ₀	~	10-17	10-17	10-17	10_11	10-17	10-17	10_12	10-15
Weights		93	1	10_4	10_4	10-5	10_6	9_01	10-5	10-5	10_5
Weig		۹ ₂	ı	101	101	10_1	10_5	10-2	10_1	10_1	100
		41	ı	103	103	100	10_1	10_1	101	1	
Actuator/ Sensor Selection		Design Objective	A (10 axial)	B (14 axial)	C (12 trans1.)	D-14 (14 trans1.) 10 ⁻¹	D-9A (9 transl.) 10 ⁻¹	E (5 rot.)	KM-23 (23 transl.) 10 ⁰	KM-17 (17 trans1.) 10 ⁰	

The LQ-controller designed for Example E employing 5 rotational transducers meets performance specifications when connected across the reduced-order design model using design parameters comparable to those in preceding examples. Moreover, it exhibits stability when connected across a maximal contiguous evaluation model that extends to include mode 33 (9.62 Hz). This is comparable to results from previous designs as indicated in Table 5-2, and in particular improves significantly upon results obtained using several minimal selections (of active transducers) much larger in number (Examples B and D).

Controller design for Example KM first employed the full set of 23 transducers shown in Fig. 5-4. The controller exhibits stability when connected across a maximal contiguous evaluation model that extends to include mode 61 (33.75 Hz). Indeed, in an evaluation model extending to include mode 100 (127.1 Hz), the only unstable mode corresponds to mode 62. This evaluation exhibits a marked improvement over any previous example, but involves the use of considerably more actuators than modes. Unfortunately, the size of the maximal stable evaluation model is sharply reduced when the 17 transducers shown in Fig. 5-5 are employed, as indicated in Table 5-2. In view of the results of Example E, the initial apparent attractiveness of the kinematic mount locations for actuator placement is substantially dimmed.

5.4 Work in Progress

Substantial efforts are underway in a coordinated manner to deepen our understanding regarding each of the key elements of the synthesis process—namely, reduced order modeling, active transducer selection, and controller feedback strategy—and how they interact in the context of wideband disturbance accommodation with ACOSS Model No. 2. The objective is to converge upon a coordinated synthesis process that can routinely generate controllers which exhibit stability when connected across the full structural model, and which display an optimal compromise between the

capacity for disturbance rejection and insensitivity to (deterministic) uncertainties in the structural model. This compromise is expected to provide the basis for an assessment of limits to performance. The specific nature of ongoing work is briefly outlined in the remainder of this section.

Reduced-order modeling. The method of autocorrelation desampling described in Section 7 of the present report is specifically designed for parameter identification of large-order finite-dimensional systems exhibiting closely-spaced characteristic frequencies and low inherent damping (e.g., ACOSS Model No. 2). The identification process requires a database consisting of discrete-time responses at each sensor to impulsive excitation at each actuator and disturbance location, such as could be generated for a vehicle in flight. Products of the identification process include an estimate of system dynamic characteristics, namely the characteristic frequencies and damping ratios. This approach to reduced-order model generation is being incorporated into the active control synthesis process. It is particularly helpful for accurately reflecting in the design model the essential effects of real system attributes -- such as time delays inherent in the operation of actuators, sensors, and discrete-data controllers -- for which explicit modeling can rapidly become cumbersome. Note that the identification process assumes the existence of a prior selection of active transducers, and therefore its employment amounts to an iterative refinement of the synthesis process.

Active transducer selection. In the work reported herein, attention has been focused upon the selection of actuators. All designs have employed colocated actuator-sensor pairs based upon the results of the actuator selection. Although colocation is known to be advantageous for use with analog output feedback controllers [Ref. 5-7] (and actually corresponds to a mild dis-location with sampled-data output feedback

controllers [Ref. 5-8]), there is no reason to impose such an a priori constraint in the context of LOG control strategy. Moreover a closer look at the active transducer selection approach being used suggests good reasons for providing an independent selection of sensors. Recall that actuators are selected by extracting a (minimal) subcollection from a class A of transducer candidates that approximates, in turn, each element from a collection & of objective vectors in a linear least-squares sense. The collection \mathcal{A} consists of column vectors from the $\Phi^{T}B_{A}$ matrix in Eq. (5-1), and the collection \mathcal{B} consists of row vectors from the DΦ matrix in Eq. (5-3). Speaking loosely, one may say that the actuators are selected (by both function and location) so as to be minimal in number and maximal in influence upon the regulation of the LOS error vector (not at all unlike the U.S. Marine Corps looking "for a few good men"). Reexamination of Eqs. (5-1) through (5-3) suggests a promising dual approach to independent sensor selection, i.e., to select sensors (by both function and location) so as to be minimal in number and provide maximal information about the (unknown) disturbs ices. More precisely, the same linear least-squares minimization is carried out, but in this case the candidate collection A consists of column vectors from the Cpt or C_V matrices in Eq. (5-2) representing displacement or rate sensors, and the collection ${\mathcal B}$ consists of column vectors from the disturbance influence matrix \$^TBD in Eq. (5-1). Independent selection of sensors according to this recipe is being incorporated into the synthesis process.

Controller feedback strategy. In order to make a careful assessment of the role played by reduced-order modeling and active transducer selection in the overall synthesis process, controller designs executed in connection with work reported to date have exclusively employed the textbook LQG approach. The results, however, increasingly confirm the initial expectation that a satisfactory design for the type of structure under investigation will be unlikely to evolve without careful attention to robustness-enhancing modification of the LQG feedback

strategy. Clear guidelines for realizing such modifications are given in Reference 5-9, in which well-known frequency-domain synthesis techniques for single-input single-output systems are appropriately generalized for application with multiple-input multiple-output systems. Guidelines for robustness-enhancing modifications are given relative to the behavior of the maximum and minimum singular values of certain system transfer matrices as a function of frequency. This approach to bringing frequency-domain insight to bear upon LOG design (which is developed purely in time-domain terms) is being incorporated into the synthesis process.

References

- 5-1. Hegg, D.R., "A Controlled Experiment for ACOSS Design,"
 ACOSS-Eleven Third Interim Technical Report, Vol. 2, Report
 CSDL-R-1598, Charles Stark Draper Laboratory, Cambridge, MA,
 December 1982; Section 5.
- 5-2. Hegg, D.R. and Kissel, G.J., "Progress on Synthesis of Active Control for Broadband Disturbance Accommodation," ACOSS-Eleven Fourth Interim Technical Report, Vol. 2, Report CSDL-R-1648, Charles Stark Draper Laboratory, Cambridge, MA, August 1983; Sections 2 and 3.
- 5-3. Henderson, T., "Active Control of Space Structures (ACOSS)
 Model 2," Report C-5437, Charles Stark Draper Laboratory,
 Cambridge, MA, September 1981.
- 5-4. Henderson, T., "Modifications to ACOSS Model No. 2 Design;
 Technical Report, Data Base (Final)," Report CSDL-R-1585, Charles
 Stark Draper Laboratory, Cambridge, MA, October 1982.
- 5-5. Fogel, E. et. al., ACOSS-Eleven Second Interim Technical Report, Vol. 2: Active Controller Designs, Report CSDL-R-1583, Charles Stark Draper Laboratory, Cambridge, MA, August 1982.
- 5-6. Kwakernaak, H. and Sivan, R., <u>Linear Optimal Control Systems</u>, Wiley, New York, NY, 1972.

- 5-7. Canavin, J.R., "The Control of Spacecraft Vibrations using Multivariable Output Feedback," AIAA/AAS Astrodynamics Conference, Palo Alto, CA, August 7-9, 1978.
- 5-8. McClamroch, N.H., "Sampled Data Control of Flexible Structures using Non-colocated Velocity Feedback," ACOSS-Eleven Fourth Interim Technical Report, Vol. 2, Report CSDL-R-1648, Charles Stark Draper Laboratory, Cambridge, MA, August 1983; Section 4.
- 5-9. Doyle, J.C. and Stein, G., "Mutlivariable Feedback Design:

 Concepts for a Classical/Modern Synthesis," IEEE Trans. Automatic

 Control, Vol. AG-26, No. 1, Feb. 1981, pp. 4-16.

SECTION 6

STABILIZATION OF FLEXIBLE STRUCTURES USING SAMPLED DATA FEEDBACK

6.1 Overview

There is substantial interest in use of feedback control techniques to achieve active stabilization of flexible structures. Most previous research has focused on use of analog feedback techniques for achieving such stabilization. In this section we examine the possible use of sampled data feedback to achieve stabilization of a flexible structure. One standard controller form consists of a state estimator and estimated state feedback. The estimator gains and control gains can be chosen using standard techniques; however, explicit conditions on the gains for which the closed loop is stable are not available. In this section, the suggested controller form consists of an output estimator and estimated output feedback. Use of an output estimator is required since the desired output feedback cannot generally be physically measured. Two cases where the feedback depends only on velocity measurement data and only on displacement measurement data are considered. In each case explicit conditions on the gains are given for which the closed loop is guaranteed to be stable.

6.2 Recursions for Sampled Data Controlled Flexible Structures

A sampled data controlled flexible structure can be defined as a distributed parameter system, where the input to the structure is the output of an ideal zero order hold and the output from the structure is

sampled. Although distributed parameter models typically involve infinite dimensional variables, our analysis is based on a finite dimensional model, as could be obtained using finite element approximations

$$M\ddot{q} + Kq = Bu \tag{6-1}$$

For simplicity in the subsequent development no structural damping is included. The structural displacement vector $\mathbf{q} = (\mathbf{q}_1, \dots, \mathbf{q}_n)$ and force input vector $\mathbf{u} = (\mathbf{u}_1, \dots, \mathbf{u}_m)$. The mass matrix M and structural stiffness matrix K are assumed symmetric and positive definite. The input influence matrix B is assumed to be dimensionless.

The input u to the structure is defined in terms of the input sequence u_k by the ideal zero order hold relation [Ref. 6-1]

$$u(t) = u_k, kT \le t < kT + T$$
 (6-2)

The fixed value T>0 is the constant sampling time. This open loop sampled data controlled structure can be viewed as a discrete time system with input sequence u_k , where $k=0,1,\cdots$.

Let Φ be a n×n nonsingular modal matrix which simultaneously diagonalizes the matrices M and K [Ref. 6-2] according to

$$\phi^{T}M\phi = I$$
 , $\phi^{T}K\phi = \Omega^{2}$

where I is the n×n identity matrix and $\Omega^2 = \operatorname{diag}(\omega_1^2, \cdots, \omega_n^2)$ is a n×n diagonal matrix of squares of the structural frequencies. Superscript "T" denotes matrix transpose; the two distinct uses of the symbol "T" in the subsequent development should cause no confusion. Introduce the coordinate change

so that Eq. (6-1) can be written as

$$\ddot{\eta} + \Omega^2 \eta = \Phi^{\mathrm{T}} \mathrm{Bu} \tag{6-3}$$

It is easy to solve the vector equation Eq. (6-3), using the constraint specified by Eq. (6-2), to obtain

$$n_{k+1} = (\cos\Omega T) n_k + \Omega^{-1} (\sin\Omega T) n_k + \Omega^{-2} (I - \cos\Omega T) \Phi^T B u_k$$
 (6-4)

$$\dot{\eta}_{k+1} = -\Omega(\sin\Omega T)\eta_k + (\cos\Omega T)\dot{\eta}_k + \Omega^{-1}(\sin\Omega T)\Phi^T Bu_k$$
 (6-5)

where $\eta_k = \eta(kT)$, $\dot{\eta}_k = \dot{\eta}(kT)$, and $\sin\Omega T = diag(\sin(\omega_1 T), \cdots, \sin(\omega_n T))$, $\cos\Omega T = diag(\cos(\omega_1 T), \cdots, \cos(\omega_n T))$.

Although the first order recursive equations Eqs. (6-4), (6-5) could be used in our development, it is convenient to make use of second order recursive equations in $\hat{\eta}_k$ or η_k alone.

Solving for η_k from Eq. (6-5) and substituting into Eq. (6-4), the second order recursion for $\mathring{\eta}_k$ alone is obtained

$$\dot{\eta}_{k+1} - 2(\cos\Omega T)\dot{\eta}_k + \dot{\eta}_{k-1} = \Omega^{-1}(\sin\Omega T)\phi^T B(u_k - u_{k-1})$$
 (6-6)

Solving for η_k from Eq. (6-4) and substituting into Eq. (6-5), the second order recursion for η_k alone is obtained

$$\eta_{k+1} - 2(\cos\Omega T)\eta_k + \eta_{k-1} = \Omega^{-2}(I - \cos\Omega T)\Phi^T B(u_k + u_{k-1})$$
 (6-7)

The velocity recursion Eq. (6-6) forms the basis for our analysis using velocity feedback; the displacement recursion Eq. (6-7) forms the basis for our analysis using displacement feedback. Similarity of these two second order recursions means that parallel developments can be used for the cases of velocity feedback and of displacement feedback. It should be noted that the recursions Eqs. (6-4) through (6-7) involve no numerical approximation; they are valid for any sampling time T > 0.

6.3 Importance of Controller Dynamics

As discussed in References 6-3 and 6-4, use of constant gain output feedback to stabilize a sampled data controlled flexible structure involves a number of subtle issues. In particular, the only available explicit conditions for stability, stated in terms of the gains and the sampling time, require that the input influence matrix and the output influence matrix satisfy a certain consistency condition; in general, satisfaction of this condition is not compatible with possible physical locations of actuators and sensors. Although future progress in this area will, no doubt, be made, the objective of this work is to consider use of dynamic feedback to stabilize a sampled data controlled flexible structure.

One standard dynamic controller form consists of a state estimator and estimated state feedback. The form of such a dynamic controller is presented; but explicit conditions on the gains for which the closed loop is guaranteed to be stable are not easily obtained.

Consequently, in this section we use an output estimator to construct an estimated output feedback from the output measurements actually available. The estimated output expression is chosen so that the consistency condition specified in References 6-3 and 6-4 is satisfied. Consequently, explicit conditions on the gains can be given for which the closed loop is guaranteed to be stable.

The development is first presented for the case of velocity feedback; then a parallel development is given for the case of displacement feedback. The two developments strongly depend on a fundamental stability theorem for second order recursions.

6.4 Stabilization Based on Estimated State Feedback

A standard sampled data controller form consisting of a state estimator and estimated state feedback is now described; in the analog case such a controller has been referred to as modern modal control [Ref. 6-5].

We assume the measured output is given by

$$y_k = C_d^q(kT) + C_v^{\dot{q}}(kT)$$

where $C_{\mathbf{d}}$ and $C_{\mathbf{v}}$ are dimensionless output influence matrices. The control input $\mathbf{u}_{\mathbf{k}}$ is assumed to satisfy

$$u_{k} = -\frac{G_{0}^{c}}{T^{2}} \hat{\Phi n_{k}} - \frac{G_{1}^{c}}{T} \hat{\Phi n_{k}}$$
 (6-8)

where the displacement and velocity estimates $\hat{\eta}_k$ and $\hat{\eta}_k$ are generated via the estimator equations

$$\hat{\eta}_{k+1} = (\cos\Omega T) \hat{\eta}_k + \Omega^{-1} (\sin\Omega T) \hat{\eta}_k + \Omega^{-2} (I - \cos\Omega T) \Phi^T B u_k$$

$$+ G_0^e (y_k - C_d \Phi \hat{\eta}_k - C_v \Phi \hat{\eta}_k)$$

$$\hat{\hat{\eta}}_{k+1} = -\Omega(\sin\Omega T) \hat{\eta}_k + (\cos\Omega T) \hat{\hat{\eta}}_k + \Omega^{-1}(\sin\Omega T) \Phi^T B u_k$$

$$+ G_1^e(y_k - C_d \Phi \hat{\eta}_k - C_v \Phi \hat{\eta}_k)$$

This general form for the controller/estimator is parameterized by the controller gain matrices G_0^c , G_1^c and the estimator gain matrices G_0^e , G_1^e .

As is usual, it is convenient to define the estimator errors

$$\hat{\eta}_k \stackrel{\Delta}{=} \eta_k - \hat{\eta}_k$$

$$\hat{\eta}_{k} \stackrel{\Delta}{=} \hat{\eta}_{k} - \hat{\eta}_{k}$$

so that the closed loop equations can be written as

$$\eta_{k+1} = [\cos\Omega T - \Omega^{-2}(I - \cos\Omega T)\phi^T BG_0^c \phi]\eta_k$$

+
$$[\Omega^{-1}(\sin\Omega T) - \Omega^{-2}(I - \cos\Omega T)\phi^TBG_1^c\phi]\mathring{\eta}_k$$

$$+ \left[\boldsymbol{\Omega}^{-2} (\mathbf{I} - \cos \boldsymbol{\Omega} \mathbf{T}) \boldsymbol{\phi}^{\mathrm{T}} \mathbf{B} \mathbf{G}_{0}^{\mathbf{c}} \boldsymbol{\phi} \right] \tilde{\boldsymbol{\eta}}_{k}^{\mathbf{c}} + \left[\boldsymbol{\Omega}^{-2} (\mathbf{I} - \cos \boldsymbol{\Omega} \mathbf{T}) \boldsymbol{\phi}^{\mathrm{T}} \mathbf{B} \mathbf{G}_{1}^{\mathbf{c}} \boldsymbol{\phi} \right] \tilde{\boldsymbol{\eta}}_{k}^{\mathbf{c}}$$

$$n_{k+1} = [-\Omega(\sin\Omega T) - \Omega^{-1}(\sin\Omega T) \phi^T B G_0^c \phi] n_k$$

+
$$[\cos\Omega T - \Omega^{-1}(\sin\Omega T) \phi^T BG_1^c \phi] \eta_k$$

$$+ \left[\Omega^{-1}(\sin\Omega T)\phi^{T}BG_{0}^{c}\phi\right]\tilde{\eta}_{k} + \left[\Omega^{-1}(\sin\Omega T)\phi^{T}BG_{1}^{c}\phi\right]\tilde{\tilde{\eta}}_{k}$$

$$\tilde{\eta}_{k+1} = [\cos\Omega T - G_0^e C_d \Phi] \tilde{\eta}_k + [\Omega^{-1}(\sin\Omega T) - G_1^e C_v \Phi] \tilde{\eta}_k$$

$$\tilde{\eta}_{k+1} = \left[-\Omega(\sin\Omega T) - G_0^e C_d \Phi\right] \tilde{\eta}_k + \left[\cos\Omega T - G_1^e C_v \Phi\right] \tilde{\eta}_k$$

Thus a separation between the estimator dynamics and the controller dynamics is achieved, so that the estimator gains and the feedback gains can be chosen independently. Usual methods for selection of the gains can be applied: linear-quadratic-Gaussian optimal control theory or pole placement techniques. Under suitable controllability and observability assumptions there is a guarantee that gains do exist for which the closed loop is stable. However, for the general controller form given in Eq. (6-8) there are no known explicit conditions on the gains for which the closed loop is guaranteed to be stable. Such explicit conditions are not required for a single design; however, if additional tuning of the gains is necessary the availability of explicit stabilization conditions is desirable.

In the next two subsections, modifications of the controller defined by Eq. (6-8) are presented; these modifications are such that explicit conditions on the gains for which the closed loop is stable can be obtained.

6.5 Stabilization Based on Estimated Output Velocity Feedback

In this subsection we consider a sampled data controlled structure where the control input \mathbf{u}_k depends only on velocity output measurements given by

$$y_k^V = C_v^{\dagger}(kT)$$

where $C_{\mathbf{v}}$ is a dimensionless output influence matrix. In particular, the control input $\mathbf{u}_{\mathbf{k}}$ is assumed to satisfy the first order recursion

$$u_k - u_{k-1} = -\frac{G_0^c}{T} F \phi \hat{\eta}_k + \frac{G_1^c}{T} F \phi \hat{\eta}_{k-1}$$
 (6-9)

and the velocity estimates $\hat{\eta}_k$ are generated via the estimator equations

$$\hat{\hat{\eta}}_{k+1} - 2(\cos\Omega T) \hat{\hat{\eta}}_{k} + \hat{\hat{\eta}}_{k-1} = \Omega^{-1}(\sin\Omega T) \Phi^{T} B(u_{k} - u_{k-1})
+ \Phi^{T} C_{v}^{T} G_{0}^{e}(y_{k}^{v} - C_{v} \Phi \hat{\hat{\eta}}_{k}) - \Phi^{T} C_{v}^{T} G_{1}^{e}(y_{k-1}^{v} - C_{v} \Phi \hat{\hat{\eta}}_{k-1})$$
(6-10)

This general form for the controller/estimator is parameterized by the controller gain matrices G_0^c , G_1^c , the estimator gain matrices G_0^e , G_1^e , and the feedback matrix F. Use of an estimator is required since, under subsequent conditions imposed on the feedback matrix F, the function $F_q^e(kT)$ cannot generally be directly measured.

We now show that this form for the controller/estimator represents a suitable choice to achieve the desired closed loop objectives. As is usual, it is convenient to define the estimator error

$$\tilde{n}_{k} \stackrel{\Delta}{=} \tilde{n}_{k} - \hat{n}_{k}$$

so that the closed loop equations can be written as

$$\mathring{\eta}_{k+1} - \left[2 \cos \Omega T - \Omega^{-1} (\sin \Omega T) \Phi^{T} B \frac{G_{0}^{c}}{T} F \Phi \right] \mathring{\eta}_{k}$$

$$+ \left[I - \Omega^{-1} (\sin \Omega T) \Phi^{T} B \frac{G_{1}^{c}}{T} F \Phi \right] \mathring{\eta}_{k-1} = (6-11)$$

$$\Omega^{-1} (\sin \Omega T) \Phi^{T} B \left[\frac{G_{0}^{c}}{T} F \Phi \mathring{\eta}_{k}^{c} - \frac{G_{1}^{c}}{T} F \Phi \mathring{\eta}_{k-1}^{c} \right]$$

$$\mathring{\eta}_{k+1} - [2 \cos \Omega T - \phi^T c_v^T G_0^e C_v \phi] \mathring{\eta}_k + [I - \phi^T c_v^T G_1^e C_v \phi] \mathring{\eta}_{k-1} = 0 \quad (6-12)$$

Thus a separation between the estimator dynamics and the controller dynamics is achieved. Moreover, the dynamics of each is characterized by a second order recursion.

The matrix coefficients in Eq. (6-12), by specification, are symmetric if the estimator gain matrices G_0^e , G_1^e are chosen to be symmetric. The matrix coefficients in Eq. (6-11), however, are not necessarily symmetric. In order to obtain this property, we choose the feedback matrix F according to

$$F = B^{T} \Phi(\sin\Omega T) \Omega^{-1} T^{-1} \Phi^{-1}$$
 (6-13)

consequently, the matrix coefficients in Eq. (6-11) are symmetric if the control gain matrices G_0^c , G_1^c are chosen to be symmetric.

Thus, explicit conditions for stability of the closed loop can be stated.

Theorem 6-1. Suppose that the feedback matrix F is given by Eq. (6-13); suppose that the control gain matrices G_0^c , G_1^c are symmetric and satisfy:

- (a) $2[I + \cos\Omega T] \Phi^T F^T [G_1^C + G_0^C] F \Phi$ is positive definite,
- (b) $2[I \cos\Omega T] \Phi^T F^T [G_1^C G_0^C] F \Phi$ is positive definite,
- (c) G_1^c is positive definite, and
- (d) the matrix pair $([I + \cos\Omega T]^{-1}[I \cos\Omega T], \Phi^T F^T)$ is completely controllable;

suppose that the estimator gain matrices G_0^e , G_1^e are symmetric and satisfy:

- (e) $2[I + \cos\Omega T] \phi^T C_v^T [G_1^e + G_0^e] C_v^{\phi}$ is positive definite,
- (f) $2[I \cos\Omega T] \phi^T c_v^T [G_1^e G_0^e] c_v^{\phi}$ is positive definite,
- (g) G_1^e is positive definite, and
- (h) the matrix pair $([I + \cos\Omega T]^{-1}[I \cos\Omega T], C_{v}^{\Phi})$ is completely observable.

Then the closed loop defined by recursion Eqs. (6-6), (6-9), and (6-10) is geometrically stable.

Proof. Using Eq. (6-13), the closed loop characteristic polynomial is

$$\det \left\{z^{2}\mathbf{I} - \left[2\cos\Omega\mathbf{T} - \phi^{T}\mathbf{F}^{T}\mathbf{G}_{0}^{c}\mathbf{F}\phi\right]z + \left[\mathbf{I} - \phi^{T}\mathbf{F}^{T}\mathbf{G}_{1}^{c}\mathbf{F}\phi\right]\right\}$$

$$\times \det \{z^{2}I - [2\cos\Omega T - \phi^{T}C_{v}^{T}G_{0}^{e}C_{v}^{e}\phi]z + [I - \phi^{T}C_{v}^{T}G_{1}^{e}C_{v}^{e}\phi]\}$$

Based on the stability result given in Section 6.8 (Appendix), assumptions (a) through (d) can be shown to guarantee that all zeros of the first factor above lie inside the unit disk. Similarly, assumptions (e) through (h) can be shown to guarantee that all zeros of the second factor above lie inside the unit disk. Thus the closed loop is stable.

The conditions stated in Theorem 6-1 clearly constitute sufficient conditions for stability of the closed loop using sampled data velocity output feedback. The conditions are not generally necessary since we have imposed the requirement that the matrix coefficients which define the characteristic polynomial be symmetric. However, the conditions on the matrix gains can always be satisfied and the conditions are in explicit form; hence the conditions should prove useful as a basis for gain selection.

One special case of the general result is obtained when the a priori requirements that $G_0^c = G_1^c$ and $G_0^e = -G_1^e$ are imposed. We obtain the controller/estimator form

$$u_{k} = -\frac{G^{c}}{T} F \phi \hat{\eta}_{k}$$
 (6-14)

where

$$\hat{\hat{\eta}}_{k+1} - 2(\cos\Omega T) \hat{\hat{\eta}}_{k} + \hat{\hat{\eta}}_{k-1} = \Omega^{-1}(\sin\Omega T) \Phi^{T} B(u_{k} - u_{k-1})$$

$$- \Phi^{T} C_{v}^{T} G^{e} \{ (y_{k}^{v} + y_{k-1}^{v}) - C_{v} \Phi(\hat{\hat{\eta}}_{k} + \hat{\hat{\eta}}_{k-1}^{v}) \} \qquad (6-15)$$

Thus u_k depends explicitly only on the velocity measurement sums $y_k^v + y_{k-1}^v$. Conditions for closed loop stability are given next.

Corollary 6-2. Suppose that the feedback matrix F is given by Eq. (6-13); suppose that the control gain matrix G^{C} is symmetric and satisfies:

- (a) $[I + \cos\Omega T] \phi^T F G^C F \Phi$ is positive definite,
- (b) G^c is positive definite, and
- (c) the matrix pair $([I + \cos\Omega T]^{-1}[I \cos\Omega T], \Phi^T F^T)$ is completely controllable;

suppose that the estimator gain matrix Ge is symmetric and satisfies:

- (d) [I $\cos \Omega T$] $\phi^T c_v^T G^e c_v^T \phi$ is positive definite,
- (e) Ge is positive definite, and
- (f) the matrix pair $([I + \cos\Omega T]^{-1}[I \cos\Omega T], C_{v}^{\phi})$ is completely observable.

Then the closed loop defined by recursion Eqs. (6-6), (6-14), and (6-15) is geometrically stable.

Although the controller/estimator form given by Eqs. (6-9), (6-10) is more general than the form given by Eqs. (6-14), (6-15), it is often the case that the latter form is sufficient to obtain substantial active damping using sampled data velocity feedback. Moreover, it is always possible to choose gain matrices according to the relatively simple conditions specified in Corollary 6-2.

6.6 Stabilization Based on Estimated Output Displacement Feedback

In this subsection we demonstrate that displacement feedback of the form

$$y_k^d = C_d^q(kT)$$

can be used to stabilize a sampled data controlled structure. The development is parallel to that given previously for velocity feedback. Suppose that the control input $\mathbf{u}_{\mathbf{k}}$ satisfies the first order recursion

$$u_k + u_{k-1} = -\frac{G_0^c}{T^2} F \phi \hat{\eta}_k + \frac{G_1^c}{T^2} F \phi \hat{\eta}_{k-1}$$
 (6-16)

and the displacement estimates $\hat{\eta}_k$ are generated via the estimator equations

$$\hat{\eta}_{k+1} - 2(\cos\Omega T)\hat{\eta}_{k} + \hat{\eta}_{k-1} = \Omega^{-2}(I - \cos\Omega T) \phi^{T}B(u_{k} + u_{k-1})$$

$$+ \phi^{T}C_{d}^{T}G_{0}^{e}(y_{k}^{d} - C_{d}\phi\hat{\eta}_{k}) - \phi^{T}C_{d}^{T}G_{1}^{e}(y_{k-1}^{d} - C_{d}\phi\hat{\eta}_{k-1})$$
(6-17)

The controller/estimator is parameterized by the controller gain matrices G_0^c , G_1^c , the estimator gain matrices G_0^e , G_1^e , and the feedback matrix F. Since a subsequent condition is imposed on the matrix F such that Fq(kT) cannot generally be directly measured, our use of an estimator is justified.

If the estimator error is defined as

$$\hat{n}_{k} \stackrel{\Delta}{=} n_{k} - \hat{n}_{k}$$

the closed loop equations can be written as

$$\eta_{k+1} - \left[2 \cos \Omega T - \Omega^{-2} (I - \cos \Omega T) \Phi^{T} B \frac{G_{0}^{c}}{T^{2}} F \Phi \right] \eta_{k} \\
+ \left[I - \Omega^{-2} (I - \cos \Omega T) \Phi^{T} B \frac{G_{1}^{c}}{T^{2}} F \Phi \right] \eta_{k-1} =$$

$$\Omega^{-2} (I - \cos \Omega T) \Phi^{T} B \left[\frac{G_{1}^{c}}{T^{2}} F \Phi \tilde{\eta}_{k} - \frac{G_{1}^{c}}{T^{2}} F \Phi \tilde{\eta}_{k-1} \right]$$
(6-18)

$$\tilde{\eta}_{k+1} - \left[2 \cos \Omega T - \phi^{T} c_{d}^{T} G_{0}^{e} c_{d} \phi \right] \tilde{\eta}_{k}$$

$$+ \left[I - \phi^{T} c_{d}^{T} G_{1}^{e} c_{d} \phi \right] \tilde{\eta}_{k-1} = 0$$
(6-19)

Separation between the estimator dynamics and the control dynamics is achieved, with each being characterized by a second order vector recursion.

The matrix coefficients in Eq. (6-19) are symmetric if the estimator gain matrices G_0^e , G_1^e are chosen to be symmetric. The

matrix coefficients in Eq. (6-18) are not generally symmetric, even if the controller gain matrices G_0^c , G_1^c are symmetric, unless the feedback matrix F is given by

$$\mathbf{F} = \mathbf{B}^{\mathsf{T}} \Phi \left(\mathbf{I} - \cos \Omega \mathbf{T} \right) \Omega^{-2} \mathbf{T}^{-2} \Phi^{-1} \tag{6-20}$$

Explicit conditions for stability of the closed loop are given in the following.

Theorem 6-3. Suppose that the feedback matrix F is given by Eq. (6-20); suppose that the control gain matrices G_0^c , G_1^c are symmetric and satisfy:

- (a) $2[I + \cos\Omega T] \Phi^T F^T [G_1^C + G_0^C] F \Phi$ is positive definite,
- (b) $2[I \cos\Omega T] \Phi^T F^T [G_1^C G_0^C] F \Phi$ is positive definite,
- (c) G_1^c is positive definite, and
- (d) the matrix pair $([I + \cos\Omega T]^{-1}[I \cos\Omega T], \Phi^T F^T)$ is completely controllable;

suppose that the estimator gains G_0^e , G_1^e are symmetric and satisfy:

- (e) $2[I + \cos\Omega T] \phi^T c_d^T [G_1^e + G_0^e] c_d^e$ is positive definite,
- (f) $2[I \cos\Omega T] \phi^T c_d^T [G_1^e G_0^e] c_d^e$ is positive definite,
- (g) G_1^e is positive definite, and
- (h) the matrix pair $([I + \cos\Omega T]^{-1}[I \cos\Omega T], C_d^{\phi})$ is completely observable.

Then the closed loop defined by recursion Eqs. (6-7), (6-16), and (6-17) is geometrically stable.

Proof. The closed loop characteristic polynomial is

$$\det \{\mathbf{z^2}\mathbf{I} - [2\mathbf{cos}\Omega\mathbf{T} - \boldsymbol{\phi^T}\mathbf{F^T}\mathbf{G_0^c}\mathbf{F}\boldsymbol{\phi}]\mathbf{z} + [\mathbf{I} - \boldsymbol{\phi^T}\mathbf{F^T}\mathbf{G_1^c}\mathbf{F}\boldsymbol{\phi}]\}$$

$$\times \det \left\{ \mathbf{z}^{2}\mathbf{I} - \left[2\cos\Omega\mathbf{T} - \phi^{T}\mathbf{c}_{\mathbf{d}}^{T}\mathbf{g}_{0}^{\mathbf{e}}\mathbf{c}_{\mathbf{d}}^{\mathbf{e}}\phi \right]\mathbf{z} + \left[\mathbf{I} - \phi^{T}\mathbf{c}_{\mathbf{d}}^{T}\mathbf{g}_{1}^{\mathbf{e}}\mathbf{c}_{\mathbf{d}}^{\mathbf{e}}\phi \right] \right\}$$

As in the proof of Theorem 6-1, the assumptions can be shown to guarantee that all zeros of the characteristic polynomial lie inside the unit disk. Thus the closed loop is stable. \square

Conditions stated in Theorem 6-3 are sufficient conditions for stability of the closed loop using sampled data displacement output feedback. The conditions are not generally necessary since we have imposed the requirement that the matrix coefficients which define the characteristic polynomial be symmetric. The conditions imposed on selection of the matrix gains in Theorem 6-3 can always be satisfied; hence the conditions should prove useful as a basis for gain selection.

An interesting special case is obtained by imposing the a priori requirements that $G_0^c = -G_1^c$ and $G_0^e = G_1^e$. In this case we obtain the controller/estimator form

$$u_{k} = \frac{G^{c}}{T^{2}} F \Phi \hat{\eta}_{k}$$
 (6-21)

where

$$\hat{\eta}_{k+1} - 2(\cos\Omega T)\hat{\eta}_{k} + \hat{\eta}_{k-1} = \Omega^{-2}(I - \cos\Omega T) \Phi^{T}B(u_{k} + u_{k-1})$$

$$-\Phi^{T}C_{d}^{T}G^{e}[(y_{k}^{d} - y_{k-1}^{d}) - C_{d}\Phi(\hat{\eta}_{k} - \hat{\eta}_{k-1})]$$
(6-22)

Thus u_k depends explicitly only on the displacement measurement difference $y_{k-1}^d - y_{k-2}^d$. Conditions for closed loop stability are given next.

Corollary 6-4. Suppose that the feedback matrix F is given by Eq. (6-20); suppose that the control gain matrix G^{c} is symmetric and satisfies:

- (a) $[I \cos\Omega T] \phi^T F^T G^C F \phi$ is positive definite,
- (b) G^C is postive definite, and
- (c) the matrix pair $([I + \cos\Omega T]^{-1}[I \cos\Omega T], \Phi^T F^T)$ is completely controllable;

suppose that the estimator gain matrix G^{e} is symmetric and satisfies:

- (d) [I + $\cos\Omega T$] $\phi^T C_d^T G^e C_d^e \phi$ is positive definite;
- (e) Ge is positive definite, and
- (f) the matrix pair $([I + \cos\Omega T]^{-1}[I \cos\Omega T], C_d^{\Phi})$ is completely observable.

Then the closed loop defined by recursion Eqs. (6-7), (6-21), and (6-22) is geometrically stable.

Although the controller/estimator form given by Eqs. (6-16), (6-17) is more general than the form given by Eqs. (6-21), (6-22) it is often the case that the latter form is sufficient to obtain substantial active damping using sampled data displacement feedback. Moreover, it is always possible to choose gain matrices according to the relatively simple conditions specified in Corollary 6-4.

6.7 Conclusions

Three different forms for a controller/estimator have been presented. Under appropriate controllability and observability assumptions the existence of gains for which the closed loop is stable is guaranteed in each case. The controller form based on estimated state feedback is most general and is suitable for closed loop design using optimal control or pole placement techniques; however explicit conditions on the gains for which the closed loop is stable are not apparent. The considered cases based on estimated output feedback would seem to be most suitable where it is desired to tune the gains subject to satisfaction of the stability constraint.

We have not examined these stabilization conditions for the gains in detail. These conditions, stated in Theorems 6-1 and 6-3 and Corollaries 6-2 and 6-4, are effectively represented by suitable matrix inequalities. For a fixed flexible structure and a fixed sampling time, nonlinear programming techniques could be employed to characterize the set of all gain parameters which satisfy the stated conditions and, hence, for which the closed loop is guaranteed to be stable.

We have not addressed the issues of control and observation spillover [Ref. 6-5] here, but clearly they are critical in the case where a reduced order model and modal truncation are used. As mentioned in Reference 6-6, the aliasing effects due to samp ing may exacerbate the spillover difficulties.

The theoretical results presented here should prove helpful in establishing a framework for the stabilization of a flexible structure using sampled data feedback. As should be clear, stabilization of a flexible structure, exactly taking into account the sampling effects, is a difficult and nontrivial extension of the results for analog feedback.

6.8 Appendix

The basic stability theorem for second order recursions is stated and proved. The result is expressed in terms of conditions which guarantee that the zeros of a (2n)-th order polynomial lie strictly inside the complex unit disk.

Theorem 6-5. Suppose the real $n \times n$ matrices A_1 and A_2 are symmetric. Then all 2n zeros of the polynomial

$$\det[z^2I + A_1z + A_2]$$

lie strictly inside the complex unit disk if:

- (a) $I A_1 + A_2$ is positive definite,
- (b) $I A_2$ is nonnegative definite,
- (c) $I + A_1 + A_2$ is positive definite, and
- (d) the matrix pair ($[2I A_1]^{-1}[2I + A_1]$, $[I A_2]$) is completely observable.

<u>Proof.</u> From the results in Reference 6-7, the assumptions guarantee that all 2n zeros of the polynomial

$$det[(I - A_1 + A_2)w^2 + 2(I - A_2)w + (I + A_1 + A_2)]$$

have negative real parts. The bilinear transformation

$$z = \frac{1+w}{1-w}$$

maps the zeros of the above polynomial into the 2n zeros of the polynomial

$$det[z^2I + A_1z + A_2]$$

The properties of the bilinear transformation guarantee that all 2n zeros of the latter polynomial lie strictly inside the unit disk. \square

References

- 6-1. Franklin, G. F. and Powell, J. D., <u>Digital Control of Dynamic</u>
 Systems, Addison-Wesley, Reading, MA, 1980.
- 6-2. Bellman, R., Matrix Analysis, McGraw-Hill, New York, NY, 1960.
- 6-3. McClamroch, N. H., "Sampled Data Control of Large Space Structures using Constant Gain Output Feedback: A Negative View,"

 Proceedings of 21st IEEE Conference on Decision and Control,
 Orlando, FL., Dec. 8-10, 1982, pp. 1279-1280.
- 6-4. McClamroch, N. H., "Sampled Data Control of Flexible Structures using Constant Gain Velocity Feedback," J. Guidance, Control and Dynamics (to appear).
- 6-5. Balas, M. J., "Feedback Control of Flexible Systems," <u>IEEE Trans.</u>

 <u>Automatic Control</u>, Vol. AC-23, No. 4, Aug. 1978, pp. 673-679.
- 6-6. Balas, M. J. and Johnson, C. R., "Toward Adaptive Control of Large Structures in Space," <u>Applications of Adaptive Control</u>, Academic Press, 1980, pp. 313-344.
- 6-7. Walker, J. A. and Schmitendorf, W. E., "A Simple Test for Asymptotic Stability in Partially Dissipative Symmetric Systems,"

 J. Applied Mechanics, Vol. 40, No. 4, Dec. 1973, pp. 1120-1121.

SECTION 7

ON THE USE OF AUTOCORRELATION DESAMPLING IN HIGH RESOLUTION SPECTRUM ESTIMATION

7.1 Introduction

7.1.1 Background

Many practical applications exist for power spectrum analysis techniques capable of resolving closely spaced spectral peaks. An example of current relevance is the system identification problem for large flexible space structures, such as that pictured in Figure 7-la [Reference 7-13]. Characteristic of such structures are frequency responses for the structural dynamics which exhibit closely spaced amplitude peaks, as in Figure 7-lb. Because of the nature of these frequency responses, any identification procedure for such structures based on power spectrum analysis must employ a spectrum estimator of high resolution.

Understandably, considerable attention has been given to the development of such techniques in the signal processing literature. Among those most frequently discussed are techniques which require the estimation of the parameters of an assumed model structure for the autocorrelation sequence $\{r(k)\}$, which is defined by

$$r(k) = E[x(j)x(j+k)], -\infty < k < \infty$$

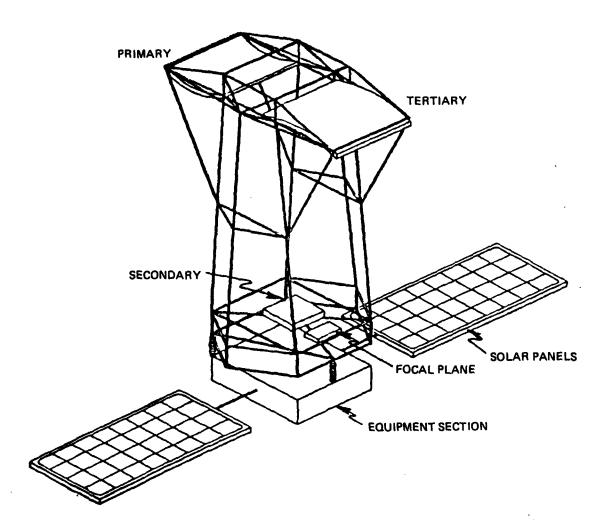
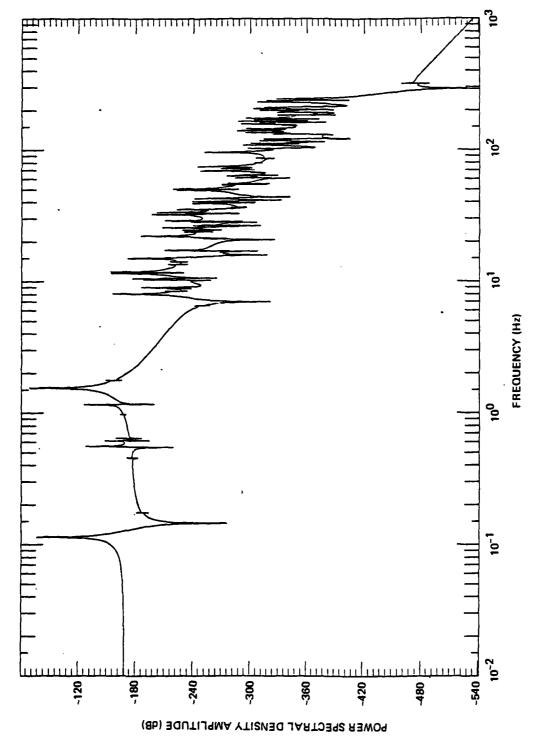


Figure 7-la. Generic space optical system: ACOSS model no. 2.



gure 7-1b. Response of ACOSS model no. 2 to wideband disturbance.

where $\{x(k)\}$ is the wide sense stationary discrete time process of interest. Noting that the power spectral density function $R(e^{j\omega})$ is defined as the Fourier transform of $\{r(k)\}$, i.e.,

$$R(e^{j\omega}) = \sum_{k=-\infty}^{\infty} r(k)e^{-j\omega k}$$

it is clear that the required power spectrum estimate for $\{x(k)\}$ can be derived directly from the model for $\{r(k)\}$ obtained via parameter estimation. No attempt will be made here to rationalize the parametric approach to spectral estimation as excellent discussions are presented elsewhere (see for example References 7-1 and 7-2). What will be discussed are factors which could cause a parametric spectrum estimator to exhibit poor frequency resolution.

Assuming an appropriate model structure is chosen for $\{r(k)\}$, it is clear that the accuracy of the parameter estimates for this model determines the accuracy and therefore the resolution of the resulting spectrum estimate. Clearly, we must identify the mechanisms which could cause parameter estimation inaccuracy in order to further understand the spectral resolution problem.

Since the parameter estimates are usually constructed from a finite number of autocorrelation estimates, errors in the latter estimates are often a major source of errors in the parameter estimates. Therefore, spectral resolution is largely determined by the manner in which autocorrelation estimation errors induce errors in the parameter estimates. Clearly, this error propagation must be limited in order for good spectral resolution to be obtainable.

The purpose of this section is to demonstrate, at least for the parametric spectrum analysis procedure discussed in Section 7.2, that error propagation can be reduced by first obtaining parametric models for certain subsequences of $\{r(k)\}$. That is, consider the M desampled autocorrelation sequences $\{\{r_{M,J}(k)\}: J=0,\cdots,M-1\}$ defined by

$$r_{M,J}(k) = r(M|k|+J), \quad -\infty < k < \infty$$
 (7-1)

It will be shown that if the quantity M is properly chosen, estimation of the parameters of $\{r(k)\}$ via parametric analysis of the M subsequences $\{\{r_{M,J}(k)\}:\ J=0,\cdots,M-1\}$ will yield results considerably less sensitive to errors in the autocorrelation estimates than those obtained by direct parametric analysis of $\{r(k)\}$ as a whole. This result suggests that a proper choice for the quantity M, which will be known as the <u>autocorrelation</u> sequence desampling interval, will result in improved spectral resolution.

Note that the work reported here is a continuation of the research discussed in Reference 7-12, where the spectrum estimation problem for continuous time processes was considered, yielding the result that spectral resolution may be considerably improved by making an appropriate choice for the autocorrelation function sampling period. In this section those situations where the sampling period is fixed or where a purely discrete time process is of interest are considered.

7.1.2 Overview

The results outlined above are obtained via examination of the parametric power spectrum estimation technique discussed in Section 7.2. This technique is based upon an assumed structure for the autocorrelation sequence $\{r(k)\}$ defined by Eq. (7-3). The parameters of this representation that must be estimated in order to obtain a model for $\{r(k)\}$ are the autocorrelation sequence mode weights $\{A_1, \cdots, A_n\}$ and the poles $\{z_1, \cdots, z_n\}$ (n will be assumed known). Parameter estimation is accomplished via techniques presented in the literature, such as the overdetermined Yule-Walker equation approach to pole estimation advocated by Beex and Scharf [Ref. 7-3], Cadzow [Ref. 7-1], and others.

The procedure discussed in Section 7.2 constructs estimates for the parameters $\{A_1, \dots, A_n\}$ and $\{z_1, \dots, z_n\}$ from a finite number of autocorrelation estimates. Errors in the parameter estimates arise from errors in the autocorrelation estimates. In Section 7.3 it will be demonstrated that the sensitivity of the parameter estimates to errors in the autocorrelation estimates is dependent upon the locations of the autocorrelation poles $\{z_1, \dots, z_n\}$ in the complex plane. Assuming

$$z_i \approx e^{j\omega_i}$$
; $i=1,\dots,n$ (7-2)

where $\{\omega_1, \dots, \omega_n\}$ are real, the results of Section 7.3 indicate that the parameter estimates will be extremely sensitive if there exist poles separated by small angles in the complex plane. Thus, in those situations where high spectral resolution is required, parameter estimation will be extremely sensitive to errors in the autocorrelation estimates, making good spectral resolution difficult to achieve.

A possible solution to this problem is to estimate the parameters of the M desampled autocorrelation sequences $\{\{r_{M,J}(k)\}:\ J=0,\cdots,M-1\}$ defined by Eq. (7-1). It can be shown that the poles of these sequences are $\{z_1^M,\cdots,z_n^M\}$. Combining this result with Eq. (7-2) indicates that a judicious choice for the desampling interval M can improve the angular distribution of the autocorrelation sequence poles. Thus with a proper choice for M we might expect the parameter estimates for the desampled autocorrelation sequences to be less sensitive to autocorrelation estimation errors than those for $\{r(k)\}$.

In Section 7.4 a procedure for estimating the parameters of $\{r(k)\}$ by first estimating the parameters of the desampled subsequences is presented. In this procedure, the parameter estimates for $\{r(k)\}$ are obtained directly from those for the subsequences using a technique which does not require M to be bounded by spectral aliasing considerations.

From the above discussion, we might expect the parameter estimates for $\{r(k)\}$ obtained via this procedure to be superior to those obtained by direct application of the procedure described in Section 7.2, thus implying an improvement in spectral resolution. Several numerical examples which demonstrate this to be the case may be found in Reference 7-14.

Finally, the report is concluded in Section 7.5 with a discussion of the obtained results.

7.1.3 Related Literature

The results of this section reveal an important relationship between desampling and spectral resolution. In addition, when these results are applied to the spectrum analysis problem for continuous time processes, it becomes apparent that a proper choice for the data sampling period is of critical importance when good resolution is desired [see Ref. 7-14]. However, the importance of proper choices for autocorrelation desampling intervals and data sampling rates has largely been ignored in the signal processing literature. The author is not aware of any publication which rigorously investigates the relationship between these quantities and spectral resolution, although rules of thumb for selecting desampling intervals and sampling periods, apparently without rigorous justification, have been mentioned in several published works. For example, sampling period selection for nonparametric spectrum analysis is discussed by Bendat and Piersol [Ref. 7-5].

The general problem of sampling period selection has been addressed, however, from the system identification perspective. Extensive treatment of the problem can be found in the econometric literature (see for example Bergstrom [Ref. 7-6]). Economic system identification problems generally possess the additional property that the system models must incorporate a priori restrictions on the model parameters to offset a lack of available data. If identification is to

be carried out via time series techniques, the system model (which is usually a system of differential equations) must be discretized in a manner which allows the incorporation of these a priori restrictions. Because this is often difficult when an exact discrete time model is used, an approximate model is often used which is produced by replacing derivatives in the differential equation model with finite differences. Obviously, the approximate model is an accurate representation of the system only if the sampling period is sufficiently small, the required degree of such smallness having been the subject of a considerable amount of research. However, such approximations are usually not required when performing spectrum estimation. Therefore, this research is of little relevance to the problem of obtaining good spectral resolution.

Astrom [Ref. 7-7] and Payne et al. [Ref. 7-8] also address the sampling period problem from the system identification perspective. Astrom is concerned with the maximum likelihood identification from sampled data of a first order linear time invariant system. He shows that the variance of the estimate for the inverse of the system time constant is minimized when the data sampling period is equal to 0.797 times the system time constant. This result has practical importance, but clearly is not relevant to the spectral resolution problem.

Payne et al. [Ref. 7-8] consider the joint determination of optimal input spectra and sampling periods for linear system identification, the criterion for optimality being the minimization of a function of Fisher's information matrix for the system parameters. They show that when the standard anti-aliasing filter is applied to the system output and the number of data samples is fixed, the optimal sampling period is $(1-\epsilon)$ times the input signal Nyquist period, ϵ being a small value related to the cutoff characteristics of the anti-aliasing filter. This does not agree with the sampling period selection guidelines suggested in Reference 7-14, the reason being that these guidelines are based on controlling error propagation, and are not concerned with the information matrix.

Finally, an important result which is relevant to the issues discussed here was reported by Kay [Ref. 7-9], who considered the problem of obtaining accurate autocorrelation estimates for a Gaussian process from sampled data. Specifically, he considered the effect of the data sampling period on the mean square error of the autocorrelation estimates. He concluded that good estimates are obtained if the data are taken at twice the Nyquist rate, with very little improvement if a higher sampling rate is used. As discussed in Reference 7-14, this result complements very nicely the sampling period selection guidelines suggested therein.

7.2 Parametric Power Spectrum Estimation

The parametric power spectrum estimation procedure to be examined when considering the effect of autocorrelation desampling on spectral resolution is outlined in this subsection. The assumed autocorrelation model upon which this procedure is based is defined, followed by a discussion of techniques used to estimate the parameters of the model.

7.2.1 The Autocorrelation Sequence Model

Assume it is desired to estimate the power spectrum of a real, wide sense stationary, discrete time process $\{x(k)\}$ via parametric analysis of its autocorrelation sequence $\{r(k)\}$ defined by

$$r(k) = E[x(j)x(j+k)], -\infty < k < \infty$$

In all that follows, it will be assumed that $\{r(k)\}$ may be represented as a finite sum of weighted complex exponentials:

$$\mathbf{r}(\mathbf{k}) = \sum_{i=1}^{n} \mathbf{A}_{i} \mathbf{z}_{i} |\mathbf{k}|, \quad -\infty < \mathbf{k} < \infty$$
 (7-3)

Here z_1 ($z_1 \neq z_j$ if $i \neq j$) is the i-th complex autocorrelation sequence pole, and A_i is the corresponding complex mode weight. The quantities $\{z_1^{-1}, \cdots, z_n^{-1}\}$ are also poles of $\{r(k)\}$ (see Eq. (7-4)), but for simplicity, whenever the term "pole" is used it will refer to one of the quantities $\{z_1, \cdots, z_n\}$. Since all terms of $\{r(k)\}$ are real, the poles and mode weights occur in complex conjugate pairs. Also, $|z_1| \leq 1$ for $i=1, \cdots, n$. Note that the power spectral density function $R(e^{jm})$ corresponding to $\{r(k)\}$ is

$$R(e^{j\omega}) = \sum_{i=1}^{n} \frac{A_{i}(1-z_{i}^{2})}{(1-z_{i}e^{-j\omega})(1-z_{i}e^{j\omega})}, \quad -\infty < \omega < \infty \qquad (7-4)$$

The use of the autocorrelation sequence model defined in Eq. (7-3) is suggested by Beex and Scharf in Reference 7-3, where it is demonstrated that Eq. (7-3) may be used to represent a wide variety of possible autocorrelation sequences. In particular, Eq. (7-3) may be used to represent the autocorrelation sequences of processes composed of sinusoids embedded in white noise. Also representable by Eq. (7-3) are the sampled output autocorrelation functions of continuous time systems with rational transfer functions driven by white noise [Ref. 7-4].

For the sake of simplicity, it will hereafter be assumed that the autocorrelation sequence order n is known. Thus the parameters of Eq. (7-4) that must be estimated in order to obtain a power spectrum estimate for $\{x(k)\}$ are the poles $\{z_1, \dots, z_n\}$ and mode weights $\{A_1, \dots, A_n\}$.

7.2.2 Parameter Estimation

Assume the 2n autocorrelation sequence samples $\{r(d), \cdots, r(d+2n-1)\}\ (d \ge 0)$ are known. Then the autocorrelation sequence poles and mode weights may be exactly determined. To see this, consider the z-transform $R^+(z)$ of $\{r(k)u(k)\}$ where $\{u(k)\}$ is the unit step sequence:

$$R^{+}(z) = \sum_{k=-\infty}^{\infty} r(k)u(k)z^{-k}$$

$$= \sum_{k=0}^{\infty} \left(\sum_{i=1}^{n} A_{i}z_{i}^{k} \right) z^{-k} = \sum_{i=1}^{n} A_{i}/(1 - z_{i}z^{-1})$$

so,

$$R^{+}(z) = \frac{\sum_{i=1}^{n} A_{i} \prod_{m=1}^{n} (1 - z_{m}z^{-1})}{\prod_{i=1}^{n} (1 - z_{i}z^{-1})}$$

$$(7-5)$$

The denominator of the above expression may be expanded to obtain

$$\prod_{i=1}^{n} (1 - z_i z^{-1}) = 1 - \sum_{i=1}^{n} a_i z^{-i}$$
(7-6)

where $\{a_1, \dots, a_n\}$ are real since the poles $\{z_1, \dots, z_n\}$ occur in complex conjugate pairs. By expanding the numerator of Eq. (7-5) in a similar manner and substituting the result along with Eq. (7-6) into Eq. (7-5), we obtain

$$R^{+}(z) = \frac{\sum_{i=0}^{n-1} b_{i}z^{-i}}{1 - \sum_{i=1}^{n} a_{i}z^{-i}}$$

Thus,

$$R^{+}(z) - \sum_{i=1}^{n} a_{i}z^{-i}R^{+}(z) = \sum_{i=0}^{n-1} b_{i}z^{-i}$$
 (7-7)

The inverse z-transform of both sides of Eq. (7-7) may be obtained by inspection, yielding

$$r(k)u(k) - \sum_{i=1}^{n} a_{i}r(k-i)u(k-i) = b_{k}$$

where $b_k = 0$ for k < 0 and k > n-1. Therefore,

$$r(k) = \sum_{i=1}^{n} a_i r(k-i), \quad k \ge n$$
 (7-8)

Cadzow [Ref. 7-1] refers to this set of equations as the "extended Yule-Walker equations".

Given the 2n autocorrelation sequence samples $\{r(d), \cdots, r(d+2n-1)\}$, a set of n extended Yule-Walker equations may be written:

$$\begin{bmatrix} r(d+n) \\ r(d+n+1) \\ \vdots \\ r(d+2n-1) \end{bmatrix} = \begin{bmatrix} r(d+n-1) & r(d+n-2) & \cdots & r(d) \\ r(d+n) & r(d+n-1) & \cdots & r(d+1) \\ \vdots & \vdots & \ddots & \vdots \\ r(d+2n-2) & r(d+2n-3) & \cdots & r(d+n-1) \end{bmatrix} \begin{bmatrix} a_1 \\ a_2 \\ \vdots \\ a_n \end{bmatrix}$$
(7-9)

Introducing matrix notation,

$$\underline{r}(d+n,1,n) = \underline{R}(d,1,n,n) \underline{a}(n)$$
 (7-10)

where

$$\underline{\mathbf{r}}(\mathbf{s},\mathbf{t},\mathbf{u}) = \begin{bmatrix} \mathbf{r}(\mathbf{s}) & \mathbf{r}(\mathbf{s}+\mathbf{t}) & \mathbf{r}(\mathbf{s}+2\mathbf{t}) & \cdot & \cdot & \mathbf{r}(\mathbf{s}+(\mathbf{u}-1)\mathbf{t}) \end{bmatrix}^{\mathbf{T}}$$
(7-11)

$$\underline{R(s,t,u,v)} = \begin{bmatrix} r(s+(v-1)t) & r(s+(v-2)t) & \cdots & r(s) \\ r(s+vt) & r(s+(v-1)t) & \cdots & r(s+t) \\ r(s+(v+1)t) & r(s+vt) & \cdots & r(s+2t) \\ \vdots & \vdots & \vdots & \vdots \\ r(s+(u+v-2)t) & r(s+(u+v-3)t) & \cdots & r(s+(u-1)t) \end{bmatrix}$$

and

$$\underline{\underline{\mathbf{a}}}(\mathbf{s}) = [\mathbf{a}_1 \cdot \cdot \cdot \mathbf{a}_{\mathbf{s}}]^{\mathrm{T}}$$

Note that $\underline{r}(s,t,u)$ is a column vector of length u, $\underline{R}(s,t,u,v)$ is a $u \times v$ matrix, and $\underline{a}(s)$ is a column vector of length s. The necessity of this notation will become apparent later.

The autoregressive coefficients $\{a_1, \dots, a_n\}$ can be determined by solving Eq. (7-10):

$$\underline{a}(n) = \underline{R}^{-1}(d,1,n,n) \underline{r}(d+n,1,n)$$
 (7-12)

Given $\{a_1, \dots, a_n\}$, the autocorrelation poles $\{z_1, \dots, z_n\}$ may be determined by obtaining the solutions to

$$z^{n} - \sum_{i=1}^{n} a_{i} z^{n-i} = 0 (7-13)$$

(see Eq. (7-6)).

Finally, the autocorrelation sequence mode weights $\{A_1, \dots, A_n\}$ may be obtained by writing Eq. (7-3) for $k = d, d+1, \dots, d+n-1$:

$$\begin{bmatrix} \mathbf{r}(d) \\ \mathbf{r}(d+1) \\ \vdots \\ \mathbf{r}(d+n-1) \end{bmatrix} = \begin{bmatrix} \mathbf{z}_{1}^{d} & \mathbf{z}_{2}^{d} & \cdots & \mathbf{z}_{n}^{d} \\ \mathbf{z}_{1}^{d+1} & \mathbf{z}_{2}^{d+1} & \cdots & \mathbf{z}_{n}^{d+1} \\ \vdots & \vdots & \ddots & \vdots \\ \mathbf{z}_{1}^{d+n-1} & \mathbf{z}_{2}^{d+n-1} & \cdots & \mathbf{z}_{n}^{d+n-1} \end{bmatrix} \begin{bmatrix} \mathbf{A}_{1} \\ \mathbf{A}_{2} \\ \vdots \\ \mathbf{A}_{n} \end{bmatrix}$$

$$(7-14)$$

In matrix notation,

$$\underline{r}(d,1,n) = \underline{V}(d,n,n) \underline{A}(n)$$

where \underline{r} is as defined in Eq. (7-11),

$$\underline{V}(s,t,u) = \begin{bmatrix}
z_1^s & z_2^s & \cdots & z_u^s \\
z_1^{s+1} & z_2^{s+1} & \cdots & z_u^{s+1} \\
\vdots & \vdots & \ddots & \vdots \\
z_1^{s+t-1} & z_2^{s+t-1} & \cdots & z_u^{s+t-1} \\
z_1^{s+t-1} & z_2^{s+t-1} & \cdots & z_u^{s+t-1}
\end{bmatrix}$$

and

$$\underline{\mathbf{A}}(\mathbf{s}) = [\mathbf{A}_1 \cdot \cdot \cdot \mathbf{A}_{\mathbf{s}}]^{\mathrm{T}}$$

Since the Vandermonde matrix V(d,n,n) is always nonsingular, we have

$$\underline{A}(n) = \underline{v}^{-1}(d,n,n) \underline{r}(d,1,n)$$
 (7-15)

Thus, the power spectrum of $\{x(k)\}$ can be calculated by performing the following steps. First, employ Eq. (7-12) to obtain the autoregressive coefficients $\{a_1, \dots, a_n\}$. Second, solve Eq. (7-13) to obtain the autocorrelation sequence poles $\{z_1, \dots, z_n\}$. Next, employ Eq. (7-15) to determine the autocorrelation mode weights $\{A_1, \dots, A_n\}$. Finally, insert $\{A_1, \dots, A_n\}$ and $\{z_1, \dots, z_n\}$ into Eq. (7-4) to obtain the power spectrum.

This procedure assumes the availability of exact autocorrelation sequence samples which is rarely the case. The more probable situation is that the N autocorrelation estimates $\{\hat{r}(d), \hat{r}(d+1), \cdots, \hat{r}(d+N-1)\}$ are available, where N \geq 2n. (The caret \hat{r} will hereafter be used to indicate an estimated quantity.) In this case, better power spectrum estimates than those obtainable by simply replacing exact with estimated autocorrelations in the procedure described above may be obtained by making the following modifications.

First note that if Eq. (7-9) is solved with "r" replaced by " \hat{r} " to obtain estimates for $\{a_1, \cdots, a_n\}$, the autocorrelation estimates $\{\hat{r}(d+2n), \cdots, \hat{r}(d+N-1)\}$ are ignored (assuming N > 2n). If these unused autocorrelation estimates are of good quality, the information embodied in them concerning $\{r(k)\}$ should be exploited. Thus the procedure for obtaining $\{\hat{a}_1, \cdots, \hat{a}_n\}$ should be modified to use all the available autocorrelation estimates. Such a modification has been suggested by Cadzow [Ref. 7-1], Beex and Scharf [Ref. 7-3], and others. They propose solving the following overdetermined set of extended Yule-Walker equations in the least squares sense to obtain $\{\hat{a}_1, \cdots, \hat{a}_n\}$:

$$\hat{\mathbf{r}}(d+n,1,N-n) = \hat{\mathbf{R}}(d,1,N-n,n) = \hat{\mathbf{a}}(n)$$
(7-16)

where the notation = is used to indicate that Eq. (7-16) possibly defines an inconsistent set of equations. Assuming $\underline{\hat{R}}(d,1,N-n,n)$ is of rank n, we have

$$\frac{\hat{\mathbf{a}}(n)}{\mathbf{n}} = \left[\frac{\hat{\mathbf{R}}^{T}(d,1,N-n,n)}{\hat{\mathbf{R}}(d,1,N-n,n)} \right]^{-1} \frac{\hat{\mathbf{R}}^{T}(d,1,N-n,n)}{\hat{\mathbf{R}}(d,1,N-n,n)} \frac{\hat{\mathbf{r}}(d+n,1,N-n)}{\hat{\mathbf{r}}(d+n,1,N-n)}$$
(7-17)

Note that estimates for $\{a_1, \dots, a_n\}$ obtained in this manner are based on all of the available autocorrelation estimates. Having determined $\{\hat{a}_1, \dots, \hat{a}_n\}$, estimates for the poles $\{z_1, \dots, z_n\}$ may be determined by solving Eq. (7-13) with a_1 replaced by \hat{a}_1 .

A similar modification is required for Eq. (7-14) to ensure that no autocorrelation estimates are "wasted" when calculating $\{\hat{A}_1, \cdots, \hat{A}_n\}$. We might consider solving

$$\hat{\mathbf{r}}(d,1,N) \triangleq \hat{\mathbf{V}}(d,N,n) \hat{\mathbf{A}}(n)$$

in the sense that $l\hat{\mathbf{r}}(d,1,N) - \hat{\underline{V}}(d,N,n)$ $\hat{\underline{A}}(n)$ is minimized (a similar technique is proposed in Reference 7-3). Since in general $\hat{\underline{V}}(d,N,n)$ will contain complex elements, this is equivalent to solving the following set of equations in the standard least squares sense:

$$\begin{bmatrix} \frac{\hat{\mathbf{r}}}{\hat{\mathbf{r}}} \\ \underline{0} \end{bmatrix} \stackrel{\mathbf{\dot{\hat{\mathbf{v}}}}}{=} \begin{bmatrix} \frac{\hat{\mathbf{v}}_{\mathbf{r}}}{\hat{\mathbf{v}}_{\mathbf{r}}} & -\frac{\hat{\mathbf{v}}_{\mathbf{i}}}{\hat{\mathbf{v}}_{\mathbf{r}}} \end{bmatrix} \begin{bmatrix} \hat{\mathbf{A}}_{\mathbf{r}} \\ \hat{\mathbf{A}}_{\mathbf{i}} \end{bmatrix}$$

$$(7-18)$$

where

$$\frac{\hat{\mathbf{r}}}{\hat{\mathbf{r}}} = \frac{\hat{\mathbf{r}}(\mathbf{d}, \mathbf{1}, \mathbf{N})}{\hat{\mathbf{v}}_{\mathbf{r}}} = \operatorname{Im}\left[\hat{\mathbf{v}}(\mathbf{d}, \mathbf{N}, \mathbf{n})\right]$$

$$\hat{\mathbf{A}}_{\mathbf{r}} = \operatorname{Re}\left[\hat{\mathbf{A}}(\mathbf{n})\right], \quad \hat{\mathbf{A}}_{\mathbf{1}} = \operatorname{Im}\left[\hat{\mathbf{A}}(\mathbf{n})\right]$$

We now have a procedure that uses all available autocorrelation estimates to construct estimates for the unknown parameters of $\{r(k)\}$. First, Eq. (7-16) is solved in the least squares sense to obtain $\{\hat{a}_1, \dots, \hat{a}_n\}$. Then Eq. (7-13) is solved with a_1 replaced by \hat{a}_1 to obtain $\{\hat{z}_1, \dots, \hat{z}_n\}$. Finally, Eq. (7-18) is solved in the least squares sense to obtain $\{\hat{A}_1, \dots, \hat{A}_n\}$. In the next subsection this procedure is analyzed to determine when it is sensitive to errors in $\{\hat{r}(d), \dots, \hat{r}(d+N-1)\}$.

7.3 The Sensitivity Issue in Parameter Estimation

In the previous subsection, a parametric spectrum estimation procedure based on techniques discussed frequently in the signal processing literature was presented. This procedure constructs estimates for the parameters $\{z_1, \cdots, z_n\}$ and $\{A_1, \cdots, A_n\}$ from the autocorrelation estimates $\{\hat{r}(d), \cdots, \hat{r}(d+N-1)\}$. If $\{\hat{r}(d), \cdots, \hat{r}(d+N-1)\}$ are replaced by exact autocorrelations, the procedure yields $\hat{z_1} = z_1$ and $\hat{A_1} = A_1$, i=1,...,n. Clearly, autocorrelation estimation errors are the sole source of errors in the parameter estimates. Therefore, the factor which governs the accuracy of $\{\hat{z_1}, \cdots, \hat{z_n}\}$ and $\{\hat{A_1}, \cdots, \hat{A_n}\}$ is the sensitivity of the estimation procedure to errors in $\{\hat{r}(d), \cdots, \hat{r}(d+N-1)\}$.

This subsection addresses the sensitivity issue. Specifically the sensitivity of the autoregressive coefficient estimates $\{\hat{a}_1, \dots, \hat{a}_n\}$ is considered. This is a reasonable approach to evaluating the sensitivity of the entire spectrum estimation procedure, since both $\{\hat{z}_1, \dots, \hat{z}_n\}$ and $\{\hat{A}_1, \dots, \hat{A}_n\}$ are derived from $\{\hat{a}_1, \dots, \hat{a}_n\}$.

The results of this subsection show that the locations of the autocorrelation poles $\{z_1, \dots, z_n\}$ in the complex plane have a significant effect on the sensitivity of $\{\hat{a}_1, \dots, \hat{a}_n\}$ to errors in $\{\hat{r}(d), \dots, \hat{r}(d+N-1)\}$. In the next subsection, resolution enhancing modifications based on these results are incorporated into the spectrum estimation procedure of Section 7.2.

7.3.1 The Measurement of Sensitivity

The estimates for the autoregressive coefficients $\{a_1, \dots, a_n\}$ are obtained via solution of Eq. (7-16) in the least squares sense. Rewriting Eq. (7-16) in terms of exact quantities, we have

$$(\underline{r} + \delta \underline{r}) = (\underline{R} + \delta \underline{R}) (\underline{a} + \delta \underline{a}) \qquad (7-19)$$

where

$$\underline{r} = \underline{r}(d+n,1,N-n) , \quad \delta\underline{r} = \underline{\hat{r}}(d+n,1,N-n) - \underline{r}(d+n,1,N-n)$$

$$\underline{R} = \underline{R}(d,1,N-n,n) , \quad \delta\underline{R} = \underline{\hat{R}}(d,1,N-n,n) - \underline{R}(d,1,N-n,n)$$

$$\underline{a} = \underline{a}(n) , \quad \delta\underline{a} = \underline{\hat{a}}(n) - \underline{a}(n)$$

Referring to Eq. (7-8) we can also write

$$\underline{\mathbf{r}} = \underline{\mathbf{R}} \underline{\mathbf{a}} \tag{7-20}$$

where <u>a</u> is the unique solution to Eq. (7-20). Thus Eq. (7-19) is a perturbed version of Eq. (7-20), with the errors in $\{\hat{\mathbf{r}}(\mathbf{d}), \dots, \hat{\mathbf{r}}(\mathbf{d}+N-1)\}$ causing the perturbations $\delta \mathbf{r}$ and $\delta \mathbf{R}$, which in turn cause the perturbation $\delta \mathbf{a}$ in the least squares solution of Eq. (7-19). Since we are interested in the sensitivity of $\{\hat{\mathbf{a}}_1, \dots, \hat{\mathbf{a}}_n\}$ to errors in $\{\hat{\mathbf{r}}(\mathbf{d}), \dots, \hat{\mathbf{r}}(\mathbf{d}+N-1)\}$, our problem is to determine a bound for the "size" of $\delta \mathbf{a}$ in terms $\delta \mathbf{r}$ and $\delta \mathbf{R}$.

Lawson and Hanson [Ref. 7-10] have calculated such bounds for the perturbed solutions of least squares problems. Their results can easily be applied to our problem, but before doing so some additional notation must be introduced. For a matrix M, let

$$\|\underline{\mathbf{M}}\| \stackrel{\Delta}{=} \max\{\|\underline{\mathbf{M}}_{\underline{\mathbf{X}}}\|: \|\underline{\mathbf{X}}\| = 1\}$$

and

$$\kappa(\underline{M}) \stackrel{\Delta}{=} \underline{\mathbb{I}}\underline{M}\underline{\mathbb{I}} \cdot \underline{\mathbb{I}}\underline{M}^{\dagger}\underline{\mathbb{I}}$$
 (7-21)

where \underline{M}^{\dagger} denotes the pseudoinverse of \underline{M} . Note that the quantity $\kappa(\underline{M})$ defined by Eq. (7-21) is known as the <u>condition number</u> of \underline{M} .

Theorems 9.12 and 9.15 (p. 51) of Lawson and Hanson may now be restated in terms of the problem of determining the sensitivity of $\delta \underline{a}$ to $\delta \underline{r}$ and $\delta \underline{R}$. Assuming $\|\delta \underline{R}\| \cdot \|\underline{R}^{\dagger}\| < 1$, we have

Rank
$$[\hat{R}(d,1,N-n,n)] = n$$
 (7-22)

and

$$\frac{1\delta\underline{a}\,\mathbf{I}}{\underline{\mathbf{I}}\underline{a}\,\mathbf{I}} \leq \frac{\kappa(\underline{R})}{1-\kappa(\underline{R})\cdot\mathbf{I}\,\delta\underline{R}\,\mathbf{I}/\,\mathbf{I}\underline{R}\,\mathbf{I}} \left(\frac{1\delta\underline{R}\,\mathbf{I}}{\underline{\mathbf{I}}\underline{R}\,\mathbf{I}} + \frac{1\delta\underline{r}\,\mathbf{I}}{\underline{\mathbf{I}}\underline{r}\,\mathbf{I}}\right) \tag{7-23}$$

Obviously it is unreasonable to expect $\|\delta R\| \cdot \|R^{\dagger}\| < 1$ always. However, the results obtained by making this assumption seem reasonable, and can be verified with numerical examples [see Ref. 7-14]. The importance of Eq. (7-22) is that it ensures the validity of Eq. (7-17). However, Ineq. (7-23) is the far more significant result. It clearly indicates that the sensitivity of δa to δR and δr is governed by $\kappa[R(d,1,N-n,n)]$. Thus the condition number of R(d,1,N-n,n) will in what follows be used as a measure of the sensitivity of $\{\hat{a}_1,\cdots,\hat{a}_n\}$ to errors in $\{r(d),\cdots,\hat{r}(d+N-1)\}$.

7.3.2 Properties of the Condition Number

It can be easily demonstrated by considering the singular value decomposition of each matrix that

$$\frac{\|\mathbf{R}\|}{\|\mathbf{R}\|} = \sigma_{\text{max}} \tag{7-24}$$

and

$$\|\underline{R}^{\dagger}\| = 1/\sigma_{\min} \tag{7-25}$$

where σ_{max} and σ_{min} denote, respectively, the maximum and minimum singular values of $\underline{R}(d,1,N-n,n)$. Combining Eqs. (7-21), (7-24), and (7-25), we get

$$\kappa(\underline{R}) = \frac{\sigma_{\text{max}}}{\sigma_{\text{min}}}$$
 (7-26)

which indicates

$$1 \leq \kappa(\underline{R})$$

From Eq. (7-23) we see that $\kappa(\underline{R}) = 1$ indicates that $\{\hat{a}_1, \dots, \hat{a}_n\}$ will be relatively insensitive to errors in $\{\hat{r}(d), \dots, \hat{r}(d+N-1)\}$, whereas $\kappa(R) >> 1$ suggests the opposite.

An additional formula for the condition number can be obtained by noting

$$\sigma_{\text{max}} = (\lambda_{\text{max}})^{1/2} \tag{7-27}$$

$$\sigma_{\min} = (\lambda_{\min})^{1/2} \tag{7-28}$$

where $\lambda_{\rm max}$ and $\lambda_{\rm min}$ denote, respectively, the maximum and minimum eigenvalues of R^TR. Combining Eqs. (7-26), (7-27), and (7-28) results in

$$\kappa(R) = \left(\lambda_{\text{max}}/\lambda_{\text{min}}\right)^{1/2} \tag{7-29}$$

7.3.3 The Effect of Pole Location

The remainder of this subsection is devoted to an investigation of the relationship between the locations of the autocorrelation poles $\{z_1, \dots, z_n\}$ and the conditioning of $\underline{R}(d,1,N-n,n)$. For the sake of simplicity, consideration is limited to the case where d=0. This is a reasonable approach, since frequently the available autocorrelation estimates are $\{\hat{r}(0), \dots, \hat{r}(N-1)\}$

Because we are concerned with the problem of obtaining good spectral resolution, it will be assumed in this subsection that $\big\{r(k)\big\}$ is characterized by

$$\mathbf{r}(\mathbf{k}) = \sum_{i=1}^{n/2} \mathbf{B}_{i} \cos \omega_{i} \mathbf{k} \qquad .(7-30)$$

where $0 < \omega_1 < \omega_{1+1} < \pi$, $i=1,\cdots,(n/2)-1$. Note from Eq. (7-3) that the poles of $\{r(k)\}$ are $\{e^{-j\omega_1},\cdots,e^{-j\omega_n/2},e^{-j\omega_1},\cdots,e^{-j\omega_n/2}\}$. That is, the pole configuration is symmetric with respect to the real axis, with the poles lying on the unit circle. The <u>autocorrelation mode frequencies</u> $\{\omega_1,\cdots,\omega_{n/2}\}$ determine the locations of the poles on the unit circle.

The conditioning of $\underline{R}(0,1,N-n,n)$ will be examined when n=2 and n=4, and the results obtained will be extrapolated for n>4. By noting for which frequencies $\{\omega_1,\cdots,\omega_{n/2}\}$ the condition number $\kappa[\underline{R}(0,1,N-n,n)]$ is relatively small, pole locations which facilitate the estimation of $\{a_1,\cdots,a_n\}$ will be made apparent. In Section 7.4, these results are used to obtain modifications which improve the resolution obtainable by the spectrum estimation algorithm of Section 7.2.

7.3.3.1 The Single Sinusoid Case

First to be considered is the case where n = 2. We have

$$r(k) = B \cos \omega k$$

and

$$\underline{R}(0,1,N-2,2) = \begin{bmatrix} r(1) & r(0) \\ r(2) & r(1) \\ \vdots & \vdots \\ r(N-2) & r(N-3) \end{bmatrix}$$

In accordance with the above discussion, we want to determine the effect of ω on $\kappa[R(0,1,N-2,2)]$.

First note that if ω approaches 0 or π , the columns of $\underline{R}(0,1,N-2,2)$ approach linear dependence. We can therefore expect $\kappa[\underline{R}(0,1,N-2,2)] >> 1$ when $\omega \simeq 0$ or $\omega \simeq \pi$. This result has an important interpretation, namely that when the angular separation of the poles $\{e^{j\omega}, e^{-j\omega}\}$ is small, $\underline{R}(0,1,N-2,2)$ will be poorly conditioned. One might then speculate as to whether $\underline{R}(0,1,N-2,2)$ will be well conditioned when the poles achieve their maximum possible angular separation $(\omega = \pi/2)$.

When $\omega = \pi/2$, $\kappa[\underline{R}(0,1,N-2,2)]$ is easily calculated by applying Eq. (7-29). We have

$$\underline{R}^{T}\underline{R} = \begin{bmatrix} r(1) & r(2) & \cdots & r(N-2) \\ r(0) & r(1) & \cdots & r(N-3) \end{bmatrix} \begin{bmatrix} r(1) & r(0) \\ r(2) & r(1) \\ \vdots & \vdots \\ r(N-2) & r(N-3) \end{bmatrix}$$

$$= \begin{bmatrix} N-2 & N-3 & \sum_{k=1}^{N-2} r(k)r(k+1) & \sum_{k=0}^{N-3} r(k)r(k+1) \\ N-3 & \sum_{k=0}^{N-3} r(k)r(k+1) & \sum_{k=0}^{N-3} (r(k)^2) \\ k=0 & k=0 \end{bmatrix}$$

$$= B^{2} \begin{bmatrix} N-2 & N-3 & N-3 \\ \sum & \cos^{2} \frac{\pi}{2} k & \sum & (\cos \frac{\pi}{2} k) [\cos \frac{\pi}{2} (k+1)] \\ k=1 & k=0 \end{bmatrix}$$

$$= B^{2} \begin{bmatrix} N-2 & N-3 & N-3 \\ N-3 & N-3 & N-3 \\ k=0 & k=0 \end{bmatrix}$$

$$= B^{2} \begin{bmatrix} N-2 & \frac{\pi}{2}k & 0 \\ k=1 & \frac{N-3}{2}\cos^{2}\frac{\pi}{2}k \\ 0 & \frac{N-3}{k=0}\cos^{2}\frac{\pi}{2}k \end{bmatrix}$$

Since

$$\lambda_{\max} = B^2 \sum_{k=0}^{N-3} \cos^2 \frac{\pi}{2} k$$

$$\lambda_{\min} = B^2 \sum_{k=1}^{N-2} \cos^2 \frac{\pi}{2^k}$$

we get

$$\kappa[\underline{R}(0,1,N-2,2)] = \begin{cases} 1 & \text{, if N even} \\ [(N-1)/(N-3)]^{1/2} & \text{, if N odd} \end{cases}$$

when $\omega = \pi/2$.

Clearly, when N is even, $\kappa[\underline{R}(0,1,N-2,2)]$ exhibits its minimum possible value when $\omega = \pi/2$. Figures 7-2a through 7-2e demonstrate the behavior of $\kappa[\underline{R}(0,1,N-2,2)]$ as a function of ω when N is even. In the figures, $1/\kappa[\underline{R}(0,1,N-2,2)]$ is plotted to facilitate the handling of those situations where $\kappa[R(0,1,N-2,2)]$ becomes unbounded.

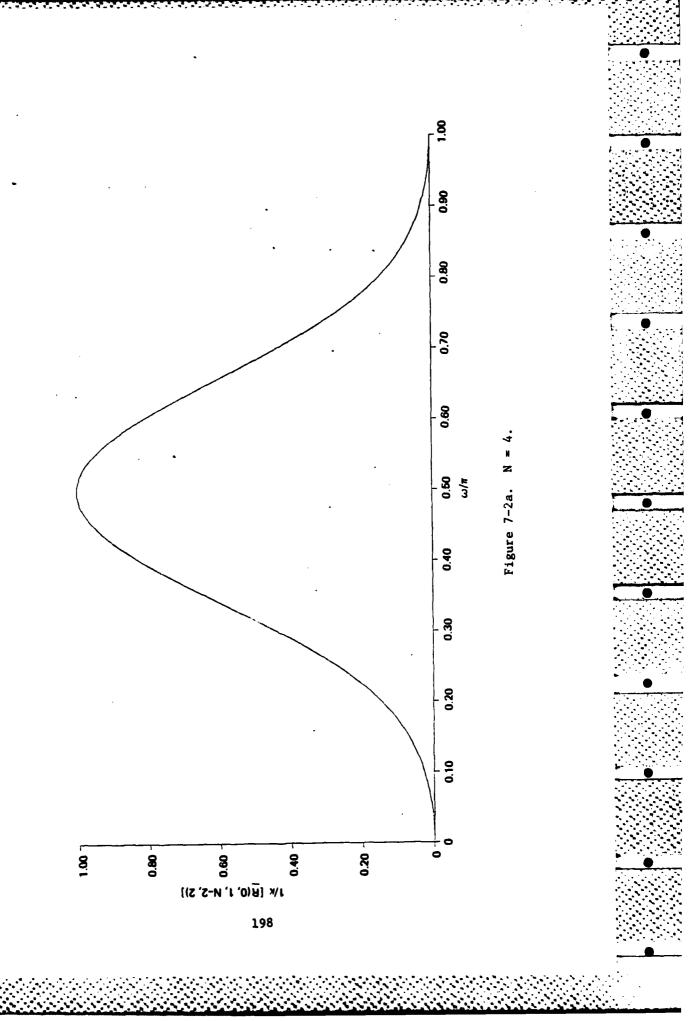
When $\omega = \pi/2$ and N is odd, $\kappa[\underline{R}(0,1,N-2,2)]$ approaches 1 as N approaches ∞ . Also, if $\kappa[\underline{R}(0,1,N-2,2)]$ is treated as a function of ω , it can be demonstrated by means of lengthy and tedious calculations that $\kappa[\underline{R}(0,1,N-2,2)]$ will exhibit a local minimum at $\omega = \pi/2$ when N is odd. Since this local minimum approaches 1 as N approaches ∞ , we might consider the possibility that the local minimum is actually a global minimum (with respect to ω) when N is odd. It appears that this is the case (see Figures 7-3a through 7-3e for evidence substantiating this claim).

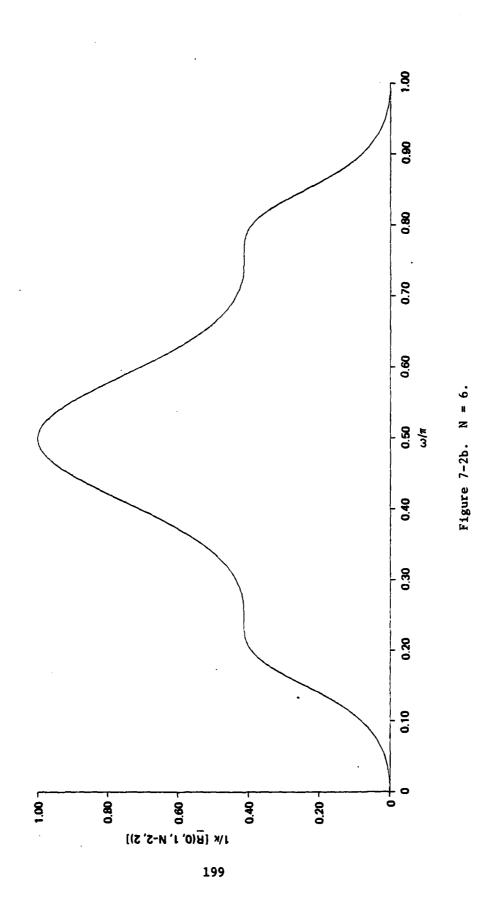
Thus it will be assumed that $\kappa[\underline{R}(0,1,N-2,2)]$ exhibits its minimum value at $\omega = \pi/2$ for all values of N. It now becomes apparent that the conditioning of $\underline{R}(0,1,N-2,2)$ depends on the angular spacing of the autocorrelation poles $\{e^{j\omega}, e^{-j\omega}\}$. If the poles are closely spaced ($\omega=0$ or $\omega=\pi$), $\kappa[\underline{R}(0,1,N-2,2)]$ will be large. If the angular separation is the maximum achievable ($\omega=\pi/2$), $\kappa[\underline{R}(0,1,N-2,2)]$ will be the minimum obtainable for the given value of N.

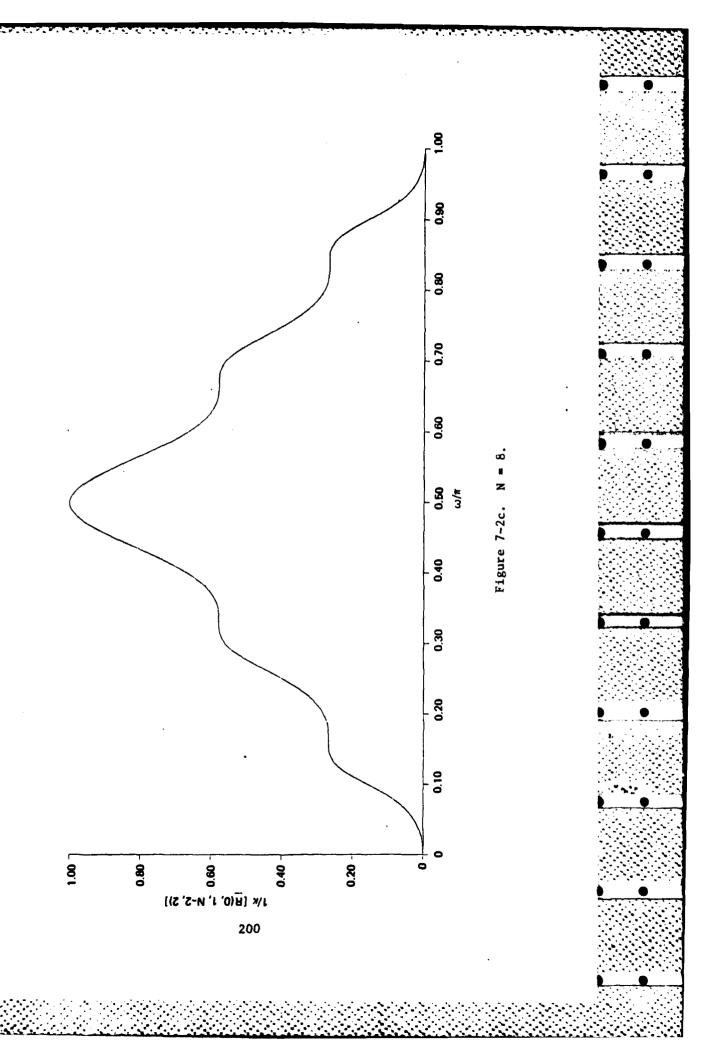
We might now consider whether these results, when appropriately modified, are applicable to the conditioning of $\underline{R}(0,1,N-n,n)$ when n is an arbitrary even number and $\{r(k)\}$ is characterized by Eq. (7-30). Specifically, the validity of the following guideline for determining the effect of the mode frequencies $\{\omega_1,\cdots,\omega_{n/2}\}$ on $\kappa[\underline{R}(0,1,N-n,n)]$ will be considered.

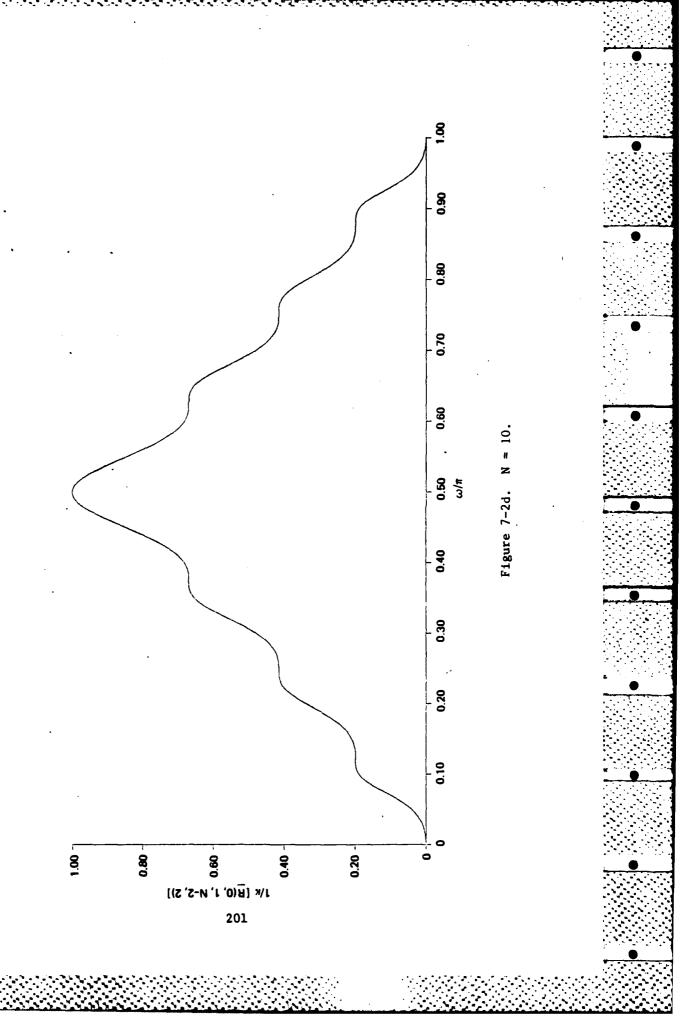
Figures 7-2. Reciprocal of the condition number of autocorrelation matrix $\underline{R}(0,1,N-2,2)$ as a function of frequency (single sinusoid case, N even).

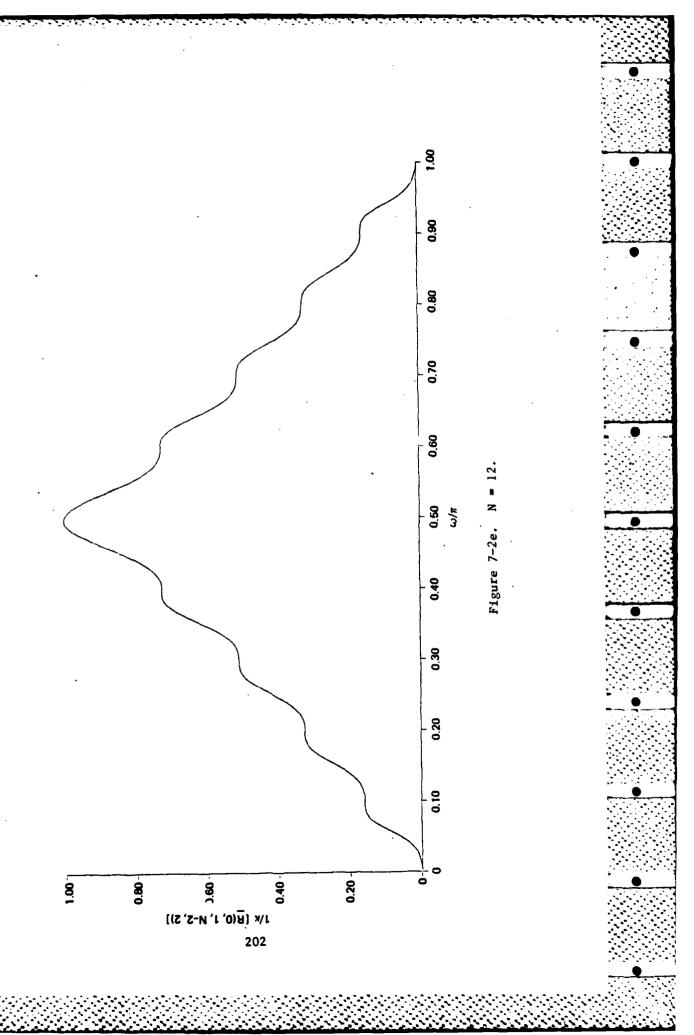
(On following pages)









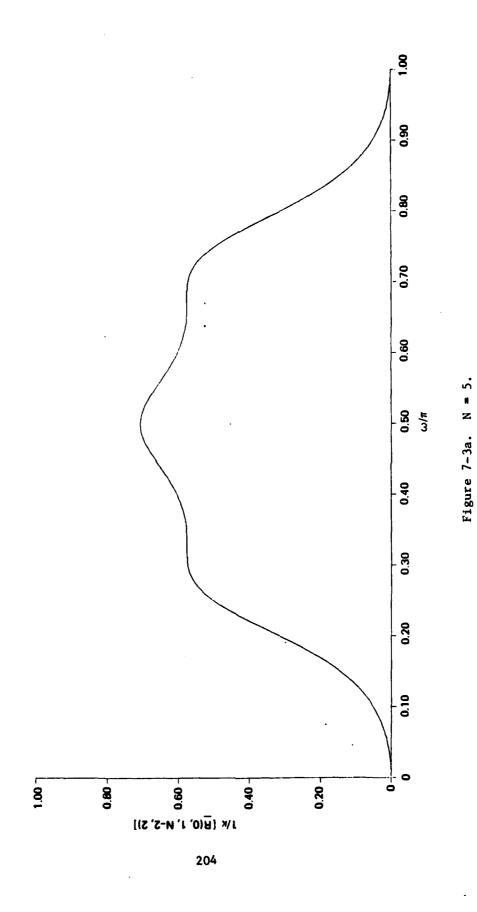


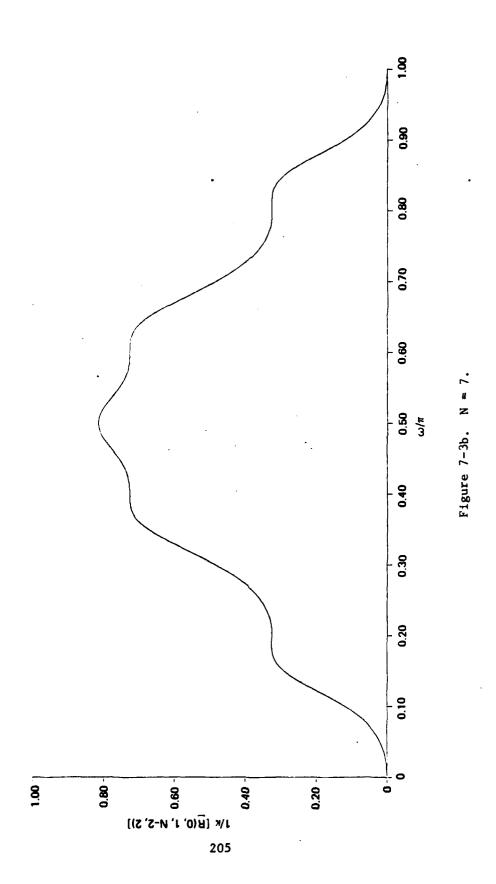
この質問のシステントの

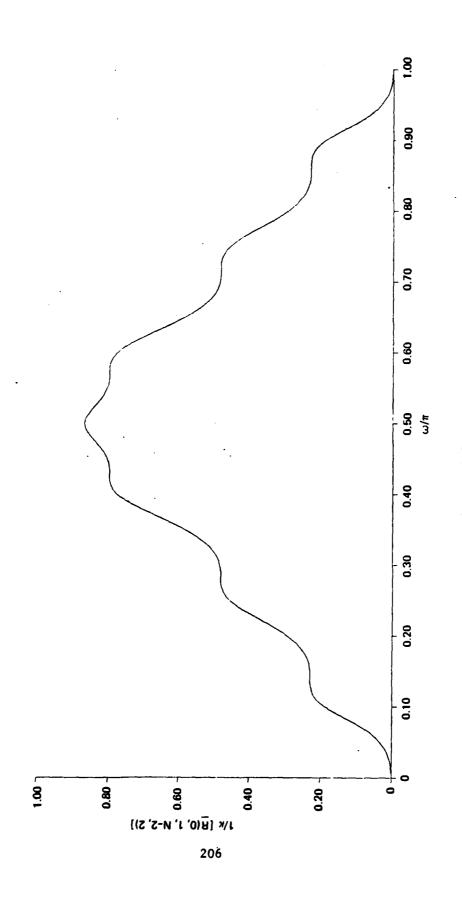
とのの意思のとうでは、最初のなかのは、一般にはないとのでは、一般にはないでは、一般にはない。これは、これのは、一般にはないない。

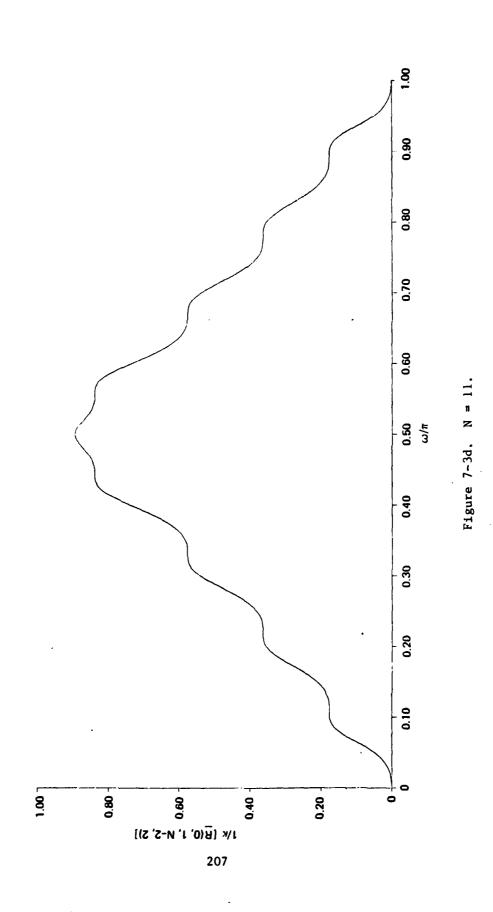
Figures 7-3. Reciprocal of the condition number of autocorrelation matrix $\underline{R}(0,1,N-2,2)$ as a function of frequency (single sinusoid case, N odd).

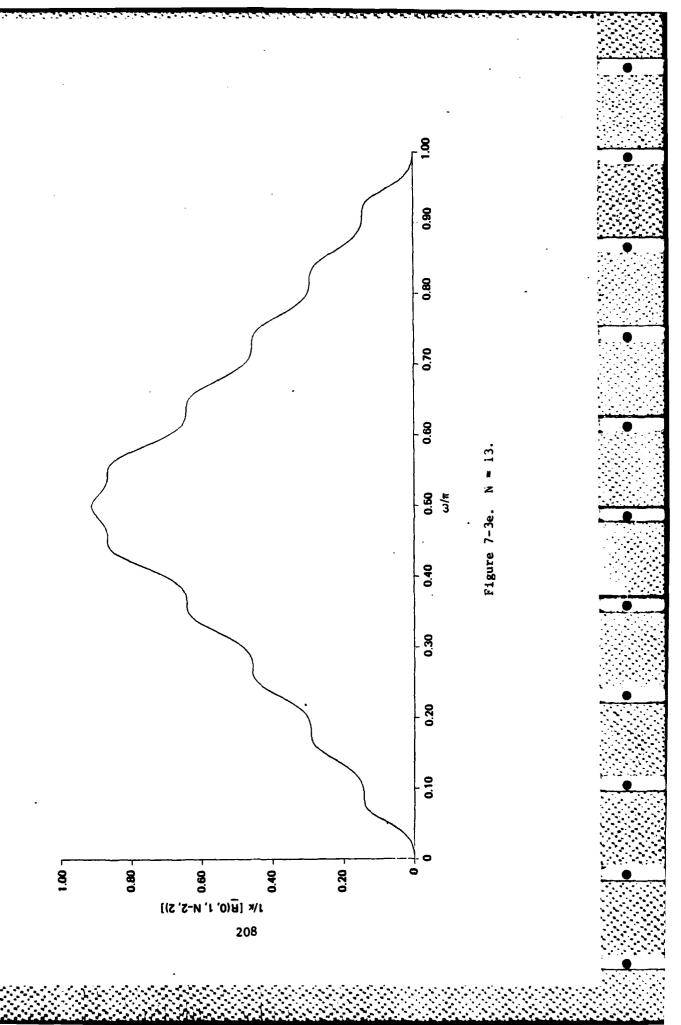
(On following pages)











Guideline 1. The conditioning of $\underline{R}(0,1,N-n,n)$ depends on the angular spacing of the poles $\{e^{\int_{-\infty}^{\infty} \frac{j\omega_n}{n/2}}, e^{-j\omega_n}, \cdots, e^{-j\omega_n/2}\}$ in the following manner. If treated as a function of $\{\omega_1, \cdots, \omega_{n/2}\}$, $\kappa[\underline{R}(0,1,N-n,n)]$ will exhibit its minimum value when the angular separation of adjacent poles is $2\pi/n$. If the separation of any two poles is much less than $2\pi/n$, then $\kappa[\underline{R}(0,1,N-n,n)] >> 1$. \square

Because of the difficulty in resolving closely spaced spectral peaks, we expect $\kappa[\underline{R}(0,1,N-n,n)]$ to depend on the angles $\{\Delta\omega_1=\omega_{1+1}-\omega_1:1=1,\cdots,(n/2)-1\}$ which separate $\{e^{j\omega_1},\cdots,e^{j\omega_n/2}\}$. But Guideline 1 is important because it suggests that $\kappa[\underline{R}(0,1,N-n,n)]$ depends not only on $\{\Delta\omega_1: i=1,\cdots,(n/2)-1\}$, but also on the angles $2\omega_1$ and $2(\pi-\omega_{n/2})$ which separate, respectively, the low frequency poles $\{e^{j\omega_1},e^{-j\omega_1}\}$ and the high frequency poles $\{e^{j\omega_1/2},e^{-j\omega_1/2}\}$.

Next the validity of Guideline 1 is demonstrated for the case where n = 4. The special significance of the spacing issue for the high and low frequency poles is also discussed.

7.3.3.2 The Two Sinusoid Case

Letting n = 4, we have

$$r(k) = B_1 \cos \omega_1 k + B_2 \cos \omega_2 k$$

and

$$\underline{R}(0,1,N-4,4) = \begin{bmatrix} r(3) & r(2) & r(1) & r(0) \\ r(4) & r(3) & r(2) & r(1) \\ \vdots & \vdots & \ddots & \vdots \\ r(N-2) & r(N-3) & r(N-4) & r(N-5) \end{bmatrix}$$

As with the single sinusoid case, we will attempt to gain insight into the problem of estimating $\{a_1, a_2, a_3, a_4\}$ by considering $\kappa[\underline{R}(0,1,N-4,4)]$. Since Eq. (7-29) indicates that to do so requires determining the roots of a fourth order polynomial (for which there is no general solution), we must approach the problem numerically.

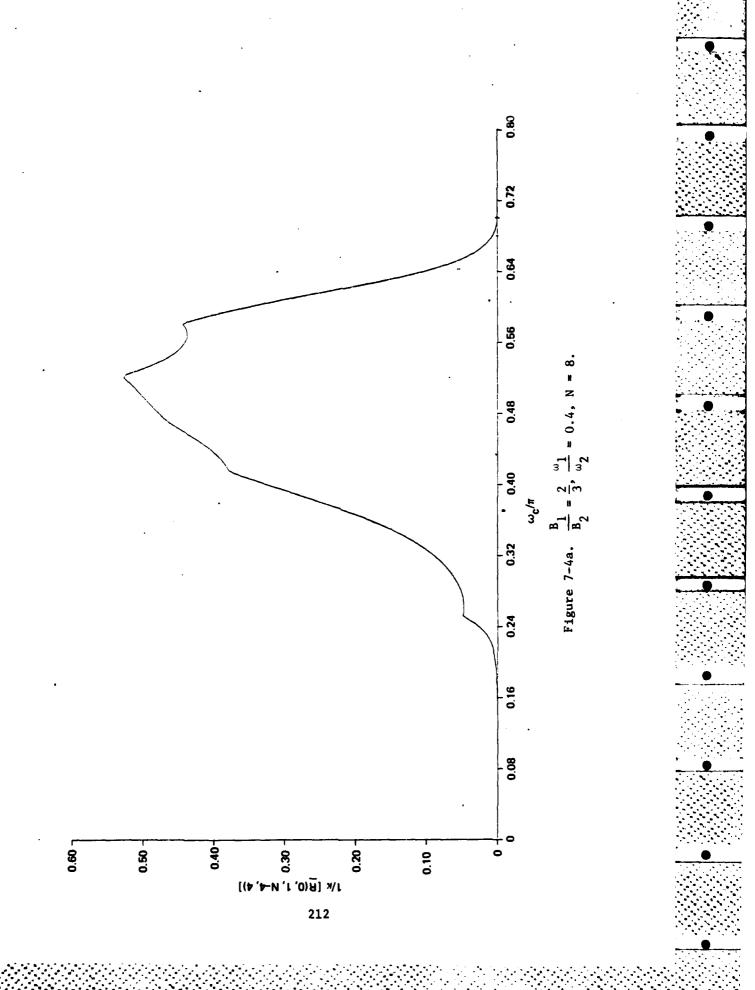
The eigenvalue solving routines of the EISPAC subroutine package [Ref. 7-11] have been used to calculate $\kappa[\underline{R}(0,1,N-4,4)]$ for various values of B_1/B_2 , ω_1/ω_2 , $\omega_c \stackrel{\Delta}{=} (\omega_1+\omega_2)/2$, and N. Of interest is the relationship between $\kappa[\underline{R}(0,1,N-4,4)]$ and ω_c . In Figures 7-4a through 7-4e this relationship is depicted for different values of B_1/B_2 , ω_1/ω_2 , and N. Note that in these plots, $1/\kappa[\underline{R}(0,1,N-4,4)]$ is plotted only for these values of ω_c such that $0 < \omega_1 < \omega_2 < \pi$. For example, $1/\kappa[\underline{R}(0,1,N-4,4)]$ is plotted only for $0 < \omega_c/\pi < 0.7$ in Fig. 7-4a.

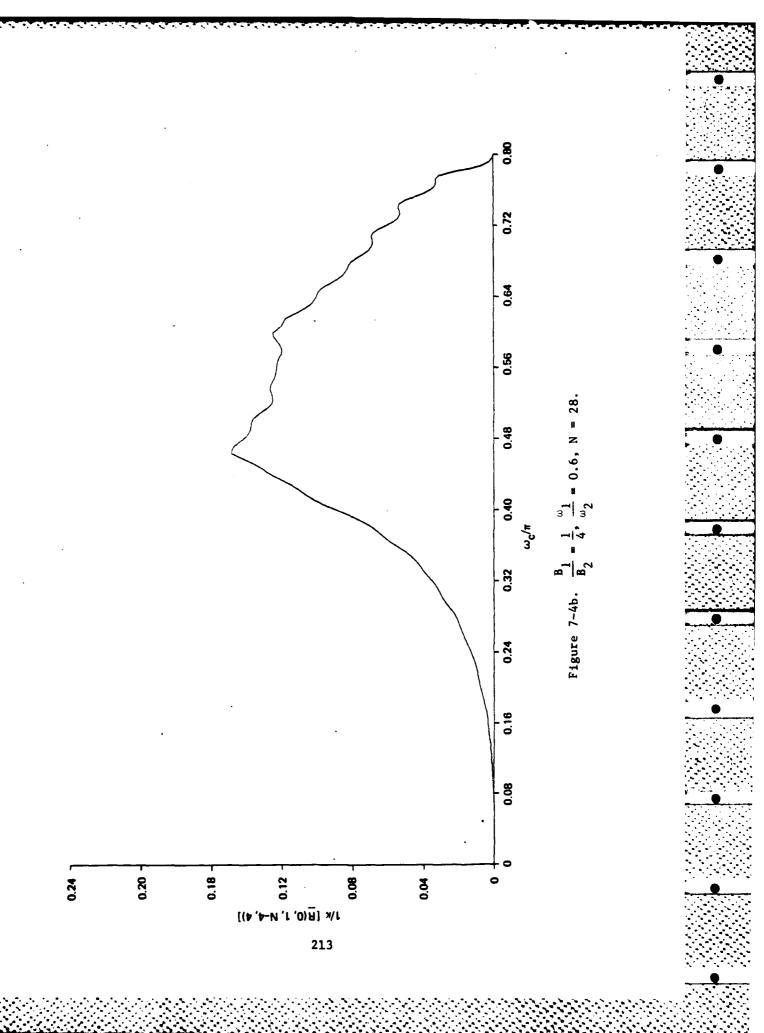
For given values of B_1/B_2 , ω_1/ω_2 , and N, let $\overline{\kappa}[\underline{R}(0,1,N-4,4)]$ denote the minimum value of $\kappa[\underline{R}(0,1,N-4,4)]$, and let $\overline{\omega}_c$ denote the value of ω_c where $\kappa[\underline{R}(0,1,N-4,4)] = \overline{\kappa}[\underline{R}(0,1,N-4,4)]$. It is instructive to fix B_1/B_2 and N, and consider $\overline{\kappa}[\underline{R}(0,1,N-4,4)]$ and $\overline{\omega}_c$ as functions of ω_1/ω_2 . In Figures 7-5 and 7-6, $\overline{\omega}_c$ and $\overline{\kappa}[\underline{R}(0,1,N-4,4)]$ are plotted against ω_1/ω_2 for N = 208 and $B_1/B_2 = 1/4$, 2/3, 1, 3/2, and 4. The value N = 208 was chosen because for given values of B_1/B_2 and ω_1/ω_2 it appears that $\overline{\omega}_c$ at N = 208 is a good approximation for $\overline{\omega}_c$ at all values of N (for example, see Table 7-1).

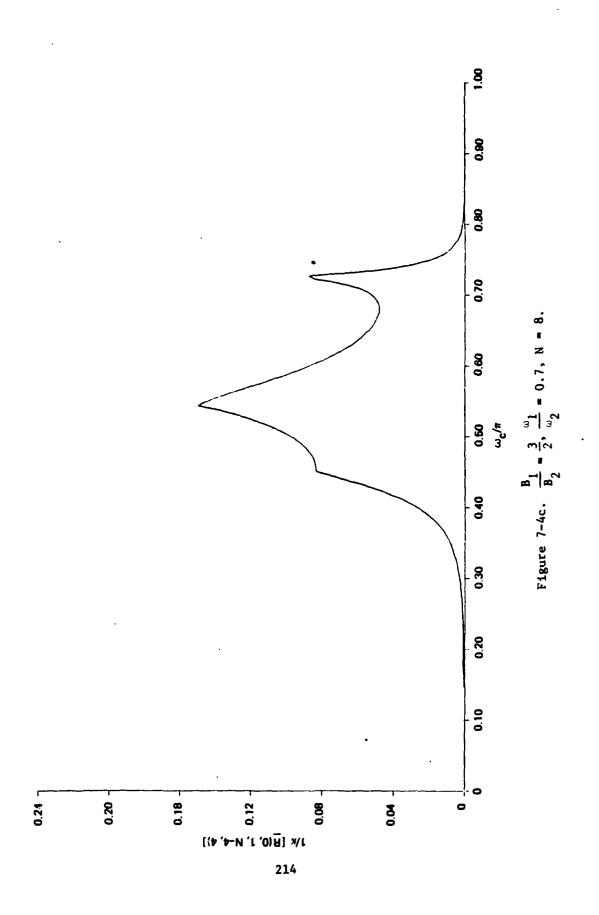
Figures 7-4, 7-5, and 7-6 now enable us to discuss the validity of Guideline 1 for the case where n = 4. First note by referring to Figure 7-6 that $\tilde{\kappa}[R(0,1,204,4)]$ appears to achieve its minimum at $\omega_1/\omega_2=1/3$ for all values of B_1/B_2 . In addition, Figure 7-5 indicates that

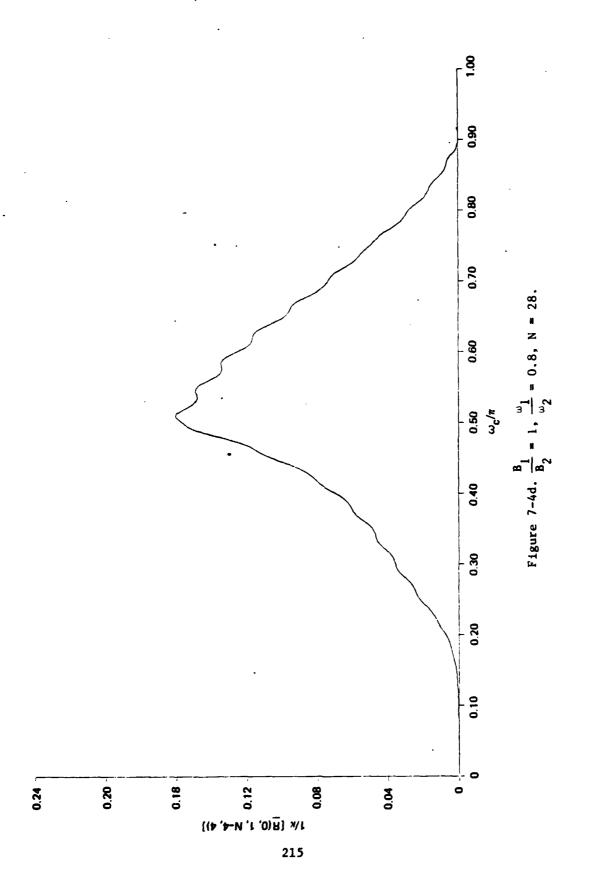
Figures 7-4. Reciprocal of the condition number of autocorrelation matrix R(0,1,N-4,4) as a function of center frequency ω_{C} (two sinusoid case).

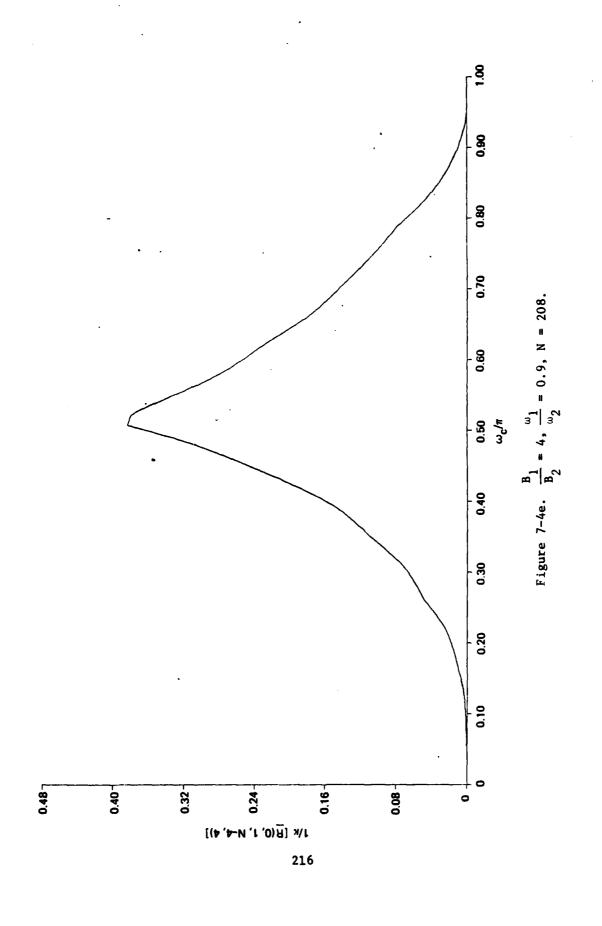
(On following pages)

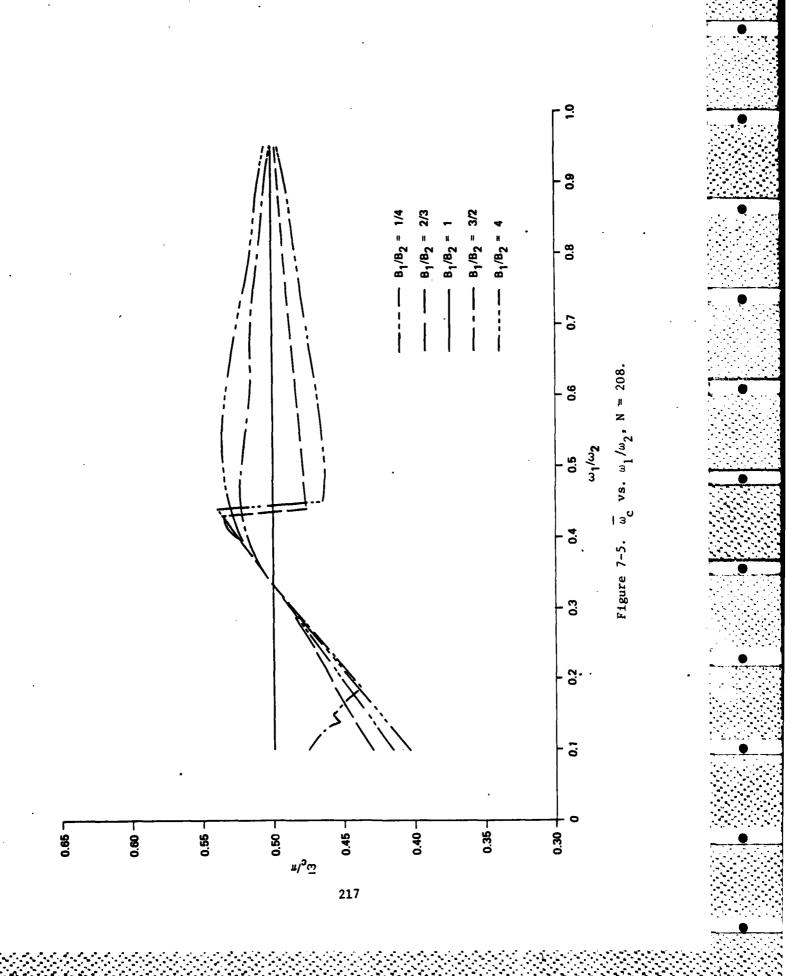












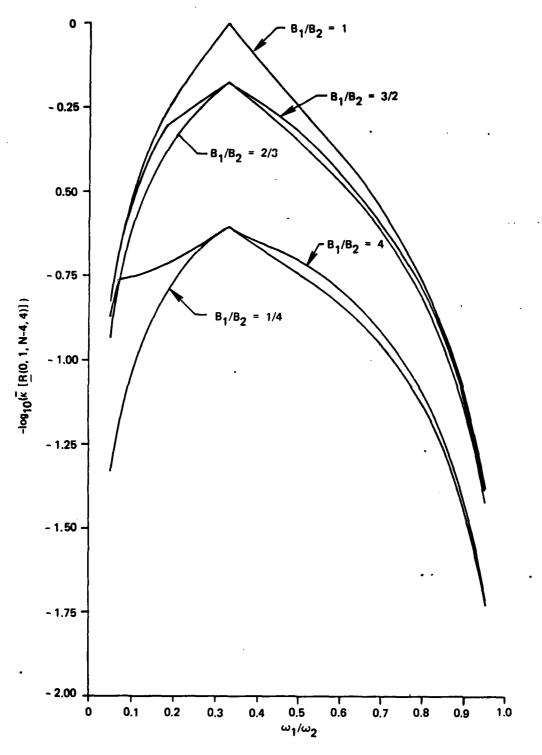


Figure 7-6. \overline{K} [\underline{R} (0, 1, N-4, 4)] vs. ω_1/ω_2 , N = 208.

Table 7-1. $\bar{\omega}_{c}$ as a function of N for $B_{1}/B_{2}=1$, and $\omega_{1}/\omega_{2}=0.9$.

N	· ω _c /π	$(\bar{\kappa}[\underline{R},0,1,N-4,4)]^{-2}$
8	0.523	0.5738×10^{-4}
13	0.568	0.3947×10^{-3}
18	0.516	0.1802×10^{-2}
23	0.537	0.4764×10^{-2}
28	0.510	0.8908×10^{-2}
`33	0.500	0.9912×10^{-2}
38	0.500	0.8536×10^{-2}
43	0.500	0.6200×10^{-2}
48	0.501	0.5422×10^{-2}
53	0.501	0.5299×10^{-2}
58	0.505	0.6109×10^{-2}
68	0.503	0.8113×10^{-2}
78	0.500	0.7215×10^{-2}
88	0.501	0.5955×10^{-2}
98	0.503	0.6764×10^{-2}
108	0.501	0.7698×10^{-2}
128	0.502	0.6225×10^{-2}
148	0.501	0.7436×10^{-2}
168	0.502	0.6432×10^{-2}
188	0.500	0.7239×10^{-2}
208	0.502	0.6598×10^{-2}

Table 7-2. $\bar{\omega}_c$ as a function of N for n=6, $B_1=B_2=B_3$, $\omega_1/\omega_3=0.8$, and $\omega_2/\omega_3=0.9$.

N	$\frac{\overline{\omega}_{\rm C}/\pi}{}$
12	0.518
22	0.626
32	0.504
42	0.500
52	0.504
62	0.504
72	0.500
82	0.500
92	0.504
102	0.500
112	0.500

 $\bar{\omega}_{\rm c} = \pi/2$ at $\omega_1/\omega_2 = 1/3$ for all values of B_1/B_2 . These results suggest that when treated as a function of ω_1 and ω_2 , $\kappa[\underline{R}(0,1,204,4)]$ assumes its minimum when $\omega_1 = \pi/4$ and $\omega_2 = 3\pi/4$, or, equivalently, when the angular separation between adjacent autocorrelation poles is $2\pi/n$. This result is suggested by Guideline 1.

Guideline I further suggests that if the angle separating any two poles is much less than $2\pi/n$, then $\kappa[\underline{R}(0,1,204,4)] >> 1$. By referring to Figures 7-4, 7-5, and 7-6, the reader will note this is clearly the situation.

Thus, it appears that Guideline 1 is valid for the case where n=4. Because of the validity of this guideline when n=2 and n=4, one might intuitively expect that it is valid for arbitrary even n. It has been the author's experience that this is the case, and in all that follows the validity of Guideline 1 will be assumed for all even values of n.

Before terminating this subsection, a result which has important implications for the spectral resolution problem must be stated. Specifically, by referring to Figure 7-5, we see that when ω_1/ω_2 is close to 1, $\overline{\omega}_c = \pi/2$. This result seems to indicate that when $\omega_1/\omega_2 = 1$, the angular spacing of the high frequency poles $\{e^{-j\omega_2}, e^{-j\omega_2}\}$ and of the low frequency poles $\{e^{-j\omega_1}, e^{-j\omega_1}\}$ is more important in determining $\kappa[\underline{R}(0,1,N-4,4)]$ than the angular separation of $\{e^{-j\omega_1}, e^{-j\omega_2}\}$, since the separation of $\{e^{-j\omega_1}, e^{-j\omega_2}\}$ does not vary much with ω_c .

It seems reasonable to consider the generalization of this result for all even values of n>2. Thus we have a second guideline for judging the effect of the mode frequencies $\{\omega_1, \cdots, \omega_{n/2}\}$ on the conditioning of $\underline{R}(0,1,N-n,n)$:

Guideline 2. For fixed $\{B_1, \dots, B_{n/2}\}$, $\{\omega_1/\omega_{(n/2)}, \dots, \omega_{(n/2)-1}/\omega_{(n/2)}\}$, and N, let $\overline{\omega}_c$ denote the value of $\omega_c = (\omega_1 + \omega_{(n/2)})/2$ where $\kappa[\underline{R}(0,1,N-n,n)]$ assumes its minimum. If $\omega_1/\omega_{(n/2)}$ is close to 1, then $\overline{\omega}_c = \pi/2$. \square

It has been the experience of the author that Guideline 2 is generally correct (for example, see Table 7-2), and therefore it will be assumed valid in all that follows.

In this subsection, the sensitivity of the spectrum estimation procedure of Section 7.2 to autocorrelation estimation errors has been examined. Specifically, guidelines have been formulated for determining the effect of the autocorrelation poles on error sensitivity. Guideline 1 applies to autocorrelation sequences describable by Eq. (7-30), whereas Guideline 2 is restricted to those sequences with $\omega_1/\omega_{(n/2)}$ close to 1. In the next subsection, these guidelines lead to modifications which improve the resolution obtainable by the procedure of Section 7.2.

7.4 The Role of Desampling in Improving Spectral Resolution

The results of the previous subsection suggest that the configuration of the autocorrelation poles in the complex plane has a significant effect on the performance of the spectrum estimation algorithm of Section 7.2. The purpose of this subsection is to show that performance can be improved considerably by desampling the autocorrelation sequence to "move" the poles to desirable locations. To this end a modified spectrum estimation procedure which employs autocorrelation desampling is constructed.

7.4.1 The Effect of Desampling the Autocorrelation Sequence

Assume $\{r(k)\}$ is representable by Eq. (7-3), and consider the desampled autocorrelation sequences $\{\{r_{M,J}(k)\}: J=0,\cdots,M-1\}$ defined by Eq. (7-1). Combining Eqs. (7-1) and (7-3), we have

$$\mathbf{r}_{M,J}(\mathbf{k}) = \sum_{i=1}^{n} (\mathbf{A}_{i} \mathbf{z}_{i}^{J}) \mathbf{z}_{i}^{M|\mathbf{k}|}$$

Clearly, each desampled sequence $\{r_{M,J}(k)\}$ has the same set of poles $\{z_1^M, \cdots, z_n^M\}$. Thus we see that desampling $\{r(k)\}$ has the effect of relocating each autocorrelation pole in the complex plane:

$$z_i \rightarrow z_i^M$$
 , $i=1,\cdots,n$

If we can further assume that $\{r(k)\}$ is representable by Eq. (7-30), then we see that desampling the autocorrelation sequence changes the angular spacing of the poles. This is a significant result in light of Guidelines 1 and 2 of Section 7.3 because it suggests that a proper choice for the desampling interval M might result in a pole configuration for the sequences $\{\{r_{M,J}(k)\}: J=0,\cdots,M-1\}$ superior to the pole configuration for $\{r(k)\}$. For such situations it is desirable to modify the spectrum estimation procedure of Section 7.2 so that the autoregressive coefficients of $\{(r_{M,J}(k)): J=0, \cdots, M-1\}$ are estimated instead of the autoregressive coefficients of $\{r(k)\}$. Since the desampled autocorrelation sequences $\{\{r_{M_*J}(k)\}: J=0,\cdots,M-1\}$ have the same poles, they also have the same autoregressive coefficients (see Eq. (7-6)). Letting $\{a_{M,1}, \dots, a_{M,n}\}$ denote the autoregressive coefficients of $\{\{r_{M,J}(k)\}: J=0,\dots,M-1\}$, with $a_{l,i}=a_{i}$, i=1, ..., the following modified spectrum estimation procedure is proposed:

- Step 1. Determine an appropriate value for M based on Guidelines 1 and 2 of Section 7.3.
- Step 2. Estimate $\{a_{M,1}, \dots, a_{M,n}\}$.
- Step 3. Estimate $\{z_1^M, \dots, z_n^M\}$ by solving Eq. (7-13) with a_1 replaced by $\hat{a}_{M,1}$.
- Step 4. Obtain $\{\hat{z}_1, \dots, \hat{z}_n\}$ from $\{\hat{z}_1^M, \dots, \hat{z}_n^M\}$.
- Step 5. Obtain $\{\hat{A}_1, \dots, \hat{A}_n\}$.

Step 1 of the above procedure is discussed in Reference 7-14. Step 3 is self explanatory. Steps 2 and 4 are discussed, respectively, in Sections 7.4.2 and 7.4.3. Step 5 is also discussed briefly in Section 7.4.3.

7.4.2 Estimation of Autoregressive Coefficients

Assuming the availability of $\{\hat{r}(0), \dots, \hat{r}(N-1)\}$, the procedure of Section 7.2 obtains $\{\hat{a}_1, \dots, \hat{a}_n\}$ by solving

$$\begin{bmatrix} \hat{\mathbf{r}}(\mathbf{n}) \\ \hat{\mathbf{r}}(\mathbf{n}+1) \\ \vdots \\ \hat{\mathbf{r}}(\mathbf{N}-1) \end{bmatrix} \stackrel{\mathbf{r}}{=} \begin{bmatrix} \hat{\mathbf{r}}(\mathbf{n}-1) & \hat{\mathbf{r}}(\mathbf{n}-2) & \cdots & \hat{\mathbf{r}}(0) \\ \hat{\mathbf{r}}(\mathbf{n}) & \hat{\mathbf{r}}(\mathbf{n}-1) & \cdots & \hat{\mathbf{r}}(1) \\ \vdots & \vdots & \ddots & \vdots \\ \hat{\mathbf{r}}(\mathbf{N}-2) & \hat{\mathbf{r}}(\mathbf{N}-3) & \cdots & \hat{\mathbf{r}}(\mathbf{N}-\mathbf{n}-1) \end{bmatrix} \begin{bmatrix} \hat{\mathbf{a}}_1 \\ \hat{\mathbf{a}}_2 \\ \vdots \\ \hat{\mathbf{a}}_n \end{bmatrix}$$
(7-31)

in the least squares sense. We might consider applying this technique to the sequence $\{r_{M,J}(k)\}$, J=0,...,M-1, to obtain $\{\hat{a}_{M,1}, \dots, \hat{a}_{M,n}\}$. Replacing " \hat{r} " with " $\hat{r}_{M,J}$ " and N with

$$N_{M,J} = \left[\frac{N - J - 1}{M} \right] + 1$$

in Eq. (7-31) we have

$$\begin{bmatrix} \hat{r}_{M,J}(n) \\ \vdots \\ \hat{r}_{M,J}(N_{M,J}-1) \end{bmatrix} = \begin{bmatrix} \hat{r}_{M,J}(n-1) & \cdots & \hat{r}_{M,J}(0) \\ \vdots & & & \vdots \\ \hat{r}_{M,J}(N_{M,J}-2) & \cdots & \hat{r}_{M,J}(N_{M,J}-n-1) \end{bmatrix} \begin{bmatrix} \hat{a}_{M,1} \\ \vdots \\ \hat{a}_{M,n} \end{bmatrix}$$

The notation $\lfloor x \rfloor$ denotes the integer satisfying $\lfloor x \rfloor \leq x < \lfloor x \rfloor + 1$, and $N_{M,J}$ denotes the number of estimates corresponding to $\{r_{M,J}(k)\}$ in $\{\hat{r}(0), \dots, \hat{r}(N-1)\}$. Noting that $\hat{r}_{M,J}(k) = \hat{r}(M|k|+J)$, we get

$$\hat{\mathbf{r}}(Mn + J, M, N_{M,J} - n) = \hat{\mathbf{R}}(J, M, N_{M,J} - n, n) \hat{\mathbf{a}}_{M}(n)$$
(7-32)

Assuming

$$N_{M_*J} \geq 2n$$

 $\frac{\hat{a}}{M}(n) = \{\hat{a}_{M,1}, \dots, \hat{a}_{M,n}\}$ may be obtained by solving Eq. (7-32) in the least squares sense.

If $|z_1| = 1$, $i=1,\cdots,n$, and M is chosen to position $\{z_1^M,\cdots,z_n^M\}$ advantageously in the complex plane (according to Guidelines 1 and 2), then one might expect $\{\hat{a}_{M,1},\cdots,\hat{a}_{M,n}\}$ obtained via Eq. (7-32) to be less sensitive than $\{\hat{a}_1,\cdots,\hat{a}_n\}$ obtained via Eq. (7-31) to errors in $\{\hat{r}(0),\cdots,\hat{r}(N-1)\}$. However, any tendency for the sensitivity of $\{\hat{a}_{M,1},\cdots,\hat{a}_{M,n}\}$ to decrease is offset by the fact that only $N_{M,J}=N/M$ of the N available autocorrelation estimates $\{\hat{r}(0),\cdots,\hat{r}(N-1)\}$ are used to calculate $\{\hat{a}_{M,1},\cdots,\hat{a}_{M,n}\}$.

Since the sequences $\{\{r_{M,J}(k)\}: J=0,\cdots,M-1\}$ share the same autoregressive coefficients $\{a_{M,1},\cdots,a_{M,n}\}$, the following technique is proposed in an effort to use all the available autocorrelation estimates to calculate $\{\hat{a}_{M,1},\cdots,\hat{a}_{M,n}\}$. Assuming

$$N_{M,J} > n$$
 , J=0, · · · , M-1

$$\sum_{J=0}^{M-1} (N_{M,J} - n) \ge n$$

let $\{\hat{a}_{M,1}, \cdots, \hat{a}_{M,n}\}$ be obtained by solving the following set of equations in the least squares sense:

$$\frac{\hat{\mathbf{r}}(Mn, M, N_{M,0} - n)}{\hat{\mathbf{r}}(Mn+1, M, N_{M,1} - n)}$$

$$\frac{\hat{\mathbf{r}}(Mn+1, M, N_{M,1} - n)}{\hat{\mathbf{r}}(Mn+M-1, M, N_{M,M-1} - n)}$$

$$\frac{\hat{R}(0,M,N_{M,0}-n,n)}{\hat{R}(1,M,N_{M,1}-n,n)}$$

$$\frac{\hat{R}(1,M,N_{M,1}-n,n)}{\hat{R}(M-1,M,N_{M,M-1}-n,n)}$$

$$\frac{\hat{R}(M-1,M,N_{M,M-1}-n,n)}{\hat{R}(M-1,M,N_{M,M-1}-n,n)}$$

As with $\{\hat{a}_{M,1}, \cdots, \hat{a}_{M,n}\}$ obtained via Eq. (7-32), one might intuitively expect $\{\hat{a}_{M,1}, \cdots, \hat{a}_{M,n}\}$ obtained via Eq. (7-33) to benefit from an advantageous pole configuration for $\{\{r_{M,J}(k)\}: J=0, \cdots, M-1\}$. However, because all available autocorrelation estimates are used, $\{\hat{a}_{M,1}, \cdots, \hat{a}_{M,n}\}$ obtained via Eq. (7-33) should be superior. Therefore, in all that follows, $\{\hat{a}_{M,1}, \cdots, \hat{a}_{M,n}\}$ will be obtained via Eq. (7-33).

Once $\{\hat{\mathbf{a}}_{\mathrm{M},1},\cdots,\hat{\mathbf{a}}_{\mathrm{M},n}\}$ have been determined, $\{\hat{z}_{1}^{\mathrm{M}},\cdots,\hat{z}_{n}^{\mathrm{M}}\}$ may be obtained as discussed previously. In the next subsection, techniques for determining $\{\hat{z}_{1},\cdots,\hat{z}_{n}\}$ from $\{\hat{z}_{1}^{\mathrm{M}},\cdots,\hat{z}_{n}^{\mathrm{M}}\}$ are presented.

7.4.3 Obtaining Pole Estimates from Desampled Sequence Pole Estimates

Consider \hat{z}_{i}^{M} written in polar form:

$$\hat{z}_{i}^{M} = |\hat{z}_{i}|^{M} \exp[j(\text{Arg }\hat{z}_{i}^{M} + 2\pi \hat{z})]$$

where Arg $\hat{z_1}^M$ denotes the principal argument of $\hat{z_1}^M$ and t is any integer. The principal argument is defined here as the unique real number which satisfies $z = |z| \exp(j \cdot \text{Arg } z)$ and $-\pi < \text{Arg } z \le \pi$ for any nonzero complex number z. Clearly,

$$\hat{z}_{i} = |\hat{z}_{i}| \exp[j(\operatorname{Arg} \hat{z}_{i}^{M} + 2\pi n)/M]$$
 (7-34)

where m is some integer satisfying

$$0 \le m \le M-1$$

In order to determine m, additional information concerning the locations of $\{z_1, \dots, z_n\}$ in the complex plane is required.

In this subsection, knowledge of

$$\omega_{\min} = \min\{|\text{Arg } z_i|: i=1,\cdots,n\}$$

and

$$\omega_{\text{max}} = \max\{\left|\text{Arg } z_i\right|: i=1,\dots,n\}$$

will be assumed, even though ω_{\min} and ω_{\max} will usually not be available. However, any appropriate spectrum estimation procedure, such as the Blackman-Tukey method [Reference 7-1, p. 908, and references therein], can be employed to obtain estimates for these quantities. Procedures will be discussed for determining m when

$$M \cdot \omega_{\text{max}} < \pi$$
 (7-35)

and when

$$2\pi < M \cdot \omega_{\min} \leq M \cdot \omega_{\max} < (\ell+1)\pi$$
 (7-36)

where t is an integer satisfying $t \ge 1$. As is discussed in Reference 7-14, Ineqs. (7-35) and (7-36) describe many situations of practical importance.

We first consider the case where Ineq. (7-35) holds. For this case, we have

$$\operatorname{Arg} \ \mathbf{z_i}^{\mathsf{M}} < \pi \tag{7-37}$$

and

$$Arg z_i = Arg z_i^{M}/M$$

for i=1,...,n. Thus if Arg $\hat{z_i}^{\rm M} < \pi$, it seems reasonable to set m = 0 in Eq. (7-34). However, if Arg $\hat{z_i}^{\rm M} = \pi$, Eq. (7-37) suggets that $\hat{z_i}^{\rm M}$ is a mathematical artifact and therefore should be ignored. This can be accomplished by setting $\hat{A_i} = 0$.

The situation becomes slightly more complicated when Ineq. (7-36) holds. From Ineq. (7-36) note that

$$0 < \left| \text{Arg } \mathbf{z_i}^{M} \right| < \pi \qquad (7-38)$$

for i=1, ...,n. Also,

$$Arg z_{1} = \begin{cases} (Arg z_{1}^{M} + \hbar\pi)/M & , & \ell \text{ even}, & 0 < Arg z_{1}^{M} < \pi \\ (Arg z_{1}^{M} - \hbar\pi)/M & , & \ell \text{ even}, & -\pi < Arg z_{1}^{M} < 0 \\ (Arg z_{1}^{M} - (\hbar\pi)/M) & , & \ell \text{ odd}, & 0 < Arg z_{1}^{M} < \pi \\ (Arg z_{1}^{M} + (\hbar\pi)/M) & , & \ell \text{ odd}, & -\pi < Arg z_{1}^{M} < 0 \end{cases}$$

Thus it seems reasonable to choose m of Eq. (7-34) as follows:

$$m = \begin{cases} 2/2 & \text{i. even, } 0 < \text{Arg } \hat{z_i}^{M} < \pi \\ -2/2 & \text{i. even, } -\pi < \text{Arg } \hat{z_i}^{M} < 0 \\ -(2+1)/2 & \text{i. odd, } 0 < \text{Arg } \hat{z_i}^{M} < \pi \\ (2+1)/2 & \text{i. odd, } -\pi < \text{Arg } \hat{z_i}^{M} < 0 \end{cases}$$

If Arg $\hat{z_i}^M = 0$ or Arg $\hat{z_i}^M = \pi$, then in light of Eq. (7-38), $\hat{z_i}^M$ can be assumed spurious and should be ignored by setting $\hat{A_i} = 0$.

Once the pole estimates for $\{r(k)\}$ have been obtained, the procedure discussed in Section 7.2 may be used to estimate $\{A_1, \dots, A_n\}$. For those cases where it is not necessary to constrain any of $\{\hat{A}_1, \dots, \hat{A}_n\}$ to be equal to zero, Eq. (7-18) is solved in the least squares sense to obtain $\{\hat{A}_1, \dots, \hat{A}_n\}$. When it is necessary to set $\hat{A}_1 = 0$, the i-th columns of $\hat{\underline{V}}_T$ and $\hat{\underline{V}}_1$ in addition to the i-th elements of $\hat{\underline{A}}_T$ and $\hat{\underline{A}}_1$ must be deleted before Eq. (7-18) is solved.

7.5 Conclusion

In a number of applications including radar Doppler processing and system identification, it is necessary to obtain power spectrum estimates which exhibit good resolution of closely spaced spectral magnitude peaks. Currently there is a great deal of research being conducted which addresses the problem of improving the resolution obtained by power spectrum estimation techniques.

In this section a new approach to the resolution problem was presented. Specifically, a procedure for obtaining spectrum estimates from autocorrelation sequence estimates was analyzed to determine its sensitivity to errors in the autocorrelation estimates. The results of this analysis clearly demonstrate that the locations of the autocorrelation poles in the complex plane have a significant effect on the error sensitivity of the spectrum analysis procedure which was under consideration. In particular, it appears that error sensitivity becomes a particularly acute problem when poles are closely spaced, thus indicating the difficulty encountered when high resolution spectrum estimates are sought.

As a remedy for this problem, a modified spectrum estimation procedure was proposed which employs autocorrelation desampling as a means of artificially separating closely spaced poles, thus relieving the error sensitivity problem. The unique features of this procedure are that it employs all available autocorrelation estimates, and that the size of the desampling interval used is not bounded by spectral aliasing considerations. The improved resolution obtained by this modified procedure is demonstrated via numerical examples in Reference 7-14.

Thus, by posing the spectral resolution problem as one of decreasing error sensitivity, we have observed that resolution can be considerably improved by placing the poles of the autocorrelation sequence in desirable locations by desampling. Since appropriate choices

for desampling intervals may be obtained easily and with a minimum of a priori knowledge (see Ref. 7-14), the results of this section should be quite valuable to the researcher requiring high resolution power spectrum estimation.

References

- 7-1. Cadzow, J.A. "Spectral Estimation: An Overdetermined Rational Model Equation Approach," Proceedings of the IEEE, Vol. 70, No. 9, Sept. 1982, pp. 907-939.
- 7-2. Robinson, E.A. "A Historical Perspective of Spectrum Estimation,"

 Proceedings of the IEEE, Vol. 70, No. 9, Sept. 1982, pp. 885-907.
- 7-3. Beex, A.A. and Scharf, L.L., "Covariance Sequence Approximation for Parametric Spectrum Modeling," <u>IEEE Trans. Acoustics, Speech, and Signal Processing</u>, Vol. ASSP-29, No. 5, Oct. 1981, pp. 1042-1052.
- 7-4. Perl, J. and Scharf, L.L., "Covariance-Invariant Digital Filtering," <u>IEEE Trans. Acoustics, Speech, and Signal Processing</u>, Vol. ASSP-25, No. 2, Apr. 1977, pp. 143-151.
- 7-5. Bendat, J.S. and Piersol, A.G., Measurement and Analysis of Random Data, Wiley, New York, NY, 1966.
- 7-6. Bergstrom, A.R. ed., Statistical Inference in Continuous Time

 Economic Models, Elsevier, New York, NY, 1976.
- 7-7. Astrom, K.J., "On the Choice of Sampling Rates in Parametric Identification of Time Series," <u>Information Sciences</u>, Vol. 1, 1969, pp. 273-278.
- 7-8. Payne, R.L., Goodwin, G.C. and Zarrop, M.B., "Frequency Domain Approach for Designing Sampling Rates for System Identification,"

 <u>Automatica</u>, Vol. 11, 1975, pp. 189-191.

- 7-9. Kay, S.M., "The Effect of Sampling Rate on Autocorrelation
 Estimation," IEEE Trans. Acoustics, Speech, and Signal Processing,
 Vol. ASSP-29, No. 4, Aug. 1981, pp. 859-867.
- 7-10. Lawson, C.L. and Hanson, R.J., Solving Least Squares Problems, Prentice-Hall, Englewood Cliffs, NJ, 1974.
- 7-11. Smith, B.T. et al., Matrix Eigensystem Routines EISPACK Guide, Springer-Verlag, New York, NY, 1976.
- 7-12. Fogel, E., "Structure Identification--The Resolution Problem and Its Solution," ACOSS-Eleven Third Semiannual Technical Report, CSDL-R-1598, Charles Stark Draper Laboratory, Cambridge, MA, December 1982; Section 2.
- 7-13. Henderson, T., "Active Control of Space Structures (ACOSS)
 Model 2," Report C-5437, Charles Stark Draper Laboratory,
 Cambridge, MA, September 1981.
- 7-14. Villalba, M.J., "On the Use of Autocorrelation Desampling in High Resolution Spectrum Estimation," S.M. Thesis, Dept. of Aeronautics and Astronautics, Massachusetts Institute of Technology, Cambridge, MA, June 1984.

SECTION 8

A CUBIC SPLINE BASED APPROXIMATION SCHEME FOR THE ESTIMATION OF PARAMETERS IN HYBRID SYSTEMS INVOLVING BEAMS WITH ATTACHED TIP BODIES

8.1 Introduction

Important classes of proposed shuttle-attached payloads and free flying space structures consist of long, slender, flexible trussed masts with massive tip bodies. In anticipation of the need for high fidelity models for the dynamics of structures of this type (for purposes of dynamic interaction and stability studies and eventually control design) we develop numerical approximation schemes for the identification of distributed parameter models describing the transverse vibration of flexible beams with attached tip bodies.

Using the Euler-Bernoulli theory to describe the vibratory motion of the beam, imposing all necessary simple boundary conditions (e.g., clamped ends, pinned ends) and using force and moment relations to derive the boundary conditions which describe the motion at the ends with tip bodies, one obtains a coupled system of ordinary and partial differential equations. Systems such as this are often referred to as hybrid systems. Effects due to externally applied loads to either the beam or the tip bodies are modeled and appear as nonhomogeneous terms in either the partial differential equation describing the vibration of the beam or in the boundary conditions describing the motion of the tip bodies.

The identification problem is formulated as a least squares fit to data. It is assumed that displacement measurements at various positions along the beam at various times have been provided and estimates of unknown parameters appearing in the model (e.g. flexural stiffness, mass density, rigid body mass properties) are sought by minimizing the sum of the squares of the differences between the output of the model and the given observations. The fact that the constraints in the problem are infinite dimensional and distributed in nature necessitates the development of approximation schemes.

Our general approach is similar in spirit to that which was described in References 8-1 and 8-3 for similar classes of problems. We rewrite the coupled system of ordinary and partial differential equations governing the dynamics of the system as an abstract operator evolution equation (AEE) in an appropriate Hilbert space. Using cubic spline based subspaces and a Galerkin-like approach applied to the AEE we are led naturally to a sequence of approximating identification problems in each of which the constraining state equations are finite dimensional. Using linear semigroup theory we are able to prove that each of the approximating problems admits a solution which in some sense approximates the solution to the original identification problem. As a result of the finite dimensionality of the constraints, such a solution is easily found using standard techniques and readily available software. These ideas will be made more precise in Sections 8.2 and 8.3. In Section 8.4 we discuss a numerical example, while in Section 8.5 we outline some of the possible extensions to the results which are presented here.

In what is to follow, the spaces $H^k(a,b)$ denote the Sobolev spaces of real-valued functions defined on the interval [a,b] whose (k-1)st derivatives are absolutely continuous and whose k-th derivatives are square integrable on [a,b]. These spaces are assumed to be endowed with the usual inner products which are given by

$$\langle f, g \rangle_k = \sum_{j=1}^k \int_a^b D^j f D^j g$$

where D denotes the differentiation operator. For a function f(x,t), f is said to be an element in $L^2([0,T], H^k(a,b))$ if the mapping $t \to f(\cdot,t)$ is a square integrable function from [0,T] into $H^k(a,b)$. The function f is said to be an element in $C^k([0,T], H^k(a,b))$ if the mapping $t \to f(\cdot,t)$ is an ℓ -times continuously differentiable function from [0,T] into $H^k(a,b)$.

8.2 The Identification Problem and its Abstract Formulation

Although our methods are applicable to a wide class of parameter estimation problems involving hybrid systems describing the transverse vibration of flexible beams with attached tip bodies, for ease of exposition we outline our general approach for the simple problem of identifying the flexural stiffness EI and linear mass density ρ for a beam of length ℓ clamped at one end and cantilevered at the other with a tip mass of magnitude m (cf. Fig. 8-1).

Using the Euler-Bernoulli theory and elementary Newtonian mechanics [Ref. 8-12] we obtain the following coupled system of ordinary and partial differential equations describing the deflection of the beam:

$$pu_{tt}(x,t) = -EIu_{xxxx}(x,t) + f(x,t), x \in (0,l), t > 0$$
 (8-1)

$$mu_{tt}(\ell,t) = EIu_{xxx}(\ell,t)$$
, $t > 0$ (8-2)

where f(x,t) denotes an externally applied transverse load at position x at time t. The boundary conditions at the clamped end are

$$u(0,t) = 0$$
, $u_{x}(0,t) = 0$, $t > 0$ (8-3)

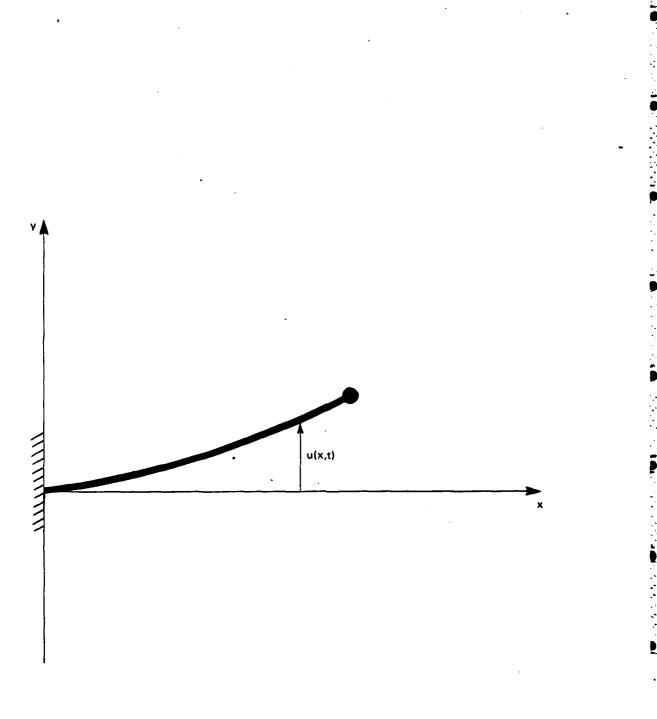


Figure 8-1. Deformed cantilevered beam with tip body.

corresponding to zero displacement and zero slope, while at the cantilevered end we have

$$u_{XX}(t,t) = 0 , t > 0$$
 (8-4)

which corresponds to a zero bending moment. The initial conditions are given by

$$u(x,0) = \phi(x)$$
, $u_{+}(x,0) = \psi(x)$, $x \in [0, L]$ (8-5)

Let
$$\{\hat{\mathbf{u}}(\mathbf{x_i}, \mathbf{t_j})\}_{\substack{i=1,\dots,\nu\\j=1,\dots,\mu}}$$
, $\mathbf{x_i} \in [0,\ell]$, $i=1,\dots,\nu$, $\mathbf{t_j} \in [0,T]$,

 $j=1,\dots,\mu$ denote displacement measurements taken from the actual physical system and let Q be a fixed subset of R^2 . We formulate the identification problem as a constrained least squares fit to data:

(ID) Find $q=(q_1, q_2)^T \in Q$ which minimizes

$$J(q) = \sum_{i=1}^{\nu} \sum_{j=1}^{\mu} |u(x_i, t_j; q) - \hat{u}(x_i, t_j)|^2$$

subject to $u(\cdot,\cdot; q)$ being a solution to Eqs. (8-1) through (8-5) with EI = q_1 and $\rho = q_2$.

The infinite dimensionality of the constraining dynamical system clearly necessitates the use of some form of approximation in order to solve the above optimization problem. Our approach centers upon the construction of an (in some sense) equivalent abstract operator formulation for the system Eqs. (8-1) through (8-5). Rewriting Eqs. (8-1) and (8-2) in state space form will help to motivate what follows. Letting $z_1(t) = u_t(\ell,t)$, $z_2(x,t) = u_{xx}(x,t)$ and $z_3(x,t) = u_t(x,t)$, Eqs. (8-1) and (8-2) yield

$$\frac{\partial}{\partial t} \begin{bmatrix} z_1 \\ z_2 \\ z_3 \end{bmatrix} = \begin{bmatrix} \frac{EI}{m} & \frac{\partial}{\partial x} z_2(\ell, \cdot) \\ \frac{\partial^2}{\partial x^2} & z_3 \\ -\frac{EI}{\rho} & \frac{\partial^2}{\partial x^2} & z_2 \end{bmatrix} + \begin{bmatrix} 0 \\ 0 \\ \frac{1}{\rho} \end{bmatrix} f$$

with
$$u(x,t) = \int_{0}^{x} \int_{0}^{\tau} z_2(\sigma,t) d\sigma d\tau$$
.

We require the following three assumptions:

- (A1) There exist positive constants m_1 , M_1 , m_2 , M_2 such that $q=(q_1,q_2)^T$ ϵ 0 implies $m_1 \leq q_1 \leq M_1$ and $m_2 \leq q_2 \leq M_2$.
- (A2) The specified initial conditions ϕ and ψ are such that $\phi \in H^2(0, \mathbb{L})$ and $\psi \in H^0(0, \mathbb{L})$.
 - (A3) The function f is an element in $L^2([0,T], H^0(0,t))$.

For each $q=(q_1,q_2)^T$ ϵ Q, let Z_q be the Hilbert space consisting of the elements in the space $Z=R\times H^0(0,L)\times H^0(0,L)$ together with the inner product $\langle \cdot\,,\cdot\rangle_q$ given by

$$\langle (w_1, u_1, v_1), (w_2, u_2, v_2) \rangle_q$$

$$= mw_1w_2 + q_1 \langle u_1, u_2 \rangle_0 + q_2 \langle v_1, v_2 \rangle_0$$

$$= mw_1w_2 + q_1 \int_0^2 u_1u_2 + q_2 \int_0^2 v_1v_2$$
(8-6)

Define the operators $\mathscr{A}(q)$: $\mathscr{D} \subset Z_q + Z_q$ by

$$\mathcal{D} = \{(w,u,v) \in Z_q: u \in H^2(0,\ell), v \in H^2(0,\ell), \\ v(0) = Dv(0) = 0, u(\ell) = 0, w = v(\ell)\}$$

$$\mathcal{A}(q)(v(l),u,v) \stackrel{\Delta}{=} (\frac{q_1}{m} Du(l), D^2v, \frac{-q_1}{q_2} D^2u)$$

It is easily argued that the operators $\mathscr{A}(q)$ are densely defined, dissipative (in fact, conservative) and skew-self-adjoint. This in turn implies that they are closed and maximal dissipative. Therefore for each $q=(q_1,q_2)^T$ ϵ Q, the operator $\mathscr{A}(q)$ is the infinitesimal generator of a \mathscr{C}_0 -semigroup of contractions $\{S(t;\,q)\colon\ t\geq 0\}$ on Z_q .

For each t \geq 0 and each q ϵ Q define F(t; q) ϵ Z_q by

$$F(t; q) \stackrel{\Delta}{=} (0, 0, \frac{1}{q_2} f(\cdot, t))$$
 (8-7)

and consider

$$z(t; q) = S(t; q)z_0 + \int_0^t S(t-\tau; q)F(\tau; q)d\tau$$
 (8-8)

where $z_0 \in Z$. For each $q \in Q$ and $z_0 \in Z$ the function $z(\cdot; q)$ given by Eq. (8-8) is a well defined continuous mapping of the non-negative real numbers into the space Z. Moreover, it is a mild solution [Ref. 8-9] to the abstract evolution equation initial value problem in z given by

$$\dot{z}(t) = \mathcal{A}(q)z(t) + F(t; q)$$

$$z(0) = z_0$$

Under the additional hypotheses that $z_0 = (\psi(t), D^2\phi, \psi) \in \mathcal{D}$ and $f \in C^1([0,T], H^0(0,t))$ we obtain a classical solution to the system Eqs. (8-1) through (8-5) via the equivalence

$$z(t; q) = (u_t(t,t; q), u_{xx}(\cdot,t; q), u_t(\cdot,t; q))$$
 (8-9)

where once again $u(\cdot,\cdot;q)$ denotes the solution to Eqs. (8-1) through (8-5) corresponding to EI = q_1 , and $\rho = q_2$.

In light of Eq. (8-9) and our remarks above we define, for each $x \in [0, 1]$ and each $z=(w,u,v) \in Z$, the bounded operators C(x): Z + R by

$$C(x)z = \int_{0}^{x} \int_{0}^{\tau} u(\sigma)d\sigma d\tau$$

and rewrite the identification problem (ID) in the form given by:

(ID) Find q € Q which minimizes

$$J(q) = \sum_{i=1}^{\nu} \sum_{j=1}^{\mu} |C(x_i)z(t_j; q) - \hat{u}(x_i, t_j)|^2$$
 (8-10)

where z(t; q) is given by Eq. (8-8).

In the next section we use this abstract formulation of our identification problem to construct a sequence of cubic spline based finite dimensional approximating identification problems which are readily solved using conventional techniques and whose solutions can be shown to, in some sense, approximate solutions to problem (ID).

8.3 The Approximation Schemes and Convergence Results

The construction of our sequence of approximating identification problems is based upon the replacement in Eq. (8-10) of the function

 $z(\cdot; q)$ having infinite dimensional range in Z by a sequence of approximating functions $z^N(\cdot; q)$ having ranges in successively higher but finite dimensional cubic-spline-based subspaces of Z.

Working abstractly at first, for each N = 1,2,*** and each q $\in \mathbb{Q}$ let Z_q^N be a finite dimensional subspace of Z_q which is contained in \mathscr{D} . Let P_q^N denote the orthogonal projection of Z_q onto Z_q^N with respect to the $\langle \cdot, \cdot \rangle_q$ inner product given by Eq. (8-6). Using the standard Galerkin approach we define the linear operators $\mathscr{N}(q)\colon Z_q^N + Z_q^N$ by $\mathscr{N}(q) \stackrel{\Delta}{=} P_q^N \mathscr{N}(q)$. The finite dimensionality of the Z_q^N implies that each of the $\mathscr{N}(q)$ are bounded (although not necessarily uniformly in N). This in turn implies that each of the $\mathscr{N}(q)$ generates a \mathscr{C}_0 -semigroup of bounded linear operators $\{S_q^N(t;q)\colon t\geq 0\}$ on Z_q^N . Furthermore the fact that the operators $\mathscr{N}(q)$ are conservative with respect to the $\langle \cdot, \cdot \rangle_q$ inner product and the P_q^N are orthogonal projections yields

$$\langle x^{N}(q)z^{N}, z^{N}\rangle_{q} = \langle P_{q}^{N}x^{j}(q)z^{N}, z^{N}\rangle_{q} = \langle x^{j}(q)z^{N}, z^{N}\rangle_{q} = 0$$

for each $z^N \in Z_q^N$ and hence that the semigroups $\{S^N(t;\,q)\colon t\ge 0\}$ are in fact contractions. Defining $z^N(t;\,q)$ by

$$z^{N}(t; q) \stackrel{\Delta}{=} S^{N}(t; q)P_{q}^{N} z_{0} + \int_{0}^{t} S^{N}(t-\tau; q)P_{q}^{N} F(\tau;q)d\tau$$
 (8-11)

with $z_0 = (\psi(l), D^2\phi, \psi)$ and F(t; q) given by Eq. (8-7), we formulate the approximating identification problems as:

(IDN) Find $q \in Q$ which minimizes

$$J^{N}(q) = \sum_{i=1}^{\nu} \sum_{j=1}^{\mu} |C(x_{i})z^{N}(t_{j}; q) - \hat{u}(x_{i},t_{j})|^{2}$$

For each N = 1,2,..., let $\{B_j^N\}_{j=-1}^{N+1}$ denote the standard cubic B-splines on the interval [0,t] corresponding to the partition $\Delta^N \equiv \{0,\frac{t}{N},\frac{2}{N},\cdots,t\}$ [Ref. 8-10] and let $\{\hat{B}_j^N\}_{j=-1}^N$ and $\{\bar{B}_j^N\}_{j=1}^{N+1}$ denote the modified cubic B-splines which satisfy $\hat{B}_j^N(t) = 0$, $j = -1,2,\cdots,N$, and $\bar{B}_j^N(0) = D\bar{B}_j^N(0) = 0$, respectively. Then

$$\hat{B}_{j}^{N}(x) = B_{j}^{N}(x), \quad j = -1, \dots, N-2,$$

$$\hat{B}_{N-1}^{N}(x) = B_{N}^{N}(x) - 4B_{N-1}(x)$$

$$\hat{B}_{N}^{N}(x) = B_{N}^{N}(x) - 4B_{N+1}(x)$$

and

$$\bar{B}_{1}^{N}(x) = B_{0}^{N}(x) - 2B_{1}^{N}(x) - 2B_{-1}^{N}(x)$$

$$\bar{B}_{1}^{N}(x) = B_{1}^{N}(x), \quad j = 2, \dots, N+1$$

Define $S^3(\Delta^N) \stackrel{\Delta}{=} \operatorname{span} \left\{ E_j^N \right\}_{j=-1}^{N+1}$, $\hat{S}^3(\Delta^N) \stackrel{\Delta}{=} \operatorname{span} \left\{ \hat{E}_j^N \right\}_{j=-1}^N$, $\bar{S}^3(\Delta^N) = \operatorname{span} \left\{ \bar{E}_j^N \right\}_{j=1}^{N+1}$ and

$$z^{N} = \{(v(t), u, v) \in Z: u \in \hat{S}^{3}(\Delta^{N}), v \in \bar{S}^{3}(\Delta^{N})\}$$

Since $S^3(\Delta^N) \in H^2(0, L)$, it is immediately clear from the above definitions that $Z^N \subseteq \mathscr{D}$ for all N. Let Z_q^N be the Hilbert space comprised of the space Z^N together with the $\langle \cdot , \cdot \rangle_q$ inner product.

Defining

$$\Phi_{j}^{N} \stackrel{\triangle}{=} (0, \hat{B}_{j}^{N}, 0) , j = -1, \dots, N$$

$$\Psi_{j}^{N} \stackrel{\triangle}{=} (\bar{B}_{j}^{N}(2), 0, \bar{B}_{j}^{N}) , j = 1, \dots, N+1$$
(8-12)

it is easily seen that $Z^N = \operatorname{span} \left\{ \Phi_j^N \right\}_{j=-1}^N + \operatorname{span} \left\{ \Psi^N \right\}_{j=1}^{N+1}$, $\left\{ \Phi_j^N \right\}_{j=-1}^N \bigcup \left\{ \overline{\Psi}_j^N \right\}_{j=1}^{N+1}$ is a basis for Z^N and hence that Z_q^N is a (2N+3)-dimensional subspace of Z_q^N .

Using the standard normal equation characterization for the orthogonal projection $\mathbf{P}_{q}^{\mathbf{N}}$,

$$\langle P_q^N z - z, z^N \rangle_q = 0$$
 , $z \in Z_q$, $z^N \in Z_q^N$ (8-13)

the vector representation ζ^N for $z^N=P_q^Nz$ with respect to the basis given by Eq. (8-12) where z=(w,u,v) can be computed as

$$\zeta^{N} = \left[M_{q}^{N}\right]^{-1} \bar{z}_{q}^{N}$$

where

$$M_{\mathbf{q}}^{\mathbf{N}} = \begin{bmatrix} C_{\mathbf{q}}^{\mathbf{N}} & 0 \\ \vdots & \ddots & \vdots \\ 0 & D_{\mathbf{q}}^{\mathbf{N}} \end{bmatrix}$$

with

$$\begin{bmatrix} c_{\mathbf{q}}^{N} \end{bmatrix}_{i,j} = q_{1} \int_{0}^{\hat{x}} \hat{B}_{i}^{N} \hat{B}_{j}^{N}, \quad i,j = -1, \cdots, N$$

$$\begin{bmatrix} D_{\mathbf{q}}^{N} \end{bmatrix}_{i,j} = m \bar{B}_{i}^{N}(\hat{x}) \bar{B}_{j}^{N}(\hat{x}) + q_{2} \int_{0}^{\hat{x}} \bar{B}_{i}^{N} \bar{B}_{j}^{N}, \quad i,j = 1, \cdots, N+1$$

$$\begin{bmatrix} \bar{u}_{\mathbf{q}}^{N} \end{bmatrix}_{i} = q_{1} \int_{0}^{\hat{x}} u \hat{B}_{i}^{N}, \quad i = -1, \cdots, N$$

$$\begin{bmatrix} \bar{v}_{\mathbf{q}}^{N} \end{bmatrix}_{i} = m w \bar{B}_{i}^{N}(\hat{x}) + q_{2} \int_{0}^{\hat{x}} v \bar{B}_{i}^{N}, \quad i = 1, \cdots, N+1$$

Using the normal equations Eq. (8-13) with $z=\mathcal{A}(q)z^N$ one finds that the matrix representation $A^N(q)$ for the operator $\mathcal{A}^N(q)$ is given by

$$A^{N}(q) = \left[M_{q}^{N}\right]^{-1} K_{q}^{N}$$

where

$$\mathbf{K}_{\mathbf{q}}^{\mathbf{N}} = \begin{bmatrix} 0 & \mathbf{E}_{\mathbf{q}}^{\mathbf{N}} \\ -[\mathbf{E}_{\mathbf{q}}^{\mathbf{N}}]^{\mathbf{T}} & 0 \end{bmatrix}$$

with

$$\left[E_{\mathbf{q}}^{N}\right]_{\mathbf{i}\mathbf{j}} = -\mathbf{q}_{1} \int_{0}^{\mathbf{i}} D\overline{B}_{\mathbf{i}}^{N} D\overline{B}_{\mathbf{j}}^{N}$$
, $\mathbf{i} = -1, \dots, N$, $\mathbf{j} = 1, \dots, N+1$

In the context of the cubic-spline based framework described above, the approximating identification problems (IDN) take the form:

(IDN) Find $q \in Q$ which minimizes

$$J^{N}(q) = \sum_{i=1}^{\nu} \sum_{j=1}^{\mu} \left| \sum_{k=-1}^{N} \zeta_{k}^{N}(t_{j}; q) \hat{\beta}_{k}^{N}(x_{i}) - \hat{u}(x_{i}, t_{j}) \right|^{2}$$

subject to

$$\zeta^{N}(t; q) = \exp(A^{N}(q)t)\zeta_{0}^{N}(q) + \int_{0}^{t} \exp(A^{N}(q)(t-\tau))\gamma^{N}(\tau; q)d\tau$$
 (8-14)

where the expression given by Eq. (8-14) is the vector form of Eq. (8-8) with respect to the basis of Eq. (8-12); $\gamma^N(t;q)$ is the vector representation for $P_q^N F(t;q)$; $\zeta_0^N(q)$ is the vector representation for $P_q^N(\psi(t), D^2\phi, \psi)$; and

$$\hat{\beta}_{j}^{N}(x) = C(x)\Phi_{j}^{N} = \int_{0}^{x} \int_{0}^{\tau_{\alpha}^{N}} \hat{\beta}_{j}^{N}(\sigma) d\sigma d\tau$$
, $j = -1, \dots, N$

Noting that Eq. (8-14) is the classical variation of parameters form of the solution to the (2N+3)-dimensional linear ordinary differential equation initial value problem

$$\dot{\xi}^{N}(t) = A^{N}(q)\xi^{N}(t) + \gamma^{N}(t; q)$$
 (8-15)

$$\zeta^{N}(0) = \zeta_{0}^{N}(q)$$
 (8-16)

we observe that the finite dimensionally constrained optimization problem given above is one which can be solved using any one of a number of standard numerical techniques and readily available software.

We now briefly outline some of our theoretical convergence results. We first note that using standard continuous dependence results for ordinary differential equations it is not difficult to argue that for each N = 1,2,*** fixed, $z^N(t; q)$ depends continuously upon q. This in turn implies that $J^N(q)$ depends continuously upon q and hence, since Q was assumed to be compact, that each of the approximating identification problems (IDN) admits a solution.

Our fundamental convergence results are summarized in the following two theorems.

Theorem 8-1. Let $\{q^N\}$ be a sequence in Q with $q^N + q^* \in Q$. Then

$$z^{N}(t; q^{N}) + z(t; q^{*})$$
 in $z_{q^{N}}$

for each t > 0 where z(t; q) and $z^{N}(t; q)$ are given by Eqs. (8-8) and (8-11), respectively.

Theorem 8-2. Let \overline{q}^N be a solution to the N-th approximating identification problem (IDN). Then the sequence $\{\overline{q}^N\}$ admits a convergent subsequence $\{\overline{q}^N_k\}$ with $\overline{q}^N_k + \overline{q} \in Q$ as $k + \infty$. Moreover, \overline{q} is a solution to the original identification problem (ID).

<u>Proof.</u> Theorem 8-2 is easily proven using Theorem 8-1. Indeed, the existence of \overline{q}^N for each N is easily inferred from our earlier remarks. The existence of $\{\overline{q}^{Nk}\}$ and \overline{q} is a direct consequence of Q being a compact subset of R^2 . Using Theorem 8-1 and the fact that \overline{q}^N is a solution to the N-th approximating identification problem, we have for any $q \in Q$:

$$J(q) = \lim_{k \to \infty} J^{N_k}(\overline{q}^{N_k}) \leq \lim_{k \to \infty} J^{N_k}(q) = J(q)$$

and the result follows.

Using the triangle inequality, the Lebesgue dominated convergence theorem, and the fact that $\|S^N(t;q)\|_q \le 1$, $t \ge 0$, $q \in 0$, Theorem 8-1 follows easily once we have argued that the following two propositions hold.

<u>Proposition 8-3.</u> $P_q^N \rightarrow I$ strongly in Z_q , uniformly in q, for q $\in Q$.

Proposition 8-4. If $q^{N} + q^{*}$ as $N + \infty$ then

$$|s^{N}(t; q^{N})P_{qN}^{N}z - P_{qN}^{N}S(t; q*)z|_{qN} + 0$$

for each $z \in Z$, uniformly in t, for t in compact subsets of $[0,\infty)$.

Proof of Propositions. For $z=(w,u,v) \in Z$, let $P_{qN}^N z=(v^N(\ell), u^N, v^N)$. Using standard error estimates for interpolatory splines [Ref. 8-11, Theorem 4.6] and the Schmidt inequality [Ref. 8-11, Theorem 1.5] it can be shown that if $z \in \mathcal{D}' = \{z \in \mathcal{D}: u,v \in H^4(0,\ell)\}$ then

$$u^{N} + u, \quad v^{N} + v \quad \text{in } H^{2}(0, 2)$$
 (8-17)

Proposition 8-3 then follows from the facts that the P_q^N are uniformly bounded (being orthogonal projections) and that \mathcal{D}^t is uniformly dense in Z_q with respect to $q \in Q$.

Proposition 8-4 is proven with the aid of the following version of a well known approximation result from the theory of semigroups known as the Trotter-Kato theorem [Refs. 8-6, 8-9].

Theorem 8-5. Let $\{B, \| \cdot \| \}$ and $\{B^N, \| \cdot \|_N \}$, $N = 1, 2, \cdots$ be Banach spaces and let $\mathbb{I}^N \colon B \to B^N$ be bounded linear operators. Assume further that T(t) and $T^N(t)$ are linear \mathscr{C}_0 -semigroups on B and B^N with infinitesimal generators A and A^N respectively. If

- (i) $\lim_{N\to\infty} \|\Pi^N z\|_N = \|z\|, \quad z \in B$;
- (ii) there exist constants M, ω independent of N such that $\|\textbf{T}^N(\textbf{t})\|_N \leq \text{Me}^{\omega \textbf{t}} \text{ for } \textbf{t} \geq 0 \ ;$
- (iii) there exists a set $D \subset B$ such that $D \subset Dom(A)$, $\overline{D} = B$ and $\overline{(\lambda_0 A)D} = B$ for some $\lambda_0 > 0$ and for which for all $z \in D$ we have $\lim_{N \to \infty} \|A^N \Pi^N z \Pi^N Az\|_N = 0$;

then $\lim_{N\to\infty} \|T^N(t)\Pi^N z - \Pi^N T(t)z\|_{N} = 0$ for all $z \in B$ uniformly in t on compact subsets of $[0,\infty)$.

Making the identifications $B = Z_{q*}$, $B^N = Z_{qN}^N$, $\Pi^N = P_{qN}^N$, T(t) = S(t; q*), $T^N(t) = S^N(t; q^N)$, $A = \mathcal{A}(q*)$, and $A^N = \mathcal{A}^N(qN)$, Proposition 8-4 will clearly follow if we can demonstrate that hypotheses (i) through (iii) hold.

Now (i) is a direct consequence of Proposition 8-3, while the fact that $\{S(t; q^*): t \ge 0\}$ and $\{S^N(t; q^N): t \ge 0\}$ are both contraction semigroups implies that (ii) holds with M = 1 and ω = 0. Choosing

 $D = Dom(\mathscr{A}(q^*)^2), \text{ we have that } D \subset Z_{q^*}, D = Dom(\mathscr{A}(q^*)^2) \subset Dom(\mathscr{A}(q^*)^2) = \mathscr{D} \text{ and } \overline{\lambda_0} - \overline{(q^*)D} = \overline{\mathscr{D}} = Z_{q^*} \text{ for all } \lambda_0 > 0.$ Linear semigroup theory [Ref. 8-9] implies that $\bigcap_{k=1}^{\infty} Dom(\mathscr{A}(q^*)^k)$ is dense in Z_q^* and hence that $\overline{D} = \overline{Dom(\mathscr{A}(q^*)^2)} = Z_{q^*}$. Finally, noting that that $D \subset \mathscr{D}'$,

$$\left\| \mathcal{A}^{N}(q^{N})P_{qN}^{N} z - P_{qN}^{N} \mathcal{A}(q^{*})z \right\|_{qN} = \left\| P_{qN}^{N} \mathcal{A}(q^{N})P_{qN}^{N} z - P_{qN}^{N} \mathcal{A}(q^{*})z \right\|_{qN}$$

$$\leq \left\| \mathcal{A}(q^{N})P_{qN}^{N} z - \mathcal{A}(q^{*})z \right\|_{qN}$$

$$\leq \left\| \left(\mathcal{A}(q^{N}) - \mathcal{A}(q^{*}) \right)P_{qN}^{N} z \right\|_{qN} + \left\| \mathcal{A}(q^{*})(P_{qN}^{N} - 1)z \right\|_{qN}$$

and recalling the definition of $\mathcal{A}(q)$, the \mathbb{H}^2 convergence in Eq. (8-17), and the fact that $q^N + q^*$ as $N + \infty$, we have that the last two terms in the inequality above tend toward zero as $N + \infty$ and hence that (111) obtains and the result is proven.

8.4 A Numerical Example

We applied our method to the problem of estimating the flexural stiffness EI and linear mass density ρ of a beam of length $\ell=1$ clamped at one end and cantilevered at the other end with an attached tip mass of magnitude 1.5. The system was assumed to be initially at rest and then excited by an impulse at position x=1 at time t=0. We approximated the impulse input by

$$f(x,t) = 20 e^{-2t} e^{-20(1-x)}$$

We solved the resulting approximating identification problems (IDN) using the IMSL [Ref. 8-5] routine ZXSSQ. This routine is an iterative Levenberg-Marquardt Newton's-method/steepest-descent hybrid algorithm [Refs. 8-7, 8-8]. The necessary gradients and entries in the Jacobian matrix are computed numerically using finite difference approximations and a rank one update to minimize the number of function calls to evaluate J required in each iteration. The method requires that initial start-up values for EI and ρ be provided.

The evaluation of J necessitates the integration of the initial value problem Eqs. (8-15) and (8-16). This is accomplished using the IMSL routine DGEAR, a variable order Adams Predictor Corrector Method [Ref. (8-4].

Choosing EI = 1.0 and ρ = 3.0, observations $\hat{\mathbf{u}}(\mathbf{x_i}, \mathbf{t_j})$ were generated by solving the system Eqs. (8-1) through (8-5) using a Galerkin method and the system's first three natural mode shapes. We specified data at x = 0.5, 0.625, 0.75, 0.875, 1.0 and t = (0.2)i, i = 1,2,...,10. Our results are summarized in Table 8-1.

Table 8-1. Convergence of approximations for beam example.

N	ĒĪΝ	−N P	J _N
2	0.99763	3.02617	0.39 × 10 ⁻⁵
3	0.99938	3.03821	0.46×10^{-5}
4	0.995101	3.05439	0.48×10^{-5}
5	0.996111	3.04091	0.40×10^{-5}
6	0.99946	2.99761	0.35 × 10 ⁻⁵
True Value	1.0	3.0	

8.5 Concluding Remarks

Although we have only discussed the application of our methods to a simple problem involving a cantilevered beam with an attached tip mass, it is in fact the case that our general approach is applicable to rather broad classes of problems. Some of the possible extensions to the results presented here include:

- a. The inclusion of terms which model damping effects into the dynamical equations [Ref. 8-1];
- b. Attached tip body or bodies having nonzero moments of inertia and mass center offsets;
- c. Articulated structures;
- d. The estimation of other parameters in addition to the flexural stiffness and mass density of the beam. For example, the identification of the rigid body mass properties of the tip body, damping parameters, and parameters which appear in the initial conditions and the externally applied loads;
- e. The inclusion of effects due to axially directed loading; and
- f. The use of more sophisticated models for the transverse vibration of the beam (e.g. the Timoshenko theory [Ref. 8-2]).

We are currently investigating another cubic spline based numerical approximation method for the identification problems discussed above. This method involves the use of an appropriate energy inner product and standard Galerkin approach applied directly to the ordinary and partial differential equations which describe the dynamics of the system. It has the potential to offer a significant improvement in computational efficiency over the schemes which were discussed here. Theoretical convergence results and our numerical findings will be discussed in a future report.

References

- 8-1. Banks, H.T. and Crowley, J.M., "Parameter Estimation for Distributed Systems Arising in Elasticity," Report 81-38, Institute for Computer Applications in Science and Engineering (ICASE), Hampton, VA, 1981.
- 8-2. Banks, H.T. and Crowley, J.M., "Parameter Estimation in Timoshenko Beam Models," Report 82-22, ICASE, Hampton, VA, 1982.
- 8-3. Burns, J.A. and Cliff, E.M., "An Approximation Technique for the Control and Identification of Hybrid Systems," Proceedings of the Third VPI&SU/AIAA Symposium on the Dynamics and Control of Large Flexible Spacecraft, Blacksburg, VA, June 1981.
- 8-4. Gear, C.W., Numerical Initial Value Problems in Ordinary Differential Equations, Prentice Hall, Englewood Cliffs, NJ, 1971.
- 8-5. International Mathematics and Statistical Libraries, Ninth Edition, Houston, TX, 1983.
- 8-6. Kurtz, T.G., "Extensions of Trotter's Operator Semigroup Approximation Theorem," <u>J. Functional Analysis</u>, Vol. 3, 1969, pp. 354-375.
- 8-7. Levenberg, K., "A Method for the Solution of Certain Non-linear Problems in Least Squares," Quarterly Applied Math., Vol. 2, 1944, pp. 164-168.
- 8-8. Marquardt, D.W., "An Algorithm for Least Squares Estimation of Nonlinear Parameters," J. SIAM, Vol. 11, No. 2, 1963.
- 8-9. Pazy, A., Semigroups of Linear Operators and Applications to

 Partial Differential Equations, Springer-Verlag, New York, NY,

 1983.
- 8-10. Prenter, P.M., Splines and Variational Methods, Wiley-Interscience, New York, NY, 1975.
- 8-11. Schultz, M.H., Spline Analysis, Prentice Hall, Englewood Cliffs, NJ, 1973.

8-12. Storch, J. and Gates, S., "Planar Dynamics of a Uniform Beam with Rigid Bodies Affixed to the Ends," Report CSDL-R-1629, Charles Stark Draper Laboratory, Cambridge, MA, May 1983.

DISTRIBUTION LIST

addresses		number
		of copies
Richard W. Carman RADC/OCSP	WARRENSH LA	5
· ·		
RADC/TSTD		1.
FIFFISS AFB NY 13441		
FADC/DAP		2
GRIFFISS AFB NY 13441		
MINISTRATOR		12
DEF TECH INF CTR		
ATTN: DTIC-DDA CAMERON STA BG 5		
ALEXANDRIA VA 22314		
Charles Stark Draper Lab		5
555 Technology Square		
Cambridge, MA 02139		
Sharles Stark Draper Lab		1
Attn: Dr. Keto Soosaar		
555 Technology Square		
Cambridge, MA 02139		
NASA Headquarters		1
ATTN: Mr. J. B. Dahlgren		
Code RTH-6 Washington, DC 20546		
	ALL ALL MANNEY SALVA.	
General Research Corporation		1
Attn. Mr. R. Strunce 7655 Old Springhouse Road		
McClean VA 22102		

こうこう こうけいしょう こうしょうしょう しょうしょうしょう こうしゅうしゅ こうしゅうしゅ こうしゅうしゅうしゅうしゅ かんしゅうしゅうしゅうしゅうしゅうしゅう

Charles Stark Draper Lab Attn: Dr. Daniel R. Hegg 555 Technology Square M.S60	1
Cambridge, MA 02139	
ARPA/STO Attn: Lt Col A. Herzberg 1400 Wilson Blvd Aclington, VA 22209	i
APPA/STO	1
riverside Research Institute	
tn Mr. A. DeVilliers 701 N Ft. Myer Drive, Suite 711 Arlington, VA 22209	
Aiverside Research Abtn: HALO Library, Mr. Bob Passut 1701 N. Ft. Myer Drive	
Arlington, VA 22209	
the state of the s	
Itek Corp Optical Systems Division 10 Maguire Rd.	ı
Lexington, MA 02173	
Ferkin Elmer Corp Attn: Mr. H. Levenstein Electro Optical Division	
Main Avenue Norwalk, CT 06856	
4ttn: Mr. George Speak	1
M.S. B_156 Obliver City, CA 09230	
Hughes Aircraft Company Attn: Mr. Ken Beale Centinela Teale Sts Culver City, CA 90230	i

Air Force Flight Dynamics Lab Attn+ Dr. Lynn Rogers Wright Patterson AFB, OH 45433		1
AFWL/FIBG Attn: Mr. Jerome Pearson Wright Patterson AFB, OH 45433		1
Air Force Wright Aero Lab. FIGC Attn. Siva S. Banda Wright Patterson AFB, OH 45433		1.
Air Force Institute of Technology Attn: Prof. R. Calico/ENY Aright Patterson AFB, OH 45433		i
Rerospace Corp. Attn: Dr. G.T. Tseng 2350 E. El Segundo Blvd El Segundo, CA 90245	CTIES AN INC.	3
Aerospace Corp. Attn: Mr. J. Mosich 2350 E. El Segundo Blvd El Segundo, CA 90245	TORU AN ACT	1
Asrospace Corp/Bldg 125/1054 Attn: Mr. Steve Burrin Advanced Systems Tech Div. 2400 E El Segundo Blvd El Segundo, CA 90245		1
Attn: Mr. Lawrence Weeks		
SD/YCD Attn: YCPT/Capt Gajewski f.O. Box 92960 Worldway Postal Center		i

Grumman Aerospace Corp Attn: Dr. A. Mendelson South Oyster Bay Road Satnpage, NY 11714	1
OUSDR&E/DS Attn. Mr. A. Bertapelli Room 3D136 Pentagon, Washington, DC 20301	1
Jet Propulsion Laboratory Dr. S. Szermay 4000 Dak Grove Drive Pasadena, CA 91103	
MIT/Lincoln Laboratory Actn: S. Wright F.O. Box 73 Lexington, MA 02173	
MIT/Lincoln Laboratory Attn: Dr. D. Hyland P.O. Box 73 Lexington, MA 02173	
MIT/Lincoln Laboratory Attn: Dr. N. Smith P.O. Box 73 Lexington, MA 02173	
Control Dynamics Co. Attn: Dr. Sherman Seltzer Suite 1414 Executive Plaza 555 Sparkman Drive Huntsville, AL 35805	
Lockheed Space Missile Corp. Attn. A. A. Woods, Jr., 0/62-E6 p.O. Box 504	5

Lockheed Missiles Space Co. Attn: Mr. Paul Williamson 3251 Hanover St. Palo Alto, CA 94304		
General Dynamics Attn: Ray Halstenberg Convair Division 5001 Keary Villa Rd San Diego, CA 92123	TORY ATT TO BREAK SURFERING TO THE PROPERTY OF THE	
STI Sttn: Mr. R.C. Stroud 20065 Stevens Creek Blvd. Copertions, CA 95014		
MASA Langley Research Ctr Actn: Dr. Earle K. Huckins II Or. M. F. Card Langley Station, Bldg 12938, Hampton, VA 23665	ms 230	2
NASA Johnson Space Center Attn: Robert Piland Ms. EA Mouston, TX 77058	H her votalist 4	1
McDonald Douglas Corp Attn: Mr. Read Johnson Douglas Missile Space System 5301 Bulsa Ave Huntington Beach, CA 92607	s Div	1
Integrated Systems Inc. Actn: Dr. N. K. Gupta and M. G 151 University Avenue, Suite Palo Alto, California 94301	. Lyons 400	5
Ecaing Aerospace Company Attn: Mr. Leo Cline P.O. Box 3999 Seattle, WA 98124 MS 8 W-23		1
TRW Defense Space Sys Group Attn: Ralph Twens Bldg 82/2054 One Space Park Redondo Beach, CA 90278	en e	1

TRW Attn: Mr. Len Pincus Bldg R-5, Room 2031 Redondo Beach, CA 90278	
Attn: Dr. K.T. Alfriend Naval Research Laboratory Code 7920	1
Airesearch Manuf. Co. of Calif. Attn: Mr. Oscar Buchmann 2525 West 190th St. Torrance, CA 90509	i
Analytic Decisions, Inc. Attn: Mr. Gary Glaser 1401 Wilson Blvrlington, VA 22209	1
Ford Aerospace & Communications Corp. Ors. I. P. Leliakov and P. Barba, MS/G80 3939 Fabian way Falo Alto, California 94304	1
Center for Analysis Mr. James Justice 13 Corporate Plaza Newport Beach, CA 92660	1
W. J. Schafer Associates Dr. R. Kappesser Soite 800 1901 Fort Meyer Drive Arlington, VA 22209	i
Jeneral Research Corp Actn. Mr. Thomas Zakrzewski 7455 Old Springhouse Pond	1
Air Force Weapons Laboratory Attn: Lt Col D. Washburn ARAA Kirtland AFB, NM 87117	2

Karman Sciences Corp. Attn: Dr. Walter E. Ware 1500 Garden of the Gods Road P.O. Box 7463 Calorado Springs, CO 80933	1
MRJ, Inc. 10400 Eaton Place Suite 300 Fairfax, VA 22030	1
Enoton Research Associates Actn. mr. Jim Myer P.O. Box 1318 La Jolla, CA 92038	1
Rockwell International Attn: Russell Loftman (Space Systems Group) Mail Code - SL56) 12214 Lakewood Blvd Journey, CA 90241	1
Science Applications, Inc. Attn: Mr. Richard Ryan 3 Preston Court Bedford, MA 01730	1
U.S. Army Missile Command Altn: DRSMI-RAS/Mr. Fred Haak Redstone Arsenal, AL	1
Naval Electronic Systems Command Attn: Mr. Charles Good PME_106-4 National Center I Washington, DC 20360	1
Lockheed Palo Alto Research Laboratory Attn: Dr. J. N. Aubrum, 0/52-56 3251 Hanover Street Palo Alto, California 94304-1187	2
U.S. Army/DARCOM Actn: Mr. Bernie Chasnov AMC Bldg SOOI Eisenhower Ave Alexandria, VA 22333	1

Honeywell Inc. 2 Attn: Dr. Thomas B. Cunningham Actn: Dr. Michael F. Barrett 2600 Ridgway Parkway MN 17-2375 Minneapolis, MN 55413 2 MASA Marshal Space Flight Center Attn. Dr. J. C. Blair, EDO1 Henry B. Waites Marshal Space Flight Centér, AL 35812 TRW Attn: Robert Benhabib 61dg 82/2024 One Space Park Redondo Beach, CA 90278 MASA Langley Research Center eitn Dr. L. Pinson MS - 230 Sampton, VA 23665 H. R. Textron Attn. Mr. Richard Quartararo 2485 McCabe Way Irvine, CA 92714 1 . Naval Research Lab Attn: W. Bennett Mail Code: 7926 Washington, DC 20375

Richard Canson Jun 84

COLOROS COLORO

MISSION of Rome Air Development Center

RADC plans and executes research, development, test and selected acquisition programs in support of Command, Control Communications and Intelligence (C³I) activities. Technical and engineering support within areas of technical competence is provided to ESD Program Offices (POs) and other ESD elements. The principal technical mission areas are communications, electromagnetic guidance and control, surveillance of ground and aerospace objects, intelligence data collection and handling, information system technology, ionospheric propagation, solid state sciences, microwave physics and electronic reliability, maintainability and compatibility.